

# Recent Advances in Theory and Applications of Electromagnetic Metamaterials

Guest Editors: Weiren Zhu, Ivan D. Rukhlenko, Roman E. Noskov, Ronghong Jin, and Ji Zhou



---

# **Recent Advances in Theory and Applications of Electromagnetic Metamaterials**

## **Recent Advances in Theory and Applications of Electromagnetic Metamaterials**

Guest Editors: Weiren Zhu, Ivan D. Rukhlenko,  
Roman E. Noskov, Ronghong Jin, and Ji Zhou



---

Copyright © 2015 Hindawi Publishing Corporation. All rights reserved.

This is a special issue published in "International Journal of Antennas and Propagation." All articles are open access articles distributed under the Creative Commons Attribution License, which permits unrestricted use, distribution, and reproduction in any medium, provided the original work is properly cited.

## Editorial Board

- |                                 |                                  |                                 |
|---------------------------------|----------------------------------|---------------------------------|
| Ana Alejos, Spain               | Flaminio Ferrara, Italy          | N. Nasimuddin, Singapore        |
| Mohammod Ali, USA               | Vincenzo Galdi, Italy            | Miguel Navarro-Cia, UK          |
| Jaume Anguera, Spain            | Claudio Gennarelli, Italy        | Mourad Nedil, Canada            |
| Rodolfo Araneo, Italy           | Sotirios K. Goudos, Greece       | Symeon Nikolaou, Cyprus         |
| Ercument Arvas, USA             | Rocco Guerriero, Italy           | Giacomo Oliveri, Italy          |
| Alexei Ashikhmin, USA           | Kerim Guney, Turkey              | Pablo Otero, Spain              |
| Herve Aubert, France            | Song Guo, Japan                  | Athanasiос Panagopoulos, Greece |
| Paolo Baccarelli, Italy         | Mohamed Himdi, France            | Ikmo Park, Korea                |
| Xiulong Bao, Ireland            | Tamer S. Ibrahim, USA            | Josep Parrón, Spain             |
| Toni Björninen, Finland         | Mohammad Islam, Malaysia         | Matteo Pastorino, Italy         |
| Stefania Bonafoni, Italy        | M. R. Kamarudin, Malaysia        | Massimiliano Pieraccini, Italy  |
| Djuradj S. Budimir, UK          | Kyeong Jin Kim, USA              | Xianming Qing, Singapore        |
| Paolo Burghignoli, Italy        | Ahmed A. Kishk, Canada           | Ahmad Safaai-Jazi, USA          |
| Shah N. Burokur, France         | Slawomir Koziel, Iceland         | Safieddin Safavi-Naeini, Canada |
| Giuseppe Castaldi, Italy        | Luis Landesa, Spain              | Magdalena Salazar-Palma, Spain  |
| Felipe Cátedra, Spain           | Ding-Bing Lin, Taiwan            | Stefano Selleri, Italy          |
| Marta Cavagnaro, Italy          | Angelo Liseno, Italy             | John J. Shynk, USA              |
| Deb Chatterjee, USA             | Pierfrancesco Lombardo, Italy    | Prabhakar Singh, India          |
| Shih Yuan Chen, Taiwan          | Giampiero Lovat, Italy           | Raffaele Solimene, Italy        |
| Yu Jian Cheng, China            | Lorenzo Luini, Italy             | Gino Sorbello, Italy            |
| Renato Cicchetti, Italy         | Atsushi Mase, Japan              | Seong-Youp Suh, USA             |
| Lorenzo Crocco, Italy           | Diego Masotti, Italy             | Sheng Sun, Hong Kong            |
| Claudio Curcio, Italy           | David W. Matolak, USA            | Larbi Talbi, Canada             |
| Francesco D'Agostino, Italy     | Giuseppe Mazzarella, Italy       | Luciano Tarricone, Italy        |
| Maria E. De Cos, Spain          | C. F. Mecklenbräuker, Austria    | Parveen Wahid, USA              |
| Tayeb A. Denidni, Canada        | Massimo Migliozi, Italy          | Yuanxun Ethan Wang, USA         |
| Giuseppe Di Massa, Italy        | Mark Mirotznik, USA              | Wen-Qin Wang, China             |
| Michele D'Urso, Italy           | Ahmed T. Mobashsher, Australia   | Shiwen Yang, China              |
| Hala A. Elsadek, Egypt          | Ananda S. Mohan, Australia       | Yuan Yao, China                 |
| Francisco Falcone, Spain        | J.-M. Molina-Garcia-Pardo, Spain | Jingjing Zhang, Denmark         |
| Miguel Ferrando Bataller, Spain | Marco Mussetta, Italy            |                                 |

## Contents

**Recent Advances in Theory and Applications of Electromagnetic Metamaterials**, Weiren Zhu, Ivan D. Rukhlenko, Roman E. Noskov, Ronghong Jin, and Ji Zhou  
Volume 2015, Article ID 982325, 2 pages

**Dielectric Behavior of Low Microwave Loss Unit Cell for All Dielectric Metamaterial**, Tianhuan Luo, Bo Li, Qian Zhao, and Ji Zhou  
Volume 2015, Article ID 291234, 6 pages

**High Power Efficiency Buck Converter Design for Standalone Wind Generation System**, Yigeng Huangfu, Ruiqing Ma, Bo Liang, and Yuren Li  
Volume 2015, Article ID 751830, 9 pages

**High-Directivity Antenna Array Based on Artificial Electromagnetic Metamaterials with Low Refractive Index**, Zhigang Xiao, Jiang Yao, and Shaoquan Yin  
Volume 2015, Article ID 294598, 6 pages

**Taming the Electromagnetic Boundaries via Metasurfaces: From Theory and Fabrication to Functional Devices**, Xiangang Luo, Mingbo Pu, Xiaoliang Ma, and Xiong Li  
Volume 2015, Article ID 204127, 80 pages

**Resonances in Reverse Vavilov-Cherenkov Radiation Produced by Electron Beam Passage over Periodic Interface**, Gerard Granet, Petr Melezik, Anatoliy Poyedinchuk, Seil Sautbekov, Yuriy Sirenko, and Nataliya Yashina  
Volume 2015, Article ID 784204, 10 pages

**Photonic Wannier-Stark Ladder from Coupled Electromagnetic Cavities**, Shahzad Anwar, Sucheng Li, Weixin Lu, and Bo Hou  
Volume 2015, Article ID 360359, 6 pages

**Recent Advances in the Modeling of Transmission Lines Loaded with Split Ring Resonators**, Jordi Naqui, Lijuan Su, Javier Mata, and Ferran Martín  
Volume 2015, Article ID 792750, 13 pages

**Polarization-Independent and Angle-Insensitive Metamaterial Absorber Using 90-Degree-Rotated Split-Ring Resonators**, Jia-Qi Feng, Wei-Dong Hu, Qing-Le Zhang, Hua Zong, Hui Huang, Yu-Ting Jin, Yu-Ming Wu, Zhan Xu, Xin Lv, and Li-Ming Si  
Volume 2015, Article ID 240691, 6 pages

**Compact Microstrip Bandpass Diplexer Based on Twist Revised Split Ring Resonators**, Jian Li, Yongjun Huang, Xuefeng Zhao, and Guangjun Wen  
Volume 2015, Article ID 698714, 6 pages

## Editorial

# Recent Advances in Theory and Applications of Electromagnetic Metamaterials

Weiren Zhu,<sup>1</sup> Ivan D. Rukhlenko,<sup>1,2</sup> Roman E. Noskov,<sup>3</sup> Ronghong Jin,<sup>4</sup> and Ji Zhou<sup>5</sup>

<sup>1</sup>Advanced Computing and Simulation Laboratory ( $A\chi L$ ), Department of Electrical and Computer Systems Engineering, Monash University, Clayton, VIC 3800, Australia

<sup>2</sup>ITMO University, Saint Petersburg 197101, Russia

<sup>3</sup>Max Planck Institute for the Science of Light, 91058 Erlangen, Germany

<sup>4</sup>Department of Electronic Engineering, Shanghai Jiao Tong University, Shanghai 200240, China

<sup>5</sup>State Key Lab of New Ceramics and Fine Processing, School of Materials Science and Engineering, Tsinghua University, Beijing 100084, China

Correspondence should be addressed to Weiren Zhu; weiren.zhu@monash.edu

Received 28 July 2015; Accepted 28 July 2015

Copyright © 2015 Weiren Zhu et al. This is an open access article distributed under the Creative Commons Attribution License, which permits unrestricted use, distribution, and reproduction in any medium, provided the original work is properly cited.

The advancement of modern electromagnetic technologies strongly relies on the development of original theoretical approaches and new artificial materials. Metamaterials are recently developed artificially engineered materials made of subwavelength electric circuits instead of atoms or molecules, which are the basic elements interacting with electromagnetic radiation. The design of metamaterials enables intriguing applications and manipulating electromagnetic waves in many ways beyond those achievable with natural materials. For the purpose of fully realizing the potential of metamaterials, this special issue aimed to attract original research and review articles that will stimulate the continuing efforts on the understanding of metamaterials and exploring their applications in electromagnetic engineering. The issue has received a total of 27 submissions, 8 of which were accepted for publication after peer reviewing. The accepted papers cover a broad area of metamaterial in both theory and applications.

The paper “Taming the Electromagnetic Boundaries via Metasurfaces: From Theory and Fabrication to Functional Devices” by X. Luo et al. presents a comprehensive review of the history and recent development of metasurfaces. More specifically, this paper focuses on the theory and applications relating to the frequency response, phase shift, and polarization state control. Based on the current status of various applications, some of the open challenges and future trends towards the application of metasurfaces are discussed.

A review titled “Recent Advances in the Modeling of Transmission Lines Loaded with Split Ring Resonators (SRRs)” by J. Naqui et al. presents the progress achieved in the modeling of coplanar waveguide transmission lines loaded with SRRs, that is, negative-permeability transmission lines. This review includes a comprehensive discussion on the effects of SRR orientation, coupling between the adjacent resonators, and coupling between the two SRRs constituting the unit cell.

The mechanism of resonances in the reverse Vavilov-Cherenkov radiation produced by a charged-particles beam propagating over periodic boundary of a dispersive left-handed medium is studied by G. Granet et al. in their paper “Resonances in Reverse Vavilov-Cherenkov Radiation Produced by Electron Beam Passage over Periodic Interface.” Conditions of radiation initiation, radiation intensity, and the possibility of the existence of different resonant effects in the reverse Vavilov-Cherenkov radiation associated with the excitation of surface waves of the periodic boundary have been studied both analytically and numerically in the approximation of a given current.

By making an analogy to the quantum counterpart in their paper “Photonic Wannier-Stark Ladder from Coupled Electromagnetic Cavities,” S. Anwar et al. present an innovative photonic Wannier-Stark ladder in the system of coupled electromagnetic cavities, where the tilted potential effect is mimicked by imposing the gradient variation of refractive

index. The geometrically progressed eigen energies of the photonic Wannier-Stark ladder are studied through both analytical derivations and numerical simulations.

In their paper “Polarization-Independent and Angle-Insensitive Metamaterial Absorber Using 90-Degree-Rotated Split-Ring Resonators,” J.-Q. Feng et al. present the design, simulation, and measurement of a polarization-independent and angle-insensitive metamaterial absorber. They take four subwavelength split-ring resonators with a 4-fold rotational symmetry to build a unit cell of the absorber, which leads to its insensitivity with respect to both polarization and incident angle of planar electromagnetic waves. The performance of such a metamaterial absorber is examined by both numerical simulations and microwave experiments in the X-band.

Metamaterials made of high-permittivity dielectric resonators offer a low-loss alternative to metal-based metamaterials. T. Luo et al., in their paper “Dielectric Behavior of Low Microwave Loss Unit Cell for All Dielectric Metamaterial,” present the preparation and characterization of calcium titanate ( $\text{CaTiO}_3$ )—a kind of incipient ferroelectrics with high dielectric permittivity and low loss, which can be utilized for constructing all-dielectric metamaterials. The prepared  $\text{CaTiO}_3$  exhibits a high microwave permittivity of about 167 with a dielectric loss of only 0.0005, resulting in a quality factor as large as 2049.

The paper “High-Directivity Antenna Array Based on Artificial Electromagnetic Metamaterials with Low Refractive Index” by Z. Xiao et al. reports on an innovative high-gain patch antenna array using a metamaterial. By covering a metamaterial of low refractive index, the antenna array has advantages in terms of smaller number of array elements, larger element spacing, and simpler feeding network. The metamaterial antenna array also features significantly improved directivity and antenna gain.

In their paper “Compact Microstrip Bandpass Diplexer Based on Twist Revised Split Ring Resonators,” J. Li et al. experimentally demonstrate a compact microstrip bandpass diplexer, which has two close frequency channels centered at 2.16 and 2.91 GHz. The synthesized diplexer has very simple configuration and is of small size and can be potentially integrated into miniaturized RF/microwave integrated circuits.

## Acknowledgments

The authors would like to thank the International Journal of Antennas and Propagation for the opportunity to serve as guest editors of this special issue. They also sincerely thank all the authors for their contributions in this special issue and their patience with the editorial and review processes. They hope readers find interest in the papers in this special issue.

Weiren Zhu  
Ivan D. Rukhlenko  
Roman E. Noskov  
Ronghong Jin  
Ji Zhou

## Research Article

# Dielectric Behavior of Low Microwave Loss Unit Cell for All Dielectric Metamaterial

Tianhuan Luo,<sup>1</sup> Bo Li,<sup>1</sup> Qian Zhao,<sup>2</sup> and Ji Zhou<sup>3</sup>

<sup>1</sup>Advanced Materials Institute, Shenzhen Graduate School, Tsinghua University, Shenzhen 518055, China

<sup>2</sup>State Key Lab of Tribology, Department of Mechanical Engineering, Tsinghua University, Beijing 100084, China

<sup>3</sup>State Key Lab of New Ceramics and Fine Processing, Department of Materials Science and Engineering, Tsinghua University, Beijing 100084, China

Correspondence should be addressed to Bo Li; [boli@mail.tsinghua.edu.cn](mailto:boli@mail.tsinghua.edu.cn) and Qian Zhao; [zhaoqian@tsinghua.edu.cn](mailto:zhaoqian@tsinghua.edu.cn)

Received 9 December 2014; Accepted 29 January 2015

Academic Editor: Roman E. Noskov

Copyright © 2015 Tianhuan Luo et al. This is an open access article distributed under the Creative Commons Attribution License, which permits unrestricted use, distribution, and reproduction in any medium, provided the original work is properly cited.

With a deep study of the metamaterial, its unit cells have been widely extended from metals to dielectrics. The dielectric based unit cells attract much attention because of the advantage of easy preparation, tunability, and higher frequency response, and so forth. Using the conventional solid state method, we prepared a kind of incipient ferroelectrics (calcium titanate,  $\text{CaTiO}_3$ ) with higher microwave permittivity and lower loss, which can be successfully used to construct metamaterials. The temperature and frequency dependence of dielectric constant are also measured under different sintering temperatures. The dielectric spectra showed a slight permittivity decrease with the increase of temperature and exhibited a loss of 0.0005, combined with a higher microwave dielectric constant of ~167 and quality factor  $Q$  of 2049. Therefore,  $\text{CaTiO}_3$  is a kind of versatile and potential metamaterial unit cell. The permittivity of  $\text{CaTiO}_3$  at higher microwave frequency was also examined in the rectangular waveguide and we got the permittivity of 165, creating a new method to test permittivity at higher microwave frequency.

## 1. Introduction

Since increasing attention has been paid to metamaterials due to their novel physical behaviors and versatile applications, such as left-handed metamaterials (LHMs) using split ring resonators (SRRs) and metal wire arrays to produce negative effective permeability and negative permittivity, respectively [1, 2], more and more outstanding ceramic materials such as  $\text{Ba}_x\text{Sr}_{1-x}\text{TiO}_3$  (BST) are being developed and utilized to build some supernormal materials and structures, such as ferromagnetic/ferroelectric composite metamaterial (CMM) with BST rods [3], Mie resonance structures using dielectric BST particles [4, 5], the prism of negative refraction in BST columns [6], and artificial magnetic conductor with high dielectric BST arrays applied in antenna and radar [7], opening a better and more potential approach to construct various isotropic metamaterials, suitable for higher operating frequencies [4]. Although BST has been successfully applied to construct metamaterials, its higher dielectric loss of 0.001 [8] limits its realization of further novel properties.

Therefore, a substitute of the dielectric material needs to be developed and studied. To verify its excellent dielectric properties, systemic research on  $\text{CaTiO}_3$  was accomplished, mainly in two different ways including variation of dielectric constant against frequency in operating frequency range ( $10^6$  Hz~ $10^{10}$  Hz) and against temperature within  $-65^\circ\text{C}$ ~ $120^\circ\text{C}$ , respectively.

## 2. Experimental Details

To gain simplification,  $\text{CaTiO}_3$  ceramic was synthesized through conventional solid state method. All the raw powders were mixed by ball milling with zirconia media in deionized water for 30 h. The powders were pestled in agate mortar after drying, sieved through 50 or 60 mesh sieve. Then, PVA (polyvinyl alcohol, 5 wt%) was added to the sieved powders as organic binder to make the formation of the cylinder of 10 mm in diameter and 1–6 mm in height by uniaxial compression at 4 MPa with the customized mould. Finally

the cylinders were sintered at 5 or 6 kinds of temperature in the range from 1250°C to 1400°C after PVA was volatilized at 600°C, the temperature increasing rate of which is around 3°C/min.

To catch the knowledge of density variation, Archimedes drainage method was taken, to measure the size and weight of specimen as well. To explore the phase structure, X-ray diffraction (XRD-7000 X, SHIMADZU) analysis with Cu-K $\alpha$  radiation was available and accessible. The morphology and microstructure were evaluated by scanning electron microscopy (SEM) with energy dispersive spectroscopy (EDS) (JSM-7001F, JEOL) on the as-sintered and fractured surfaces. To make the microstructure much more persuasive, the JSM-6460LV, JEOL (SEM), were also utilized to verify the previous pictures. The dielectric properties were measured using the impedance analyzers Agilent HP 4192A (5 Hz~13 MHz), and Agilent E4991A (1 MHz~3 GHz). The 4192A measurements were performed at temperatures ranging from -65°C to 120°C and at the same time loaded with six different frequencies containing 10 kHz, 100 kHz, 200 kHz, 500 kHz, 800 kHz, and 1 MHz. The higher frequency dielectric properties were tested by an Agilent HP 8720ES S-Parameter network analyzer (50 MHz~20 GHz) using the Hakki and Coleman dielectric resonator method [9] with the TE<sub>011</sub> [10] and TE<sub>01δ</sub> [11] resonant mode of dielectric resonators excited, measuring the permittivity (including resonant frequency  $f$ ) and unloaded Q factor (containing  $Q * f$ ), respectively. Besides, to gain more understanding of higher microwave frequency behavior, as depicted in Figure 1, we simulated the S-parameter of transmission ( $S_{21}$ ) and reflection ( $S_{11}$ ) of the dielectric cube with Perfect Electric (PE) and Perfect Magnetic (PM) boundary conditions along  $x$  and  $y$  directions, respectively. And the propagation direction of electromagnetic wave should be along  $z$  direction. Finally the prepared single cube CaTiO<sub>3</sub> in 2 × 2 × 2 mm was examined in a rectangular waveguide by the network analyzer. Through comparing the simulation and experiment results, we can capture the permittivity of the dielectric ceramic, which has provided a new method to examine the dielectric constant on higher microwave frequency.

### 3. Results and Discussion

**3.1. XRD Plots.** Each dielectric ceramic sample has its own structure and lattice information through series of X-ray diffraction experiments of different sintering temperatures. To determine the phase of the synthesized samples, the X-ray diffraction patterns are measured and shown in Figure 2, which clearly shows orthorhombic structure for CaTiO<sub>3</sub> in incipient ferroelectric phase [12]. It has been proved that CaTiO<sub>3</sub> sintered at 1350°C has the same lattice structure as the unsintered ones (JCPDS number 42-0423, Pnma(62),  $a = 5.442 \text{ \AA}$ ,  $b = 7.642 \text{ \AA}$ ,  $c = 5.381 \text{ \AA}$ ), while being different from the other ceramics sintered at 1250°C, 1300°C, and 1400°C (JCPDS number 22-0153, Pnma(62),  $a = 5.440 \text{ \AA}$ ,  $b = 7.644 \text{ \AA}$ ,  $c = 5.381 \text{ \AA}$ ). The alteration of lattice parameters would be probably related to the appearance of defects due to the distortion in the CaTiO<sub>3</sub> lattice [13]. The red line (1350°C) and

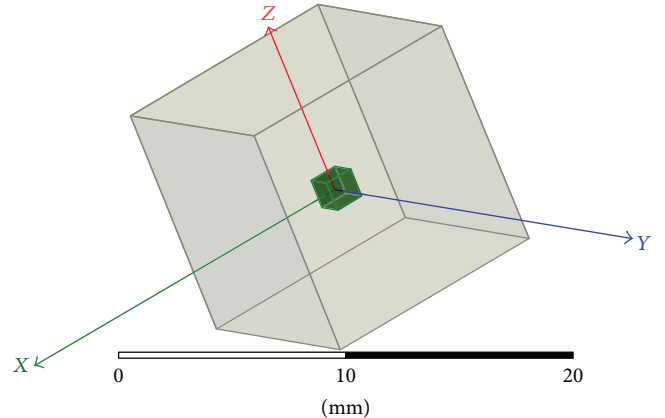


FIGURE 1: The simulation model of dielectric ceramic cube by 2 × 2 × 2 mm.

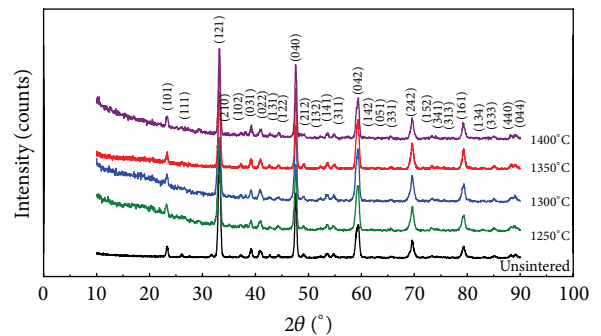


FIGURE 2: XRD patterns of CaTiO<sub>3</sub> ceramics fabricated under different sintering conditions, with respect to unsintered ones, 1250°C, 1300°C, 1350°C, and 1400°C, respectively.

black line (unsintered) have the similar diffraction situation, distinguishing from the rest sintering temperatures with slopes for the small diffraction degree.

**3.2. Basic Physical Properties.** To make sure the preparation process was excellent and the macrostructure was dense enough, the volume shrinkage and relative density measurement were applied to those samples of different sintering temperatures. Because the ceramic particles were combined with adhesive PVA, the volume and density would be changed after the sintering process. The most dense structure corresponded to best sintering temperature. As Figure 3 revealed, in this experiment, the best sintering temperature was 1350°C, at which the CaTiO<sub>3</sub> captured the largest volume shrinkage of 34.78% and the highest relative density of 97.88%.

**3.3. SEM.** Not only the macrostructure should be dense enough, but also the microstructure should have less defects to win a better dielectric behavior. Figure 4 shows the microstructures of CaTiO<sub>3</sub> ceramics on surface and section parts. From the surface and section, the most dense one was allied with Figure 4(c) occupying an average particle size of 3 μm. More pores had the presence in the phase in Figures 4(a) and 4(b), with a larger particle size in Figure 4(d). As

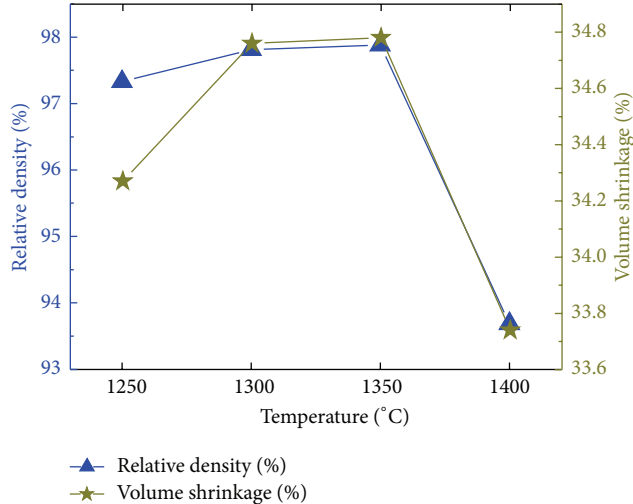


FIGURE 3: The volume shrinkage and relative density alteration of  $\text{CaTiO}_3$  against sintering temperature.

the sintering temperature increased, the number of defects decreased until the most suitable temperature ( $1350^\circ\text{C}$ ) with the most dense phase and the least pores and disorder. Above the most fitting temperature, ceramic particles would grow up and gas cavity became larger, resulting in a deep property decline.

### 3.4. Dielectric Properties

(i) *The Frequency Dependence of Dielectric Constant.* Since the application is concerned with metamaterial at microwave frequency, the frequency dependence of permittivity has to be uncovered. Just as shown in Figure 5, the lowest dielectric constant and less variable dielectric variation in sintering temperature of  $1350^\circ\text{C}$  came out, and a deep dielectric drop from 470 to 167 turned up in  $10^6 \text{ Hz} \sim 10^9 \text{ Hz}$  range. Above  $10^9 \text{ Hz}$ , the dielectric constant remained almost invariable around 167. Compared with the best sintering condition of  $1350^\circ\text{C}$  with less variable permittivity situation, the frequency dependence of the permittivity of  $1250^\circ\text{C}$ ,  $1300^\circ\text{C}$ , and  $1400^\circ\text{C}$  was much more unstable. As for  $\text{CaTiO}_3$ , it has its own dielectric response mechanism. According to Tian [14], electronic relaxation polarization plays an important role in  $10^6 \sim 10^9 \text{ Hz}$  range, as well as electronic and ionic displacement polarization during  $10^9 \sim 10^{10} \text{ Hz}$ . In  $10^6 \sim 10^9 \text{ Hz}$  frequency range, the electron energy state has changed and weakly bounded electrons are formed in partial energy levels of band gap owing to the thermal vibration of crystal lattice, defects, and impurities. The weakly bounded electrons are shared among surrounding cations and can be activated through absorbing more energy from the lattice thermal vibration and jump from lower local energy level to higher energy level. Thus, the weakly bounded electrons move from one cation to another. And their distribution in short distance will gain direction when loaded with electric field, which is just the electronic relaxation polarization. If the frequency of electric field becomes higher, the directional distribution of weakly

TABLE 1: Microwave dielectric properties of  $\text{CaTiO}_3$  at different sintering temperatures.

| Sintering $T^\circ\text{C}$ | $f$ (GHz) | $\epsilon_r$ | $\tan D$ | $Q$  | $Q \times f$ (GHz) |
|-----------------------------|-----------|--------------|----------|------|--------------------|
| 1250                        | 3.200     | 169.53       | 0.0006   | 1605 | 4188               |
| 1300                        | 3.200     | 169.21       | 0.0006   | 1803 | 5022               |
| 1350                        | 3.200     | 167.99       | 0.0005   | 2049 | 5219               |
| 1400                        | 3.200     | 167.15       | 0.001    | 785  | 2063               |

bounded electrons will be weakened and the polarization value will also decline. Therefore, the dielectric constant has a negative frequency dependence among  $10^6 \sim 10^9 \text{ Hz}$ . Above  $10^9 \text{ Hz}$ , the electronic relaxation polarization does not exist, but the electronic and ionic displacement polarization determine the main polarization mode. However, as we all know, the relative displacements between electrons and nuclei, as well as those between anions and cations, are much limited due to the strong attraction. So the dielectric constant is almost invariable with slightly increasing as the frequency increases from  $10^9 \text{ Hz}$ , which would be the excellent microwave dielectric behaviors. What is more, the situation of the lower permittivity of the sintering temperature at  $1350^\circ\text{C}$ , compared with the rest sintering conditions, can be easily understood because of more defects existing in the samples of the sintering temperatures at  $1250^\circ\text{C}$ ,  $1300^\circ\text{C}$ , and  $1400^\circ\text{C}$  (defects shown in Figure 4 and reflected in Figures 2 and 3) and contributing to the polarization.

Because this kind of ceramic is specially of the meta-materials working in microwave frequency range, the measurements of microwave dielectric properties were taken, with the resonant frequency (choosing 3.2 GHz), dielectric constant, dielectric loss, quality factor, and parameter  $Q \times f$ , listed in Table 1. Around frequency 3.2 GHz, the dielectric constant kept slightly decreasing but almost in the same level. The highest  $Q$  (2049),  $Q \times f$  (5219), and lowest dielectric loss (0.0005) were also ascribed to its dense structure and fewer defects, with the sintering temperature of  $1350^\circ\text{C}$  [15, 16]. Apparently, the dielectric properties of sintering temperature  $1400^\circ\text{C}$  had dropped down a lot owing to the deterioration under the higher temperature. Compared with previous papers involving the dielectric metamaterial,  $\text{CaTiO}_3$  has much advantage of the lower dielectric loss. This kind of low loss mainly arises from its better interior microstructure and preparation approach. And its structure type (orthorhombic) will affect its forming condition (such as the sintering temperature) and further contribute to the preparation process to some extent [12, 17]. In addition, the value of permittivity and dielectric loss can be tuned by altering the compositions of ceramics, introducing new components, or doping some additives, such as  $\text{ZrO}_2$  [18] and  $\text{CeO}_2$  [19], which will decrease and increase the permittivity of  $\text{CaTiO}_3$ , respectively, and decrease the loss tangent value in some way.

(ii) *The Temperature Dependence of Dielectric Constant.* Since we have known the frequency dependence of permittivity, another significant task that needs to be done is that we

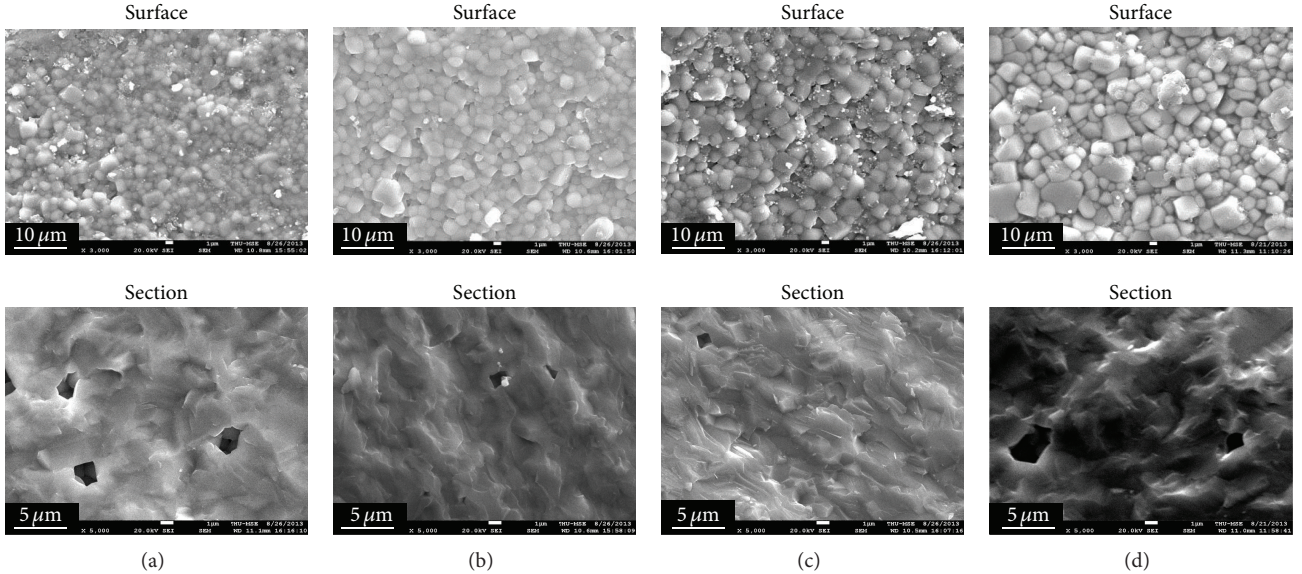


FIGURE 4: Images of Scanning Electron Microscope at different sintering temperatures for  $\text{CaTiO}_3$  at (a)  $1250^\circ\text{C}$ , (b)  $1300^\circ\text{C}$ , (c)  $1350^\circ\text{C}$ , and (d)  $1400^\circ\text{C}$  by surface and section.

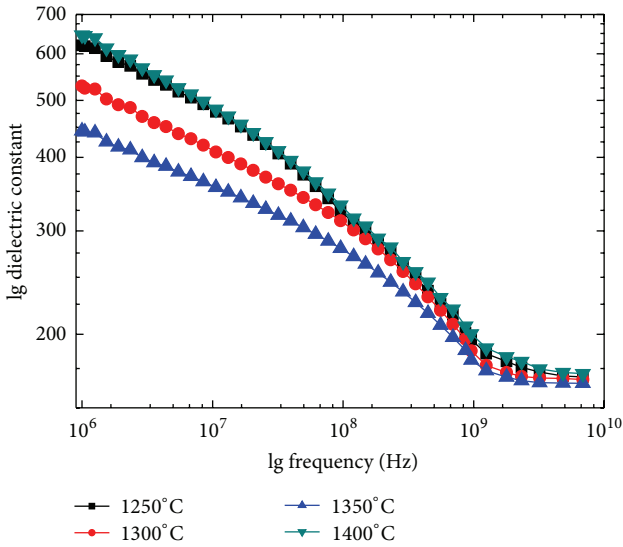


FIGURE 5: Dielectric constant variation against frequency at  $25^\circ\text{C}$  for  $\text{CaTiO}_3$  sintered at  $1250^\circ\text{C}$ ,  $1300^\circ\text{C}$ ,  $1350^\circ\text{C}$ , and  $1400^\circ\text{C}$ , respectively.

should study the temperature dependence of permittivity to reveal the variation of dielectric constant. The similar situations for each sintering temperature are displayed in Figure 6, where the decreasing dielectric constant existed when the temperature increased. This should be interpreted by the theory of Bosman and Havinga [20, 21], improved by Bartels and Smith [22], saying that the temperature dependence of permittivity is negative when  $\varepsilon_r > 20$ . Furthermore, the sintering temperature of  $1350^\circ\text{C}$  made  $\text{CaTiO}_3$  occupy a slight dielectric constant descending around 475. The phenomenon of possessing larger dielectric constant in the sintering temperatures of  $1250^\circ\text{C}$ ,  $1300^\circ\text{C}$ , and  $1400^\circ\text{C}$

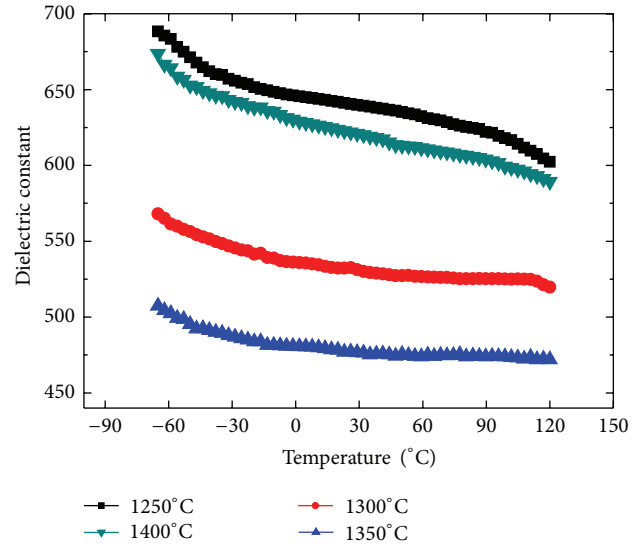


FIGURE 6: Dielectric constant variation against temperature at  $500\text{ kHz}$  for  $\text{CaTiO}_3$ , sintered at  $1250^\circ\text{C}$ ,  $1300^\circ\text{C}$ ,  $1350^\circ\text{C}$ , and  $1400^\circ\text{C}$ , respectively.

would also be attributed to the defects, contributing effective electric charge, adding the polarization possibility, and finally resulting in improved permittivity.

**3.5. Permittivity Tested at Higher Microwave Frequency.** To get further comprehension of the higher frequency resonance of  $\text{CaTiO}_3$ , a method was utilized to examine and retrieve the permittivity, based on the fact that the limited measuring technology and fewer methods could test the dielectric constant around or above  $10^{10}\text{ Hz}$ . The new method is to put

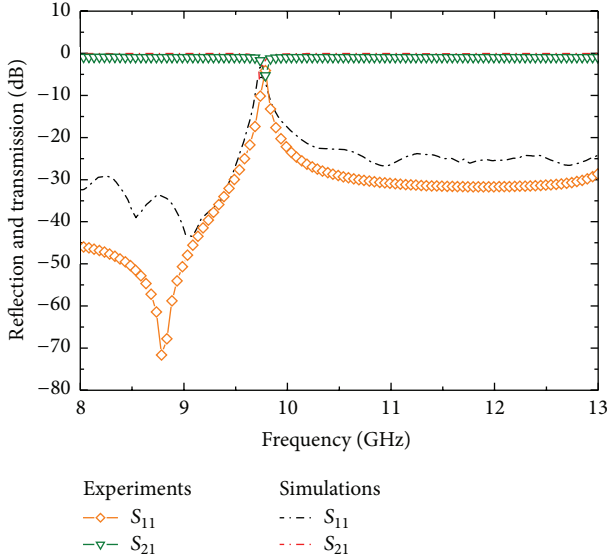


FIGURE 7: CaTiO<sub>3</sub> cube by 2 × 2 × 2 mm was tested in waveguide with the magnitude of S parameter:  $S_{21}$  of transmission and  $S_{11}$  of reflection, including the comparison of simulations and experiments on  $S_{11}$  and  $S_{21}$ .

the single cube of 2 × 2 × 2 mm specimen into a rectangular waveguide and measure the microwave S-Parameter of transmission ( $S_{21}$ ) and reflection ( $S_{11}$ ) and phase of  $S_{21}$  by an HP8720ES network analyzer. As mentioned in [4], the first resonance frequency is completely determined by dielectric constant. We can get the permittivity of the dielectric ceramics through comparing the computer simulation using the finite-difference time domain solver and experimental results from the testing in the rectangular waveguide. As demonstrated in Figure 7, the experiments and simulations of the S-Parameter have a great correspondence and consistency in the range from 8 GHz to 13 GHz. Around 9.8 GHz, -3.3 dB for  $S_{11}$  simulated and -3.6 dB for  $S_{11}$  in experiment were observed, as well as -11 dB for  $S_{21}$  simulated and -5.6 dB for  $S_{21}$  in experiment. Finally, we have got the permittivity of CaTiO<sub>3</sub> for around 165, which is extremely close to the microwave testing result.

## 4. Conclusion

Through systemic experiments, CaTiO<sub>3</sub> was fabricated by solid state method under better suitable sintering temperature of 1350°C with a volume shrinkage of 34.78%, relative density of 97.88%, which is better than the value of 95% [12]. The X-ray diffraction and SEM had shown a perovskite orthorhombic structure and a dense crystal microstructure. The dielectric spectra revealed a deep dielectric drop from 470 to 167 in the range 10<sup>6</sup> Hz~10<sup>9</sup> Hz and exhibited a lower microwave loss of 0.0005, combined with a higher microwave dielectric constant of ~167 and microwave quality factor Q of 2049 and Q × f of 5219 GHz, respectively. Also slight decrease versus temperature for the permittivity was investigated systematically. The single cube CaTiO<sub>3</sub> with a size

of 2 × 2 × 2 mm was examined in a rectangular waveguide from 8 GHz to 13 GHz, with a resonant frequency of 9.8 GHz, which agrees with the simulation. We got the permittivity of 165 for CaTiO<sub>3</sub> at higher microwave frequency, very close to the microwave result of ~167. Therefore, CaTiO<sub>3</sub> is a kind of versatile and potential metamaterial unit cell and a new dielectric examination method is created.

## Conflict of Interests

The authors declare that there is no conflict of interests regarding the publication of this paper.

## Acknowledgments

This work is supported by the National High Technology Research and Development Program of China (Grant no. 2012AA030403), the National Natural Science Foundation of China (Grant nos. 61275176 and 51032003), and the Science and Technology Plan of Shenzhen City of China (Grant nos. JCYJ20120619152711509 and JC201105180802A). Acknowledgment also goes to Professor Fuli Zhang for his helpful guidance and corrections of the paper. The appreciation of assisting in experiments is attributed to Hongya Wu, Xiaoming Liu, and Chuwen Lan, and so forth.

## References

- [1] J. B. Pendry, A. J. Holden, W. J. Stewart, and I. Youngs, "Extremely low frequency plasmons in metallic mesostructures," *Physical Review Letters*, vol. 76, no. 25, pp. 4773–4776, 1996.
- [2] J. B. Pendry, A. J. Holden, D. J. Robbins, and W. J. Stewart, "Magnetism from conductors and enhanced nonlinear phenomena," *IEEE Transactions on Microwave Theory and Techniques*, vol. 47, no. 11, pp. 2075–2084, 1999.
- [3] H. J. Zhao, L. Kang, J. Zhou et al., "Experimental demonstration of tunable negative phase velocity and negative refraction in a ferromagnetic/ferroelectric composite metamaterial," *Applied Physics Letters*, vol. 93, no. 20, Article ID 201106, 2008.
- [4] Q. Zhao, J. Zhou, F. L. Zhang, and D. Lippens, "Mie resonance-based dielectric metamaterials," *Materials Today*, vol. 12, no. 12, pp. 60–69, 2009.
- [5] Q. Zhao, L. Kang, B. Du et al., "Experimental demonstration of isotropic negative permeability in a three-dimensional dielectric composite," *Physical Review Letters*, vol. 101, no. 2, Article ID 027402, 2008.
- [6] Y. Z. Sun, Y. F. Sun, L. X. Ran, W. G. Wang, L. Peng, and Q. L. Chen, "Experimental verification on negative refraction of BST," *Scientia Sinica Physica, Mechanica & Astronomica*, vol. 40, no. 12, pp. 1476–1481, 2010.
- [7] F. L. Zhang, D. Lippens, and A. L. Borja, "Low profile small antenna using ferroelectrics cube based artificial magnetic conductor," in *Proceedings of the 4th European Conference on Antennas and Propagation (EuCAP '10)*, April 2010.
- [8] L. C. Sengupta and S. Sengupta, "Breakthrough advances in low loss, tunable dielectric materials," *Materials Research Innovations*, vol. 2, no. 5, pp. 278–282, 1999.
- [9] B. W. Hakki and P. D. Coleman, "A dielectric resonator method of measuring inductive capacities in the millimeter range," *RE*

- Transactions on Microwave Theory and Techniques*, vol. 8, no. 4, pp. 402–410, 1960.
- [10] W. E. Courtney, “Analysis and evaluation of a method of measuring the complex permittivity and permeability microwave insulators,” *IEEE Transactions on Microwave Theory and Techniques*, vol. 18, no. 8, pp. 476–485, 1970.
  - [11] J. Krupka, K. Derzakowski, B. Riddle, and J. B. Jarvis, “A dielectric resonator for measurements of complex permittivity of low loss dielectric materials as a function of temperature,” *Measurement Science and Technology*, vol. 9, no. 10, pp. 1751–1756, 1998.
  - [12] V. V. Lemanov, A. V. Sotnikov, E. P. Smirnova, M. Weihnacht, and R. Kunze, “Perovskite  $\text{CaTiO}_3$  as an incipient ferroelectric,” *Solid State Communications*, vol. 110, no. 11, pp. 611–614, 1999.
  - [13] L. S. Cavalcante, V. S. Marques, J. C. Sczancoski et al., “Synthesis, structural refinement and optical behavior of  $\text{CaTiO}_3$  powders: a comparative study of processing in different furnaces,” *Chemical Engineering Journal*, vol. 143, no. 1–3, pp. 299–307, 2008.
  - [14] S. Tian, *Physical Properties of Materials*, Beihang University Press, Beijing, China, 2001.
  - [15] A. Pashkin, S. Kamba, M. Berta et al., “High frequency dielectric properties of  $\text{CaTiO}_3$ -based microwave ceramics,” *Journal of Physics D: Applied Physics*, vol. 38, no. 5, pp. 741–748, 2005.
  - [16] H. F. Kay and P. C. Bailey, “Structure and properties of  $\text{CaTiO}_3$ ,” *Acta Crystallographica*, vol. 10, no. 3, pp. 219–226, 1957.
  - [17] H. K. Zhu, M. Liu, and H. Q. Zhou, “Effects of additives on  $\text{CaTiO}_3$  properties,” *Electronic Components & Materials*, vol. 24, no. 7, 2005.
  - [18] H. Y. Wu, J. Zhou, C. W. Lan, Y. S. Guo, and K. Bi, “Microwave memristive-like nonlinearity in a dielectric metamaterial,” *Scientific Reports*, vol. 4, p. 5499, 2014.
  - [19] E. R. Kipkoech, F. Azough, and R. Freer, “The effect of  $\text{CeO}_2$  on the microstructure and dielectric properties of  $\text{CaTiO}_3$ -based ceramics,” *European Ceramic Society*, vol. 206, no. 2, pp. 2213–2216, 2002.
  - [20] E. E. Havinga, “The temperature dependence of dielectric constants,” *Journal of Physics and Chemistry of Solids*, vol. 18, no. 2-3, pp. 253–255, 1961.
  - [21] A. J. Bosman and E. E. Havinga, “Temperature dependence of dielectric constants of cubic ionic compounds,” *Physical Review*, vol. 129, no. 4, pp. 1593–1600, 1963.
  - [22] R. A. Bartels and P. A. Smith, “Pressure and temperature dependence of the static dielectric constants of  $\text{KCl}$ ,  $\text{NaCl}$ ,  $\text{LiF}$ , and  $\text{MgO}$ ,” *Physical Review B*, vol. 7, no. 8, pp. 3885–3892, 1973.

## Research Article

# High Power Efficiency Buck Converter Design for Standalone Wind Generation System

**Yigeng Huangfu, Ruiqing Ma, Bo Liang, and Yuren Li**

*Northwestern Polytechnical University, Xi'an 710072, China*

Correspondence should be addressed to Yigeng Huangfu; [yigeng@nwpu.edu.cn](mailto:yigeng@nwpu.edu.cn)

Received 20 November 2014; Accepted 30 December 2014

Academic Editor: Weiren Zhu

Copyright © 2015 Yigeng Huangfu et al. This is an open access article distributed under the Creative Commons Attribution License, which permits unrestricted use, distribution, and reproduction in any medium, provided the original work is properly cited.

In wind generation system, the power converter efficiency is one of the key factors for the performance of the system. In those systems, DC/DC Buck converter is widely used for high power system. Considering the converter's cost and efficiency, this paper mainly focuses on the design of an improved topology Buck converter adopted for high power standalone wind generation system. The designed converter uses multi-MOSFETs in parallel instead of the IGBTs, in order to increase the conductive current as well as the converter switch frequency. From the experimental tests results, the maximum efficiency of the designed 2 kW Buck converter is up to 96% based on maximum power point tracking (MPPT) method.

## 1. Introduction

Conventional energy resources may run out in the following few decades, especially from fossil origins, which could lead to the energy shortage in the world. The energy consumption is increased dramatically in recent years. The renewable energy sources, such as solar, wind, or ocean wave energy, are considered to be the future energy solutions. Thanks to the extensive research in renewable energy field, those energies can be exploited more and more easily and properly [1–3]. Nevertheless, being neglected for a long time, power extraction techniques of these resources require more researches and developments aiming to reduce the manufacturing costs and to improve the energy efficiency [4].

Among the renewable resources, the wind energy is gaining greater visibility during the last several years as a convenient and promising energy source in the future [5]. The application of wind energy is divided into two aspects. One is a standalone wind power station with the battery as energy storage component, and the other is connect-to-grid wind turbine. In many applications, such as small villages or islands power station, the off-grid wind power generation system provides an excellent energy solution. However, they are unstable energy sources due to their primary source in nature. Thus, an energy storage component is usually added to form

a hybrid energy system. In such a system, a suitable power converter plays an important role during energy conversion and management. Generally, in order to improve the system efficiency these converters should be adaptive for wide wind speed range.

In a wind generation system, two types of converter can be usually found: a primary AC/DC converter connected directly to the wind turbine generator and a secondary DC/DC converter connected to the load. As known, the nonisolated DC/DC Buck converter is usually used in small or low power system, and the soft-switching technology is widely used to improve the efficiency. In [6], two high efficiency voltage regulators based on Buck converter with soft-switching for CPU power have been proposed, with a relatively small system power output. In a high power system, IGBTs based Buck converters with soft-switching technology are commonly used. In [7], the design of a single phase (synchronous rectification), interleaved synchronous mode bidirectional converter is given. Due to the cost limitation of the system, the soft-switching Buck converter with MOSFET rather than IGBT is used. In [8], a high efficiency zero-current switching (ZCS) Buck converter has been also presented.

The main focus of this paper is to present a low cost, high efficiency DC/DC converter design in a wind generation system. Considering the cost, efficiency, power level, and

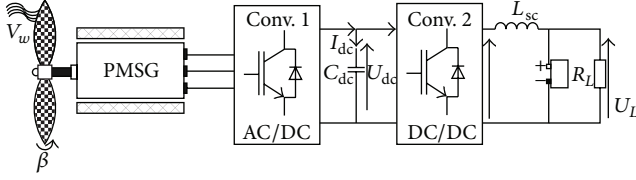


FIGURE 1: Standalone wind power generation system.

the characteristic of such a wind system, the technology of paralleled multi-MOSFETs devices is used and an optimized Buck converter topology is presented with the experimental validation.

## 2. System Structure

Generally, six parts can be distinguished in a standalone wind power generation system. They are wind turbine, permanent magnet synchronous generator (PMSG), AC/DC rectifier, DC/DC converter, storage battery, and load, respectively. The structure is presented in Figure 1.

The wind energy in nature drives the turbine to whirl. The PMSG produces the AC electrical energy, whose amplitude and frequency are variable because of the random wind speed in the nature. Through the AC/DC rectifier, the DC electrical energy with alterable amplitude is obtained. Compared with conventional Buck converter, the wide input voltage range is a novel challenge for the converter design. For system performance, the maximum power point tracking (MPPT) technology control method is used [9, 10] to ensure a stable DC output for the storage battery and load.

**2.1. Wind Turbine Characteristic.** As well known, the rated power of the wind turbine depends on the length of blade, air density, power coefficient, and wind speed. Moreover, mechanical elevation and transmission affect the rated power. The relation can be expressed by [11]

$$P_{\text{turb}} = 0.5\rho C_p(\lambda, \beta) \pi r^2 v^3 \eta, \quad (1)$$

where \$\rho\$ is the air density, \$r\$ is the blade length, \$v\$ is the wind speed, \$\eta\$ is the transmission efficiency, and \$C\_p\$ is the power coefficient depending on the pitch angle of rotor blades \$\beta\$ and the tip speed ratio \$\lambda\$. When the pitch angle is constant, \$C\_p\$ depends only on tip speed ratio \$\lambda\$, as shown in Figure 2.

The tip speed ratio is defined by

$$\lambda = \frac{r\omega}{v}, \quad (2)$$

where \$\omega\$ is the angular speed of wind turbine.

When the turbine operates at its optimal point, the rated wind speed \$v\$ can be thus expressed as a function of the wind turbine speed:

$$v = \frac{r\omega}{\lambda_{\text{opt}}}. \quad (3)$$

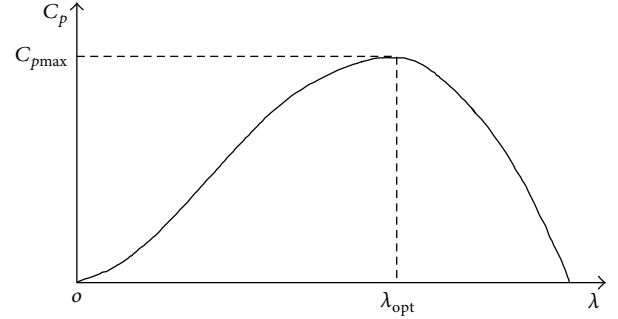


FIGURE 2: Blade characteristic: \$C\_p\$ versus \$\lambda\$.

From (1) and (3), the output power from wind turbine can be expressed by

$$P_{\text{MPPT}} = 0.5\rho C_{p\max} \pi r^2 \left( \frac{r\omega}{\lambda_{\text{opt}}} \right)^3 \eta = K_{\text{opt}} \omega^3 \quad (4)$$

with

$$K_{\text{opt}} = \frac{\rho \pi r^5 C_{p\max}}{\lambda_{\text{opt}}^3}. \quad (5)$$

The turbine torque is defined as the ratio of the mechanical power to the rotational turbine speed:

$$T_{\text{opt}} = \frac{P_{\text{MPPT}}}{\omega} = K_{\text{opt}} \omega^2. \quad (6)$$

Equations (4) and (6) provide the relation between the maximal mechanical power and the turbine speed, as well as the relation between the maximal torque and the turbine speed. When the wind generation system works at its maximum power point under a given wind speed, the wind speed and tip speed ratio can be calculated by (3).

With different wind speeds, the output power and torque of turbine and their maximum point are shown in Figure 3. Figure 3(a) presents the mechanical output power versus the wind speed. Figure 3(b) presents the mechanical output torque versus the wind speed.

**2.2. Permanent Magnet Synchronous Generator (PMSG) Characteristic.** The permanent magnet machines are used more and more in the variable speed drives. The PMSG used in the presented system is a generator with radial magnetization [12]. Thus, the synchronous rotating coordinate \$d\$-\$q\$ axis has the same speed with the rotor magnetic poles. The stator voltage equations of PMSG can be expressed by

$$u_d = R_s i_d + L_d \frac{di_d}{dt} + \frac{d\psi_f}{dt} - \omega_e L_q i_q, \quad (7)$$

$$u_q = R_s i_q + L_q \frac{di_q}{dt} + \omega_e (L_d i_d + \psi_f),$$

where \$u\_d\$ and \$u\_q\$ are \$d\$-\$q\$ axis voltages, respectively; \$i\_d\$ and \$i\_q\$ are \$d\$-\$q\$ axis currents, respectively; \$L\_d\$ and \$L\_q\$ are \$d\$-\$q\$ axis self-inductances, respectively; \$\omega\_e\$ is the electricity angular velocity

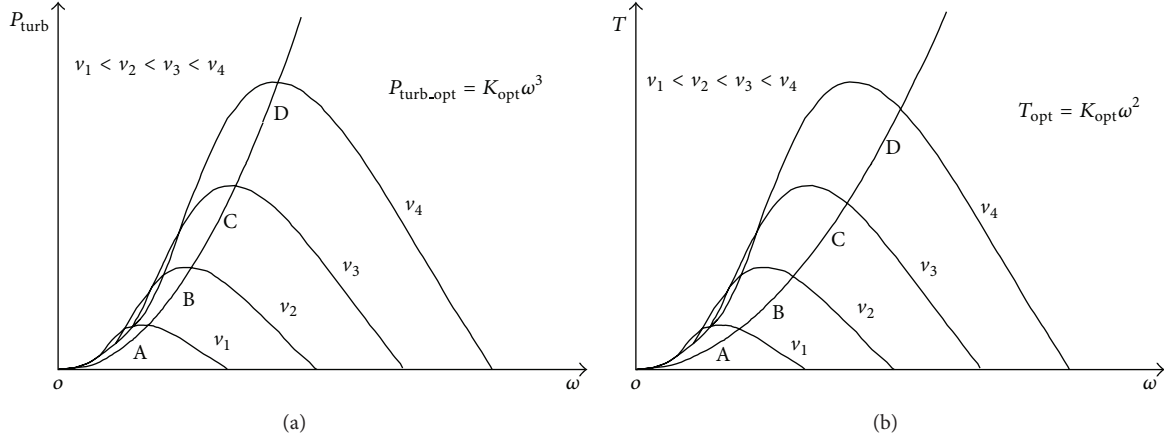


FIGURE 3: Output characteristic of wind turbine.

with  $\omega_e = p\omega$ ;  $p$  is the pairs of poles; and  $\psi_f$  is the flux linkage of permanent magnet.

The equation of electromagnetic torque can be calculated as

$$T_{\text{em}} = 1.5p[\psi_f i_q + (L_d - L_q)i_q i_d]. \quad (8)$$

In the case of a nonsalient pole machine,  $L_d = L_q$ . The equation above can be therefore rewritten by

$$T_{\text{em}} = 1.5p\psi_f i_q. \quad (9)$$

Thus the electromagnetic torque depends only on the  $q$  axis component current. The flux is constant, and the torque is proportional to the current  $i_q$ .

**2.3. Discussion on MPPT Control Method.** The common maximum power point tracking (MPPT) methods such as optimum tip speed ratio, power curve control, and climbing mountain can be found in the literature [13, 14].

With the method of optimum tip speed ratio, the wind speed  $v$  and turbine speed  $\omega$  have to be measured at first. The result of the ratio  $\lambda = r\omega/v$  is then compared with the optimum ration of tip speed  $\lambda_{\text{opt}}$  shown in Figure 2. The error is sent to the controller to adjust the duty cycle of PWM for power converter. This method has a clear physical conception and a simple theory. However, it is necessary to measure the wind speed and turbine speed precisely. The control block diagram of this method is shown in Figure 4.

The wind speed is difficult to detect accurately due to the randomness and intermission of wind in nature. Furthermore, the use of wind speed sensor will increase the cost of the system. In addition, the optimum tip speed ratio is defined by turbine generator manufacturer, which is not easy to obtain. As a consequence, this method is rarely used in actual applications.

If the power curve control method is used, only turbine angular speed needs to be measured. According to (4), the power curve can be obtained at certain wind speed. Thus, the maximum power point can be obtained. At this time, the error between the actual output power and the given

reference power is used as the input of controller. The control block diagram of power curve is shown in Figure 5.

The disadvantage of this method is that the output power of generator and the optimum power curve should be known. The use of the turbine torque sensor also increases the cost of the system. In addition, the maximum power curve is usually obtained by offline test. The variation of parameters during system operation will affect the efficiency of the maximum power tracking method in the system.

The climbing mountain method overcomes the disadvantages of the two methods mentioned above. This method uses an empirical search algorithm for control purpose. Thus the measurements of wind speed and the power curve of the generator are not needed. The wind turbine speed can be regulated by changing the generator output power. The search algorithm adjusts continuously the PWM duty cycle until system operates at its maximum power point. The control block diagram of climbing mountain is shown in Figure 6.

During the PWM regulation, if the duty cycle step change is too big, the oscillation will take place. In this case, the regulated maximum power point by this method is far away from the real optimal value. Thus the performance of system is decreased. If the PWM duty cycle step change is too small, the tracking method cannot converge to optimal point rapidly. In this paper, a variable duty cycle change step is used for climbing mountain method. The control algorithm flow chart is shown in Figure 7.

Because the energy storage adopts four VRLA batteries in parallel, the terminal voltage is almost constant. Actually, maximization of output current achieves the highest power control. After program initialization, the initial output current  $I$  is detected. The  $I_{\text{max}}$  is the maximum current under the same wind speed, and the  $I_1$  is the output current at next sample time. When the error between  $I_1$  and  $I_{\text{max}}$  is larger than preset  $\alpha$ , the duty cycle should be reinstalled. Otherwise, the duty cycle remains unchanged. If the output current  $I_1$  is much lower than maximum current  $I_{\text{max}}$  and  $I_1 - I_{\text{max}} < -\alpha$ , the duty cycle should make adjustment with disturbance duty. Then, the output current is measured again, denoted by  $I_2$ . Similarly, the output current  $I_2$  also compares with  $I_{\text{max}}$ .

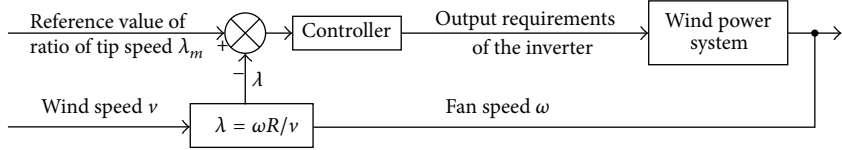


FIGURE 4: Block diagram of optimum tip speed ratio.

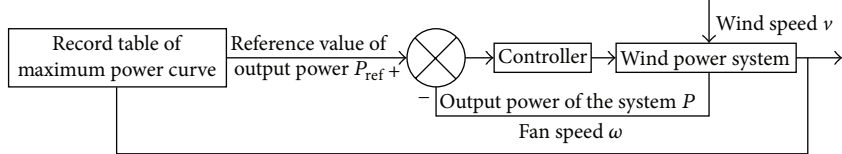


FIGURE 5: Block diagram of power curve control.

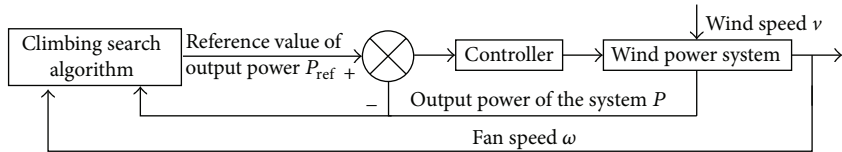


FIGURE 6: Block diagram of climbing mountain.

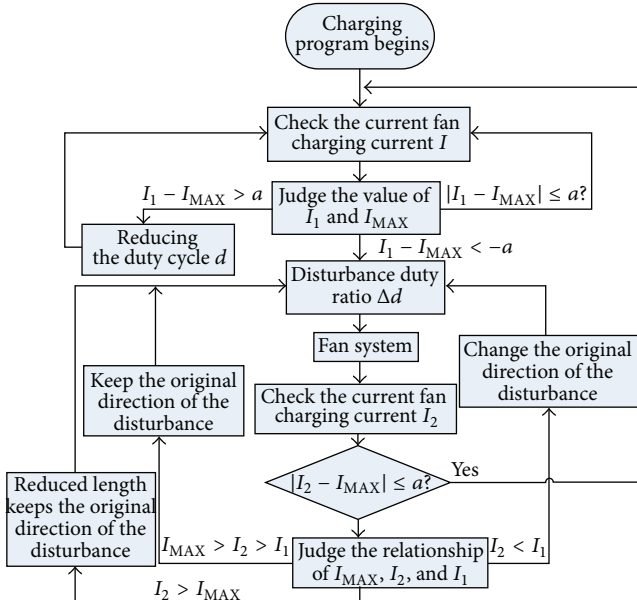


FIGURE 7: Flow chart of MPPT using climbing mountain method.

If  $|I_2 - I_{\max}| < \alpha$ . If  $I_{\max} > I_2 > I_1$ , increase the disturbance duty according to the original direction. If  $I_2 < I_1$ , decrease the disturbance duty according to the opposite direction.

### 3. Buck Converter Design

Buck converter is a typical DC/DC device, which has been used widely in DC regulated power supply, photovoltaic

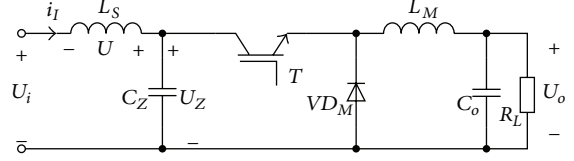


FIGURE 8: The conventional Buck converter topological structure.

system, DC motor regulated speed, LED illumination, and other electrical power and electronics systems [15–17].

In a wind generation system, the output voltage of the rectifier from the PMSG is usually higher than the battery voltage (DC bus voltage). For voltage reduction between the rectifier output and the DC bus, the Buck converter is used widely due to its simple structure, low cost, and easy control.

**3.1. Conventional Buck Converter.** The topology of a conventional nonisolated Buck converter is shown in Figure 8.

In a wind generation system, the converter has a long and wide wire connection from the forestage due to the height of the wind turbine. Thus there exists a great stray inductance  $L_s$ . When the switch is off, the input current  $i_I$  passes through the inductance  $L_s$ , which leads to

$$\begin{aligned} U_i &= -L_s \frac{di_I}{dt} + U_z, \\ i_I &= C_z \frac{dU_z}{dt}. \end{aligned} \quad (10)$$

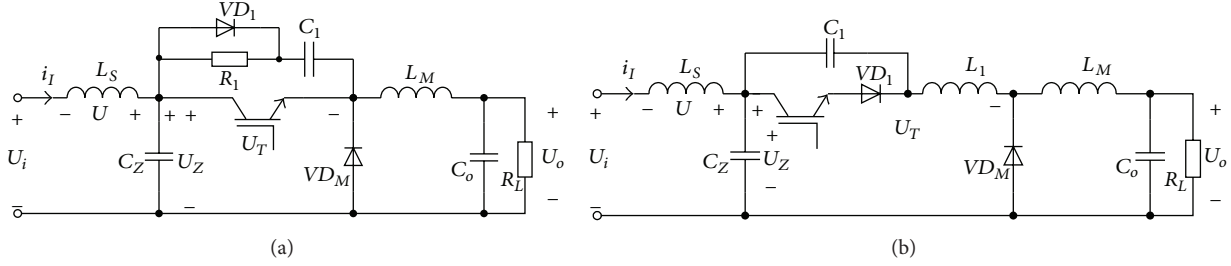


FIGURE 9: The improved Buck converter topological structure.

The solution of the above two equations is

$$U_z = U_i + \sqrt{\frac{L_s}{C_z}} I_I \sin\left(\frac{t}{\sqrt{L_s C_z}}\right). \quad (11)$$

The maximum value of the equation above can be calculated as follows:

$$U_{z \max} = U_i + \sqrt{\frac{L_s}{C_z}} I_I. \quad (12)$$

With the presence of a stray inductance, a high amplitude voltage spike  $U_{z \max}$  will be produced, if the converter does not include an absorption capacity. When the input current  $i_I$  is higher, the value of  $U_{z \max}$  is greater. Therefore, the use of an absorption capacitance  $C_z$  is necessary. However the capacitance value  $C_z$  should be selected carefully, especially in high frequency.

With a higher output power of the wind generation system, the electric wires are greater and longer, leading to the increase of the stray inductance. In high power applications, the change of current is significant when the power device works at high frequency, resulting in the huge voltage spike between the switch ends.

This phenomenon is common especially in high power Buck converter. The voltage spike at switch-off and the current spike at switch-on yield high electric stress. Sometimes, it can even break down the power device, such as MOSFET or IGBT. The switching loss can be significant. Thus the converter efficiency is usually between 60% and 80%.

In order to overcome these shortages, the suppression of voltage or current spike and the improvement of the efficiency become the key issue in high power Buck converter design. An improved Buck converter topology is proposed in the following section.

**3.2. Improved Buck Converter.** The absorption circuit plays the crucial function for removing or decreasing the voltage spike in high power Buck converter. Two different absorption circuits, called RCD and LCD absorption, respectively, are presented in Figure 9.

In this paper, the resistance  $R_1$ , the capacitance  $C_1$ , and the diode  $VD_1$  consist of the RCD absorption circuit in Figure 9(a). The inductance  $L_1$ , the capacitance  $C_1$ , and the diode  $VD_1$  consist of LCD absorption circuit in Figure 9(b).

In Figure 9(a), the RCD absorption circuit can eliminate the voltage spike when the power device is switched off. But

the energy stored in capacitor is dissipated to resistance in the circuit. Thus the system efficiency is decreased.

In this topology, the relation between converter voltage and current can be expressed by

$$U_i = -L_s \frac{di_I}{dt} + U_T + L_M \frac{di_I}{dt} + U_o, \quad (13)$$

$$i_I = C_1 \frac{dU_T}{dt}.$$

The maximum value of the solution of the above two equations is

$$U_{T \max} = U_i - U_o + \sqrt{\frac{L_s + L_M}{C_1} I_I^2 + (U_i - U_o)^2}. \quad (14)$$

The absorption capacity  $C_1$  plays an important role in suppression of the voltage spike.

When the switch is on,  $R_1$ ,  $C_1$ , and switch device  $T$  build a discharge circuit. The stored energy in absorption capacity  $C_1$  from the voltage spike is consumed by the resistance  $R_1$ . Considering the maximum discharge current of capacity  $C_1$  as  $I_{T \max}$ , discharge time as  $\tau$ , power loss in resistor as  $P_{\text{loss}}$ , and the switch frequency as  $f$ , the following expression can be obtained, ignoring the conduction voltage drop:

$$I_{T \max} = \frac{U_{T \max}}{R_1}, \quad (15)$$

$$\tau = 2R_1 C_1,$$

$$P_{\text{loss}} = \frac{1}{2} f C_1 U_{T \max}^2.$$

The values of  $I_{T \max}$  should be smaller for security of the switch device. That means the resistance  $R_1$  should be big enough. But if the value of  $R_1$  is too big, it will affect the discharge time and thereby the efficiency. The  $C_1$  and  $R_1$  in the circuit should use the noninductive elements due to their good high frequency characteristic.

A LCD absorption circuit can also decrease the voltage spike in the Buck converter. The LCD topology is presented in Figure 10(b). The resistance is not used in this kind of circuit. Thus the loss energy is equal to zero in theory. This topology is also called zero-voltage switches (ZVS). Due to the resonance of the inductance  $L$  and capacitance  $C$ , it can both accelerate the switch speed and reduce the voltage spike. Thus, the switching loss can be minimized.

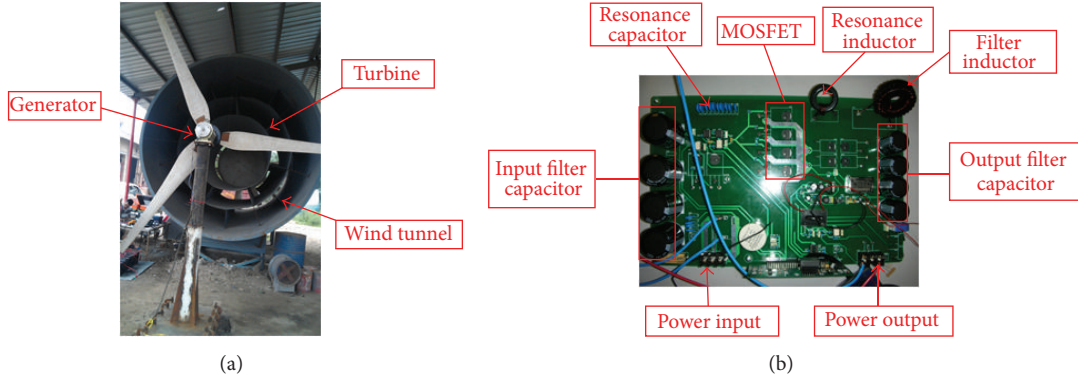


FIGURE 10: The actual wind generation system for experiment.

When LC resonance takes place, its resonant frequency can be calculated by

$$f_r = \frac{1}{2\pi\sqrt{L_1 C_1}}. \quad (16)$$

In order to reduce the influence on the PWM control, the resonant frequency of inductance  $L_1$  and capacitance  $C_1$  should be 4 to 10 times greater than switch frequency  $f$ . That is,

$$f_r = Nf, \quad (17)$$

where the value of  $N$  should be between 4 and 10. The value of resonance inductance  $L_1$  and capacitance  $C_1$  can be calculated by

$$L_1 = \frac{Z_r}{2\pi f_r}, \quad (18)$$

$$C_1 = \frac{1}{2\pi f_r Z_r},$$

where  $Z_r$  is the resonant impedance. This impedance depends on voltage and current of LC resonance circuit.

In this paper, the topology of Buck converter with LCD absorption is adopted.

In high power converter applications, IGBTs are commonly used in the literature, whereas the MOSFETs are rarely adopted. Considering switch frequency and cost, the use of multi-MOSFETs in parallel is proposed in this paper for a 2 kW Buck converter. The converter uses four MOSFETs in parallel to increase the conduction current. Each MOSFET has 44 A conduction current at 20°C and 500 V withstand voltage.

#### 4. Experiment Result

The experimental system consists of a 2 kW wind turbine and generator, with power converter, four batteries rated at 200 Ah in parallel, and load. The test platform and the designed DC/DC Buck converter are presented in Figure 10. The experimental parameters are displayed in Tables 1, 2, 3, 4, 5 and 6.

TABLE 1: Wind turbine parameter.

|                            |        |
|----------------------------|--------|
| Number of blades           | 3      |
| Blade radius               | 1.7 m  |
| Optimum ratio of tip speed | 6.7    |
| Maximum power coefficient  | 0.42   |
| Nominal wind speed         | 10 m/s |
| Cut-in wind speed          | 3 m/s  |
| Cut-off wind speed         | 22 m/s |

TABLE 2: PMSG parameter.

|                      |         |
|----------------------|---------|
| Nominal power        | 2 kW    |
| Nominal rotor speed  | 450 rpm |
| Nominal current      | 7 A     |
| Line-to-line voltage | 190 V   |
| Number of pole pairs | 4       |
| Winding resistance   | 1.1 ohm |
| Winding inductance   | 14.1 mH |

TABLE 3: Rectifier parameter.

|                           |           |
|---------------------------|-----------|
| Full bridge               | 3         |
| Conductive current        | 35 A      |
| Reverse breakdown voltage | 1600 V    |
| Operation temperature     | -55~150°C |

TABLE 4: DC bus parameter.

|                 |         |
|-----------------|---------|
| Capacitance     | 2200 uF |
| Maximum voltage | 500 V   |
| Maximum current | 50 A    |

The experimental test results at the wind speed of 8 m/s are shown in Figures 11 and 12. It can be concluded that the measured data is in agreement with the theory analysis in Figure 11.

From Figure 12, it can be seen that, with the designed converter topology, the minimum efficiency of the Buck

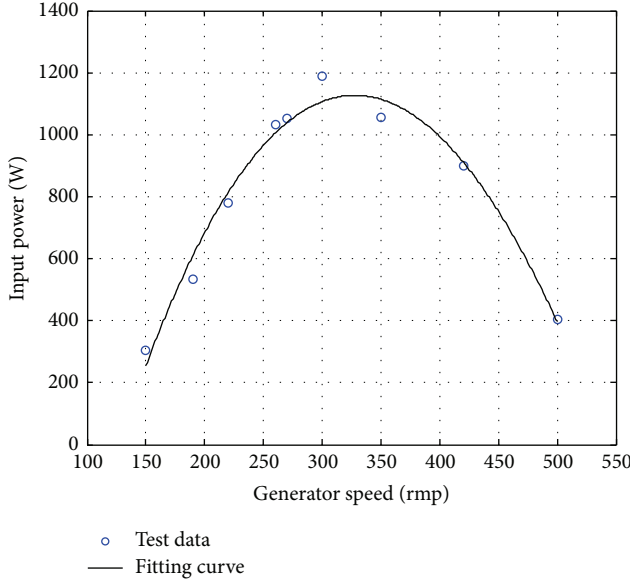


FIGURE 11: The input power of Buck converter versus generator speed at 8 m/s.

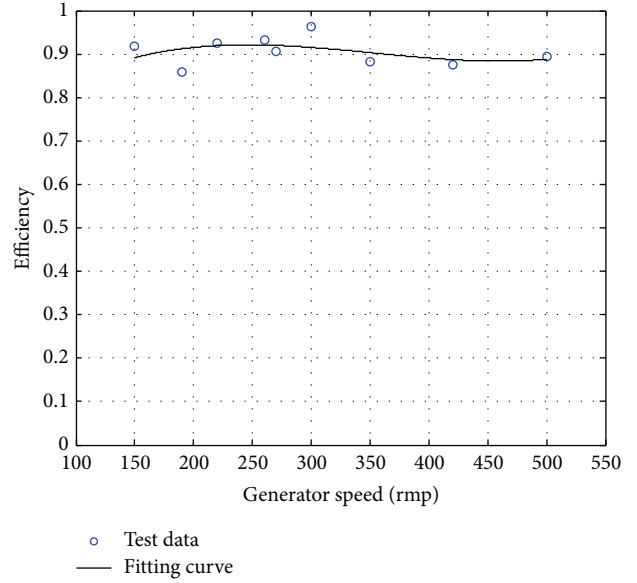


FIGURE 12: The efficiency of Buck converter versus generator speed.

TABLE 5: Buck converter parameter.

|                           |                            |
|---------------------------|----------------------------|
| Input filter capacitance  | $470 \times 4 \mu\text{F}$ |
| Switch device             | IXYS44N50                  |
| Resonance capacitance     | $10 \mu\text{F}$           |
| Resonance inductance      | $1.2 \mu\text{H}$          |
| Diode                     | DSEI60-06                  |
| Output filter capacitance | $47 \times 4 \mu\text{F}$  |
| Output filter inductance  | $200 \text{ mH}$           |
| Switch frequency          | $20 \text{ kHz}$           |

TABLE 6: VRLA parameter.

|                                  |                           |
|----------------------------------|---------------------------|
| Battery capacity                 | $200 \times 4 \text{ Ah}$ |
| Nominal voltage                  | $48 \text{ V}$            |
| Maximum charge/discharge current | $56 \text{ A}$            |
| Charge/discharge rate            | $0.1 \text{ C}$           |

converter is 86%, and the maximum efficiency point can reach 96%.

Figure 13 shows the experiment curve of input power for Buck converter versus generator power at 10 m/s wind speed. The generator gives over 2 kW power output at 240 rpm. The parallel MOSFETs structure in the improved Buck converter can work without any problem under high power output level.

The experimental results show that the improved Buck converter has a good performance in the high power wind system. In addition, a comparison of the two absorption circuits, RCD and LCD, is also made. Figure 14 shows a 23 A charge current to VRLA battery for converter RCD and LCD tests.

Comparing Figures 15 and 16, the voltage spike is clearly more significant in RCD absorption circuit. Thus, the switching loss in RCD circuit is greater than in LCD circuit.

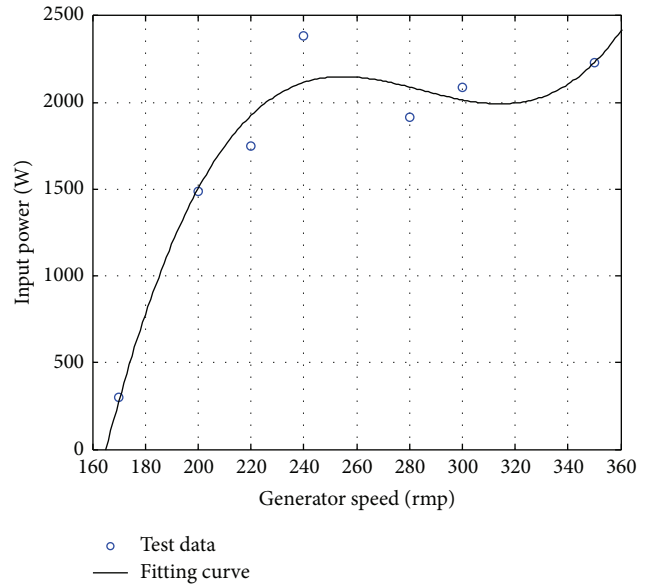


FIGURE 13: The input power of Buck converter versus generator speed at 10 m/s.

Moreover, owing to the consumptive resistance, the efficiency of this absorption circuit is very low. The experiment results show that the RCD circuit efficiency is only around 45~65%.

## 5. Conclusion

In recent years, the cost of wind energy is close to the traditional thermal power generation. Furthermore, it is a clean energy without any pollution. The wind energy is a common energy in nature. In this paper, an off-grid wind generation system is presented and discussed. A high power efficiency converter is designed based on the DC/DC Buck

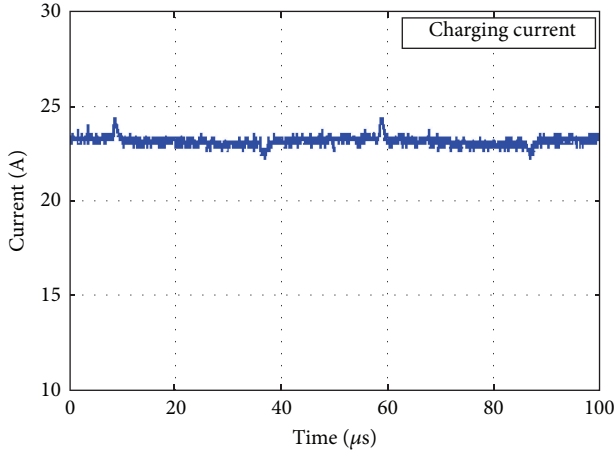


FIGURE 14: The charge current for VRLA battery.

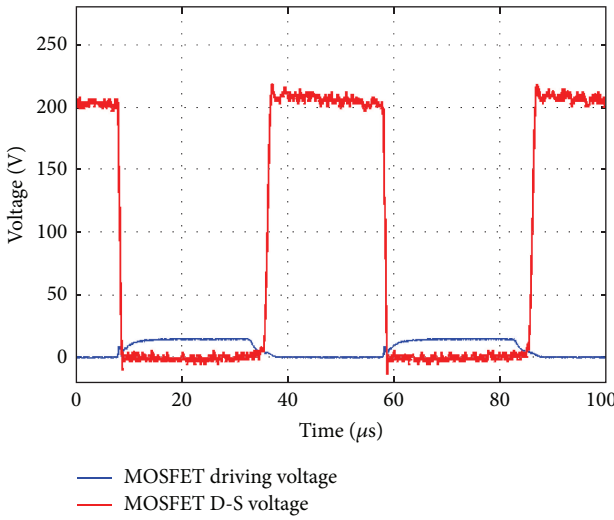


FIGURE 15: The Buck converter with LCD absorption circuit.

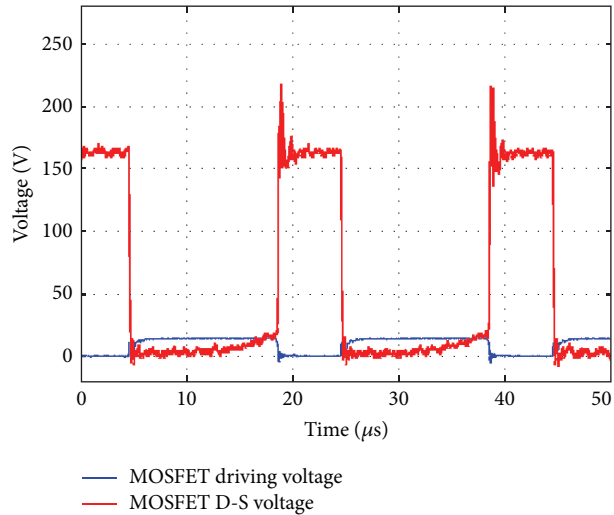


FIGURE 16: The Buck converter with RCD absorption circuit.

converter topology. Considering the characteristic of wind generation, maximum power point tracking technology is preferred.

An improved efficient LCD combinational circuit in the Buck converter is proposed for a 2kW off-grid wind generation system. In order to reduce the system cost, instead of IGBT device the paralleled multi-MOSFET structure is also used.

The experiments results show that the improved MOSFET based Buck converter with LCD absorption circuit can work without problem at 2kW power output level. The maximum efficiency of the designed converter is up to 96%. The proposed converter topology and control method provide a valid solution for wind turbine applications.

## Conflict of Interests

The authors declare that there is no conflict of interests regarding the publication of this paper.

## References

- [1] N. Lior, "Energy resources and use: the present situation and possible paths to the future," *Energy*, vol. 33, no. 6, pp. 842–857, 2008.
- [2] P. D. Lund, "Effects of energy policies on industry expansion in renewable energy," *Renewable Energy*, vol. 34, no. 1, pp. 53–64, 2009.
- [3] P. A. Østergaard, "Reviewing optimisation criteria for energy systems analyses of renewable energy integration," *Energy*, vol. 34, no. 9, pp. 1236–1245, 2009.
- [4] J. Wen, Y. Zheng, and F. Donghan, "A review on reliability assessment for wind power," *Renewable and Sustainable Energy Reviews*, vol. 13, no. 9, pp. 2485–2494, 2009.
- [5] M. Hoogwijk, B. de Vries, and W. Turkenburg, "Assessment of the global and regional geographical, technical and economic potential of onshore wind energy," *Energy Economics*, vol. 26, no. 5, pp. 889–919, 2004.
- [6] J. Wei and F. C. Lee, "Two novel soft-switched, high frequency, high-efficiency, non-isolated voltage regulators—the phase-shift buck converter and the matrix-transformer phase-buck converter," *IEEE Transactions on Power Electronics*, vol. 20, no. 2, pp. 292–299, 2005.
- [7] J. Zhang, J.-S. Lai, R.-Y. Kim, and W. Yu, "High-power density design of a soft-switching high-power bidirectional dc-dc converter," *IEEE Transactions on Power Electronics*, vol. 22, no. 4, pp. 1145–1153, 2007.
- [8] Y. C. Chuang and Y. L. Ke, "High efficiency battery charger with a buck zero-current-switching pulse-width-modulated converter," *IET Power Electronics*, vol. 1, no. 4, pp. 433–444, 2008.
- [9] K.-Y. Lo, Y.-M. Chen, and Y.-R. Chang, "MPPT battery charger for stand-alone wind power system," *IEEE Transactions on Power Electronics*, vol. 26, no. 6, pp. 1631–1638, 2011.
- [10] Y.-Y. Hong, S.-D. Lu, and C.-S. Chiou, "MPPT for PM wind generator using gradient approximation," *Energy Conversion and Management*, vol. 50, no. 1, pp. 82–89, 2009.
- [11] S. Heier, *Grid Integration of Wind Energy Conversion Systems*, John Wiley & Sons, Chichester, UK, 1998.

- [12] T. J. E. Miller, *Brushless Permanent-Magnet and Reluctance Motor Drives*, Oxford University Press, New York, NY, USA, 1989.
- [13] K. A. Stol and M. J. Balas, "Periodic disturbance accommodating control for blade load mitigation in wind turbines," *Journal of Solar Energy Engineering*, vol. 125, no. 4, pp. 379–385, 2003.
- [14] Q. Wang and L. Chang, "An intelligent maximum power extraction algorithm for inverter-based variable speed wind turbine systems," *IEEE Transactions on Power Electronics*, vol. 19, no. 5, pp. 1242–1249, 2004.
- [15] V. Mummadi, "Fourth order buck converter for photovoltaic maximum power point tracking applications," in *Proceedings of the IEEE International Conference on Sustainable Energy Technologies (ICSET '08)*, pp. 295–300, 2008.
- [16] S. K. Mazumder, M. Tahir, and S. L. Kamisetty, "Wireless PWM control of a parallel DC-DC buck converter," *IEEE Transactions on Power Electronics*, vol. 20, no. 6, pp. 1280–1286, 2005.
- [17] H. F. Bilgin, K. N. Köse, G. Zenginobuz et al., "A unity-power-factor buck-type PWM rectifier for medium/high-power DC motor drive applications," *IEEE Transactions on Industry Applications*, vol. 38, no. 5, pp. 1412–1425, 2002.

## Research Article

# High-Directivity Antenna Array Based on Artificial Electromagnetic Metamaterials with Low Refractive Index

Zhigang Xiao, Jiang Yao, and Shaoquan Yin

Physics and Electron Communication Department, Leshan Normal University, Leshan, Sichuan 614004, China

Correspondence should be addressed to Zhigang Xiao; zhigangxiaols@gmail.com

Received 25 March 2015; Accepted 28 May 2015

Academic Editor: Weiren Zhu

Copyright © 2015 Zhigang Xiao et al. This is an open access article distributed under the Creative Commons Attribution License, which permits unrestricted use, distribution, and reproduction in any medium, provided the original work is properly cited.

Planar metamaterials (MTMs) with low refractive index are proposed as a cover in a high-gain patch antenna array configuration. This MTMs array antenna has the following features: the number of array elements significantly decreases compared with the conventional array; the elements spacing is larger than a wave length by far; the feeding network is simpler. MTMs are made of two layers of periodic square metallic grids and placed above the feeding array. With the same aperture size, the directivity of MTMs-cover antenna array is higher than the conventional antenna array. The simulation results show that an array of  $2 \times 2$  patch elements integrated with MTMs yields about 26 dB of directivity which is higher than that of conventional  $8 \times 8$  patch array. Furthermore, on the condition of the same aperture size, an array patch with  $4 \times 4$  elements integrated with the MTMs-cover has an equivalent gain compared with the conventional patch array with  $16 \times 16$  array elements. Obviously, the former has a simpler feeding network and higher aperture efficiency. The experimental work has verified that the  $2 \times 2$  array case and the measured results have good agreement with the simulation.

## 1. Introduction

The traditional antenna technology to achieve the high directivity needs multiple radiating elements to fabricate the antenna array. The spacing between radiating elements is normally 50% to 70% of a wavelength. If the number of the array elements increases, it will increase propagation loss and make the feeding network become more complicated [1]. Emergence of the metamaterials (MTMs) provides a new technology to improve antenna innovation. A large number of research works have been achieved in obtaining the high directivity of antenna by using MTMs [2–9]. MTMs can be fabricated through various ways such as photonic crystal [2, 3], electromagnetic band gap (EBG) structure, frequency selective surface (FSS) [4–6], and other periodic artificial material which can be designed to have a low refractive index [7–9].

An ordinary microstrip patch antenna has the gain of about 7 dB. If a single patch is covered by a layer of MTMs, the gain will increase to about 20 dB. Compared with the conventional antenna array, a single feed source integrated with the MTMs-cover can obtain the same antenna gain or

higher. However, the antenna with MTMs-cover has higher aperture efficiency and simpler structure. And the manufacturing is relatively easy. If the feeding source is antenna array with MTMs-cover, the array becomes a sparse array of which the elements' spacing is more than one wavelength. The antenna array to meet the above conditions can achieve higher antenna gain. Meanwhile, because the number of the elements decreases, the array elements spacing becomes larger which results in the feeding network becoming simpler.

This paper presents a high-directivity antenna array model based on MTMs with low refractive index. A four-element array ( $2 \times 2$  patch) excited by the coaxial probe is used as the source, and MTMs, which are made of the planar periodic metallic grids and have a low refractive index, are used as the cover. The simulated and measured results show that, on the condition of the same aperture size, the  $2 \times 2$  microstrip patches array integrated with MTMs-covers has high directivity about 26 dB which is better than the conventional antenna array. The  $4 \times 4$  patch array with MTMs-cover may replace the conventional  $16 \times 16$  patch array, and they have similar high directivity.

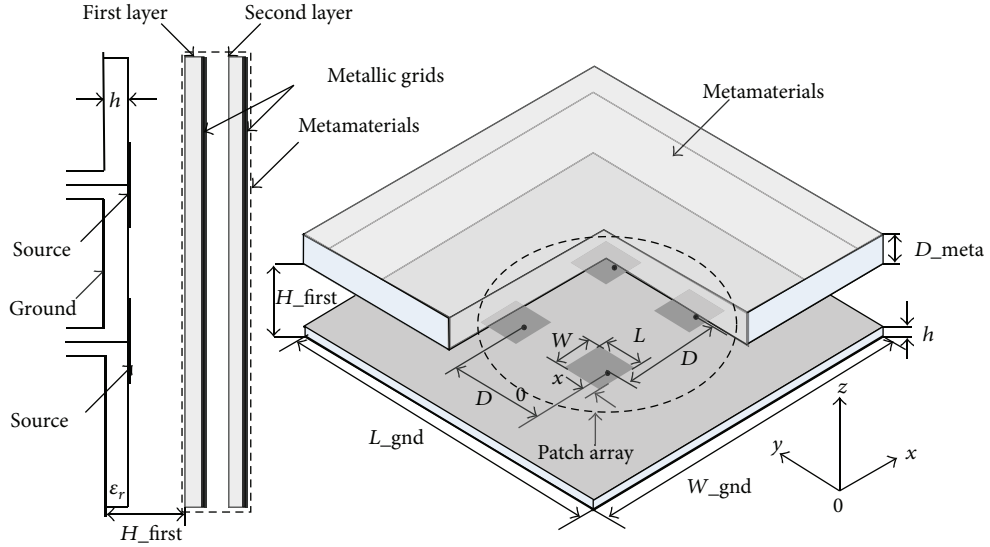


FIGURE 1:  $2 \times 2$  element antenna array integrated with MTMs-cover.

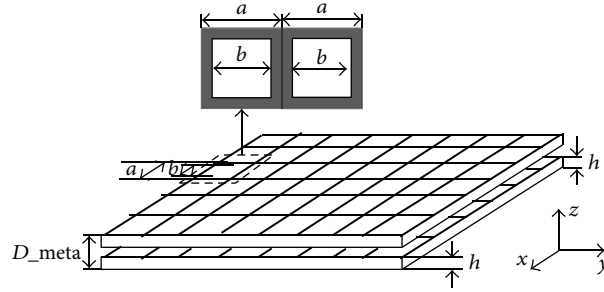


FIGURE 2: Metallic grids structure with low refractive index.

## 2. Antenna Array Structure and Simulation Results

The  $2 \times 2$  patch array integrated with planar MTMs-cover is shown in Figure 1. The source is the  $2 \times 2$  element patch array and fed by the coaxial probe, respectively. MTMs-cover with low refractive index is made of two layers of planar periodic metallic grids, as shown in Figure 2. The parameters of structure are designed carefully to operate at the Ku band and 14.6 GHz is suitable. The patch arrays and metallic grids are printed on a 1.5 mm thick microwave printed circuit board (PCB) substrate ( $\epsilon_r = 2.2$ ). The metallic grid cell size is shown as follows:  $a = 5.8$  mm and  $b = 4.6$  mm. The thickness of MTMs-cover is  $D_{meta} = 5.4$  mm, and the height from MTMs-cover to the ground is  $H_{first} = 7.1$  mm. The operating frequency of the array is 14.6 GHz. The patch elements have the same parameters:  $(L, W, x_0) = (5.2$  mm, 6.1 mm, 1.8 mm), and element spacing is  $D = 2.5\lambda_{(14.6\text{ GHz})}$ . The ground has the size  $(L_{gnd}, W_{gnd}) = (240$  mm, 240 mm), which is slightly larger than the area (230 mm  $\times$  230 mm) size of forty cells of the metallic grids.

Array element spacing ( $D$ ) is a very important parameter. For the conventional antenna arrays, element spacing is about

$0.5\lambda \sim 1.0\lambda$ , where  $\lambda$  is the operating wavelength. If the spacing is larger than this range, the grating lobe is obvious. If the spacing is lower than this range, the mutual coupling becomes strong. Therefore, the element spacing is defined at approximately  $0.7\lambda$ . However, for the antenna array with MTMs-cover, the spacing is considerably larger than  $1.0\lambda$ . Our research results show that the antenna array with MTMs-cover can show its value only when the element spacing is about  $D = 2.5\lambda_{(14.6\text{ GHz})}$ .

The radiation performance of the conventional  $2 \times 2$  element patch array and the  $2 \times 2$  element array integrated with MTMs-cover (both having the same element spacing  $D = 2.5\lambda_{(14.6\text{ GHz})}$ ) is analyzed by CST Microwave Studio. (Here, authors would like to express their sincere gratitude to the CST Company.) Figure 3 shows the comparison of their radiation patterns. The red curve indicates the case of conventional patch array. Without MTMs-cover, if the element spacing is greatly larger than  $2.0\lambda$ , the grating lobes and the directivity performance become worse, respectively. However, the array with MTM-cover has good directivity and lower side lobes.

Figure 4 shows the three-dimensional radiation patterns of the two antenna arrays. It is obvious that MTMs-cover has

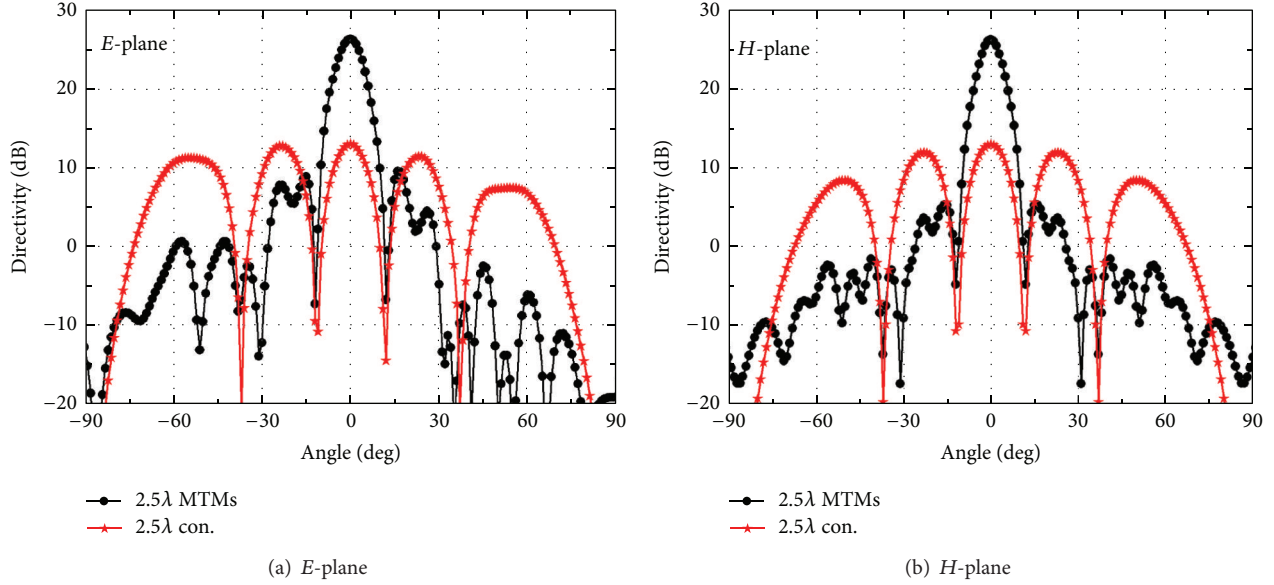


FIGURE 3: Radiation patterns of MTMs-cover array and the conventional type ( $D = 2.5\lambda_{(14.6 \text{ GHz})}$ ): (a)  $E$ -plane; (b)  $H$ -plane.

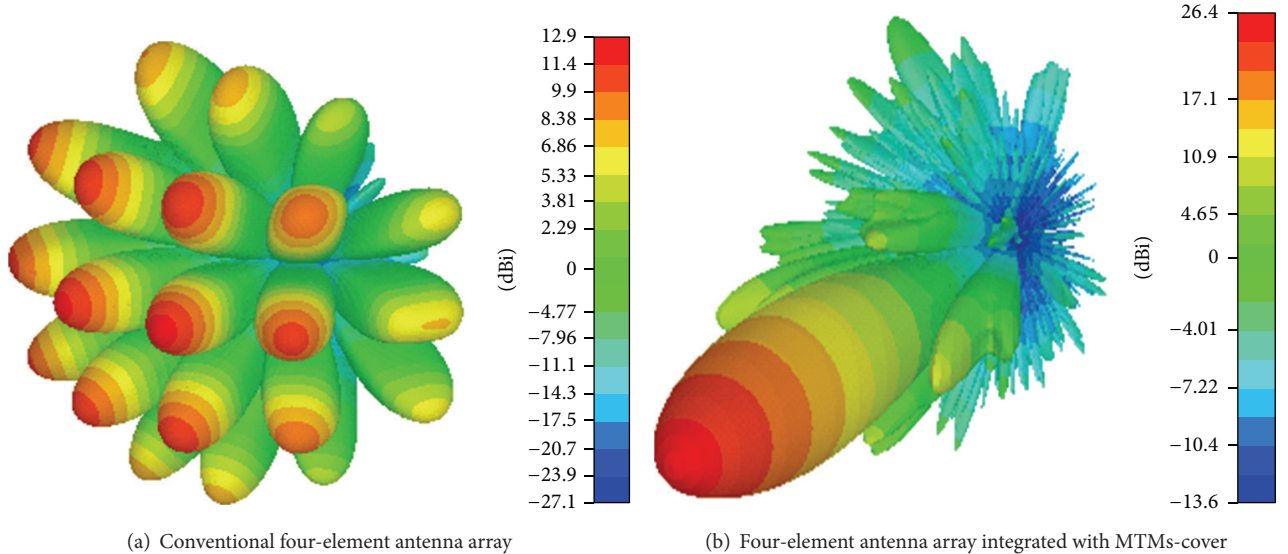


FIGURE 4: Three-dimensional radiation patterns of MTMs-cover array and the conventional type: (a) conventional  $2 \times 2$  element antenna array; (b)  $2 \times 2$  element antenna array with MTMs-cover.

effect similar to “optical lens,” which is capable of focusing the diffuse scattering electromagnetic wave for directive radiation.

Figure 5 illustrates the return loss of conventional patch and MTMs-cover type. The central operating frequency is 14.6 GHz. The conventional array has wider bandwidth. Because of the existence of MTMs-cover, the antenna impedance matching becomes worse when operating frequency is lower than the 14.4 GHz. Antenna impedance mismatching can be improved by adjusting parameters of the metallic grids.

The directivity of antenna array is calculated as follows:  $D_{\text{dir}}$  (dB) =  $10 \log(k \cdot 4\pi A / \lambda_0^2)$ , where  $A$  is the physical area

of the antenna ground and  $k$  (0~1) is the effective coefficient. Given  $k = 1$ , the theoretical value of the maximum directivity is  $D_{\text{max}}$  (dB) =  $10 \log(4\pi A / \lambda_0^2)$ . Here the area of the aperture is  $A = 240 \text{ mm} \times 240 \text{ mm}$  and  $\lambda_0 = 20.55 \text{ mm}$  (14.6 GHz); therefore the maximum directivity is  $D_{\text{max}}$  (dB) = 32.3 dB. The simulation result is  $D_{\text{dir}}$  (dB) = 26.3 dB. The aperture efficiency of the antenna is  $k = \log^{-1}(D_{\text{dir}}/10)/\log^{-1}(D_{\text{max}}/10) = 0.25$ . The aperture efficiency is relatively lower. The result shows that the aperture area in this case is larger for the  $2 \times 2$  array. If the higher directivity is not necessary, the physical area of the antenna can be properly reduced to increase the aperture efficiency. On the other hand, to keep the same physical area of the antenna and increase the number of

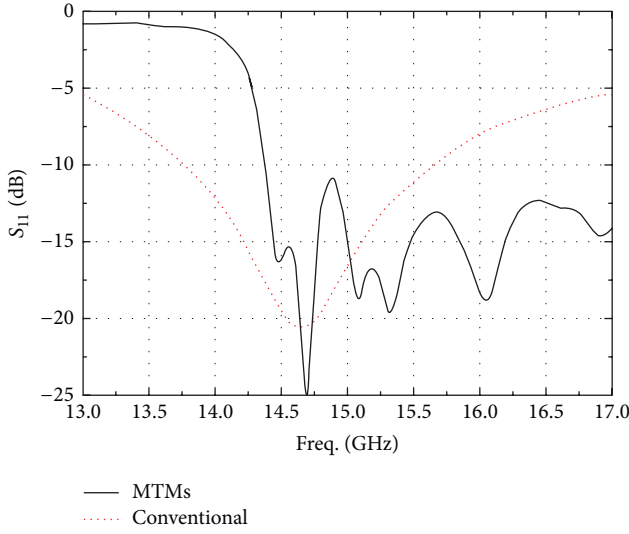


FIGURE 5: Return loss comparison of the conventional patch and MTM-cover type.

the array elements, it can be ensured that the antenna has higher directivity with improved aperture efficiency.

### 3. Experimental Results

In order to verify the theoretical analysis results, the antenna prototype is fabricated according to the structure parameters of the model. Figure 6 shows the  $2 \times 2$  element patch source, the assembled antenna with MTMs-cover, and the antenna in the anechoic chamber. The  $2 \times 2$  element patch array is fed by the 50 ohm coaxial line, and the feeding signal is provided through a power divider. Two layers of the metallic grids are fixed by using twelve nylon rods and installed to the ground plate.

Figure 7 shows the radiation patterns of the antenna prototype. Simulation results are in good agreement with measurements, which shows that the antenna design obtains success. It is worth noting that the fabrication error of prototype with two-layer metallic grids will affect the test results. In order to achieve good results, the prototype assembly need to be finely adjusted, which avoids as much as possible the physical influence.

### 4. Discussion

Through increasing the number of array elements, the conventional antenna array can obtain better directivity. Similarly, the method is also applicable to the antenna array with MTMs-cover. In  $2 \times 2$  case, if the aperture area of the antenna with MTMs-cover remains invariable and the number of array elements increases to  $4 \times 4$ , the antenna aperture efficiency will be enhanced obviously. The simulated radiation patterns of  $2 \times 2$  array and  $4 \times 4$  array with MTMs-cover are shown in Figure 8, respectively. The operating frequency is 14.6 GHz and the element spacing is

$D = 2.5\lambda_{(14.6 \text{ GHz})}$ . The  $2 \times 2$  array has a directivity of about 24.8 dB, while the directivity of  $4 \times 4$  array is improved to approximately 29.14 dB. The aperture efficiency of  $4 \times 4$  array is about 0.48. It is clear that increasing array elements improves the aperture efficiency obviously.

For MTMs-cover antenna array, using more array elements is a better approach to improve the antenna aperture efficiency. In addition, selection of the array element spacing is also a critical factor. Figure 9 shows that the aperture efficiency of  $2 \times 2$  elements and  $4 \times 4$  elements antenna array varies with the array element spacing change, respectively. The antenna array with MTMs-cover must be a sparse array, and the element spacing is in a reasonable range. In this case, the optimum spacing is about  $2.5\lambda_{14.6 \text{ GHz}}$ ; otherwise it cannot achieve the expected results.

Without considering the transmission loss, when the aperture area is  $240 \text{ mm} \times 240 \text{ mm}$ , the maximum theoretical directivity of conventional  $16 \times 16$  element antenna array is approximately 32.3 dB. Considering all the loss, the antenna array aperture efficiency is about  $-3 \text{ dB}$ , so the directivity is about 29.3 dB, which is equivalent to that of  $4 \times 4$  elements antenna array with MTMs-cover. However, the  $4 \times 4$  elements antenna array with MTMs-cover has simpler and easier fabricated feeding network compared with conventional array. These advantages show that the  $4 \times 4$  elements antenna array with the simper feeding network can replace the conventional  $16 \times 16$  element antenna array, so as to achieve the goal of making complex design become simpler.

### 5. Conclusion

The patch antenna array integrated with MTMs-cover proposed in this paper can markedly improve the antenna aperture efficiency and the antenna directivity. This type of antenna has the following characteristics: reduction of the number of array elements does not reduce the antenna directivity; increasing of the spacing of array element is beneficial to simplify a feeding network so as to reduce cost or provide extra space to other components on PCB substrate. A conventional  $16 \times 16$  element antenna array can be replaced by a  $4 \times 4$  elements antenna with MTMs-cover, and they have the same high directivity. The research results have a potential application to a large printed high-gain antenna array system.

### Conflict of Interests

The authors declare that there is no conflict of interests regarding the publication of this paper.

### Acknowledgments

This work was supported by Major Project of Education Department in Sichuan Foundation (no. 11ZA157). In addition, the authors would like to express their sincere gratitude

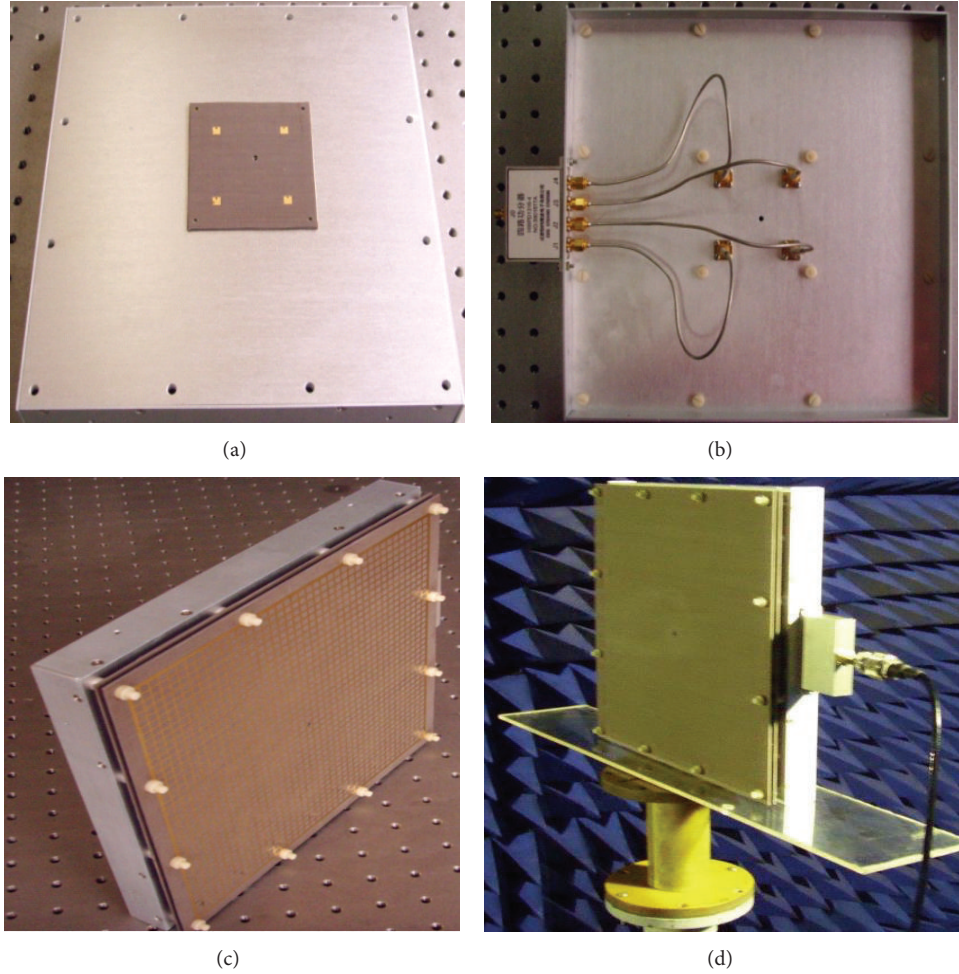


FIGURE 6: Photographs of patch antenna array and measured status in the anechoic chamber: (a)  $2 \times 2$  element patch antenna array; (b) back view of the antenna array; (c) patch array with MTMs-cover; (d) MTMs-cover antenna in the anechoic chamber.

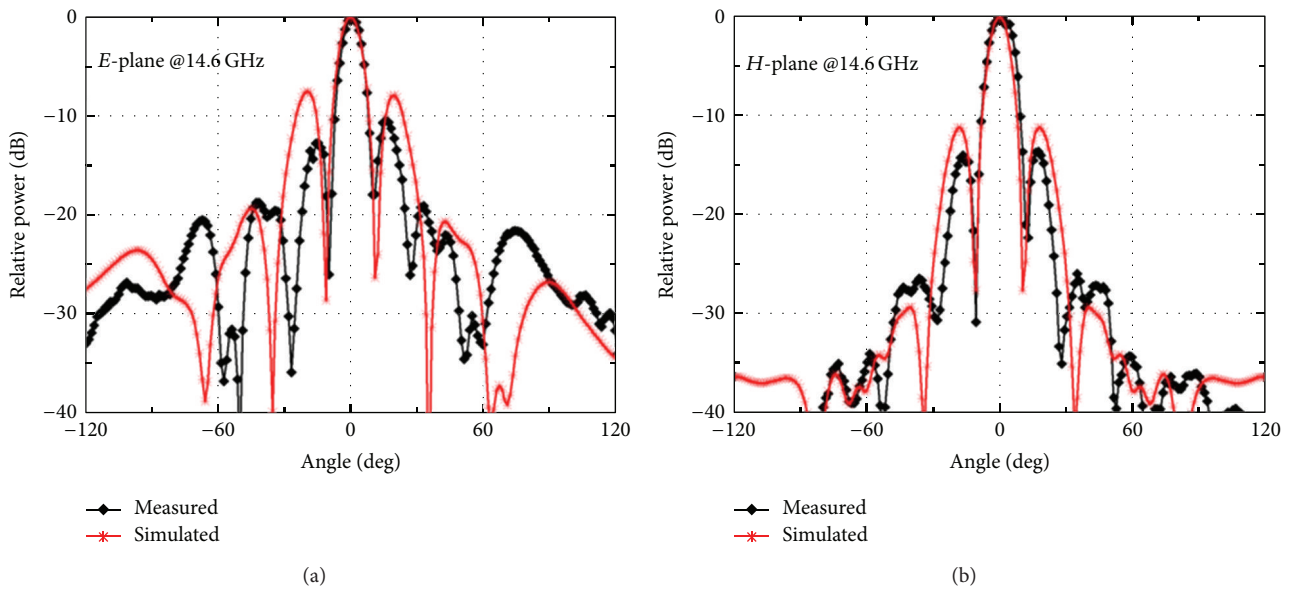


FIGURE 7: Radiation patterns of  $2 \times 2$  element patch array with MTMs-cover: (a) *E*-plane; (b) *H*-plane.

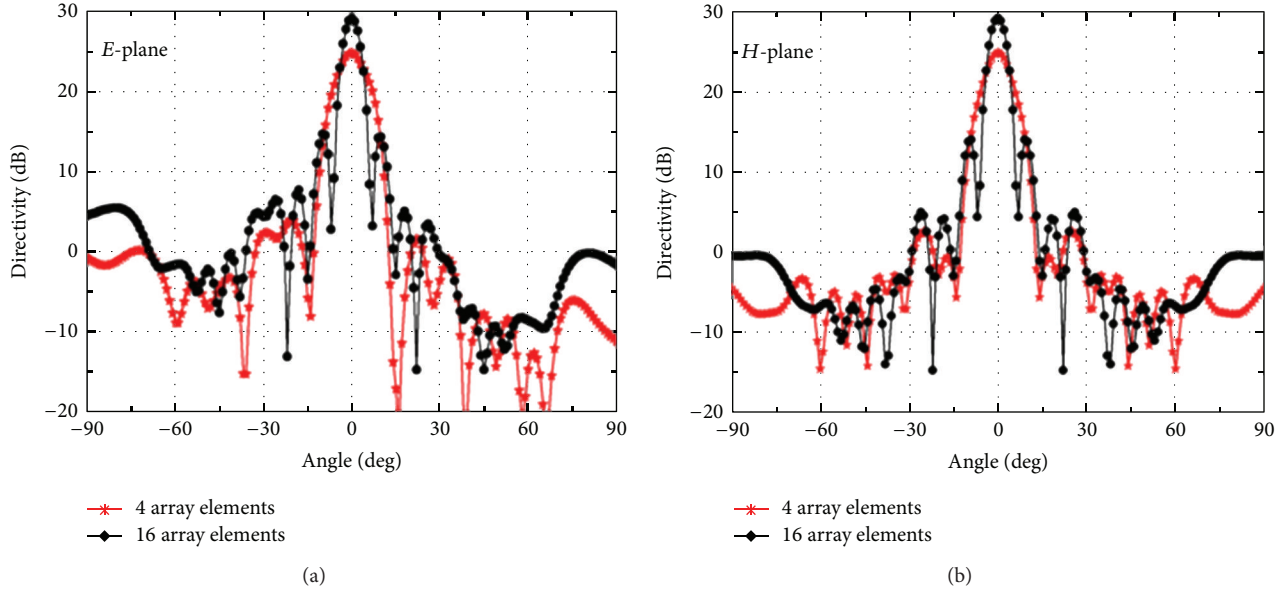


FIGURE 8: Antenna radiation patterns of the two arrays with MTMs-cover ( $D = 2.0\lambda_{14.6\text{GHz}}$ ): (a)  $E$ -plane; (b)  $H$ -plane.

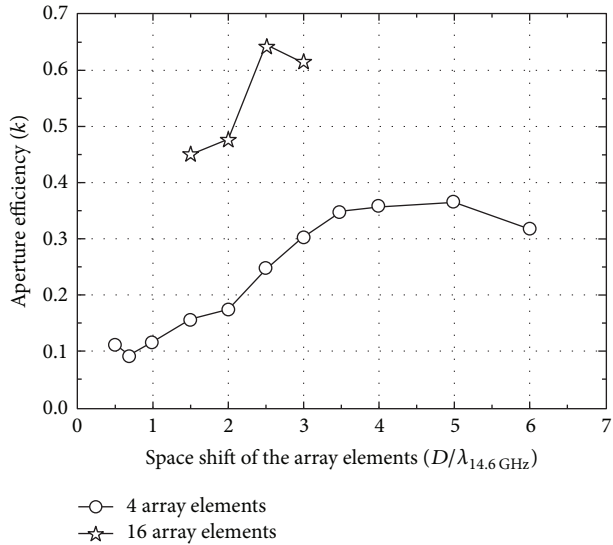


FIGURE 9: Aperture efficiency and element spacing of the two MTMs-cover arrays.

to the CST China, for providing the evaluated software for the simulation.

## References

- [1] E. Levine, G. Malamud, S. Shtrikman, and D. Treves, "A study of microstrip array antennas with the feed network," *IEEE Transactions on Antennas and Propagation*, vol. 37, no. 4, pp. 426–434, 1989.
- [2] M. Thèvenot, M. S. Denis, A. Reineix, and B. Jecko, "Design of a new photonic cover to increase antenna directivity," *Microwave and Optical Technology Letters*, vol. 22, no. 2, pp. 136–139, 1999.
- [3] B. Temelkuran, M. Bayindir, E. Ozbay et al., "Photonic crystal-based resonant antenna with a very high directivity," *Journal of Applied Physics*, vol. 87, no. 1, pp. 603–605, 2000.
- [4] A. R. Weily, L. Horvath, K. P. Esselle, B. C. Sanders, and T. S. Bird, "A planar resonator antenna based on a woodpile EBG material," *IEEE Transactions on Antennas and Propagation*, vol. 53, no. 1, pp. 216–223, 2005.
- [5] S. Wang, A. P. Feresidis, G. Goussetis, and J. C. Vardaxoglou, "High-gain subwavelength resonant cavity antennas based on metamaterial ground planes," *IEE Proceedings: Microwaves, Antennas and Propagation*, vol. 153, no. 1, pp. 1–6, 2006.
- [6] Y. J. Lee, J. Yeo, R. Mittra, and W. S. Park, "Design of a high-directivity Electromagnetic Band Gap (EBG) resonator antenna using a frequency-selective surface (FSS) superstrate," *Microwave and Optical Technology Letters*, vol. 43, no. 6, pp. 462–467, 2004.
- [7] S. Enoch, G. Tayeb, P. Sabouroux, N. Guérin, and P. Vincent, "A metamaterial for directive emission," *Physical Review Letters*, vol. 89, no. 21, pp. 213902-1–213902-4, 2002.
- [8] Q. Wu, P. Pan, F.-Y. Meng, L.-W. Li, and J. Wu, "A novel flat lens horn antenna designed based on zero refraction principle of metamaterials," *Applied Physics A: Materials Science and Processing*, vol. 87, no. 2, pp. 151–156, 2007.
- [9] H. Xu, Z. Zhao, Y. Lv, C. Du, and X. Luo, "Metamaterial superstrate and electromagnetic band-gap substrate for high directive antenna," *International Journal of Infrared and Millimeter Waves*, vol. 29, no. 5, pp. 493–498, 2008.

## Review Article

# Taming the Electromagnetic Boundaries via Metasurfaces: From Theory and Fabrication to Functional Devices

**Xiangang Luo, Mingbo Pu, Xiaoliang Ma, and Xiong Li**

*State Key Laboratory of Optical Technologies on Nano-Fabrication and Micro-Engineering, Institute of Optics and Electronics, Chinese Academy of Sciences, Chengdu 610209, China*

Correspondence should be addressed to Xiangang Luo; lxx@ioe.ac.cn

Received 26 March 2015; Accepted 25 June 2015

Academic Editor: Weiren Zhu

Copyright © 2015 Xiangang Luo et al. This is an open access article distributed under the Creative Commons Attribution License, which permits unrestricted use, distribution, and reproduction in any medium, provided the original work is properly cited.

As two-dimensional metamaterials, metasurfaces have received rapidly increasing attention from researchers all over the world. Unlike three-dimensional metamaterials, metasurfaces can be utilized to control the electromagnetic waves within one infinitely thin layer, permitting substantial advantages, such as easy fabrication, low cost, and high degree of integration. This paper reviews the history and recent development of metasurfaces, with particular emphasis on the theory and applications relating to the frequency response, phase shift, and polarization state control. Based on the current status of various applications, the challenges and future trends of metasurfaces are discussed.

## 1. Historical Remarks

Metasurface is a two-dimensional (2D) analogy of metamaterials [1, 2], which are artificial three-dimensional (3D) structures with subwavelength inclusions as well as effective constitutive parameters not occurring in natural materials. In the last years, metamaterials with negative, zero-refractive-index, and other exotic phenomena have enabled novel functionalities, such as invisibility cloaking [3] and perfect imaging [4]. Although metamaterials have achieved great success in the entire spectrum, great challenges still exist in the large-scale fabrication and the design of devices with broadband response, especially in the visible frequency range [5]. As alternatives, metasurfaces were proposed to tune the behavior of electromagnetic wave within one infinitely thin layer. Since metasurfaces are extremely thin and much easier to be fabricated than metamaterials, they have become one of the most promising researching areas in electromagnetics and optics [5]. As noted by Holloway et al., current optical metamaterials are actually often limited to construction of metasurfaces as a result of the huge fabrication obstacles [6].

Since James Clark Maxwell formulated his famous equations in 1863, it has been known that all electromagnetic problems can be solved if one knows the constitutive

parameters, initial and boundary conditions [7]. Actually, the essence of metamaterials is the precise design of constitutive parameters, whereas metasurfaces can be treated as a modification of boundary condition since they possess theoretically vanishing thickness. From this point of view, one can conclude that both metamaterials and metasurfaces can provide complete control over the electromagnetic fields. As illustrated in Figure 1, metasurface could replace traditional metamaterials in many conditions, such as invisibility cloak, perfect lens, and high-efficiency radiators [3, 4, 8, 9]. It should be noted that the interface between metamaterials and normal materials can be also regarded as a novel metasurface boundary condition, where many optical properties can be engineered without resorting to the bulk properties of the metamaterials [10]. In particular, exotic surface waves at these metasurfaces have also attracted great attention.

Although the upsurge in attention has been paid to metasurfaces only recently, the actual concept of metasurface is far from new. In fact, the electromagnetic theory of metasurface can be dated back to 1902, when Wood reported his notable anomaly [11] and Levi-Civita gave the boundary relations for a metallic sheet with vanishing thickness [12]. The discoveries of Wood and Levi-Civita have promoted the development of two areas, which are long treated as independent of each

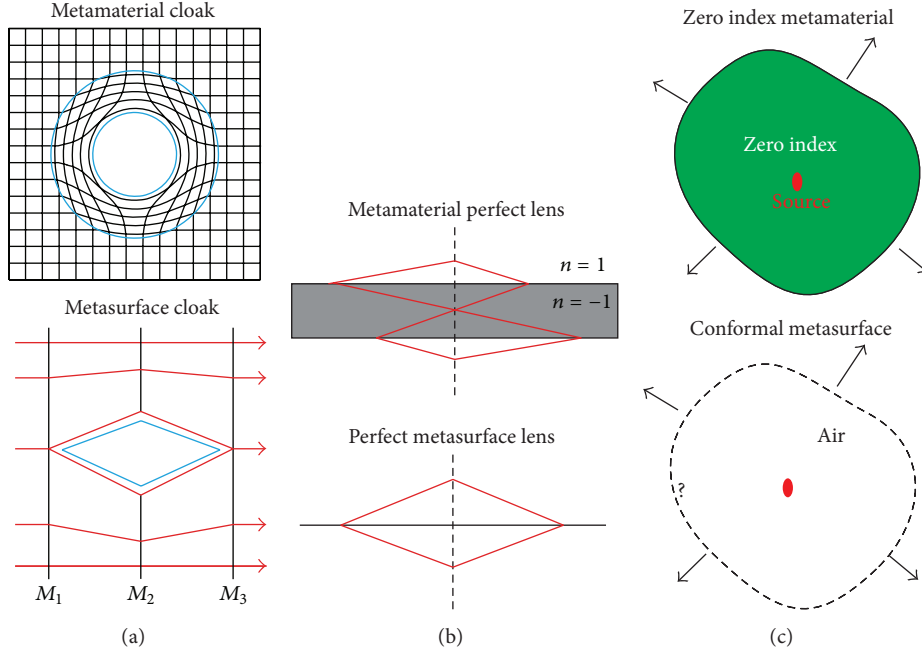


FIGURE 1: Comparison of metamaterials with metasurfaces. (a) Metasurface cloak. (b) Perfect metasurface lens. (c) Conformal metasurface versus traditional zero index metamaterial. Figures are reproduced from [2].

other. One research area of metasurface is about the surface plasmon polariton (SPP), which is a particular solution of surface wave at metal-dielectric surface; the other includes frequency selective surface (FSS), impedance sheet, and various types of planar antenna arrays. In the optical regime, the two areas begin to overlap with each other [13], since most of the metals in the metasurfaces become plasmonic at this particular frequency range. Indeed, it will be shown that the SPP and ordinary electromagnetic wave in metasurfaces can be deduced from a unified theory.

In recent years, there are a lot of research articles and review papers regarding the topic of metasurfaces. As an attempt to distinguish the concept of metasurface from previous FSS, Holloway et al. suggested that the different concepts can be classified according to the length scales [6]. Nevertheless, it is difficult to separate FSS and metasurface from the perspective of electromagnetic interactions, since both of them can be well described by effective impedance, although FSS is only intended to modify the frequency dependent transmission/reflection.

In this review, we attempt to give a unified perspective to the development of metasurfaces. The mechanism and applications of these metasurfaces are discussed in detail with an outlook for future development. As shown in Figure 2, there are many categories in the applications of metasurfaces: spectrum filters (including FSS [14–16], color filters [17], Fano resonances [18–25], and modulators [26–29]), plasmonic components for near-field optics [30–34], amplitude manipulation devices (absorbers [35–38] and antireflection coatings [39–42]), phase shifters (geometric phase [43, 44] and impedance-induced [19, 45] and plasmon-induced [2, 46]

phase shifter), antennas, and other electromagnetic devices [47–50].

## 2. Overview of Theoretical Approach

As implied by its name, metamaterial can be treated as an effective medium with complex permittivity  $\epsilon$  and permeability  $\mu$ . In the last several years, the effective medium theory (EMT) has been successfully applied in the analysis of metamaterials. Various methods, such as field averaging and S-parameters retrieving, have been proposed to obtain these effective parameters [51]. Although metasurface is an analogy of metamaterials with reduced dimensionality, the effective medium theory turns out to be less useful since the thickness of metasurface is approaching zero [6]. Indeed, the definition of permittivity and permeability is ambiguous in such a thin layer [52].

In this section, we would like to give an overview of the impedance theory for simple metasurfaces [2]. Instead of the susceptibilities, the electric impedance and magnetic impedance are adopted to connect the electric and magnetic fields at the boundaries of metasurfaces. For simplicity of discussion, the discussion in this paper is confined in uniaxial metasurfaces. First, the impedance boundary condition for metasurface is deduced from a general slab with given constitutive parameters and thickness. Second, some possible applications are discussed based on the properties of metasurfaces.

As depicted in Figure 3, the electromagnetic boundary condition requires that the tangent components of both electric fields  $E$  and magnetic fields  $H$  are continuous across

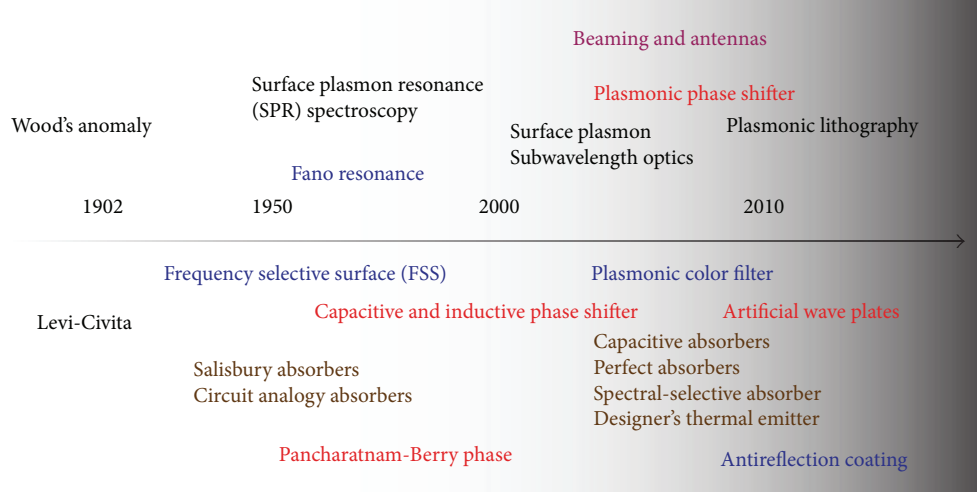


FIGURE 2: History and applications of metasurfaces.

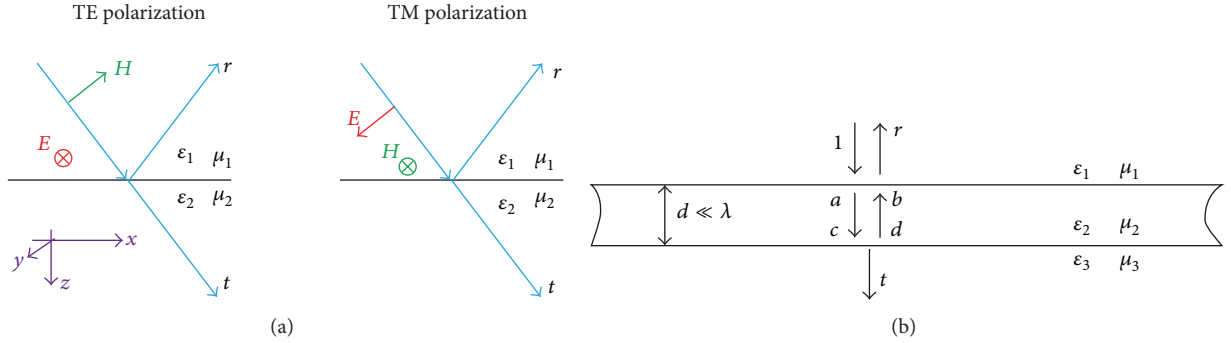


FIGURE 3: Boundary conditions at the interface between (a) two media and (b) a slab embedded in the two half spaces. Figures are reproduced from [2].

the interface between two dielectric media. For both the transverse electric (TE) polarization and the transverse magnetic (TM) polarization, the boundary conditions can be written as

$$\begin{aligned} 1 + r &= t, \\ Y_1(1 - r) &= Y_2 t, \end{aligned} \quad (1)$$

where  $r = E_{yr}/E_{yi}$  and  $t = E_{yt}/E_{yi}$  for TE polarization and  $r = E_{xr}/E_{xi}$  and  $t = E_{xt}/E_{xi}$  for TM polarization. The horizontal admittance for each medium is defined as  $Y_i = H_{xi}/E_{yi}$  for TE polarization and  $Y_i = H_{yi}/E_{xi}$  for TM polarization (here  $i$  is the index of layer). From Maxwell equations, one can obtain

$$\begin{aligned} \nabla \times E &= -\mu\mu_0 \frac{\partial H}{\partial t}, \\ \nabla \times H &= \epsilon\epsilon_0 \frac{\partial E}{\partial t}. \end{aligned} \quad (2)$$

Applying (2) to (1), the admittance can be obtained as

$$Y_i = \begin{cases} \frac{k_{zi}}{\mu_i\mu_0\omega} = \frac{\sqrt{\epsilon_i\mu_i k_0^2 - k_x^2}}{\mu_i\mu_0\omega}, & \text{for TE,} \\ \frac{\epsilon_i\epsilon_0\omega}{k_{zi}} = \frac{\epsilon_i\epsilon_0\omega}{\sqrt{\epsilon_i\mu_i k_0^2 - k_x^2}}, & \text{for TM.} \end{cases} \quad (3)$$

Here,  $k_x$  is the horizontal wave vector in this system, which is continuous for all planar multilayers. If light is illuminated from the air side, the incidence angle is  $\theta_i = \arcsin(k_x/k_0)$ . From (1) and (3), the reflection and transmission coefficients can be then expressed as follows:

$$\begin{aligned} t &= \frac{2Y_1}{Y_1 + Y_2}, \\ r &= \frac{Y_1 - Y_2}{Y_1 + Y_2}. \end{aligned} \quad (4)$$

It should be noted that (3) and (4) are identical to the traditional Fresnel equations, except that the horizontal wave

vector instead of the ambiguous incidence angle is used here. Our approach has also an advantage of simplicity since the reflection and transmission coefficients for both of the two polarization states keep the same.

As shown in Figure 3(b), for a thin slab sandwiched by two different media, the boundary conditions are

$$\begin{aligned} 1 + r &= a + b, \\ Y_1(1 - r) &= Y_2(a - b), \\ c + d &= t, \\ Y_2(c - d) &= Y_3t, \end{aligned} \quad (5)$$

where 1, 2, and 3 denote the three layers and  $a, b, c$ , and  $d$  are the coefficients for the counter-propagating waves inside the slab. By definition, there is

$$\begin{aligned} a &= c \exp(-ik_{z2}h), \\ b &= d \exp(ik_{z2}h). \end{aligned} \quad (6)$$

For extremely thin metasurface where  $|k_z h| \ll 1$ , it follows that

$$\begin{aligned} a &= c(1 - ik_{z2}h), \\ b &= d(1 + ik_{z2}h). \end{aligned} \quad (7)$$

From (7), one can derive that

$$\begin{aligned} a + b &= c(1 - ik_{z2}h) + d(1 + ik_{z2}h) \\ &= (c + d) + ik_{z2}h(c - d), \\ a - b &= c(1 - ik_{z2}h) - d(1 + ik_{z2}h) \\ &= (c - d) - ik_{z2}h(c + d). \end{aligned} \quad (8)$$

Here, we focus on the case when the permittivity and/or permeability of the middle layer is larger than that of the surrounding space. For nonmagnetic layer,  $Y_2 \gg Y_3$ ; thus,  $c - d \ll c + d$ , so (8) approximates as

$$\begin{aligned} a + b &= (c + d), \\ a - b &= \frac{Y_3}{Y_2}t - ik_{z2}ht. \end{aligned} \quad (9)$$

Inserting (9) into (5), there is

$$\begin{aligned} 1 + r &= t, \\ Y_1(1 - r) &= Y_3t - iY_2k_zht. \end{aligned} \quad (10)$$

Comparing with the electric impedance boundary conditions

$$\begin{aligned} 1 + r &= t, \\ Y_1(1 - r) &= Y_3t + Y_e t, \end{aligned} \quad (11)$$

one can derive the electric admittance for this slab:

$$Y_e = -iY_2k_{z2}h = \begin{cases} -i\frac{\varepsilon_2k_0^2 - k_x^2}{\mu_0\omega}h \approx -i\omega\varepsilon_2\varepsilon_0h \\ -i\omega\varepsilon_2\varepsilon_0h. \end{cases} \quad (12)$$

When the permeability  $\mu$  is much larger than  $\varepsilon$ ,  $Y_2 \ll Y_3$ ; thus,  $c - d \gg c + d$ , so (8) approximates as

$$\begin{aligned} a + b &= c + d - ik_{z2}h(c - d), \\ a - b &= c - d. \end{aligned} \quad (13)$$

As a result, there is

$$1 + r = t - ik_{z2}h\frac{Y_3}{Y_2}t, \quad (14)$$

$$Y_1(1 - r) = Y_3t.$$

Since the magnetic impedance boundary conditions can be written as

$$\begin{aligned} 1 + r &= t + Z_m Y_3 t, \\ Y_1(1 - r) &= Y_3t, \end{aligned} \quad (15)$$

thus the magnetic impedance could be derived as

$$Z_m = -i\frac{k_{z2}h}{Y_2} = \begin{cases} -i\omega\mu_2\mu_0h \\ -i\frac{\varepsilon_2\mu_2k_0^2 - k_x^2}{\varepsilon_2\varepsilon_0\omega}h \approx -i\omega\mu_2\mu_0h. \end{cases} \quad (16)$$

Clearly, the above assumption is valid even for oblique incidence as long as  $k_z h$  is much smaller than unit and the constitutive parameters are much larger than unit. The expressions in (12) and (16) are similar to the previous results obtained from radiation problem [53].

In the following, we will only discuss the case of thin structures without magnetic response. From (11), the reflection and transmission coefficients are

$$\begin{aligned} r &= \frac{Y_1 - Y_3 - Y_e}{Y_1 + Y_3 + Y_e}, \\ t &= \frac{2Y_1}{Y_1 + Y_3 + Y_e}. \end{aligned} \quad (17)$$

These equations can be considered as the *revised Fresnel equations* for metasurfaces. In principle, there are two kinds of waves: one with  $k_{\parallel} < k_0$  and the other with  $k_{\parallel} > k_0$ . When  $k_x < k_0$ , waves will transmit from the upper space to the lower one. There is an abrupt change in the phase and amplitude in the reflection and transmission coefficients.

When  $k_x > k_0$ , the surface plasmon modes can be derived by enforcing the reflection and transmission coefficients simultaneously to be infinite. For a single interface between dielectric and metal, this condition for (4) becomes  $Y_1 + Y_2 = 0$ , leading to a propagation constant for TM polarization:

$$\beta = k_x = k_0 \sqrt{\frac{\varepsilon_1\varepsilon_2}{\varepsilon_1 + \varepsilon_2}}. \quad (18)$$

Since the discussion is confined to the case of nonmagnetic response, there is no solution for TE polarization.

For an electric layer embedded in an infinite dielectric medium (insulator-metal-insulator, IMI), the guiding wave

can be obtained similarly as  $Y_1 + Y_3 + Y_e = 0$ . It follows that the propagation constant can be derived from

$$\frac{\varepsilon_1}{\sqrt{\varepsilon_1 k_0^2 - \beta^2}} + \frac{\varepsilon_3}{\sqrt{\varepsilon_3 k_0^2 - \beta^2}} + \frac{Y_e}{\varepsilon_0 \omega} = 0. \quad (19)$$

If one assumes  $\varepsilon_1 = \varepsilon_3$ , there is [54]

$$\beta = k_0 \sqrt{\varepsilon_1 - \left( \frac{2Y_1}{Y_e} \right)^2}. \quad (20)$$

Considering the fact that  $Y_e = -i\omega\varepsilon_2\varepsilon_0 h$ , there is

$$\beta = \sqrt{\varepsilon_1 k_0^2 + \left( \frac{2\varepsilon_1}{\varepsilon_2 h} \right)^2}. \quad (21)$$

According to (21), the wavelength of the coupled SPP approaches zero along with the decrease of the thickness [55].

For metal-insulator-metal (MIM) structure, the above approximation is not valid anymore. The accurate propagation constant should be derived by directly solving Maxwell's equations with boundary conditions:

$$\tanh \left( \frac{\sqrt{\beta^2 - \varepsilon_d k_0^2 h}}{2} \right) = -\frac{\varepsilon_d \sqrt{\beta^2 - \varepsilon_m k_0^2}}{\varepsilon_m \sqrt{\beta^2 - \varepsilon_d k_0^2}}. \quad (22)$$

In the microwave frequencies, many metals behave as nearly perfect conductors, so that no SPP can be found in ideal planar metal surfaces. Instead, if the metal surface is perforated by subwavelength holes, the effective permittivity can be arbitrarily tuned to sustain spoof SPP [56], where

$$\begin{aligned} \mu_x = \mu_y &= \frac{8\alpha^2 \mu_h}{\pi^2 p^2}, \\ \varepsilon_x = \varepsilon_y &= \frac{\pi^2 p^2 \varepsilon_h}{8a^2} \left( 1 - \frac{\pi^2 c^2}{a^2 \omega^2 \varepsilon_h \mu_h} \right). \end{aligned} \quad (23)$$

The plasmon frequency is the cutoff frequency:

$$\omega_{pl} = \frac{\pi c}{\sqrt{\varepsilon_h \mu_h}}. \quad (24)$$

As will be shown in Section 3.6, spoof SPPs have been successfully utilized in the design of groove antennas in the microwave frequencies.

### 3. Applications of Metasurfaces

As shown in the previous discussion, the waves in metasurfaces have many exotic properties, including the extremely short wavelength, abrupt phase change, and strong achromatic dispersion. Based on these properties, traditional electromagnetic laws and theory, such as the theory of diffraction limit, laws of reflection and refraction, the Fresnel equation, and absorption theory, should be revised correspondingly [2]. Practically, the revised theorem could find many applications as follows.

**3.1. Frequency Selective Surfaces.** Frequency selective surfaces (FSSs) are planar, periodic arrays of conducting patches on a substrate or a periodic array of apertures in a conducting sheet, which are used to filter electromagnetic waves [14]. The spectral responses of these structures are affected by various physical and electrical parameters, including the shape and type of their constituting elements. These FSSs can be designed to demonstrate low-pass, high-pass, band-pass, or band-stop behavior. Over the years, they have been extensively used in a variety of applications ranging between radar radomes, radar absorbers, and so on [14].

Early in 1919, Marconi and Franklin granted a patent that the contribution of a parabolic reflector was mimicked by using half-wavelength metallic wires [14]. Owing to the great potential military applications, FSSs have been the subject of intensive study since the 1960s.

The performance of FSS can be interpreted by the impedance and equivalent circuit theory, combined with the boundary condition. For a nonmagnetic freestanding metasurface, the band-pass and band-stop FSSs correspond to parallel and series type LC circuits, respectively. One common feature of the traditional FSSs is that the size of the resonant elements and their spacing are comparable to half a wavelength at the desired frequency of operation [58]. Since the electromagnetic response is a collective effect, the finite surface must include a large number of the constituting elements and be illuminated by a planar phase front to obtain the desired frequency response. At some conditions, such as radomes at lower frequencies, FSSs of relatively small electrical dimensions that are less sensitive to incidence angle and can operate for nonplanar phase fronts are highly desirable. In order to achieve this purpose, Sarabandi and Behdad proposed a new type of FSS. The structure consists of a periodic array of small metallic patches printed on one side of a dielectric substrate and a wire grid structure printed on the other side, both with the same period. The periodicity of the printed patterns is much smaller than the wavelength of the operating wavelength. The validity of this concept was demonstrated by numerical simulations and experiments.

One of the recent challenges for FSS is to optimize the frequency spectra with respect to angle of incidence and polarization of the waves impinging on it. In principle, multilayered FSS can improve these performances, but with oversized profiles. By using cavity mode whose resonant frequency is angle-independent, it was recently demonstrated that annular apertures array can show angle and polarization-independent transmission properties [15].

Ideal FSSs require that the transmission/reflection at the band edge changes sharply, which cannot be satisfied by most single-layer FSSs. In 2011, we proposed a novel plasmonic FSS with sharp band edges. By making use of plasmon hybridization, the bandwidth of the filter is tunable over a large range from 56.6 to 182.2 THz with magnetic and electric couplings between adjacent unit cells, as shown in Figures 4(c)–4(f).

More recently, the unique spectral properties of FSS were utilized to mimic many quantum phenomena, such as electromagnetically induced transparency (EIT) [59–61] and Fano resonance [19, 20, 62]. The interactions of different modes in the metasurfaces were tuned independently to

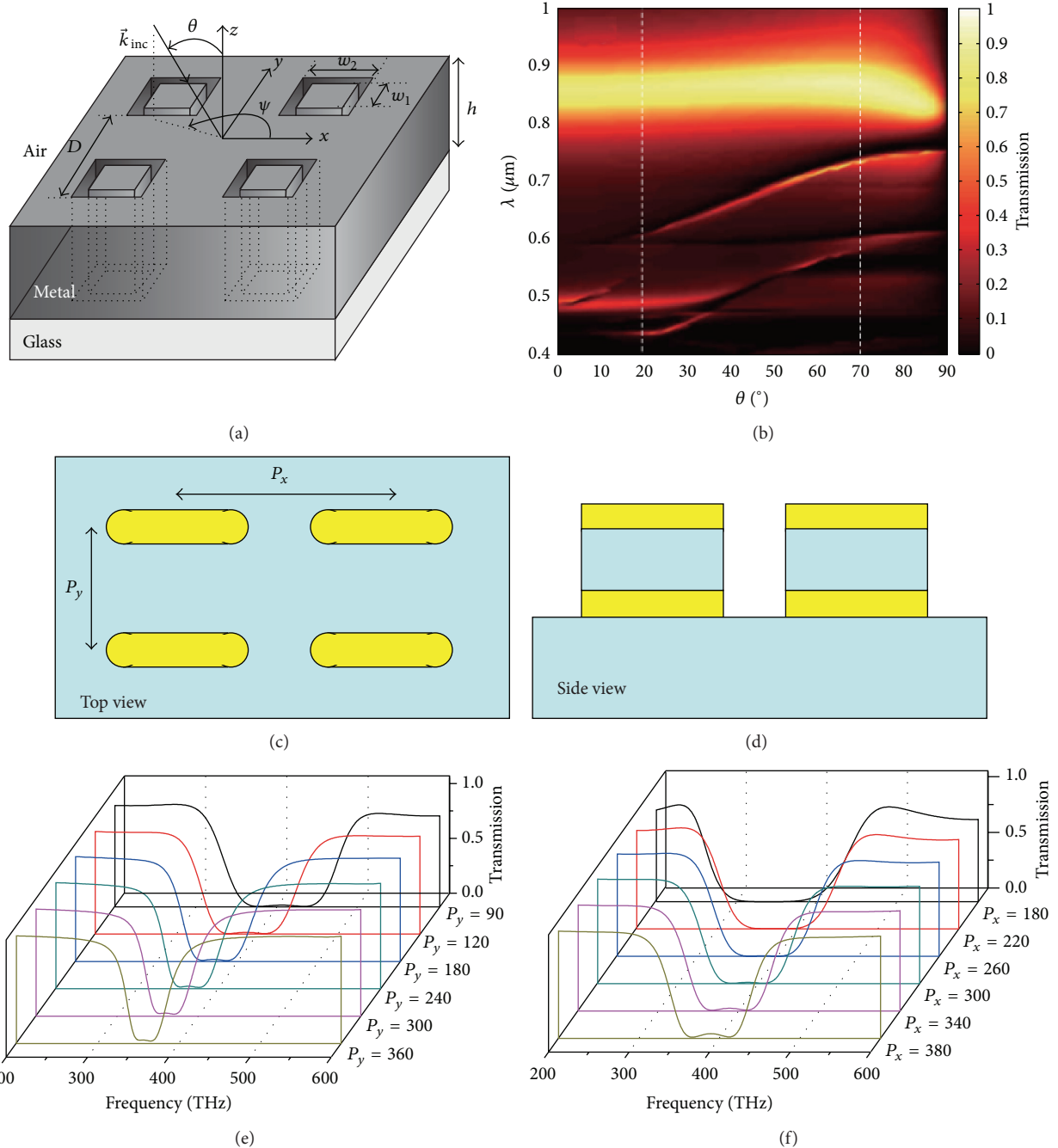


FIGURE 4: (a) Sketch of the large-angle FSS. (b) Evolution of the transmission efficiency as a function of the angle of incidence and incident wavelength. (c, d) Top and side views for the tunable band-stop FSS. (e, f) Evolution of the transmission spectra with different geometric parameters. Figures are reproduced from (a, b) [15] and (c)–(f) [57].

achieve the desired spectral distribution of reflection and transmission. In 2007, Fedotov et al. reported a resonance response with a very high quality factor in a planar metasurface with symmetry breaking in the shape of its structural elements [20]. It was shown that this symmetry breaking enabled the excitation of trapped modes, that is, modes that are weakly coupled to free space. The interference of trapped mode and normal mode makes the transmission spectrum be of the famous Fano shape.

In order to give a rigorous theory of Fano resonance in metasurfaces, we studied the electric and magnetic responses of a planar metasurface with perturbed periodicity [19]. Rigorous sheet impedance theory was given to analyze the electric-magnetic and magnetic-magnetic coupling effect. Interestingly, perturbation of the widths of wire pairs makes the adjacent metallic particles couple with each other. Q-factor as large as 100 has been theoretically obtained accompanying huge field enhancement, as described in Figure 5.

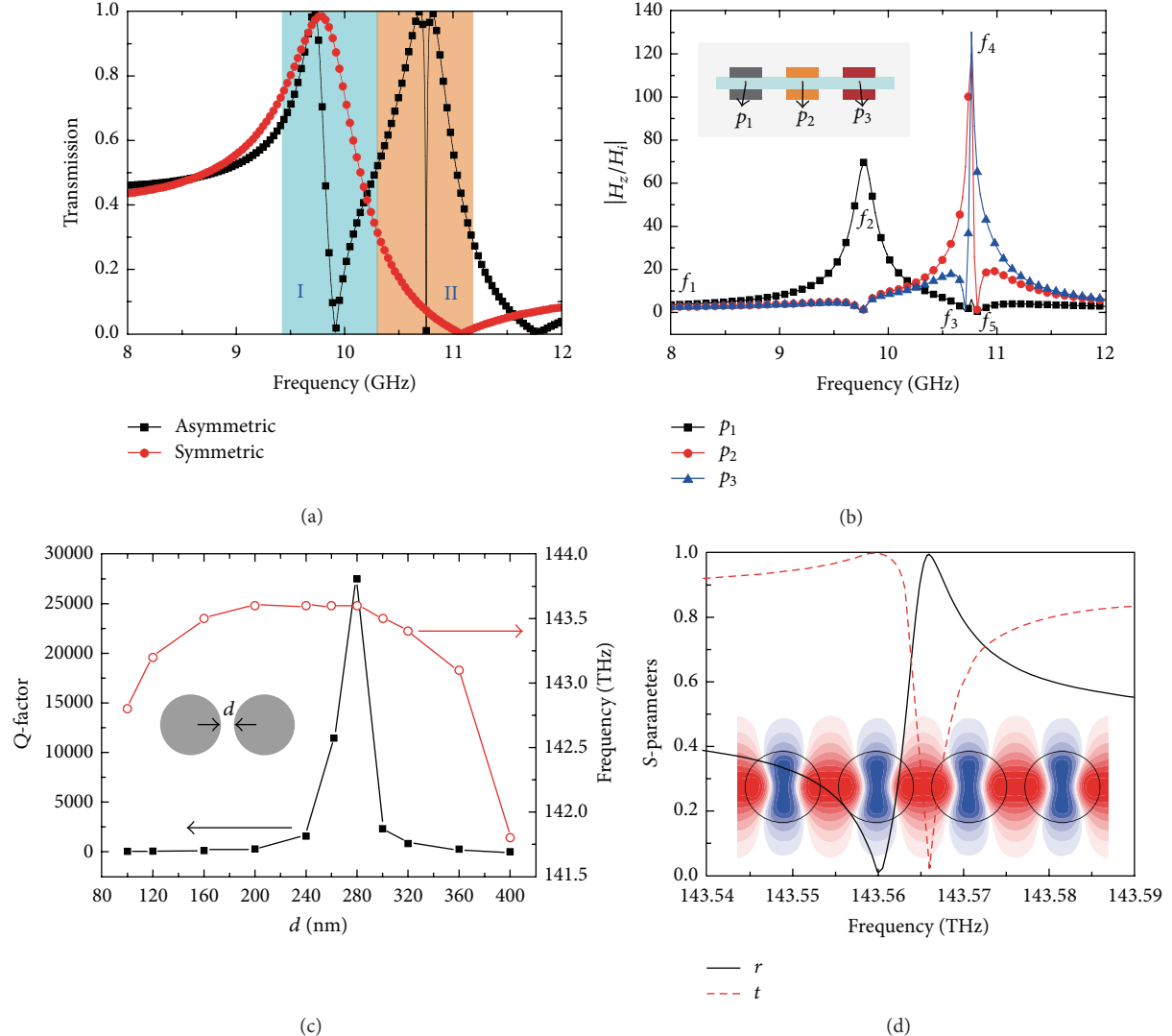


FIGURE 5: (a) Transmission coefficients for the symmetric and asymmetric metasurface slabs. Region I shows typical asymmetric line shape of Fano resonance. Region II demonstrates the ultrasharp resonance peak induced by interelement coupling. (b) Normalized magnetic fields (Hz) at the center of these resonators. The inset shows the unit cell and the points where the magnetic fields are extracted. (c) Quality factor of a cylinder array. (d) Scattering parameters of this array. Inset shows the distribution of the electric fields at resonant frequency. Figures are reproduced from (a, b) [19] and (c, d) [63].

It was believed that this kind of periodicity perturbation can provide a general approach for Fano resonance with ultrastrong local field enhancement.

Since there are three resonant peaks, the magnetic impedance can be written as a combination of individual magnetic resonances, as described by equivalent LC circuit model:

$$Z_m = \sum_{n=1}^3 Z_{mn} = \sum_{n=1}^3 \frac{i\omega L_n}{1 - \omega^2 L_n C_n}. \quad (25)$$

Here,  $L_1$ ,  $L_2$ ,  $L_3$ ,  $C_1$ ,  $C_2$ , and  $C_3$  are the corresponding inductances and capacitances. By fitting (25) with the retrieved magnetic sheet impedance, the LC parameters can be obtained as  $L_1 = 0.295$  nH,  $L_2 = 0.273$  nH,  $L_3 = 0.27$  nH,

$C_1 = 0.896$  pF,  $C_2 = 0.8$  pF, and  $C_3 = 0.794$  pF. The corresponding resonance frequencies are 9.79 GHz, 10.77 GHz, and 10.87 GHz.

Similar to the magnetic sheet impedance, the magnetic sheet current is also a summation of all the individual sheet currents:

$$j_m = \sum_{n=1}^3 j_{mn}, \quad (26)$$

where

$$j_{mn} = \frac{2Z_0 Z_{mn}}{Z_m + 2Z_0} H, \quad n = 1, 2, 3. \quad (27)$$

Using (25), (26), and (27), the sheet currents for different resonators can be easily calculated. The current of the first

resonator dominates at frequencies around 9.79 GHz. On the contrary, the second and third resonators dominate the frequency region around 10.8 GHz. Besides, one can find that the first resonator is out of phase with the other two resonators for  $9.79 \text{ GHz} < f < 10.77 \text{ GHz}$ . Also, for  $10.77 \text{ GHz} < f < 10.87 \text{ GHz}$ , the third one is out of phase with the others.

In fact, the  $\pi$  phase shift between these resonators is the key of resonant enhancement of sheet current. As an example, at frequency 10.82 GHz, there are  $|Z_{m1}| \ll |Z_{m2}| \approx |Z_{m3}|$  and  $|Z_{m1}| \ll |Z_{m1}|$ . Thus, we have

$$\begin{aligned} j_{m1} &\ll Z_0 H_i, \\ j_{m2} &= \frac{i\sqrt{L_2 L_3 (L_2 + L_3) (C_2 + C_3)}}{L_3 C_3 - L_2 C_2} H_i, \\ j_{m3} &= -j_{m2} = \frac{i\sqrt{L_2 L_3 (L_2 + L_3) (C_2 + C_3)}}{L_2 C_2 - L_3 C_3} H_i. \end{aligned} \quad (28)$$

It is interesting that the second and third sheet currents in (28) are out of phase. As a result, even higher enhancement factor and narrower bandwidth can be achieved by decreasing the difference between  $\omega_2$  and  $\omega_3$ .

Up to date, a great deal of previously proposed or demonstrated metasurfaces and nanostructures require the use of metallic inclusions, leading to large ohmic loss, a serious limitation to obtain ultrahigh Q-factor and huge field enhancement when Fano resonance occurs. In 2014, a new type of Fano resonance in silicon rods array was reported, and the maximum Q-factor was achieved at a rather large gap width between adjacent rods [63]. It was also different from the previously reported Fano resonance in photonics crystal slab [64], where the maximum Q-factor corresponds to a vanishing hole diameter.

In the optical regime, FSS can be utilized to realize color filtering [17, 65]. Xu et al. demonstrated plasmonic MIM nanoresonator structures to filter white light into individual colors [17]. The key concept of their method is to use the linear dispersion of plasmon to realize the photon-plasmon-photon conversion efficiently at specific resonant wavelengths (Figure 6). Compared with the aforementioned color-filtering methods, the new design significantly improved the absolute transmission, pass bandwidth, and compactness. In addition, the filtered light is naturally polarized, making it attractive for direct integration in liquid crystal displays (LCDs) without a separate polarizer layer.

FSS can be also utilized in selective solar absorbers to suppress infrared reradiation. Owing to the frequency-independent absorption, the equilibrium temperature of an irradiated blackbody in vacuum is only  $80^\circ\text{C}$ . In order to realize frequency selective transmission and absorption, multilayered films were utilized. Nevertheless, high-temperature instability limits the highest operating temperatures. In 1974, Horwitz used an array of deep holes in a metal to realize selective solar absorbers with ratios of solar absorbance to thermal emittance of 30:1 at temperatures of about  $200^\circ\text{C}$  [66]. Recently, we proposed a multilayered pyramidal array made of tungsten to demonstrate the selective solar absorption [67].

The broadband absorber is made up of a periodic array of multilayered truncated pyramids. The absorbance is about 99% from  $0.28 \mu\text{m}$  to  $1.5 \mu\text{m}$  for both TE polarization and TM polarization at room temperature or high temperature (966 K).

**3.2. Polarization-Manipulating Metasurfaces.** Polarization plays an important role in electromagnetic waves since a majority of phenomena are polarization sensitive. Manipulation of polarization has been a hot topic for quite a long time. Traditional birefringent and chiral medium have the ability of polarization modulation. However, these traditional media need large thickness to accumulate enough phase shift between the perpendicular components of the incident electric fields. Thus, the optical systems involving polarization applications have become complex and bulky.

With the help of metasurface-assisted law of polarization conversion (MLPC), one can greatly improve the performance and enable high conversion efficiency and ultra-thin thickness [2]. In general, metasurfaces for polarization manipulation include transmissive and reflective types and can be classified into anisotropic and chiral ones from the viewpoint of the structure properties.

**3.2.1. Transmissive Anisotropic Metasurface Polarizer.** It is well known that polarization states of light can be changed by naturally occurring anisotropic media as the two axes possess different refractive indexes ( $n_+$  and  $n_-$ ), leading to a relative phase shift between the two axes. However, as the difference between  $n_+$  and  $n_-$  is typically small, the thickness of traditional polarizers is required to be much larger than the operational wavelength. Moreover, the working bandwidth is narrow because the phase shift is frequency dependent.

As an alternative, metasurfaces provide new opportunities to achieve polarization manipulation with ultrathin artificial structures, including strip gratings and meander lines [68, 69]. In particular, Wang et al. utilized a single-layer metasurface with asymmetric cross-shaped apertures and demonstrated an ultrathin ( $0.29\lambda$ ) terahertz quarter-wave plate [70].

The physical foundation of the polarization control with metasurface is the metasurface-assisted polarization conversion (MLPC), that is, the revised Fresnel equations [2], which can also be written as

$$\begin{aligned} r_x &= \frac{Y_1 - Y_3 - Y_{ex}}{Y_1 + Y_3 + Y_{ex}}, \\ t_x &= \frac{2Y_1}{Y_1 + Y_3 + Y_{ex}}, \\ r_y &= \frac{Y_1 - Y_3 - Y_{ey}}{Y_1 + Y_3 + Y_{ey}}, \\ t_y &= \frac{2Y_1}{Y_1 + Y_3 + Y_{ey}}. \end{aligned} \quad (29)$$

Based on (29), we can control the reflection and transmission for both polarization states. One particular simple example

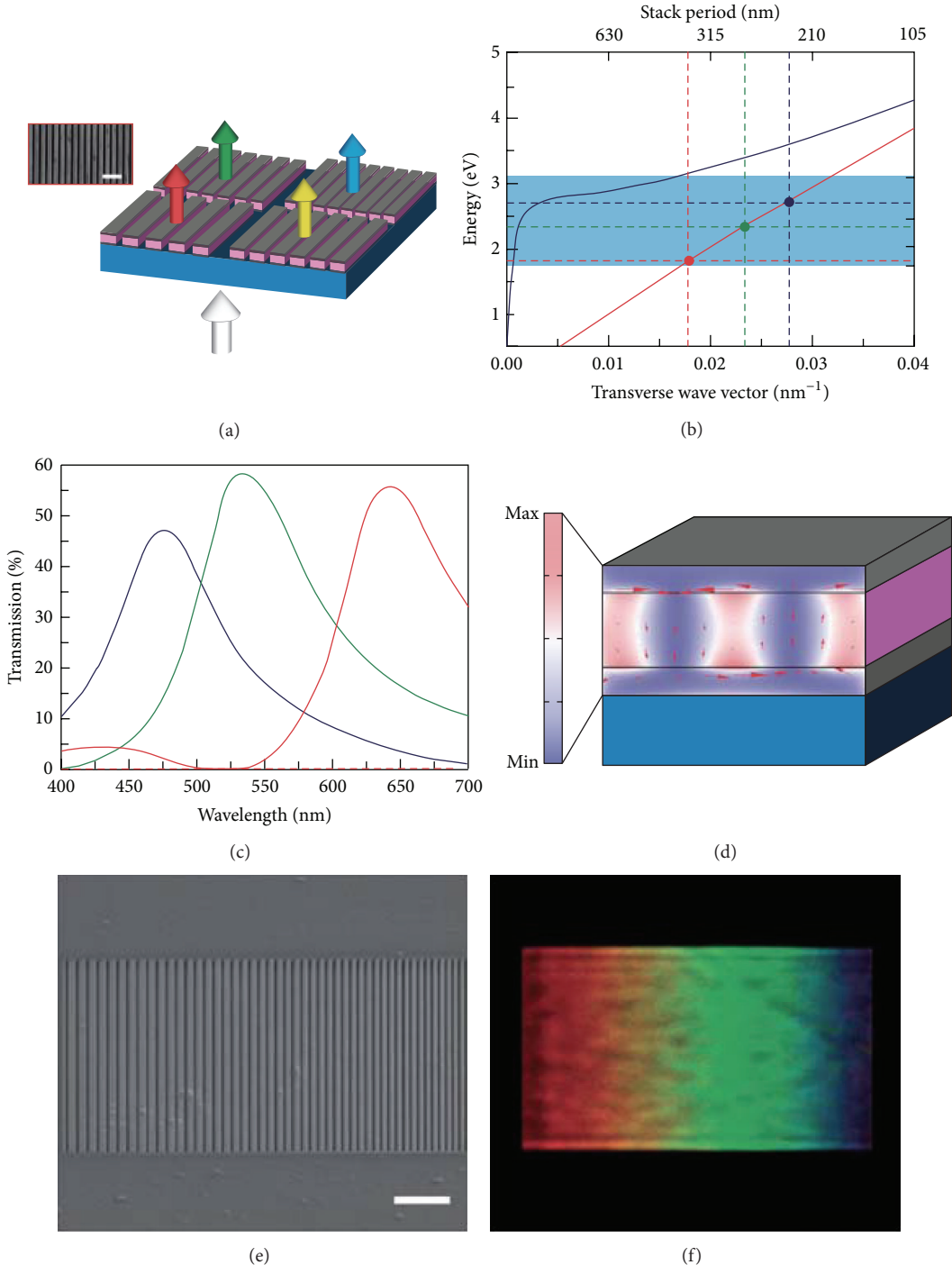


FIGURE 6: (a) Schematic diagram of the proposed plasmonic nanoresonators. Inset is the scanning electron microscopy (SEM) image of the fabricated device. Scale bar, 1  $\mu\text{m}$ . (b) Plasmon dispersions in MIM stack array. The shaded region indicates the visible range. (c) Simulated transmission spectra for the RGB filters. The solid and dash curves correspond to TM and TE illuminations, respectively. (d) Cross section of the time-average magnetic field intensity and electric displacement distribution (red arrow) inside the MIM stack at a wavelength of 650 nm with 360 nm stack period. (e) SEM image of the fabricated 1D plasmonic spectroscope with gradually changing periods from 400 to 200 nm (from left to right). Scale bar, 2  $\mu\text{m}$ . (f) Optical microscopy image of the plasmonic spectroscope illuminated with white light. Figures are reproduced from [17].

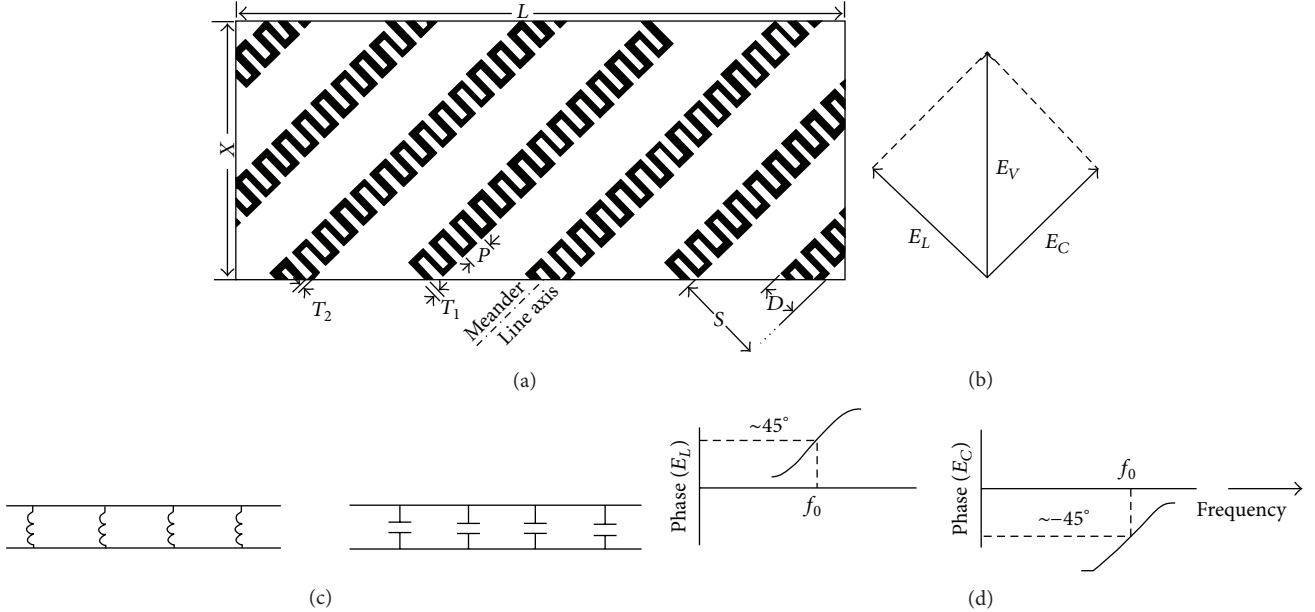


FIGURE 7: (a) Schematic of the anisotropic polarizer based on meander lines. (b) Decomposition of the incident fields along the two main axes. (c) Equivalent circuits for the two polarized waves. (d) Phase shifts for the two orthogonal polarization types. Figures are reproduced from [68].

of this kind of anisotropic metasurface is shown in Figure 7, where the gaps between the parallel strips can be taken as capacitance and the strips can effectively be equal to inductance. Therefore, the electromagnetic wave with electric perpendicular ( $E_{\perp}$ ) or parallel ( $E_{\parallel}$ ) components to the strips would be modulated by the effective capacitance and inductance. Hence, the transmitted phases of  $E_{\perp}$  and  $E_{\parallel}$  would also be, respectively, retarded and advanced. When the differential phase shift equals  $\pm 90^\circ$ , circular polarized wave would emerge.

In 2010, Euler et al. [71] designed a single-layer circularly polarized convertor using periodic split slot ring structure, and this polarization convertor can realize relative 3 dB axial ratio (AR) bandwidth of 11.75%. In 2011, a  $\lambda/20$  thick metasurface was employed to manipulate EM wave polarization with near 100% efficiency in transmission geometry [72].

Recently, Ma et al. reported a single-layer metasurface to convert the incident linearly polarized wave into circularly polarized one in a broadband [45], as shown in Figure 8. This polarizer is composed of metallic periodic structures. Two basic patterns are the metallic annular ring and 135° orientated strip. When a linearly polarized plane wave with  $E$  field along the  $x$ -axis or  $y$ -axis normally irradiates onto the polarizer, it can be converted into the circularly polarized wave. The simulated and measured results show that this polarizer can transform the incident linearly polarized light into circularly polarized one in the frequency range from 13.5 to 15.3 GHz, where the AR is less than 3 dB. The relative bandwidth of this polarizer is 17%, and its thickness is only  $\lambda/40$  ( $\lambda$  is the central working wavelength).

As depicted in Figures 8(b) and 8(d), the circular polarizer was integrated into a conventional linearly polarized

patch antenna to realize high gain and circular polarized radiation. The gain of conventional patch antenna is sharply increased from 7 dB to about 11 dB at 13.9 GHz. In addition, near-perfect circularly polarized radiation pattern is realized in the frequency band ranging from 13.55 GHz to 13.9 GHz. This metasurface-based circularly polarized antenna solved the difficulty problem of antenna design, and the radiation character was greatly improved.

The above mentioned anisotropic metasurfaces modulate the phase shift in two perpendicular directions, in a way similar to the traditional dielectric polarizers. However, this kind of single-layer metasurface suffers the half power loss; namely, the incident power is 50% reflected by the metasurface, and only half of the incident linearly polarized wave can be converted into the circularly polarized wave. To solve this problem, more layers of metallic structures are needed according to the theory proposed by Markovich et al. [73]. It is proved that the efficiency can reach 100% in the two layered metasurfaces. However, the perfect polarization transformation is limited to a single frequency, and the transformation effect deteriorates drastically away from the central frequency.

**3.2.2. Reflective Anisotropic Metasurface Polarizer.** In order to increase the polarization conversion efficiency and working bandwidth of the metasurfaces, reflective metasurfaces (or metamirrors) have been proposed by various groups [74–79]. In 2007, Hao et al. [75] proposed a circular polarizer based on an ultrathin metasurface reflector. Hao et al. [80] and Pors et al. [74] also obtained similar phenomenon at optical frequencies using orthogonally oriented electrical dipoles. Compared

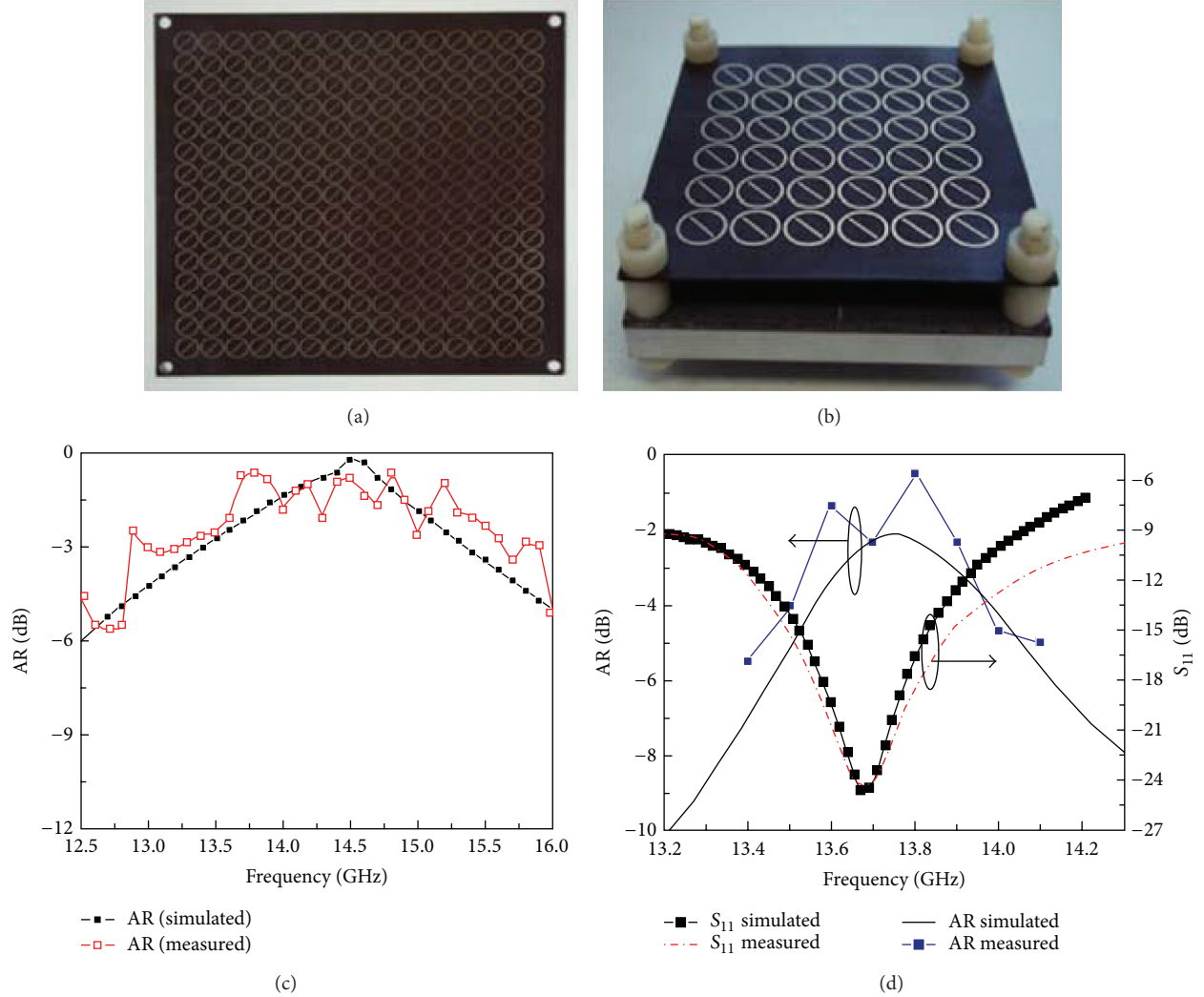


FIGURE 8: Photograph of the (a) fabricated polarizer and (b) high-gain circularly polarized patch antenna. (c, d) Measured and simulated AR for the polarizer and the antenna, respectively. Figures are reproduced from [45].

to the transmissive polarization transformers, the metamirrors have much smaller thickness due to the large anisotropy as well as higher energy efficiency since no complicated antireflection technique is applied.

Owing to the intrinsic resonance, metamirrors are often realized in narrow frequency band. In order to overcome this problem, we designed a dispersive ultrathin metamirror to extend the bandwidth [81]. In general, the impedance sheet for both the  $x$ - and  $y$ -directions can be frequency dependent. As a first attempt, we set  $Z_x$  as being constant ( $Z_x = \infty$ ) and  $Z_y$  as being highly dispersive. Since the dielectric spacer is chosen as air ( $n = 1$ ), the reflected phase shift can be calculated directly from the well-established transfer matrix method [81]:

$$\Phi_x = \pi + 2kd,$$

$$\Phi_y = \arg \left( \frac{-Z_0/Z_y - (2 - Z_0/Z_y) \exp(i2kd)}{2 + Z_0/Z_y - Z_0/Z_y \exp(i2kd)} \right), \quad (30)$$

where  $k$  is the wave vector in free space and  $d$  is the thickness of dielectric spacer. The optimal impedance for a certain relative phase shift  $\Delta\Phi$  can be calculated as

$$\frac{Z_y}{Z_0} = -\frac{1}{2} \frac{A - AB + 1 - B}{A + B}, \quad (31)$$

where  $A = \exp(i(\Delta\Phi + 2kd + \pi))$  and  $B = \exp(i2kd)$ . Subsequently, the optimal impedance required for the perfect polarization control can be obtained. The optimal impedance for  $\Delta\Phi = \pi/2$ , that for  $\pi$ , and that for  $3\pi/2$  were calculated, which vary slightly with working frequency. In particular, the required impedance for  $\Delta\Phi = \pi/2$  is mainly capacitive within the whole frequency range. For  $\Delta\Phi = \pi$ , however, the curve is separated to one capacitive region and the other inductive region at the two sides of the central frequency  $f = 0.25c/d$ , where  $c$  is the speed of light. For  $\Delta\Phi = 3\pi/2$ , the requirement of dispersion becomes mainly inductive within the entire frequency range.

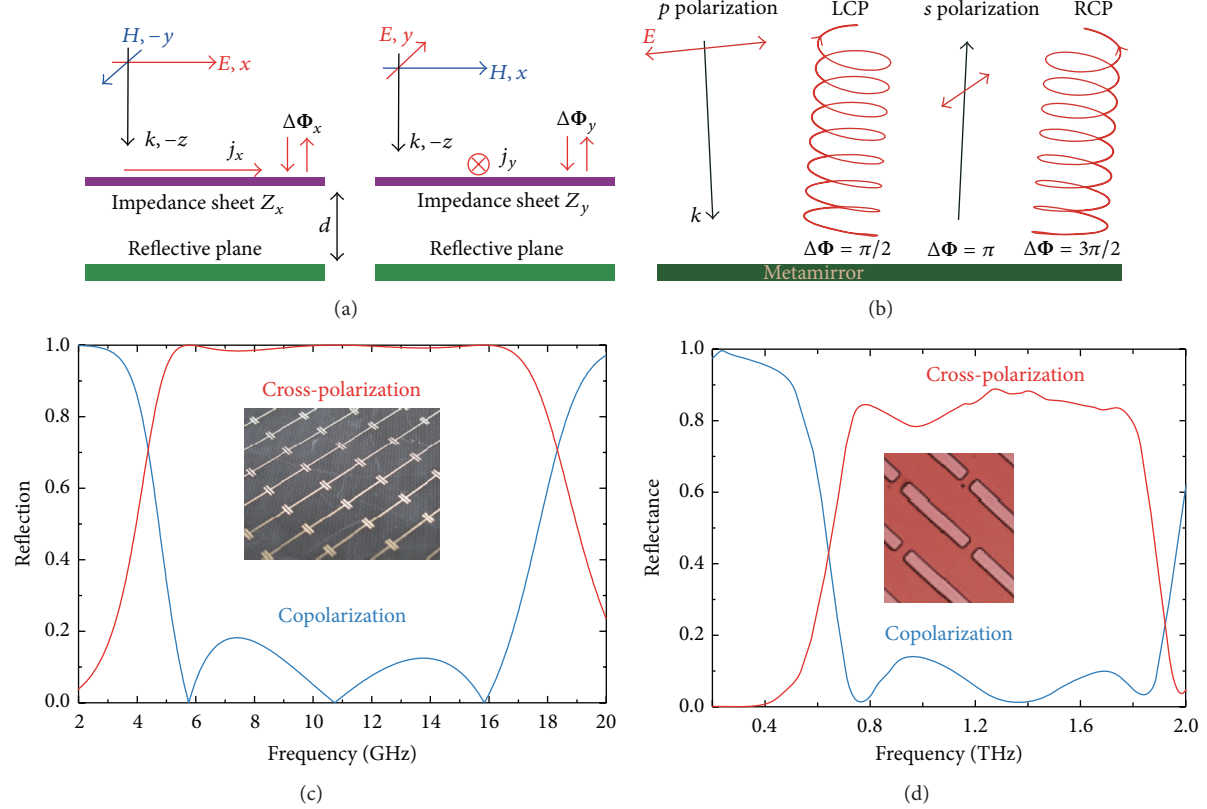


FIGURE 9: (a) Schematic of the anisotropic metamirror in  $x$ - and  $y$ -directions. (b) Schematic of polarization transformation for a  $p$  polarization incident wave. (c) Reflection coefficients for copolarized and cross-polarized components. Inset is the photograph of the fabricated sample, which is comprised of I-shaped resonators. (d) Reflectance of copolarization and cross-polarization for dipole array. Figures are reproduced from (a)-(c) [81] and (d) [77].

Using anisotropic metasurface, the optimal impedance can be approximated. Then, metamirror with I-shaped unit cell was constructed, as shown in Figure 9. The geometrical parameters were optimized using finite element method (FEM) at near normal incidence. In order to prove the above numerical results experimentally, a sample with  $40 \times 40$  unit cells was fabricated using PCB technology. The measured reflection coefficient was below  $-15$  dB in the frequency range between 5.5 and 16.5 GHz. This large relative bandwidth further confirmed the design of broadband polarization convertor. The reflective metasurface ensures the energy efficiency.

Based on the theory of broadband polarization conversion, Guo et al. [82] improved the performance of the broadband polarization convertor. In the design, it was proposed that the operation bandwidth and frequency selectivity of metasurfaces can be increased significantly with fully released dispersion management capability in two dimensions. Multiple resonance mechanism was employed to match the effective impedance of the metamirror with the ideal impedance and significantly broaden the operating bandwidth. Experimental results demonstrated that this metamirror worked well from 3.2 to 16.4 GHz with polarization conversion efficiency higher than 85%. This converter was also superior to the previous devices in the frequency band selectivity because

the operation band approximates an ideal rectangle. The rectangular coefficient, defined as the bandwidth ratio between high ( $>80\%$ ) and low ( $<20\%$ ) conversion efficiency, was high up to 0.94.

In 2013, Grady et al. experimentally demonstrated a reflective metasurface-based terahertz polarization converter that is capable of rotating a linear polarization state into its orthogonal one [77]. As depicted in Figure 9(d), the device is able to rotate the linear polarization by  $90^\circ$ , with a conversion efficiency exceeding 50% from 0.52 to 1.82 THz, with the highest efficiency of 80% at 1.04 THz. They also created multilayered structures capable of realizing near-perfect anomalous refraction.

More recently, Jiang et al. proposed an equivalent theoretical description of metasurface polarizer [78]. As examples to apply this concept, a broadband quarter-wave plate and a half-wave plate were demonstrated. Once again, this approach validated the importance of chromatic dispersion in metasurface polarization control. In a similar work, broadband metasurface polarizers were demonstrated in the visible frequencies with high-efficiency, angle-insensitive polarization transformation over an octave-spanning bandwidth [79]. Nanofabricated reflective half-wave and quarter-wave plates designed using this approach have measured polarization conversion ratios and reflection magnitudes greater than 92%

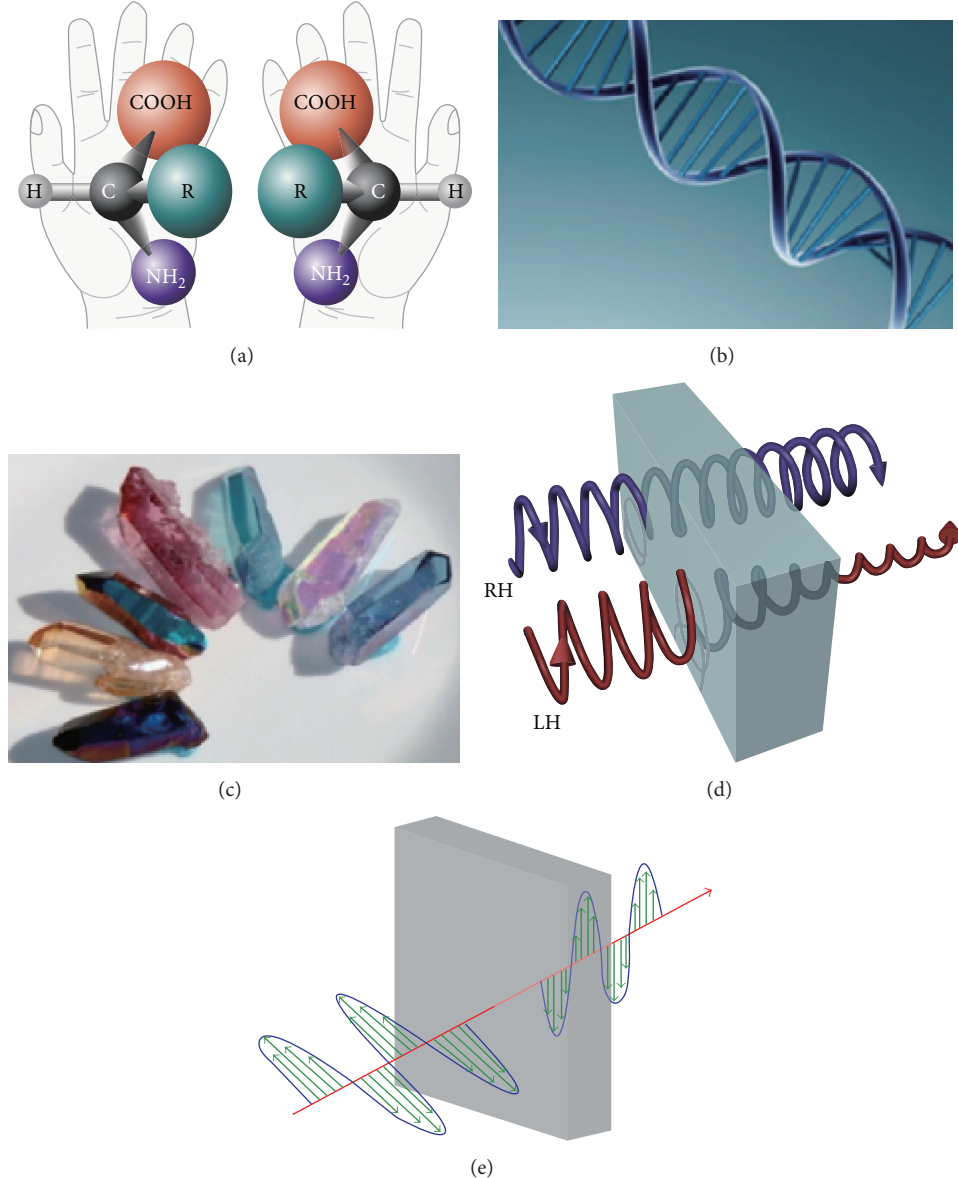


FIGURE 10: Classical naturally occurring chiral materials including (a) aminophenol, (b) DNA molecule, and (c) crystals. The chiral materials present (d) circular dichroism and (e) optical rotation character when illuminated by electromagnetic waves.

over a broad wavelength range from 640 to 1290 nm and a wide field of view up to  $\pm 40^\circ$ .

**3.2.3. Chiral Metasurface Polarizer.** Beside the anisotropic polarizers, there is another type of material suitable for polarization manipulation, which is called chiral material. Chirality refers to the materials or structures that cannot superpose with their mirror structures by only transferring or rotating the materials or structures. As depicted in Figure 10, chirality can be observed in naturally occurring media, including aminophenol, DNA molecule, and crystals.

Due to the lack of mirror symmetry, the cross-coupling between electric field and magnetic field exists in chiral materials, which is the physical original of these special electromagnetic properties. The strength of the coupling can be

represented by the chirality parameter  $\kappa$ , and thus the constitutive relation in the chiral materials can be stated as

$$\begin{pmatrix} D \\ B \end{pmatrix} = \begin{pmatrix} \epsilon_0 \epsilon & ik\sqrt{\epsilon_0 \mu_0} \\ ik\sqrt{\epsilon_0 \mu_0} & \mu_0 \mu \end{pmatrix} \begin{pmatrix} E \\ H \end{pmatrix}, \quad (32)$$

where  $\epsilon_0$  and  $\mu_0$  are the permittivity and permeability of vacuum,  $\epsilon$  and  $\mu$  are the relative permittivity and permeability, and  $\kappa$  is the strength of the coupling between the electric and magnetic fields. Negative refraction index can be obtained in chiral metamaterials while it is not necessary to realize negative permittivity and negative permeability at the same time. Chiral materials have attracted great attention for their special electromagnetic properties such as circular dichroism and optical activity. Right circularly polarized (RCP) wave

and left circularly polarized (LCP) wave would encounter different transmission coefficients at the resonances and exhibit polarization manipulation property, such as circular dichroism (CD) and optical rotation (OR). The refraction indices of the LCP wave ( $n_-$ ) and RCP wave ( $n_+$ ) are related to the chiral parameter  $\kappa$  and can be stated as  $n_{\pm} = \sqrt{\epsilon\mu} \pm \kappa$ . Therefore, negative refraction index can be obtained if the chiral parameter  $\kappa$  is large enough. As analyzed above, chiral materials can act as a kind of polarizer for their selection of circularly polarized waves. However, the cross-coupling between the electric and magnetic fields is rather weak in these natural materials, and very thick materials are often needed to produce useful CD and OR properties.

The appearance of artificial chiral structures makes it possible to realize giant CD and OR with the thickness of  $\sim\lambda/10$  at the operating frequency. Thus, due to their unique properties, chiral metamaterials promise to tailor the polarization state of electromagnetic wave and be functionalized as polarization rotators, circular polarizers, and polarization spectrum filters with ripple-free isolated transmission peaks. Furthermore, chiral metamaterials are more suitable to achieve multiband and multipolarization conversion compared to anisotropic ones.

In the extreme case, chiral material can be used to achieve circular polarization selective surface (CPSS), which was thought to be an important polarizer [83]. The ideal CPSS should have thickness much larger than the working wavelength; thus, it cannot be approximated as metasurface. In 2009, Gansel et al. [84] designed a broadband CPSS based on the periodic gold helix structure, which splits the incident circularly polarized waves in an octave bandwidth at mid-infrared frequency. Later, this helix shaped chiral metamaterial was scaled to other frequencies [85, 86].

To obtain chiral metasurfaces, the bandwidth needs to be compromised. In recent years, a great number of chiral metasurfaces have been reported in the form of twisted U-shape [87] and L-shape [88], and so forth. Ma et al. proposed chiral metasurfaces based on planar spiral structures to achieve multiband and multipolarization conversion [89].

Firstly, a multiband circular polarizer was proposed by using three layered planar spiral metasurface structure in analogy with classic spiral antenna [86]. At three distinct resonant frequencies, as shown in Figures 11(a) and 11(b), the incident linearly polarized wave with electric field parallel to one specific direction was transformed into the left-/right-handed circularly polarized waves.

Subsequently, a dual-band asymmetric chiral metasurface was constructed by using two pairs of planar spiral structures with a certain twisted angle [89], as shown in Figure 11(c). Two planar spiral structures with different radii in each layer were adopted to achieve more resonant frequencies. The incident linearly polarized wave can be converted into the circularly polarized waves with different rotation directions at four distinct resonances. This multiband chiral metasurface greatly decreased the loss of chiral metamaterials, compared to the results reported before by combining the chiral and anisotropic properties in the unit cells. This design of multiband response by putting together structures with

different size into one unit cell can also be extended to other metasurfaces and metamaterials.

In order to extend the operational bandwidth, Huang et al. [91] proposed a dual-band wideband polarization rotator which is proposed by using chiral metasurface composed of two pairs of two layered twisted split ring resonators (SRRs) in each unit. This chiral metasurface transformed the incident linearly polarized wave into its cross-polarized one at two distinct frequencies with high efficiency.

In some satellite communication systems, different circular polarization types are required, that is, LCP wave for the up-link and RCP wave for the down-link at Ku band. The usual method for the above requirement is to design two antennas with different circular polarization types as transmitter and receiver, respectively. Another solution is integrating dielectric polarizers or orthomode transducers (OMT) into the horn antennas. Though broadband polarization splitting can be realized, these methods may increase the size of the antennas.

Owing to the giant polarization conversion efficiency, the chiral metasurfaces are suitable for the construction of high performance circularly polarized antennas with multipolarization and multiband performance. As shown in Figure 12(e), a dual-band dual circularly polarized horn antenna was designed [92] based on the planar spiral chiral metasurface. The chiral metasurface converts the incident linearly polarized wave into the LCP and RCP waves at two resonance frequencies, with insertion loss less than 0.6 dB. The measured 3 dB AR bandwidths of the antenna were, respectively, 0.8% (12.4 GHz–12.5 GHz) and 1.4% (14.2 GHz–14.4 GHz). The radiation patterns of the proposed antenna for the LCP and RCP wave depicted great cross-polarization ratio, which confirmed that the dominant circular polarization was left-handed at the lower frequency and was right-handed at the higher resonance. The gain of the antenna composite was only degraded by 0.6 dB around these two resonant frequencies, in comparison with the horn antenna without the chiral metasurface. The designed antenna has the advantages of low cost and simple structure and thus could be utilized in satellite communication systems.

In order to extend the operational bandwidth, Huang et al. [91] proposed a dual-band wideband polarization rotator by using chiral metasurface composed of two pairs of two layered twisted split ring resonators (SRRs) in each unit, as shown in Figures 13(a) and 13(b). The sizes of the two pairs of SRRs are different. Therefore, this chiral metasurface transformed the incident linearly polarized wave into its cross-polarized one at two distinct frequencies with high efficiency. Pure optical activity was observed at two distinct resonant frequencies. The designed planar polarization rotator had a high transmission in the polarization rotation frequency bands and can be also easily extended for transforming polarization state at the multiple-frequency bands, which may have many potential applications in the microwave domain.

Lately, Ma et al. proposed a double-layer twisted Y-shape structure to achieve obvious circular dichroism and giant optical rotation at different frequencies [93]. The schematic geometry of the proposed metasurface is depicted in Figure 13(d). The unit cell is composed of two Y-shaped

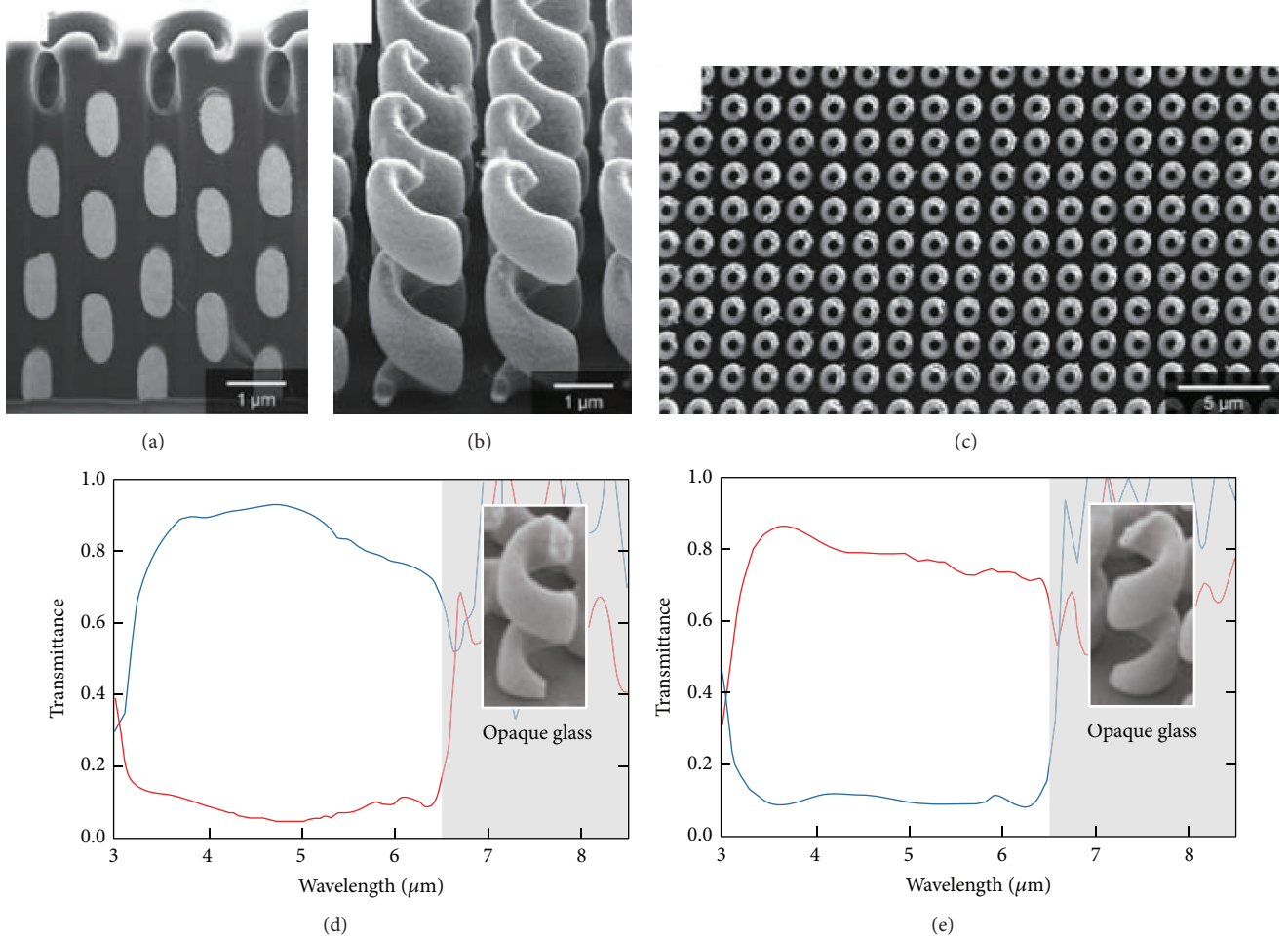


FIGURE 11: Geometry and the performance of the helix chiral metamaterial. (a) Focused-ion-beam (FIB) cut of a polymer structure partially filled with gold by electroplating. (b) Oblique view of a left-handed helix structure after removal of the polymer by plasma etching. (c) Top-view image revealing the circular cross section of the helices and the homogeneity on a larger scale. (d, e) Normal-incidence measured transmittance spectra for (d) two pitches of left-handed helices and (e) two pitches of right-handed helices. Figures are reproduced from [84].

metallic structures at a certain twisted angle printed on two sides of a dielectric lamina. The angle between the neighboring two branches of this Y-shaped structure is designed to be  $120^\circ$ . When a  $y$ -polarized wave is incident to this chiral metamaterial, circular dichroism with a great difference of 25 dB between the transmission coefficients for the circularly polarized waves is obtained at 12.28 GHz. Meanwhile,  $90^\circ$  optical rotation is observed at 12.70 GHz, where the incident  $y$ -polarized wave is transformed into its cross-polarization with a transmission coefficient of  $-1.15$  dB.

**3.3. Antireflection Metasurfaces.** In many optical devices and electrooptical equipment, the efficiency of light transmission determines to a large extent the overall performance. For example, it was reported that a normal solar panel absorbs and reflects approximately 25% and 33% of the incident solar radiation, respectively. For lens systems, the reflection would seriously reduce the imaging quality.

The first theoretical frame for analyzing antireflection coating (ARC) is Fresnel equation, which was developed in

1823 by Augustin-Jean Fresnel. Before this time, some antireflection phenomena have been already discovered by Lord Rayleigh and Joseph Von Fraunhofer [94].

In general, there are two ways to create broadband antireflection surfaces, which are based on either coating multilayer thin films or texturing the substrate surfaces with subwavelength structures. The first method is based on multilayer material with gradient refractive indices, and the latter needs only a single-layer material but gradient morphology. Due to the scarcity of optical materials with refractive indices close to air, multilayer thin films for broadband antireflection surfaces were not realizable until recently [95]. However, the mismatch in thermal properties of different materials hinders multilayer thin film applications.

One of the inspirations of ARC design comes from the natural worlds. In the eyes of some moths, broadband antireflection was observed and the physical mechanism is attributed to the effective gradient refractive index distribution. However, it was found that, in moth-eye-like structures, high-reflection frequency bands alternate with low-reflection

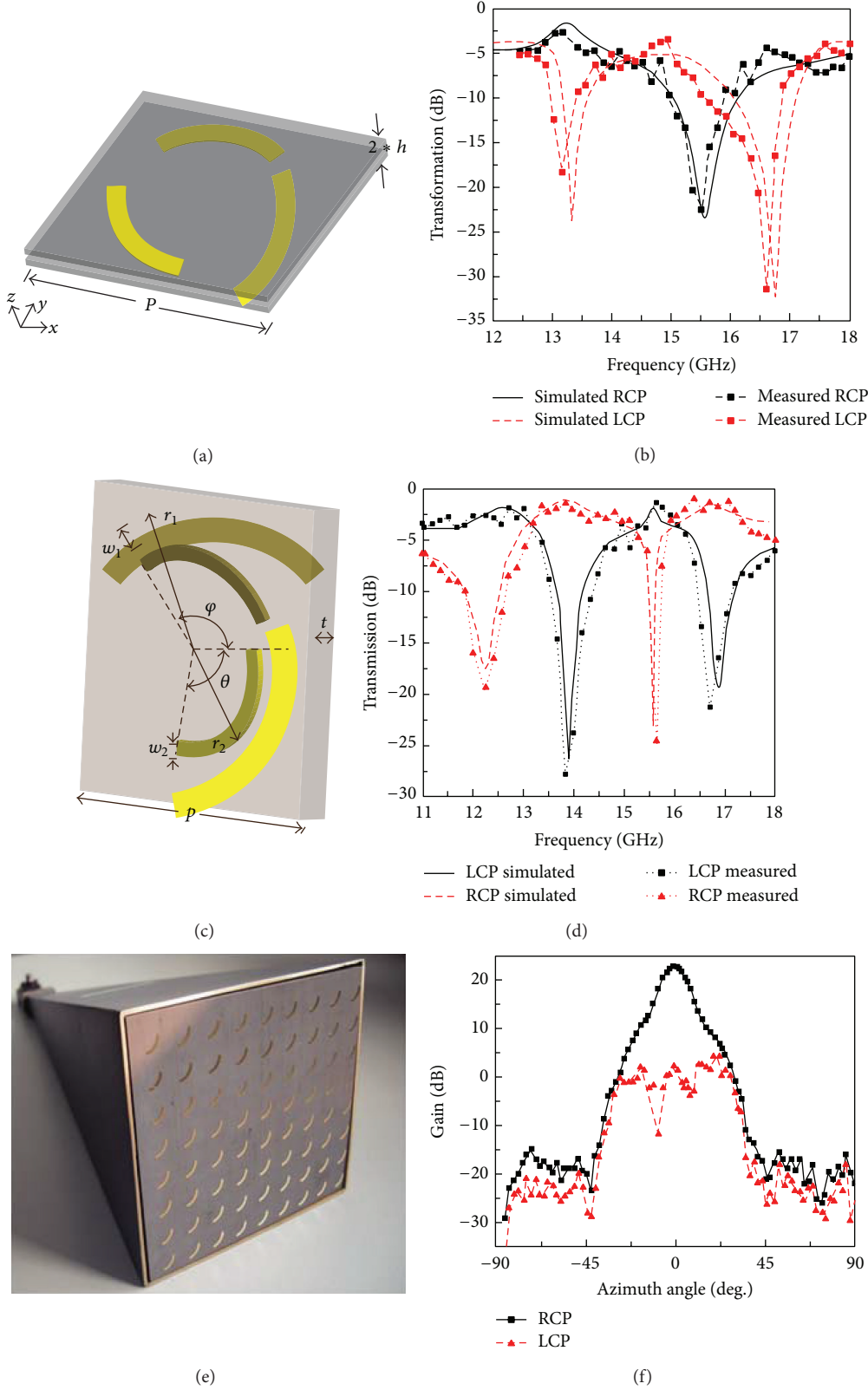


FIGURE 12: Schematic configuration of the (a) triple-band circular polarizer, (c) four-band chiral metasurface, and (e) dual-band circularly polarized horn antenna based on chiral metasurface. (b, d) Simulated and measured circular transmission for the chiral metasurface of (a) and (c). (f) Radiation patterns in LCP and RCP of the antenna at 14.35 GHz. Figures are reproduced from [86, 89, 90].

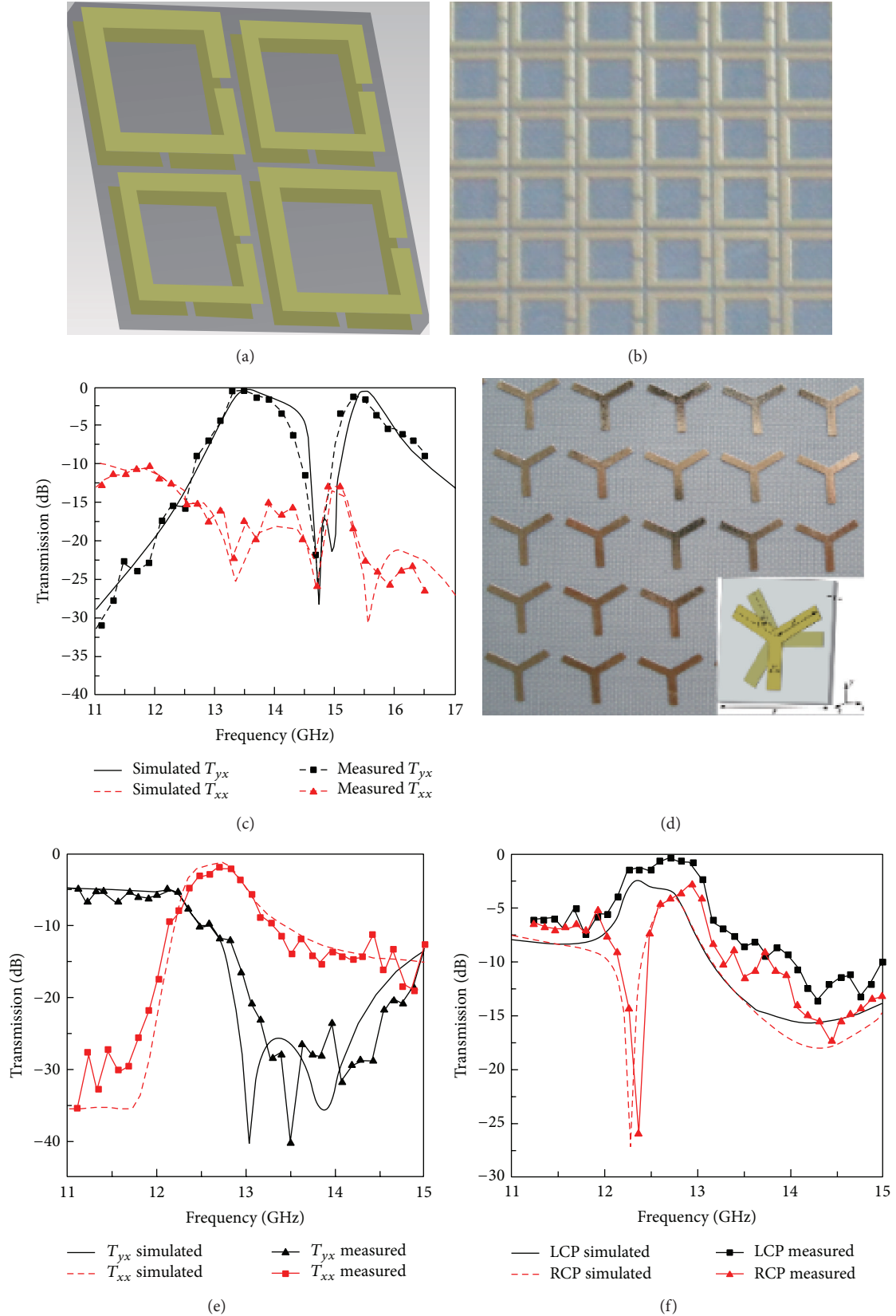


FIGURE 13: (a) Unit cell and (b) photograph of the dual-band wideband polarization rotator. (c) Transmission spectra of (b). (d) The photograph of the twisted Y-shape chiral metasurface and transmission spectra for (e) linear polarization and (f) circular polarization. Figures are reproduced from [91, 93].

frequency bands. It is of great interest for us to see if these high-reflection bands can be suppressed and hence obtain a broadband reflection approaching 0.1%. As an effort to achieve this object, it was proposed that a hybrid moth-eye structure could be used to enhance broadband antireflection properties. An ultralow average reflectance down to 0.11% over the solar spectral range has been achieved, showing a 50% enhancement in broadband antireflection capability as compared with corresponding uniform moth-eye structures.

The largest challenge faced by traditional antireflection proposals is the complex fabrication process. In 2007, biomimetic silicon nanostructures were demonstrated by Huang et al. with improved broadband and quasiomnidirectional antireflection properties [97]. In 2014, Hong et al. used laser direct writing to create microstructures on Si surfaces that reduce light reflection by light trapping [42]. By decoration of the Si nanowires with metallic nanoparticles, surface plasmon resonance can be used to further control the broadband reflections, reducing the reflection to about 0.8% across the bandwidth from 300 to 1200 nm.

Although structured surfaces with gradient dielectric constant (e.g., pyramidal rods and moth's eyes) provide rather good antireflection performance, their thicknesses and mechanical performances are not well balanced. In order to reduce both the thickness and the reflectance, the metallic metasurfaces are recently investigated for this purpose [39–41, 96, 98].

In 2008, Thoman et al. demonstrated that nanostructured gold films can serve as broadband impedance-matching coatings for substrates in the terahertz frequency range [39]. They showed in theory and experiment that the internally reflected electric field amplitude of a broadband terahertz pulse in a silicon substrate can be suppressed to below 1% of that without coating, which is at least a factor of 5 better than the best suppression achievable with bulk gold layers (see Figure 14). Subsequently, Zhou et al. examined the potential of stacked multilayer graphene as broadband terahertz (THz) antireflection coating [40]. The reflected pulses from the quartz and silicon substrates were observed to change with the layer number and doping concentration of the graphene coating. Remarkable broadband impedance matching was achieved due to optimized THz conductivity.

In a similar work, Teng et al. demonstrated broadband antireflection coatings using deep subwavelength periodic thin metallic lamellar grating [98]. As shown in Figures 14(a)–14(c), the measured reflectance from Cr grating coated sample was reduced over 99% compared with bare Si sample in the whole bandwidth of 0.06–3 THz. Recently, Zhang et al. proposed a metasurface optical antireflection coating [96]. By tuning the cross-shaped metallic patches on a dielectric spacer, the reflection coefficient can be dramatically reduced (Figures 14(d)–14(g)). The bandwidth and incidence angle range were comparable to a quarter-wave antireflection coating.

### 3.4. Perfect Absorbing Metasurfaces

**3.4.1. Single-Port Perfect Absorbing Metasurface.** Absorption phenomena of electromagnetic wave can be found anywhere

in our surrounding world. The colorful leafs and flowers are related to the frequency selective absorption of light. It was also well known that black object, such as carbon, absorbs most of the visible light. In 1860, Kirchhoff proposed the ideal blackbody absorber as “bodies can be imagined which, for infinitely small thicknesses, completely absorb all incident rays, and neither reflect nor transmit any.” Since then, the pursuit of high efficient absorbers never stops.

Along with the development of Maxwell equations and invention of radar, the electromagnetic theory of absorbers was brought out after World War II. In the review given by Hans Severin in 1956 [35], the theory of the so-called Salisbury absorber, Jaumann absorber, Dallenbach absorber, pyramidal absorber, and dipole absorber was given in detail. The dipole absorber is just the precursor of the circuit analogy absorber (CAA) [99], which is also one kind of lossy metasurface. Severin also noted that there is a conflict between the thickness and bandwidth of these absorbers. Almost half a century later, Rozanov developed a rigorous theory for the bandwidth-to-thickness ratio [100], illustrating that there is a fundamental limit for this value. Remarkably, this conclusion consists with the prediction of Planck and Masius with respect to the thickness of blackbody [101].

In recent years, broadband absorbers with optimal thickness were widely researched [38, 102–111]. Except for broadband absorbers, narrow band absorbers are also of particular importance in frequency selective applications. In 2008, Landy et al. proposed the concept of “Perfect Metamaterial Absorber” with thickness of only  $\lambda/40$ , where  $\lambda$  is the working wavelength [36]. They interpreted the principle of this absorber as the simultaneous control of electric and magnetic response such that the impedance is matched to the free space. However, it is now widely known that such impedance match does not ensure that the transmission and reflection can be simultaneously reduced to zero. As stated by Vora et al., it is ambiguous to define the  $\mu_{\text{eff}}$  and  $\epsilon_{\text{eff}}$  in such complex structures, since the metamaterial perfect absorber cannot be strictly considered as homogeneous bulk media [52].

In 2008, we extended the meta-absorber into the visible frequencies. By converting the propagating wave into surface wave, perfect absorption of light wave was demonstrated. Antisymmetric surface plasmons coupling formed by subwavelength hole array (SHA) and reflecting layer was proved to dominate the multiorders near-perfect absorption. Although only SHA was investigated in this case, the design idea, realizing perfect absorption based on structured surface combined with thick metal layers, can also be extended to other cases, such as split ring resonator (SRR) combined with metal black plate. The most fascinating potential application of SHA combined with reflecting layer is the introduction of functional material into center dielectric region to realize imaging and detecting. In 2009, we further investigated the loss mechanism of perfect absorber. It was demonstrated that the ohmic loss and the dielectric loss both contributed to the absorption. The energy exchange was recently studied to enhance the efficiency of solar cells [52]. In addition, subwavelength high performance metamaterial absorber was also demonstrated by Hao et al. for optical frequencies [112]. Experimental results show that an absorption peak of 88% is

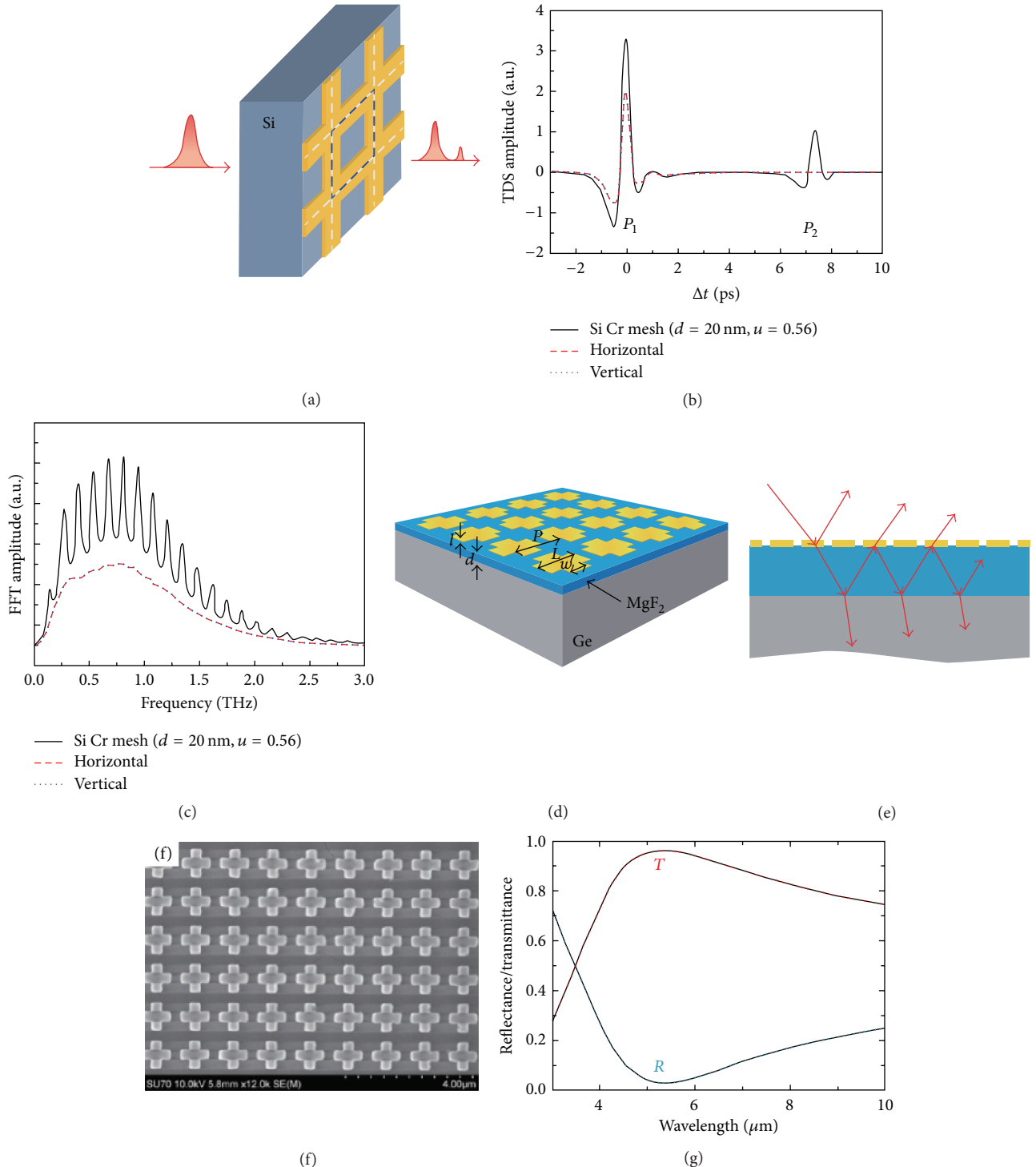


FIGURE 14: (a) A schematic of the THz measurement with THz wave normal incident from the left side of Si substrate and square mesh AR coating on the right side of Si substrate. (b) THz TDS transmission signals under normal incidence. The solid curve is for bare Si and the dashed and dotted curves are for AR-coated Si in horizontal polarization and vertical polarization, respectively. (c) FFT of the THz TDS spectra. (d) Schematic of the metasurface antireflection coating on a germanium substrate, consisting of a periodic array of gold cross-resonators on top of a dielectric layer. (e) Schematic of multireflection within the metasurface antireflection structure. (f) The SEM image of a fabricated metasurface antireflection structure. (g) Calculated optical reflectance ( $R$ ) and transmittance ( $T$ ) using full-wave numerical simulation. Figures are reproduced from (a)–(c) [41] and (d)–(g) [96].

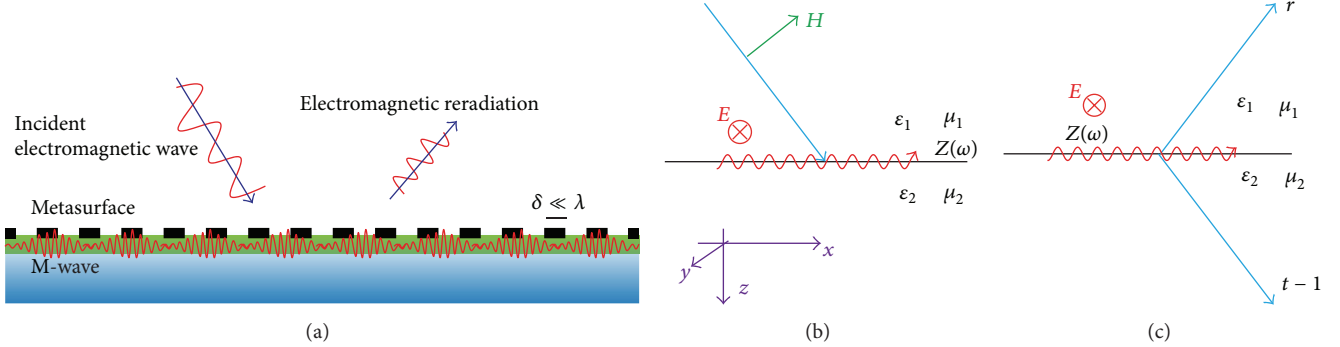


FIGURE 15: Exchange between the propagating waves and M-waves. (a) Schematic of the principle. (b) Excitation of M-wave by propagating wave. (c) Conversion of the M-wave to propagating wave. Figures are reproduced from [2].

achieved at the wavelength of  $\sim 1.58 \mu\text{m}$ . At almost the same time, Liu et al. demonstrated an infrared perfect absorber and verified its application as plasmonic sensor [113].

As shown in Figure 15, the reflection and transmission problem can be rewritten as a scattering and reradiation problem of the bounded wave [2]. The propagating wave and bounded wave (M-wave) could exchange with each other with the help of metasurface. In the far fields, we only care about propagating wave. As such, the total electromagnetic fields can be written as

$$E_{\text{total}} = E_{\text{in}} + E_{\text{sc}} = E_{\text{in}} + S \times E_{\text{in}}. \quad (33)$$

Here,  $E_{\text{sc}}$  is the scattered electric fields, which is determined by the incident electric field  $E_{\text{in}}$  and the structure function  $S$ . To realize complete absorption, the  $S$  function should be designed with no-backward scattering.

In practical applications, metallic reflecting layers are often used as a ground plane for these absorbers. As illustrated in Figure 16, we proposed a circuit model to interpret the electromagnetic interaction in these absorbers [37]. The magnetic response was mathematically treated using a modified equivalence circuit model. The relation between the reflection and impedance can be written as

$$\begin{aligned} Y_{\text{sreti}} &= \frac{1}{Z_{\text{sreti}}} \\ &= Y_0 \frac{1 - S_{11}}{1 + S_{11}} - Y_1 \frac{\exp(-ikd) - r_m \exp(ikd)}{\exp(-ikd) + r_m \exp(ikd)}, \end{aligned} \quad (34)$$

where  $Y_0$ ,  $Y_1 = \sqrt{\epsilon_1} Y_0$ , and  $Y_m = \sqrt{\epsilon_m} Y_0$  are the intrinsic admittance of vacuum, dielectric spacer, and metal and  $\epsilon_1$  and  $\epsilon_m$  are permittivities of dielectric and metal.  $k_0$  and  $k = \sqrt{\epsilon_1} k_0$  are the wave vector in the vacuum and dielectric spacer.  $r_m = (Y_1 - Y_m)/(Y_1 + Y_m)$  is the reflectivity of thick metal layer. Equation (34) is the basis of the metasurface-assisted absorption theory (MAT) [2].

Subsequently, Feng et al. showed that the bandwidth can be dramatically increased by tailoring the dispersion of metasurfaces [114]. With a thin layer of structured nichrome, a polarization-independent absorber with absorption larger than 97% was numerically demonstrated over larger than one octave bandwidth. It was shown that the bandwidth

enhancement is related to the transformation of Drude model of free electron gas in metal film to Lorentz oscillator model of bound electron in the structured metallic surface. It should be noted that the Lorentz form is just one kind of dispersion that mimics that of ideal absorbing metasurface. Thus, further engineering of the dispersion may lead to even larger bandwidth.

In addition, to meet the requirement of bandwidth enhancement, metasurface absorbers are expected to be designed to reduce the fabrication complexity of traditional absorbers. Many works have been devoted to this design. For instance, a simple method was proposed by randomly adsorbing chemically synthesized silver nanocubes onto a nanoscale thick polymer spacer layer on a gold film [115]. The film-coupled nanocubes provide a reflectance spectrum that can be tailored by varying the geometry (the size of the cubes and/or the thickness of the spacer).

In general, the maximal absorption bandwidth is limited by the optical thickness as indicated by the thickness-bandwidth ratio. For absorbers working at terahertz and higher frequencies, the physical thickness is very small even for quite large optical thickness. As a result, the thickness is not a big problem for broadband absorption at these frequencies. In contrast, the fabrication technique becomes a challenge since most of the broadband absorbers require multilayer thin films or complicated structures. Recently, we focused on the design of broadband absorber based on doped silicon, which has been considered as a new kind of metamaterials [116]. When the working frequency was larger than the plasmon frequency, doped silicon behaves as a highly lossy dielectric material. Yet a doped silicon slab by itself was not a good absorber due to the impedance mismatch between the silicon slab and free space. The power reflection at the interface was larger than 28% for refractive index  $n = 3.3$ , which was similar with nondoped silicon. In order to reduce the reflection and enhance transmission (the case for nondoped silicon) or absorption (the case for doped silicon), antireflection techniques should be used.

In the framework of transmission enhancement, the period of the grating structure should be in deep subwavelength scale to suppress non-zero-order diffractions. However, for high efficient absorber, we showed that the absorption bandwidth can be dramatically increased by utilizing

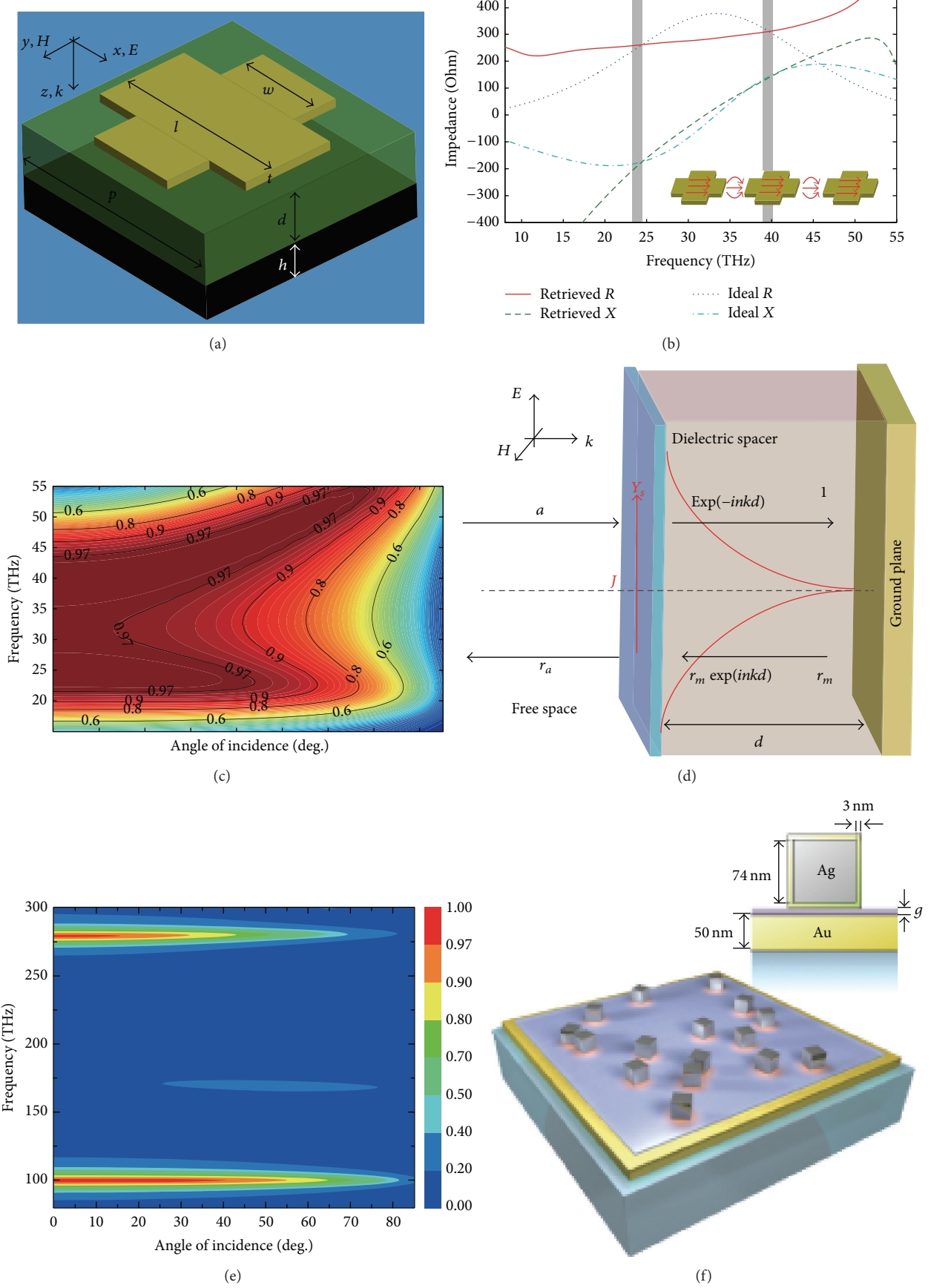


FIGURE 16: Continued.

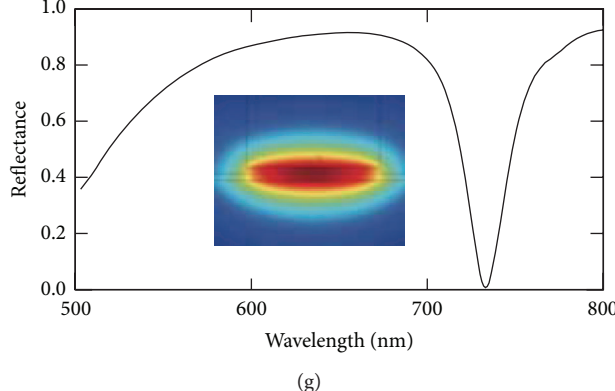


FIGURE 16: (a) Schematic of the metasurface-based absorber. (d) Physical model of the absorber, where the metasurface is described by its impedance. (b) Ideal impedance and retrieved impedance for the dispersive metasurface. (c, e) Absorption of the broadband (c) and dual narrowband (e) absorbers at different angles of incidence. (f) Schematic of the plasmonic nanocube based absorber. (g) Typical reflectance of a silver (Ag) nanocube. Figures are reproduced from (a)–(c) [114], (d, e) [37], and (f, g) [115].

both the zero- and first-order diffractions [117], as illustrated in Figure 17. Compared with previous broadband absorbers, the structure we proposed was mechanically stable and much easier to be fabricated. This idea was further extended by other researchers [104, 118]. The experimental results showed that more than 95% absorption can be obtained from 1 to 2 THz. It was also interesting to investigate whether second-order or higher-order diffraction can be utilized to increase the absorption bandwidth. In order to do this, the diffraction at higher frequencies was calculated for a two-layer grating. The relative absorption bandwidth for  $A > 90\%$  becomes larger than 150%. Further increase of layers may lead to larger bandwidth. Nevertheless, the fabrication process will become more complex and the thickness will become larger.

By stacking metasurfaces in multilayers, the absorption bandwidth could be further increased. As illustrated in Figures 18(a) and 18(b), an excellent absorber is designed with a very large bandwidth (3.26–34.65 GHz) [110]. It is shown that the total thickness of the design (14.5 mm) is only a little thicker than the minimum possible thickness dictated by the physical bound. Nevertheless, the multilayered absorber is difficult to be fabricated since the resistance of each metasurface should be accurately controlled. More recently, we fabricated a broadband absorber using magnetic controlled sputtering and optical lithography technique [2]. Since both the substrates and conducting material are transparent in the optical spectra, such absorbers could be utilized in many areas, such as smart windows and cockpits. As can be seen in Figures 18(c) and 18(d), both the optical transmittance and the microwave absorption are large enough for practical applications.

**3.4.2. Coherent Perfect Absorber.** Recently, coherent perfect absorption of light was proposed and demonstrated in a planar intrinsic silicon slab when illuminated by two beams with equal intensities and proper relative phase [119, 120]. Such a device is termed a “coherent perfect absorber” (CPA) and a “time-reversed laser.” Compared with the perfect absorbers

based on metasurfaces or plasmonic structures, the new device provides additional tunability of absorption through the interplay of absorption and interference. The coherent control of absorption is potentially useful in transducers, modulators, or optical switches [121, 122]. However, as a time-reversed process of laser, CPA is characterized by narrow bandwidth and thought to be not applicable in solar-cell and stealth technology.

As shown in Figure 19, it was demonstrated that the bandwidth of a thin film CPA can be rather large if the thickness is thin enough and the corresponding material has a specific chromatic dispersion resembling that of metal [38]. Two different regimes of metallic thin film CPA were derived based on the general CPA condition, characterized by extremely broad and moderately narrow bandwidth, respectively.

For nonmagnetic material, the CPA condition for normal incidence can be obtained:

$$\exp(inkd) = \pm \frac{n-1}{n+1}. \quad (35)$$

The  $\pm$  sign is corresponding to the symmetrical or anti-symmetrical inputs. In the previous discussion, an infinite number of discrete solutions of (35) have been found for  $kd \gg 1$ . The bandwidth is defined as the frequency width between the maximum absorption and adjacent minimum absorption and is characterized by  $\Delta f \approx c/(2nd)$ . In this case, the CPA is rather narrowband and referred to as a time-reversed process of laser.

In fact, the bandwidth of CPA can be very large if  $d$  is extremely thin ( $d \ll \lambda, |nkd| \ll 1$ ). In this case, the left side of CPA equation becomes  $1 + inkd$ , and the right side can be approximated as  $\pm(1 - 2/n)$ . As  $|nkd|$  is very small, only plus sign in the right side (symmetric mode) should be chosen and the real and imaginary parts of the refractive index ( $n'$  and  $n''$ ) become equal with

$$n' \approx n'' \approx \frac{1}{\sqrt{kd}} = \sqrt{\frac{c}{\omega d}}. \quad (36)$$

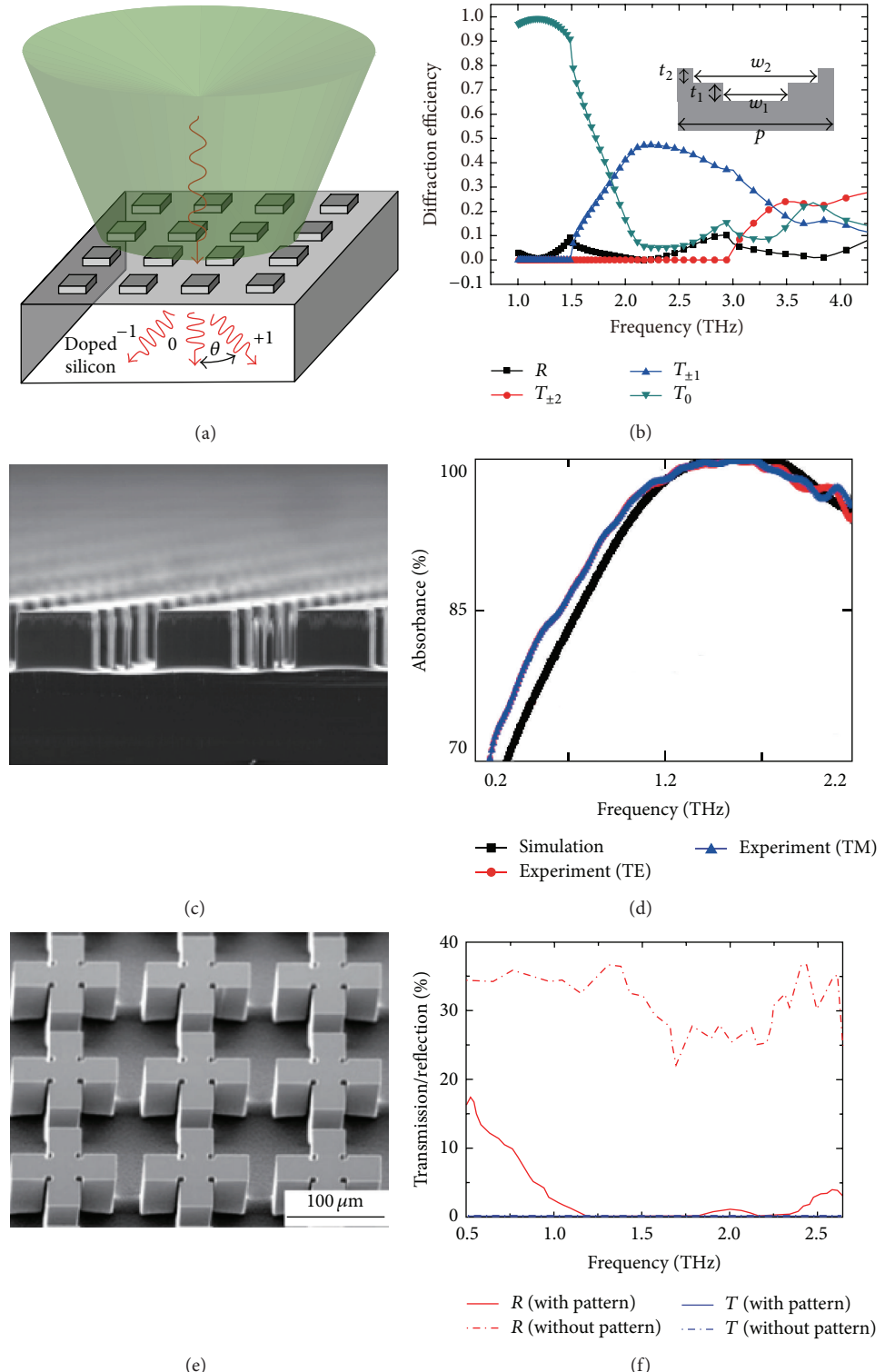


FIGURE 17: (a) Schematic of the metasurface absorber made out of silicon grating. (b) Calculated diffraction efficiency of a grating. (c) Fabricated sample. (d) Measured absorption coefficients. (e) Fabricated sample of a complex silicon grating. (f) Measured transmission and reflection coefficients with and without pattern. Figures are reproduced from (a, b) [117], (c, d) [118], and (e, f) [104].

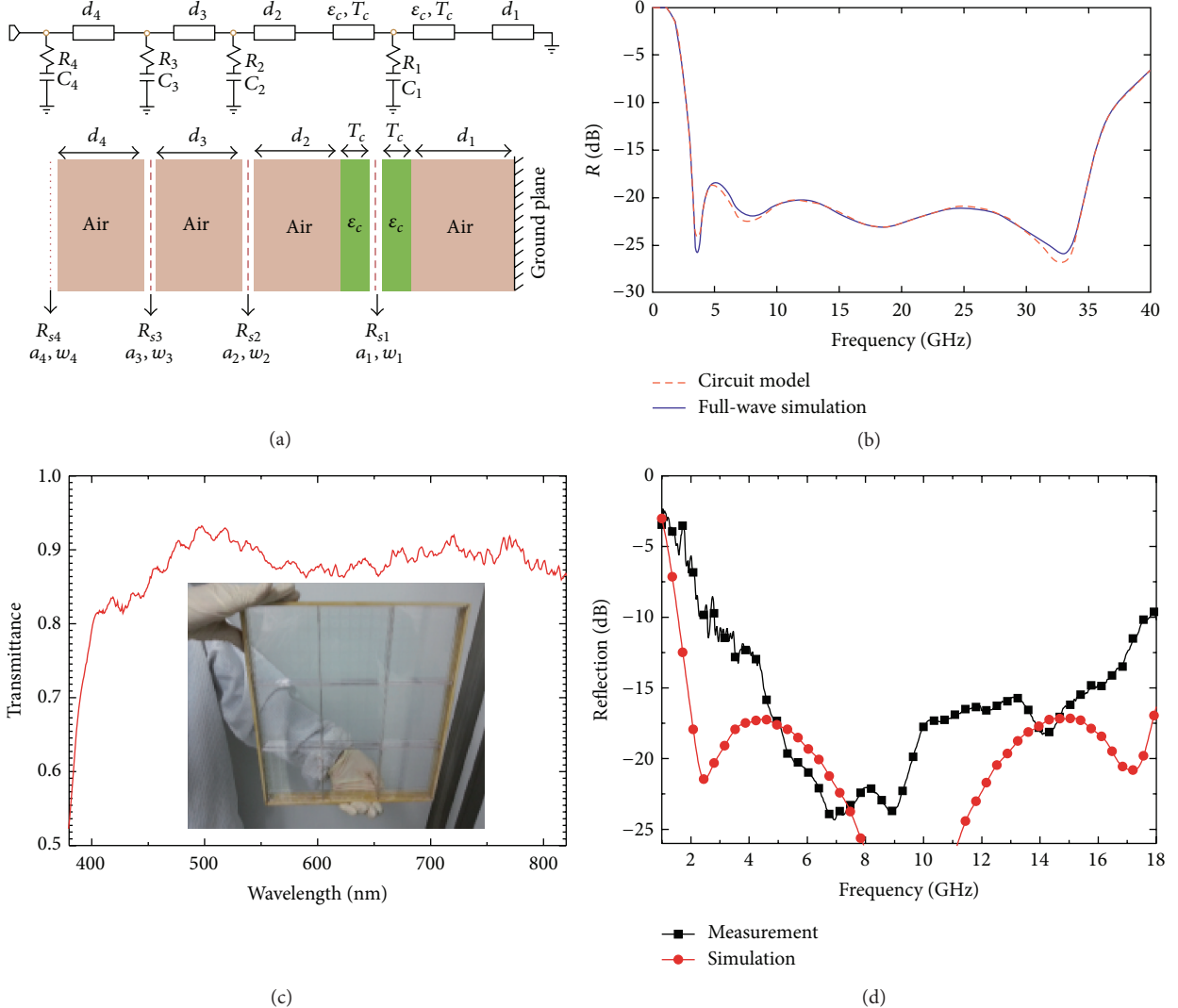


FIGURE 18: (a) The schematic of the ultrawideband absorber with optimal thickness. Top: the equivalent circuit model. Bottom: the actual realization of the absorber. The resistive layers are periodic square patches with periodicity ( $a$ ), width ( $w$ ), and sheet resistivity ( $R_s$ ). (b) The frequency response of the reflection coefficient for the ultrawideband absorber with optimal thickness obtained from both the equivalent circuit model and the full-wave simulation. (c) Optical transmittance for the optical-transparent absorber. Inset shows the photograph. (d) Microwave absorption for both the experiment and the full-wave simulation. Figures are reproduced from (a, b) [110] and (c, d) [2].

In this case,  $|nkd| \ll 1$  becomes  $\sqrt{2kd} \ll 1$ ; thus, the working regime can be approximated as  $kd \ll 1$  and the required refractive index must be much larger than unit ( $n \gg 1$ ). According to the definition of Yu and Capasso, such kind of thin film can also be thought of as a metasurface [1].

Different from the general CPA condition, the CPA condition for ultrathin film is explicit. Obviously, Drude metal could be used as natural material for CPA, with extremely broadband response. We obtained the thickness for CPA at this frequency regime:

$$d_w \approx \frac{2c}{\omega_p^2 \tau}, \quad (37)$$

where  $c$  is the speed of light in vacuum. This characteristic length is also called the Woltersdorff thickness [12], which

quantifies the thickness of a metallic film with maximum absorption for incoherent beam input in the low frequency regime. When  $d = d_w$ , the maximum absorption is 0.5, while the reflection and transmission are 0.25, respectively. For  $d < d_w$ , most of the energy is transmitted; for  $d > d_w$ , most of it is reflected.

Since the Woltersdorff thickness is independent of frequency, the absorption is very broadband. Generally, this frequency range covers all the low frequencies up to terahertz. In particular, a 0.3 nm thick tungsten film can absorb almost all the microwave and even terahertz energy under coherent condition, thus breaking the thickness limit proposed by Planck and Rozanov. Compared with the original CPA [120], the bandwidth increased more than  $10^{10}$  times. In the optical CPA, the thickness of tungsten should be increased to 17 nm,

which is still neglectable compared to the operational wavelength. The concept of ultrabroadband CPA was recently experimentally demonstrated in the microwave frequency. As shown in Figure 19(d), the absorption coefficients reach 100% at frequencies ranging from 6 to 18 GHz.

Subsequently, a customized CPA was also proposed based on the electric and magnetic resonances in a three layered metal-insulator-metal structure [123]. These kinds of resonances were attributed to the plasmon hybridization effect due to the coupling of individual resonators. Most importantly, it was found that the antisymmetrical absorption associated with magnetic resonance is almost independent of the polarization of light and angle of incidence; thus, the structure is highly suitable for coherent absorption of divergent beams (Figure 19(f)). To interpret the interaction of magnetic and electric fields with the metasurface, effect constitutive parameters are retrieved and general CPA condition for material with both electric and magnetic responses was given:

$$\exp(inkd) = \pm \frac{1-z}{1+z}, \quad (38)$$

where  $k$  is the wave vector in free space and  $d$  is the total thickness of the effective slab. The  $\pm$  signs are corresponding to the symmetrical and antisymmetrical inputs, respectively. This equation provided a general approach to the design of CPA operating at arbitrary frequencies.

The coherent control method can also be utilized to realize other functionalities. For example, Zheludev et al. proposed the application of CPA in signal processing [124]. Potential applications include but are not limited to (a) a pulse restoration (clock recovery) device to restore the form of distorted signal pulses according to that of a clock (control) pulse, (b) a coherence filter that improves the coherence of light beams by absorbing incoherent components, and (c) a coherent light-by-light modulator wherein a digital or analogue intensity- or phase-modulated control input governs signal channel output. In addition, they showed that reflection and refraction effects on phase gradient metasurfaces can be coherently controlled by a second wave [125]. In addition, Cao et al. also demonstrated the possibility of coherent subwavelength focus. Broadband operation was made possible by engineering the dispersion of the complex dielectric function, similar to the previous methods [38]. The local enhancement can be significantly improved compared to the standard plane wave illumination of a metallic nanoparticle. Their numerical simulation showed that an optical pulse as short as 6 fs can be focused to an 11 nm region.

More recently, coherent perfect rotation (CPR) of electromagnetic polarization states has been proposed by utilizing the odd time reversal symmetry in Faraday rotation [126]. Similar to coherent perfect absorption, the bandwidth of CPR is limited. The main advantage over other polarization transformers is that the polarization states can be dynamically tuned by the phase retardation. Nevertheless, it is pointed out that only Faraday rotation, but not optical activity or anisotropy, is capable of coherent perfect rotation. In our

recent work, a dynamic polarization transformer was constructed by taking advantage of the time reversal symmetry of polarization conversion in anisotropic metasurface [76]. It should be noted that no Faraday rotation effect is utilized. The working bandwidth covers the entire microwave and terahertz bands. More interestingly, it is demonstrated that the output polarization states can be easily tuned between linear polarization and arbitrary circular polarization through phase modulation.

### 3.5. Plasmonic Metasurfaces

**3.5.1. Superlens and Hyperlens.** As discussed in Section 2, some particular metasurfaces can support surface waves, such as SPPs. The last several decades have witnessed the rapid development of SPPs and related areas. One of the largest advantages of SPPs is their ability to construct superlens and hyperlens to break the diffraction limit, which prevents the imaging of subwavelength features [34]. As we demonstrated recently, the electromagnetic waves on metasurfaces are characterized by three distinct properties [2]. The most important one is the short wavelength [55], which is actually the basis to break the diffraction limit.

In 2000, Pendry firstly proposed the concept of perfect lens [4], in which the amplification of evanescent waves and perfect imaging could be obtained by a negative refraction index slab. The short wavelength characteristic of SPPs on a silver film was firstly demonstrated in 2003 [127, 128], and surface plasmon resonant interference nanolithography technique (SPRINT) was proposed to achieve resolution of half-pitch 50 nm ( $\sim 1/9$  wavelength) in 2004 [31], as shown in Figures 20(a) and 20(b). Using exposure recording scheme, Fang et al. experimentally demonstrated in 2005 that a 35 nm thick silver superlens was capable of subdiffraction imaging of half-pitch 60 nm objects ( $\sim 1/6$  wavelength) [30]. Figure 20(c) illustrates the experimental scheme of subwavelength imaging through a silver lens, where the objects were located 40 nm away from the silver superlens. Due to the superlens effect, the object of “NANO” characters was imaged on the photoresist and the average line width of images is 89 nm (Figure 20(d)). By utilizing a similar scheme, the superlens effect was also confirmed by other groups [129, 130].

The metasurface-assisted diffraction theory (MDT) can be utilized in plasmonic lithography [2], where the silver lens has practical limits, such as optical loss, surface roughness, and film thickness. To address these issues, some important studies were reported, including active lens and plasmonic reflective slab [32, 131]. Based on the reflective amplification of evanescent wave, Wang et al. experimentally achieved the deep subwavelength imaging lithography for nanocharacters with about 50 nm line width [32], as depicted in Figures 20(e) and 20(f). It was also reported that the plasmonic cavity lens can be utilized to achieve high aspect profile [132]. The profile depth of half-pitch 32 nm resist patterns was enhanced to be about 23 nm, which is much larger than the previously reported results (sub-10 nm). The resolution of SPPs imaging lithography was also extended to be half-pitch of 22 nm, whereas the quality needs to be further increased.

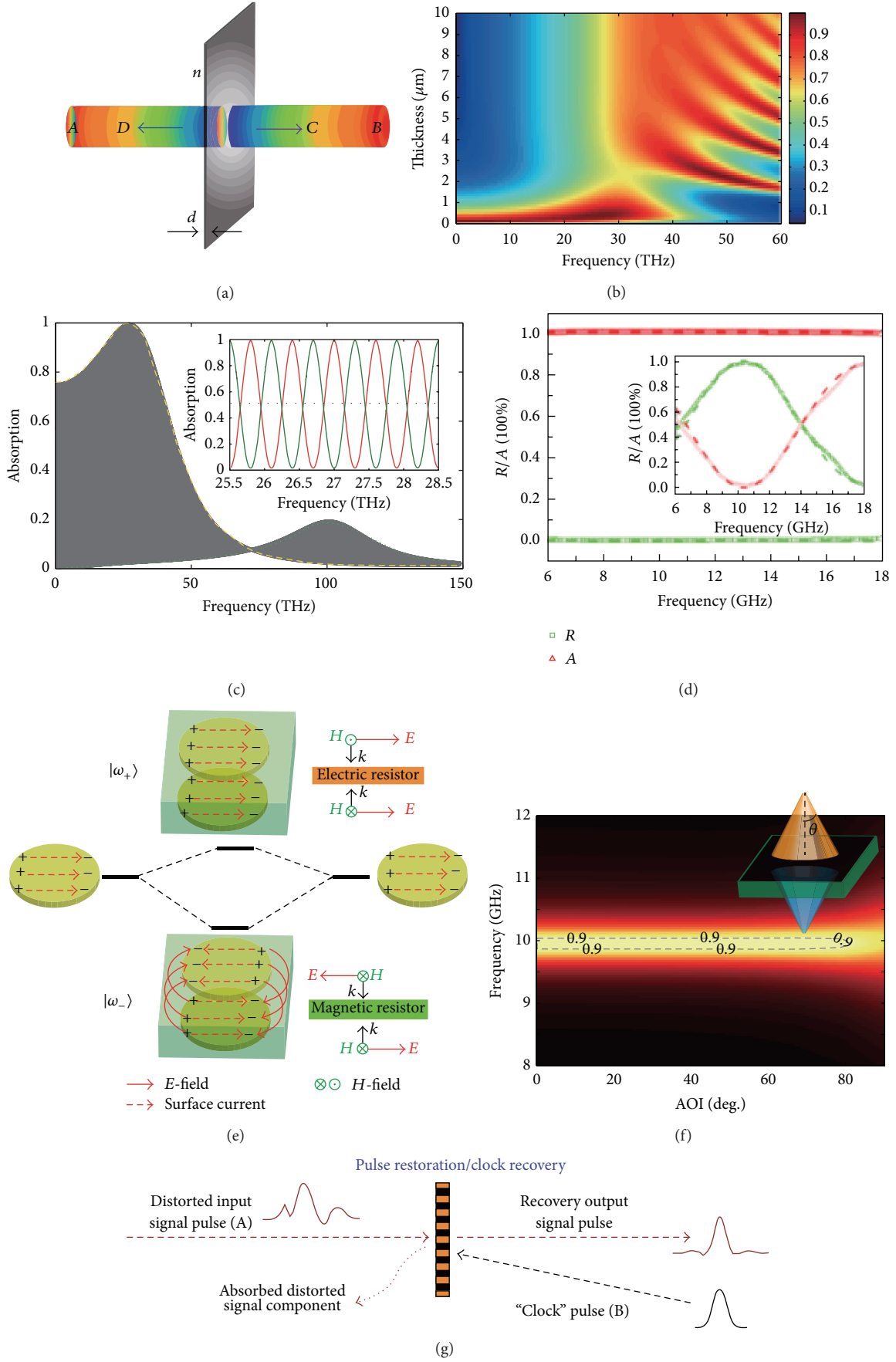


FIGURE 19: Continued.

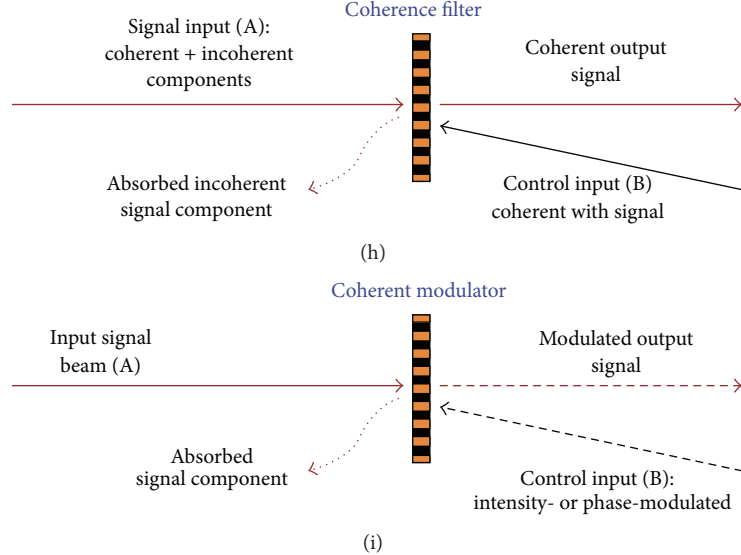


FIGURE 19: (a) Schematic of the coherent perfect absorber. (b) Absorption as a function of the frequency and the thickness of the doped silicon film. (c) Coherent absorption of a 450 nm thick doped silicon film. Red and green solid lines show the absorption for  $\Delta l$  equal to 500 and 505.56  $\mu\text{m}$ , respectively. (d) Coherent absorption of 17 nm thick tungsten for symmetrical and antisymmetrical inputs. (e) Schematic of plasmon hybridization and the effective medium description. For the symmetrical (antisymmetrical) resonance, the external  $E$ -fields ( $H$ -fields) should be parallel. (f) Coherent absorption of antisymmetrical inputs for TE polarization at oblique incidences. The inset of (f) illustrates the configuration of two coherent divergent beams with antisymmetrical phase distribution, where  $\theta$  is the divergent angle. Figures are reproduced from [38, 123]. (g)–(i) Proposed applications of metasurface CPA in signal processing. Figures are reproduced from [124].

The subdiffraction imaging model of a planar plasmonic lens can be written in the form of

$$\begin{aligned} \begin{bmatrix} E_x(x, y, z) \\ E_y(x, y, z) \\ E_z(x, y, z) \end{bmatrix} &= \int_{-\infty}^{\infty} \int_{-\infty}^{\infty} \begin{bmatrix} A_x(k_x, k_y) \\ A_y(k_x, k_y) \\ \frac{k_x A_x + k_y A_y}{-k_z} \end{bmatrix} \\ &\cdot \exp(i k_x x + i k_y y) dk_x dk_y, \\ \begin{bmatrix} A_x(k_x, k_y) \\ A_y(k_x, k_y) \end{bmatrix} & \\ &= \int_{-\infty}^{\infty} \int_{-\infty}^{\infty} \begin{bmatrix} G_x(x, y) t_x(x, y) T_x(k_x, k_y) \\ G_y(x, y) t_y(x, y) T_y(k_x, k_y) \end{bmatrix} \\ &\cdot \exp(-i k_x x - i k_y y) dx dy, \end{aligned} \quad (39)$$

where  $G(x, y)$ ,  $t(x, y)$ , and  $T(k_x, k_y)$  are the illumination function, transmission function of object, and optical transfer function (OTF) of plasmonic lens, respectively. The OTF can be obtained through transfer matrix. If there is reflection plane in the plasmonic lens, the OTF should be determined by using the fields in the photoresist layer, implying that the images can also be modulated by the reflecting layer [32].

Although the superlens provided images of nanoobjects well beyond the diffraction limit, the inherent disadvantage of near-sighted mode impedes its widespread application. It is highly desirable to utilize a plasmonic lens system which

could resolve subwavelength details of objects in far field. In 2006, Jacob et al. proposed a hyperlens composed of cylindrical metal-dielectric multilayers to magnify subwavelength details of objects so that the subwavelength features are above the diffraction limit at the hyperlens output [133]. Then, conventional microscopy can be utilized to capture the output of hyperlens to achieve far-field super resolution imaging.

**3.5.2. Plasmonic Metasurface Lens.** Based on Snell's law, traditional optical lenses must have curved surfaces to focus light. In other words, the phase retardation was accumulated by height variation much larger than the wavelength. In recent years, metasurfaces were widely utilized to achieve planar lenses, based on the metasurface-assisted law of reflection and refraction (MLRR) [2, 134]:

$$\begin{aligned} n_1 k_0 \sin \theta_1 + \nabla \Phi &= n_1 k_0 \sin \theta_3, \\ n_1 k_0 \sin \theta_1 + \nabla \Phi &= n_2 k_0 \sin \theta_2, \end{aligned} \quad (40)$$

where  $\nabla \Phi$  is the phase gradient in the metasurface plane, which is determined by the geometric structure and distribution, and may be changed by external stimuli, leading to the adaptive tuning of the law of refraction and reflection.  $n_1$  and  $n_2$  are the refractive index of media at the incident and transmit sides.  $\theta_1$ ,  $\theta_2$ , and  $\theta_3$  are the angles for incident, refracted, and reflected light.

In particular, plasmonic lenses have become one widely researched approach, which has now been demonstrated in both one-dimensional and two-dimensional cases [46, 135, 136]. These devices offered an alternative to conventional refraction microlenses. The planar and compact designs are

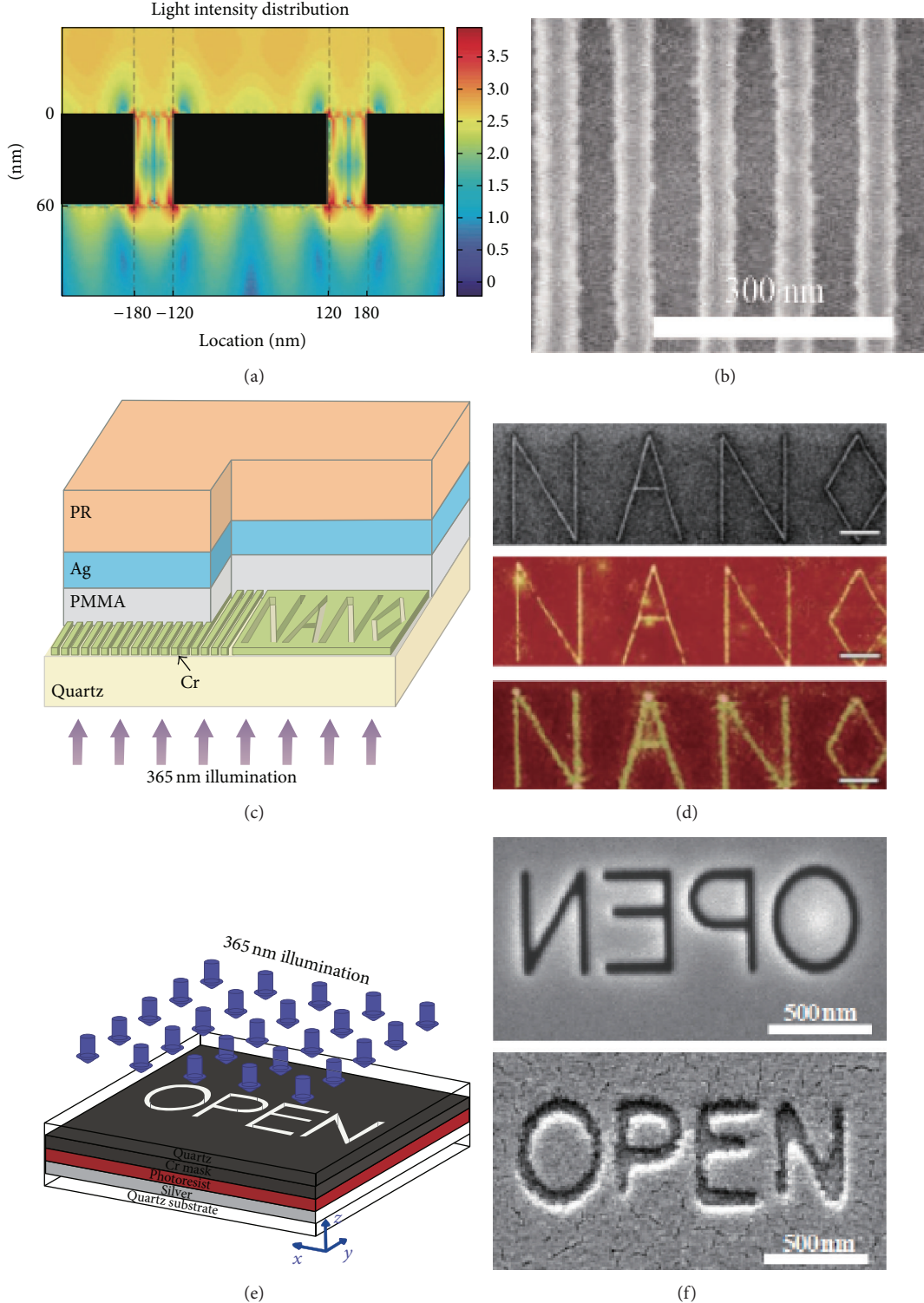


FIGURE 20: Experimental demonstration of near-sighted silver lens. (a) Numerical simulation of intensity distribution of surface plasmons. (b) SEM image of resist pattern for (a). (c) Schematic diagram of the silver superlens experiment. (d) (Top) Focused-ion-beam image of the object with 40 nm line width, (middle) AFM images of topographic characterization in resist layer with a silver superlens, and (bottom) AFM images of topographic characterization in resist layer with the 35 nm thick superlens replaced by PMMA spacer as a control experiment. (e) Schematic of imaging lithography structure with a reflective Ag lens. (f) (Top) SEM image of the mask pattern "OPEN" characters, (bottom) SEM image of resist pattern. SEM image of half-pitch 32 nm dense lines resist pattern with plasmonic cavity lens. AFM image of half-pitch 22 nm resist pattern. Inset shows its two-dimensional (2D) Fourier analysis diagram. Figures are reproduced from (a, b) [31], (c, d) [30], and (e, f) [32].

beneficial for obtaining short focal distances on the order of several micrometers.

Early in the 21st century, a novel method was proposed to manipulate the phase retardation of light at nanoscale, providing a new approach to develop various nano-optical devices, such as flat lenses, collimators, and splitters. Figure 21(a) illustrates the principle of planar lens based on width-tuned plasmonic slits. The slits transport electromagnetic energy in the form of SPPs in nanometric waveguides and provide desired phase retardations with variant phase propagation constant. Under plane wave illumination, the light energy was focused at the focal plane  $f = 0.8 \mu\text{m}$ , as shown in Figure 21(b). According to Fermat's Principle, such devices could also achieve arbitrary angle of light deflecting such as that shown in Figure 21(c).

Although the plasmonic lens is easy to be fabricated, it was only until 2008 that the experimental demonstration of such device was reported [46]. For plane wave illumination, the light was focused at the focal length of  $5.3 \mu\text{m}$ . The excellent agreement between experiment and simulation validated the design principle of this approach. It should be noted that the plasmonic version of abnormal refraction is similar to that in other metasurfaces, as shown in Figures 21(e) and 21(f).

More recently, as shown in Figure 22, Chen et al. demonstrated that the far-field focusing pattern of planar metal lens could be modulated by slits filled with phase change material ( $\text{Ge}_2\text{Sb}_2\text{Te}_5$ , GST) [135]. By varying the crystallization level of GST from 0% to 90%, the Fabry-Pérot resonance supported inside each slit can be spectrally shifted across the working wavelength at  $1.55 \mu\text{m}$ , which results in a transmitted electromagnetic phase modulation as large as  $0.56\pi$ . Based on this geometrically fixed platform, different phase fronts can be constructed spatially on the lens plane by assigning the designed GST crystallization levels to the corresponding slits, achieving various far-field focusing patterns.

In 2007, Min et al. investigated a type of metallic nano-optic lens consisting of slits with variant widths, filled with Kerr nonlinear media [139]. As shown in Figure 23(a), each slit is designed to transmit light with specific phase retardation controlled by the intensity of incident light, owing to the nonlinear response. This new lens can actively control the deflection angle and the focus length of output beam. Very recently, Hu et al. proposed an active terahertz (THz) plasmonic lens tuned by an external magnetic field [140]. Different from traditional tunable devices, the proposed active lens is tuned by changing the cyclotron frequency through manipulating magnetoplasmons (MPs). It was shown that THz wave propagating through the designed structure could be focused to a small size spot via the control of MPs. The tuning range of the focal length under the applied magnetic field (up to  $1\text{ T}$ ) is  $\sim 31$ , about 50% of the original focal length.

It should be noted that the plasmonic slit lens is polarization selective; that is, only one particularly polarized light beam could be transmitted and modulated in phase, since the SPP is intrinsically polarized. This polarization selectivity has two effects. Firstly, this effect is attractive for some cases where only one polarization type is needed. Secondly, it may become undesired for many other applications. To eliminate

this problem, rectangular or circular plasmonic holes were adopted to achieve phase modulation [136, 141]. As illustrated in Figure 24, Ishii et al. experimentally demonstrated a polarization-independent holey-metal lens [136]. They showed that by changing the radii of subwavelength holes in a metallic film, which act as single-mode waveguide elements, they can control the phase of light transmitted through the holes. Finally, it was demonstrated that the focal distance of the lens can be controlled by changing the incident wavelength.

More recently, Litchinitser et al. demonstrated that the change of hole radius along the azimuthal direction is able to generate orbital angular momentum (OAM) on the nanoscale. They proposed and experimentally demonstrated that a nanowaveguide array milled in a metal film can be used to control the wavefront of a light beam and that an optical vortex at  $532 \text{ nm}$  was produced by using such an array (see Figures 24(b) and 24(c)).

### 3.5.3. Plasmonic Metasurfaces for Sensing Applications.

Owing to the strong light-matter interaction, metasurfaces can provide a robust and efficient platform for biosensing. In particular, the surface plasmon resonance (SPR) at planar surfaces or localized surface plasmon resonance (LSPR) for nanometer-sized metallic structures is accompanied with dramatic local field enhancement [142]. The implication of the local field enhancement is twofold. Firstly, the spectra of the SPR and LSPR are highly dependent on the environment; thus, a little change of refractive index would result in a considerable spectrum shift. Secondly, the local field enhancement can be exploited to achieve surface-enhanced Raman spectroscopy (SERS) [143]. Both of the two mechanisms can be utilized for clinic detection.

As shown in Figures 25(a)–25(d), Wu et al. introduced an infrared plasmonic surface based on a Fano-resonant metasurface which exhibits sharp resonances caused by the interference between subradiant and superradiant plasmonic resonances [144]. Owing to the asymmetry, the frequency of the subradiant resonance can be precisely determined and matched to the molecule's vibrational fingerprints. In these Fano resonances, the near-field coupling of plasmonic modes is crucial to enhance the sensitivity [145, 146]. It was also demonstrated that Young's interference can be observed in plasmonic structures when two or three nanoparticles with separation on the order of the wavelength are illuminated simultaneously by a plane wave. This effect leads to the formation of intermediate-field hybridized modes with a character distinct of those mediated by near-field and/or far-field radiative effects [147].

In a similar work [148], by exploiting extraordinary light transmission phenomena through high quality factor subradiant dark modes, Yanik et al. experimentally demonstrated high figures of merits (FOMs as high as 162) for intrinsic detection limits surpassing those of the gold standard prism coupled surface plasmon sensors, as illustrated in Figures 25(e) and 25(f).

Over the past several years, the absorption effect of plasmonic metasurface has also been exploited in sensing

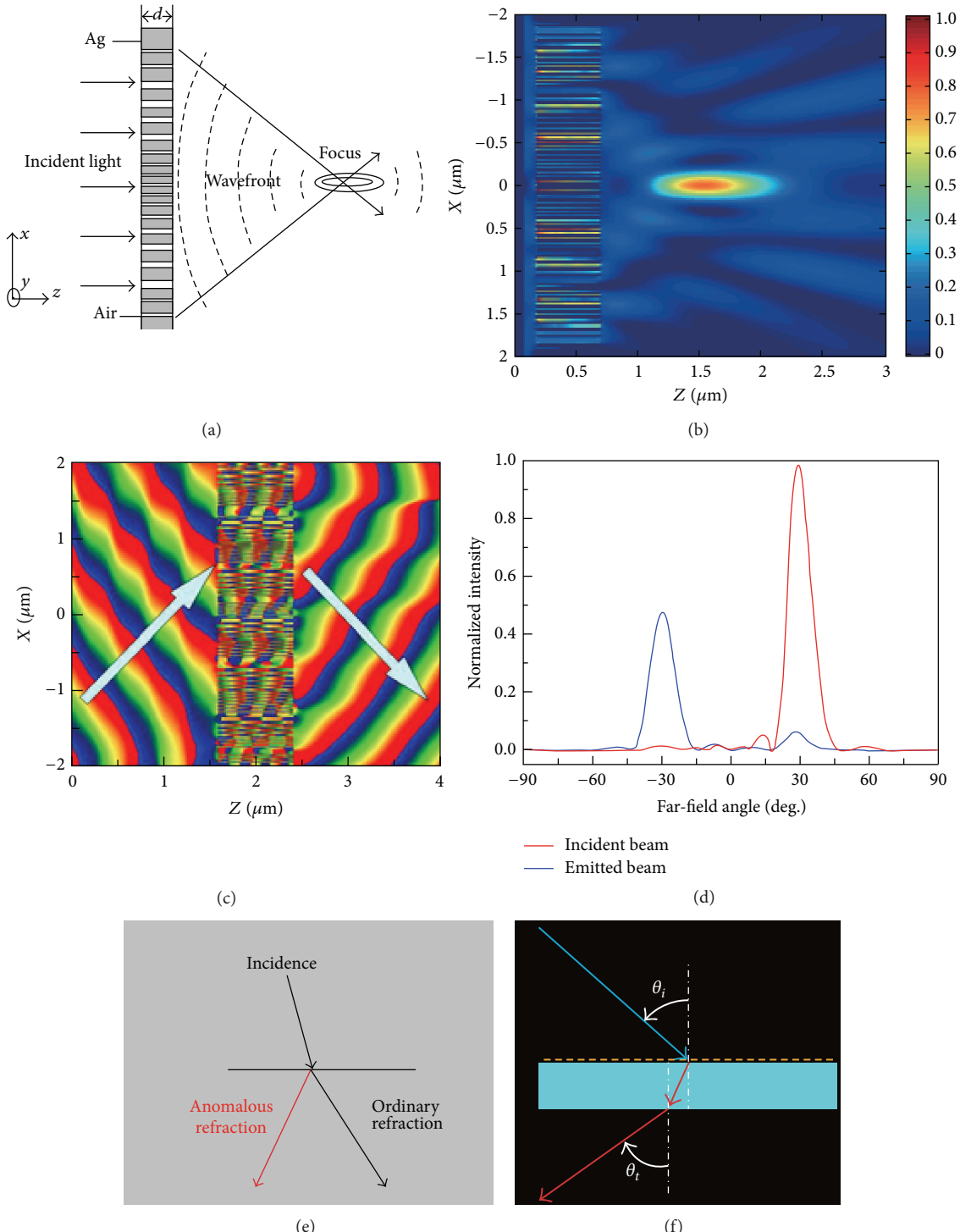


FIGURE 21: Planar slit array metal lens. (a) Schematic configuration of light focusing of planar metal nanoslit array lens. (b) Normalized Poynting Vector for light focusing of metallic nanoslits lens. (c) Calculated phase distribution of electric field for the designed deflector. Incident and deflection angles are designed as  $30^\circ$  and  $-30^\circ$ , respectively. (d) Far-field angular spectrum for the incident and emitted beams, respectively. (e, f) Schematic of the abnormal refraction in other metasurfaces. Figures are reproduced from (a)–(d) [137], (e) [134], and (f) [138].

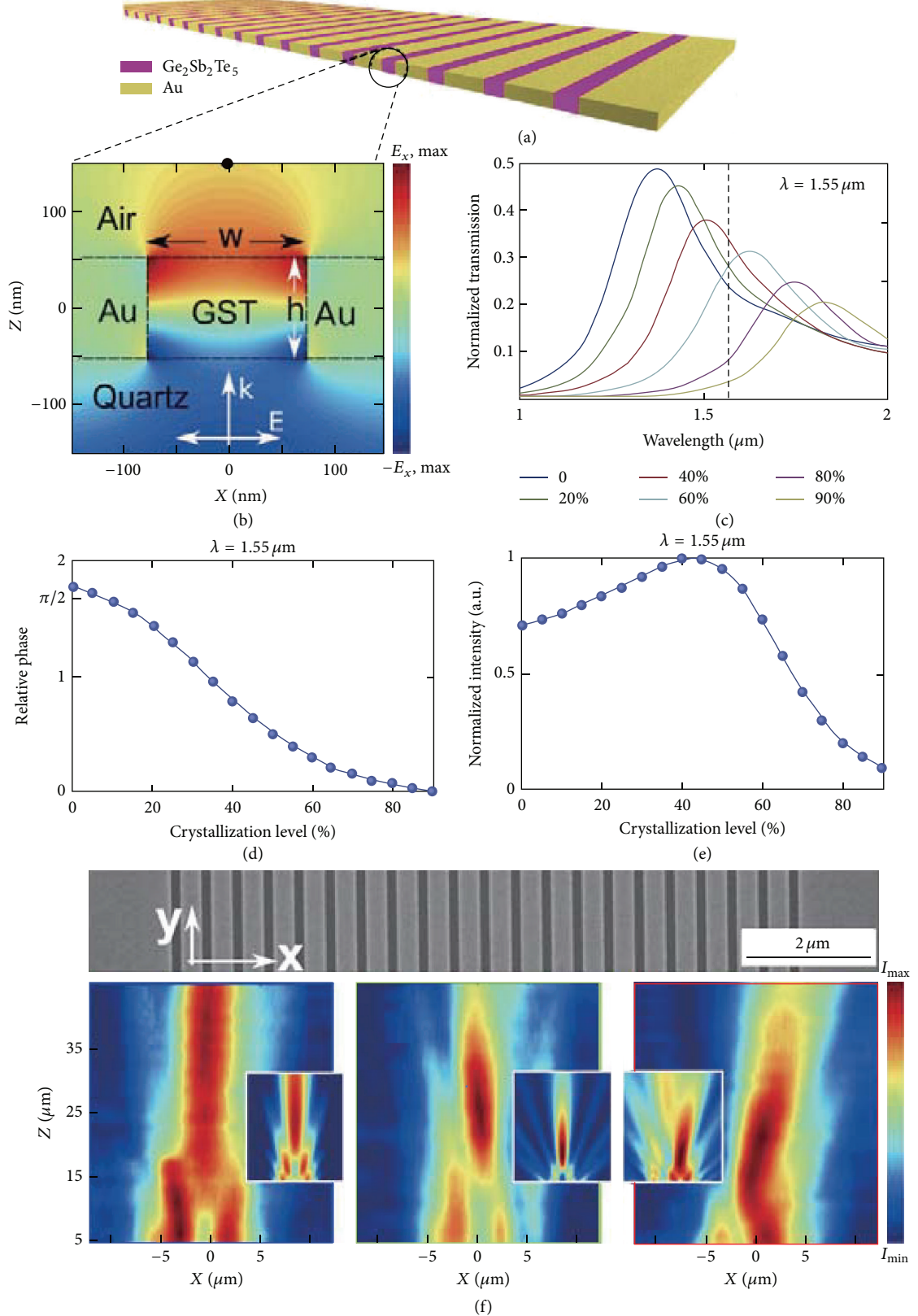


FIGURE 22: (a) Schematic diagram of the planar lens. (b) The cross section showing the  $x$ -component of the electric field of the 1st-order mode from a single slit. (c) The evolution of the single-slit transmission spectrum for different crystallization levels. (d) The relative phase and (e) the normalized electric field intensity at  $1.55 \mu\text{m}$  as functions of the crystallization level with a 5% step increment. (f) Focusing pattern measured in  $xz$ -plane by confocal scanning optical microscopy for different status of GST. Figures are reproduced from [135].

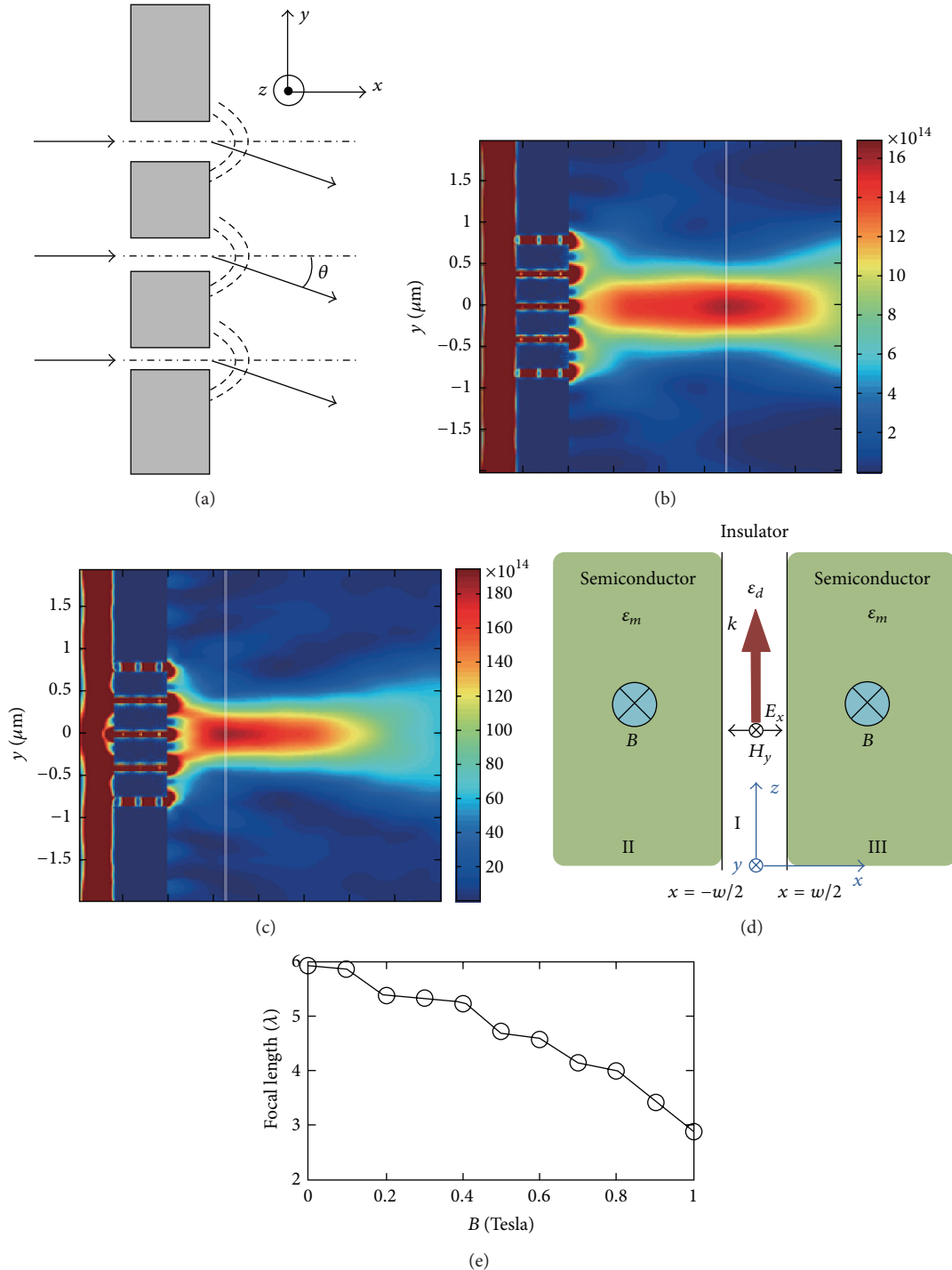


FIGURE 23: (a) Schematic view of the three-slit structure under study. (b) and (c) The FDTD simulation of electric field intensity  $|E|^2$  time-average distribution of beam focusing with a five-slit metallic lens. (d) A semiconductor-insulator-semiconductor structure in a Voigt configuration. The propagation mode is TM polarized, and the magnetic field  $B$  is applied along the  $y$ -axis. The thickness of the insulator is denoted by  $w$ . (e) FDTD-calculated focal length when the external magnetic field is increased from 0 to 1 T. Figures are reproduced from (a)-(c) [139] and (d, e) [140].

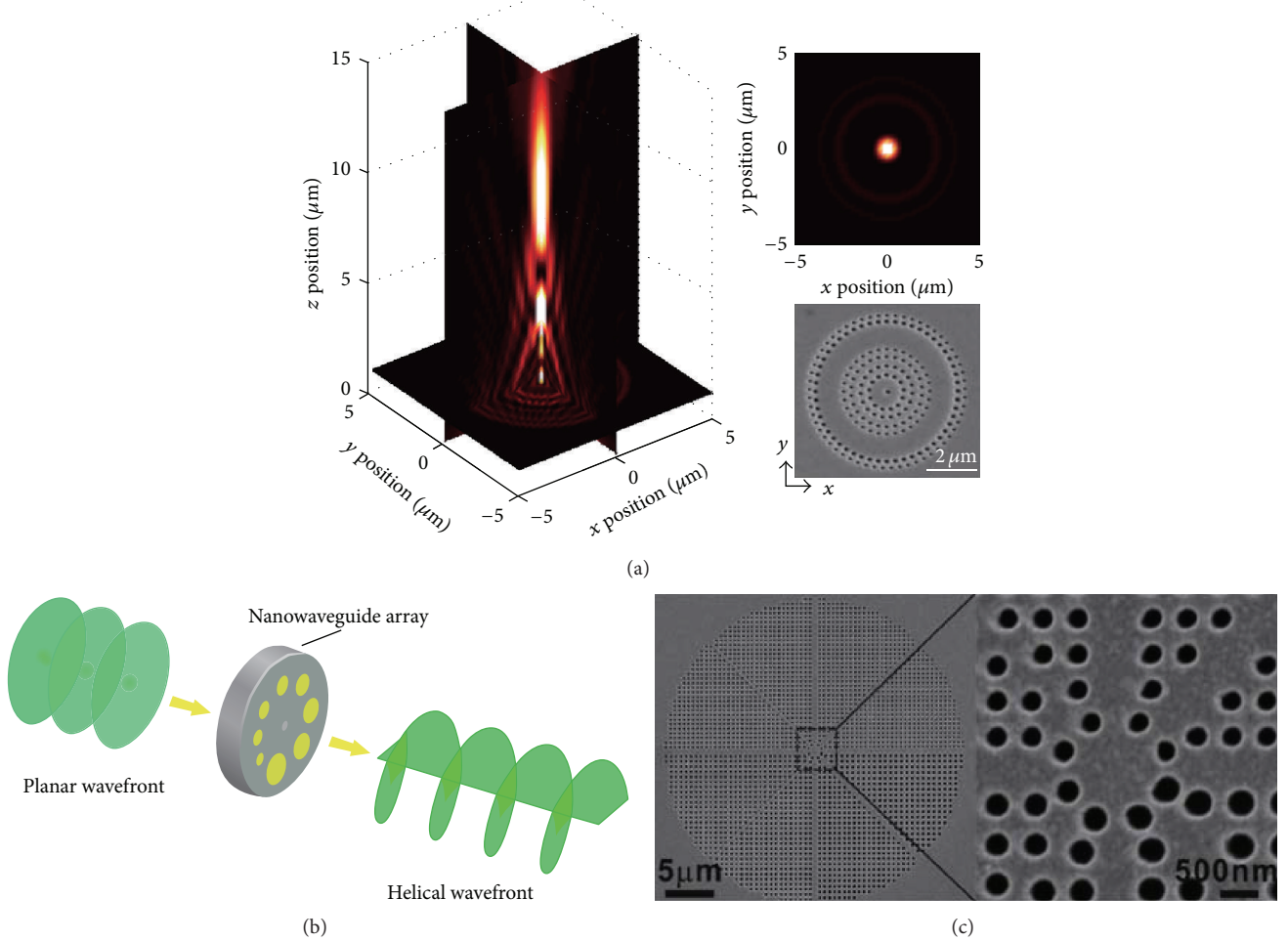


FIGURE 24: (a) Pseudocolor intensity map calculated from the analytical model of the sample. The color scale is normalized to the maximum intensity. The inset shows the beam cross section at the focal point ( $z = 10 \mu\text{m}$ ) and the SEM image of the sample. (b) Schematic of a nanowaveguide array that induces wavefront shaping for OAM generation. (c) SEM picture of the nanowaveguide array. Figures are reproduced from [136, 141].

applications. In 2011, Tittl et al. presented a simple design of plasmonic absorber based on palladium nanowires [149]. Due to hydrogen incorporation, palladium undergoes a phase transition from a metal to a metal hydride which leads to an expansion of the palladium lattice. The fabricated structure showed a reflectance of 0.5% which in combination with a complete suppression of transmission yields an absorbance of  $A \approx 99.5\%$ . As shown in Figures 26(a)–26(d), they utilized the absorber structure for hydrogen sensing and were able to reliably detect concentration down to 0.5%  $\text{H}_2$  in air with response time in the range of seconds.

More recently, it was demonstrated that graphene monolayers transferred on arrays of split ring resonators (SRRs) could exhibit resonances in the visible range. As illustrated in Figures 26(e) and 26(f), Raman enhancement factors per area of graphene up to 75 were measured, demonstrating the strong plasmonic coupling between graphene and the metasurface resonances.

Recently, an important sensing technique via multifrequency antennas was also demonstrated [151–155]. Such

antennas can efficiently detect different vibrational modes of molecular species in a window of several micrometers, where informative fingerprint spectra of many molecules are present.

Since there have already been many reviews on this topic [34, 142, 143, 156], we only give a small part of examples here. To completely understand the role of metasurface in sensing applications, we would like to suggest that the readers find more information in these literatures.

**3.6. Surface Plasmon-Inspired Metasurfaces.** In previous discussion, metasurfaces refer to arrays of subwavelength structures on thin films. More generally speaking, any kinds of subwavelength structures on such films can be regarded as metasurfaces, with novel applications in optics and electromagnetics. Early in 1998 [157], it was found that extraordinary light transmission can be observed when it passes through the subwavelength metal pinhole arrays (Figure 27). Also, adding a surface groove structure around the subwavelength aperture can break the traditional diffraction limit and achieve

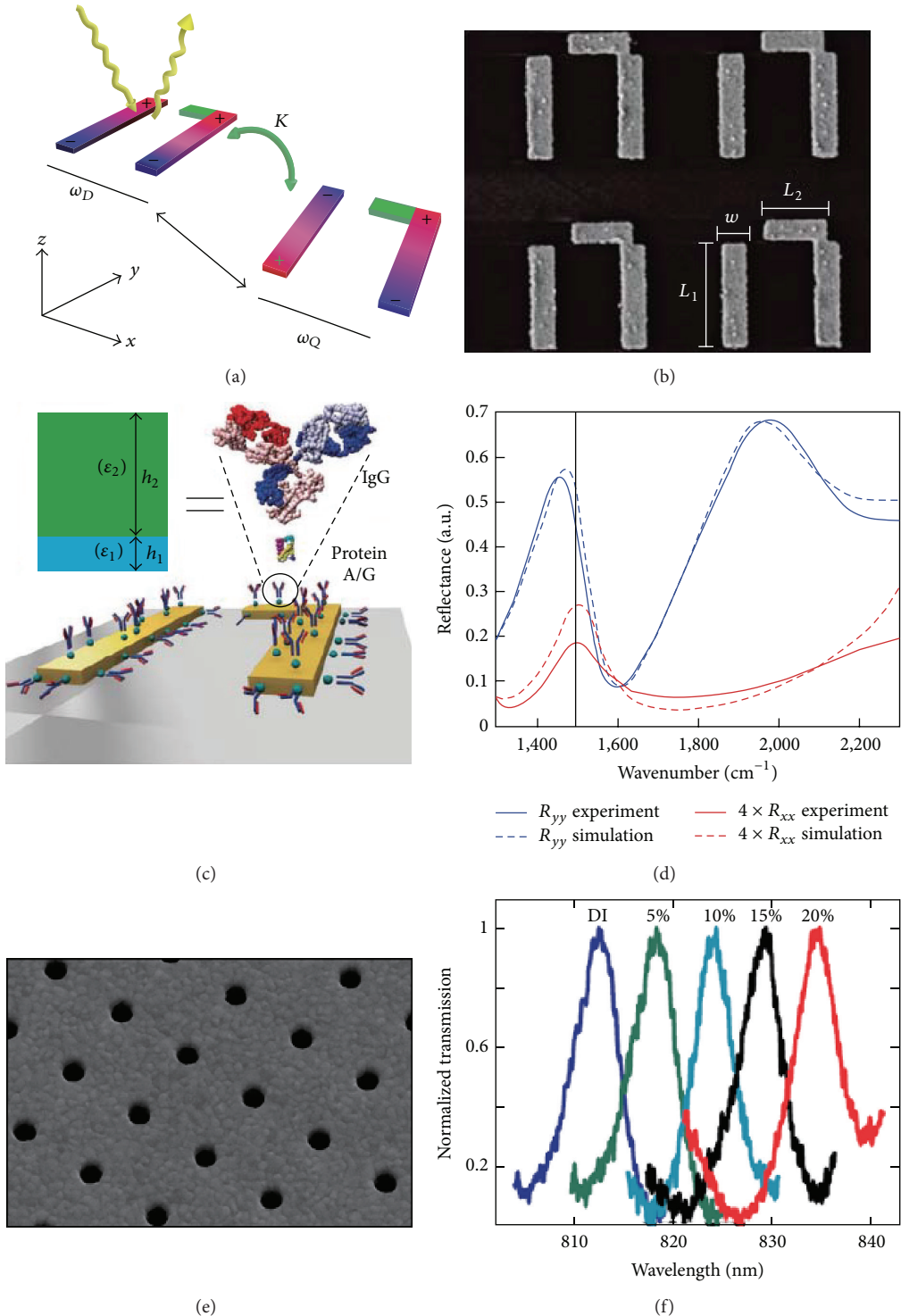


FIGURE 25: (a) Schematic representation of subradiant (Q) and superradiant (D) modes. (b) Scanning electron microscopy image of a typical fabricated sample. (c) Schematic representations of proteins' mono- and bilayers binding to the metal surface. (d) Experimental (solid) and theoretical (dashed) polarized reflectivity spectra. (e) SEM image of a fabricated metasurface consisting of hole array. (f) Resonance shift for the subradiant SPP mode with changing NaCl concentration. Figures are reproduced from (a)–(d) [144] and (e, f) [148].

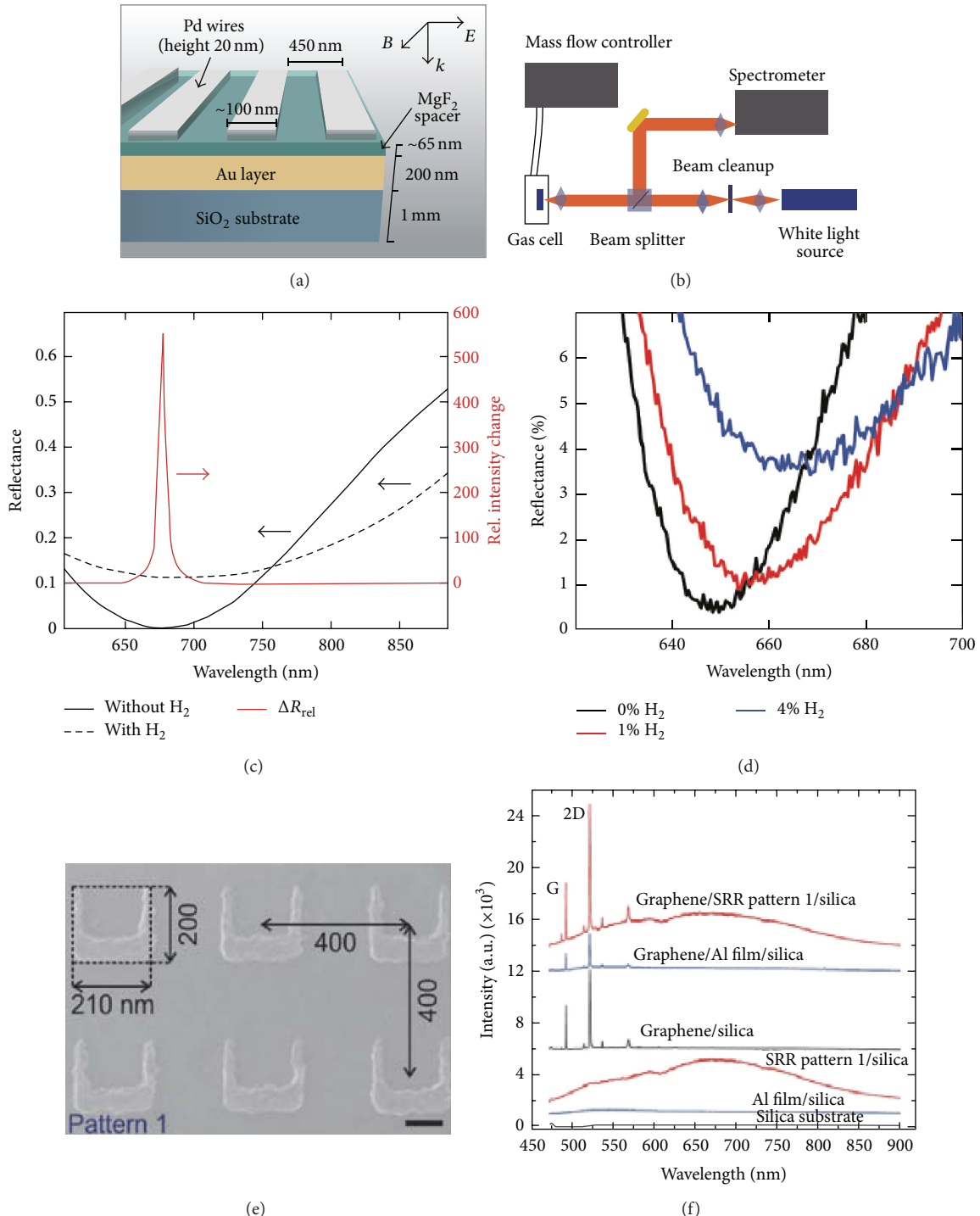


FIGURE 26: (a) A side view of the sensor. Palladium nanowires are stacked above a gold mirror. The layers are separated by a MgF<sub>2</sub> film. (b) A sketch of the experimental setup including the mass flow controllers used to set the desired hydrogen concentrations. (c) Simulated response of the sensor structure to hydrogen exposure. (d) Reflectance of the absorber for different hydrogen concentrations. (e) SEM images of split ring resonators (SRRs) on a graphene layer. (f) Experimental results of the Raman spectra for different conditions. Figures are reproduced from (a)–(d) [149] and (e, f) [150].

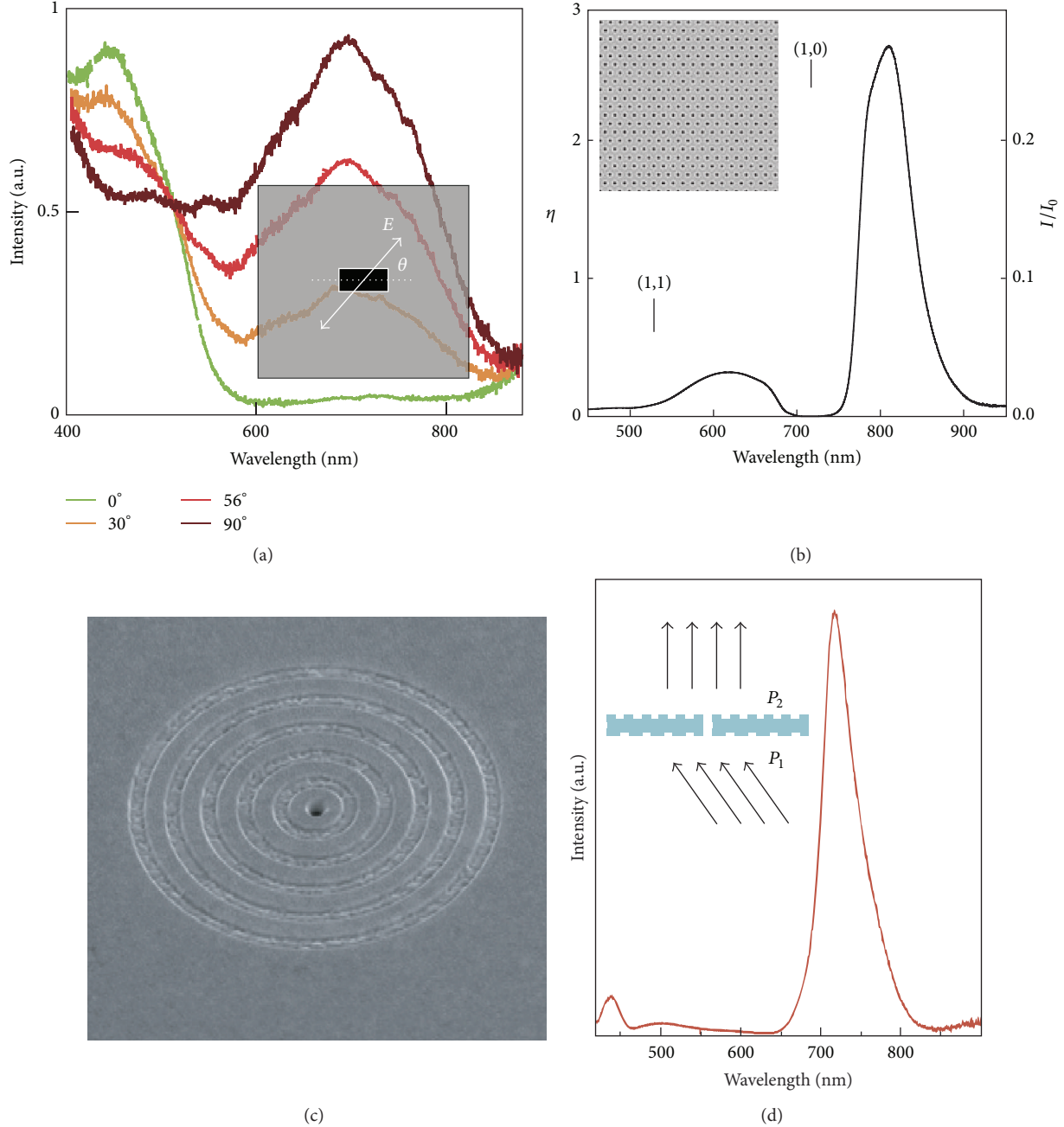


FIGURE 27: (a) Optical transmission properties of single rectangular hole in metal films. Inset shows the SEM image. (b) Transmission spectrum of hole arrays. The triangular hole array was milled in a 225 nm thick Au film on a glass substrate with an index matching liquid on the air side (hole diameter 170 nm and period 520 nm). (c) SEM image of the bull's eye structure. (d) Optical properties of the bull's eye. Figures are reproduced from [65].

highly directional energy transfer with ultrahigh transmission [158].

Subsequently, Poujet et al. firstly demonstrated an experimental extraordinary optical transmission up to 90% in the subwavelength annular apertures [159]. In spite of the metal loss, the transmission of incident light has been greatly enlarged by employing the guided mode propagating through

the annular aperture array. The subwavelength hole arrays can also act as color filters as the wavelength selectivity is directly related to the period of the holes [65]. An array of dimples is prepared by focused-ion-beam milling an Ag film. Some of the dimples were milled through to the other side so that light can be transmitted. When this structure is illuminated with white light, the transmitted colour is determined by the

period of the array. In this case, the periods were chosen to be 550 and 450 nm, respectively, to achieve the red and green colours.

Afterwards, several research groups including Martin-Moreno et al. [160] analyzed the underlying physics principle of generation of beaming effect in groove surface and pointed out that transmission enhancement of the groove is attributed to three factors as follows: surface plasmon resonance modes in the grooves, phase match of groove secondary radiation, and waveguide modes in the slot. Considering the SPs in metallic structure at the visible range, Luo and Yan established a physics model, namely, quasiperfect conductor model (QPCM), to optimize the directed radiation characteristics of SPPs [34]. In addition to beaming effect, the multi-directional radiation and abnormal homogeneous radiation phenomenon of subwavelength groove structure were also systematically discussed based on the diffraction theory.

More recently, the extraordinary transmission and beaming effect based on cycle groove structures were also expanded to other frequency bands. Pendry et al. demonstrated that even a perfect electric conductor can support surface plasmon [56]. In order to distinguish it from traditional SPs, this surface plasmon supported by groove structures in low frequency is named spoof surface plasmon (SSP). Lockyear et al. [161] demonstrated that microwave energy could be coupled into SSPs through the reflective spectrum experiment of grating structure. Lately, Akarca-Biyikli et al. [162] experimentally validated the abnormal transmission and beaming effect in the 1D groove structure. With the beaming effect and extraordinary transmission, groove structures have wide potential applications in various frequency regions, as shown in the following discussion.

**3.6.1. Surface Plasmon-Inspired Metasurfaces for Microwave Antennas.** The directional energy transfer realized in groove structure meets the requirements of high-directivity antennas and a variety of antennas have been proposed in the microwave band. For example, Huang et al. [163] used periodic groove structure in linearly polarized waveguide end slot array antenna. As shown in Figures 28(a) and 28(b), the beam angles in *E*-plane and *H*-plane were compressed to be 6 and 13 degrees, respectively. The groove shaped metasurfaces also have great contribution in reducing the level of sidelobes of slot antennas. Huang et al. proposed a method of integrating groove structures with two different periods into slot antenna to obtain low sidelobe radiation (Figures 28(c) and 28(d)). The sidelobe of the antenna with grooves was greatly decreased compared to the slot array without groove structures. Furthermore, after adding the artificial electromagnetic soft-surface structure to one-dimensional subwavelength outer groove, the antenna backward radiation was significantly reduced by 10 dB. However, the antenna gain was only increased by 0.2 dB due to long distance between the edge groove and the central feed.

For the characteristics of low cost, light weight, and low profile, microstrip patch antenna has gotten a great prospect on the area of military and civilian applications. However, due to the deterioration of surface wave, the antenna's radiation efficiency is very low, and this restricts its development.

Ying and Kildal [164] improved the radiation performance of the antenna through an artificial electromagnetic soft-surface groove onto a ground.

The groove structures can also be loaded between slot elements to achieve low coupling between the slots and thus obtain high aperture efficiency of the slot antenna arrays. The cross-coupling between the two slots was sharply decreased by 30 dB after loading the groove structure, as shown in Figures 28(e) and 28(f). Furthermore, after introducing groove structure, the gain of slot antenna array was enhanced by 4 dB, and the sidelobe level on *E*-plane is low and main lobe on *H*-plane is compressed.

The period of a traditional beaming effect based groove structure is approximate to the wavelength, and the beaming effect usually requires several periods to implement. Thus, they make the size of the whole antenna very large and bring about the low utilization of aperture. Therefore, with no sacrifice of the antenna performance, how to reduce the groove cycle has formed a research direction.

Huang et al. have still taken account for the loading of high dielectric constant medium between the grooves to reduce the groove cycle equivalently. Both single slot antenna and two-dimensional slot antenna array loaded dielectric medium with high permittivity were analyzed. The operating frequency of this antenna is 14.5 GHz, and the rectangular waveguide end slots were used as the exciting source. The dielectric constant loaded between the two neighboring grooves was 11.9, and the thickness of the loaded media silicon was 1.1 mm. The introduction of the traditional cycle-groove structure has no effect on antenna's resonant frequency, while the medium-loading groove structure makes the center resonant point of the antenna shift to the low frequency, and it has a certain impact on antenna input matching. However, the slot antenna can be kept at  $S_{11} < -10$  dB by tuning the slot length in the working frequency, meeting the needs of practical engineering. The gain of a traditional cycle-groove slot antenna is 15.11 dB, increasing by about 9 dB compared to the flat-panel slot antenna. However, the antenna gain has further improved by 3 dB after the medium-loading groove structure is used, reaching 18.29 dB. It is notable that the physical diameter of the designed antenna is smaller than the size of a traditional cycle-groove slot antenna, only three-quarters of it, but the gain has improved more significantly instead. From the radiation patterns, we can also find that the *E*-plane of a traditional cycle-groove antenna shows an obvious beaming effect.

This medium-loading method can also increase the performance of two-dimensional slot antenna array. This idea broke through the limit that the traditional array element interval is less than wavelength to widen applications of the periodic groove structure. Afterwards, media with high dielectric constant were loaded between the grooves to reduce the groove cycle equivalently without sacrificing of the antenna performance. This method featured in smaller periods compared to the traditional periodic groove structures, which results in reduced antenna aperture and inspiring more surface wave to improve further antenna gain in the performance of the antenna radiation. Furthermore, it compresses the beam angles of sides *E* and *H* to illustrate prominent

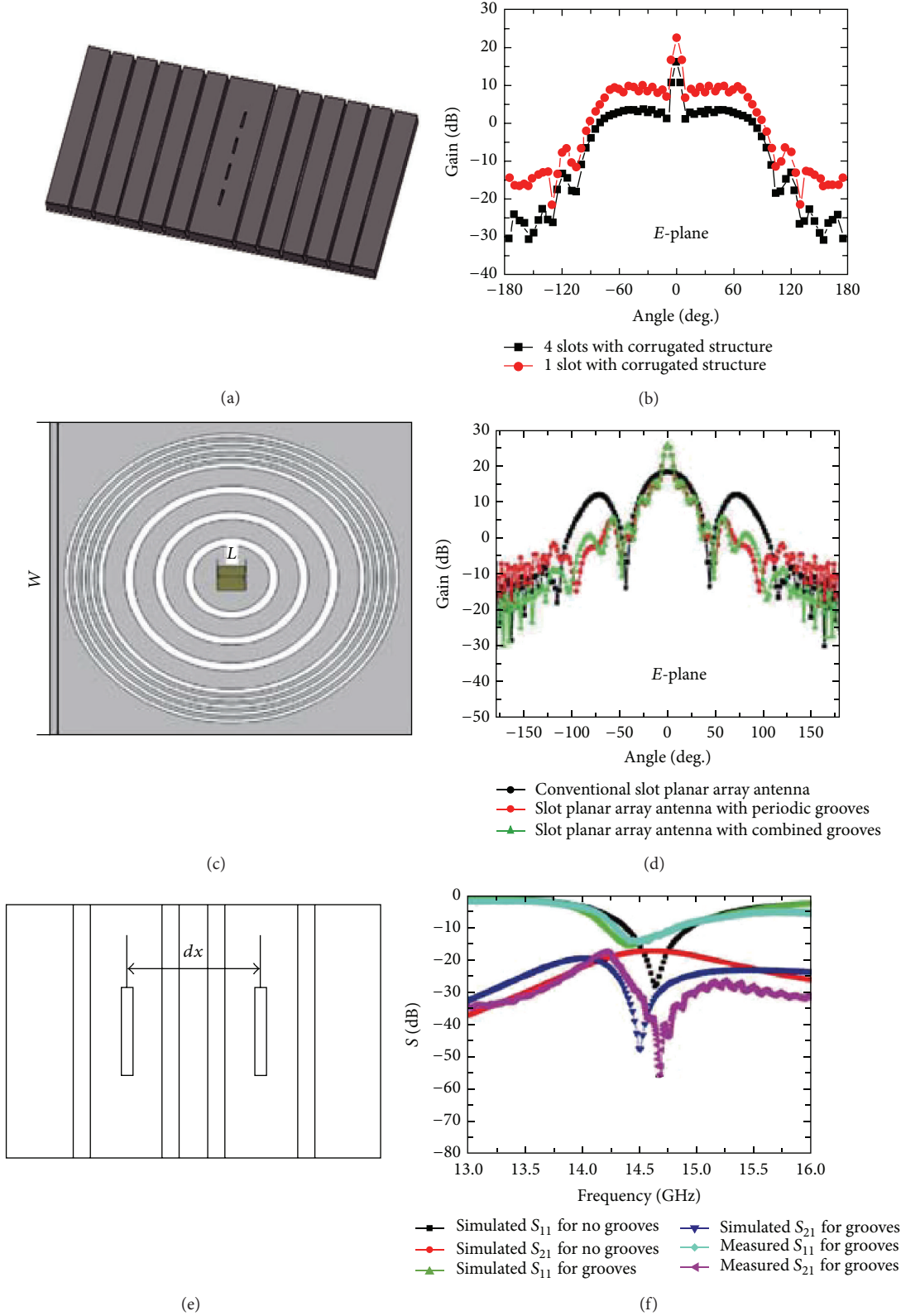


FIGURE 28: (a) Groove antennas based on slot array. (b) The *E*-plane radiation pattern for the antenna in (a). (c) Patch antennas loaded with the groove structure. (d) The *E*-plane radiation pattern for the antenna in (c). (e) Slot array antenna with low coupling. (f) Coupling efficiency of the antenna in (c). Figures are reproduced from [163].

directed radiation ability. So it can be considered that the application of this new periodic groove structure was a development direction of high-directionality antenna. It was the first time to use a periodic groove structure as a secondary source and load it between the slot array elements with interval greater than wavelength to avoid sidelobe. This idea broke through the limit that the traditional array element interval is less than wavelength to widen the applications of the periodic groove structure.

**3.6.2. Surface Plasmon-Inspired Metasurfaces for Applications in Terahertz and Mid-Infrared Regions.** One of the disadvantages of the grooves for directive radiation is that the working bandwidth is limited. Nevertheless, this is not a series problem for some applications. For instance, almost all kinds of lasers are narrowband in spectrum. In this regard, the groove structures can be integrated to lasers in order to improve their performances. By defining a metallic subwavelength slit and groove array on the facet of quantum cascade lasers (QCLs) [165], the divergence angle in the laser polarization direction is only 2.4 degrees as shown in Figure 29. Compared to the original  $9.9\text{ }\mu\text{m}$  wavelength laser without a groove array, a reduction in beam spread by a factor of 25 is achieved, without significant reductions in output power. Taking advantage of SSPs, groove array integrated terahertz QCLs were also demonstrated [166]. The beam divergence of the lasers was reduced from  $\sim 180$  degrees to  $\sim 10$  degrees, the directivity was improved by over 10 decibels, and the power collection efficiency was increased by a factor of about six compared to the original unpatterned devices. In addition, multibeam QCLs and MID-IR QCLs with integrated plasmonic polarizers were reported through combining the groove structures with QCLs by Capasso's group [167].

**3.6.3. Surface Plasmon-Inspired Metasurfaces for Applications in the Visible and Near-Infrared Regime.** The intriguing properties of plasmonic waves at metasurfaces can also be utilized to enhance the directivity of classically noncoherent or not-directive radiations. For example, spontaneous emission of fluorescent molecules or quantum dots is radiated along all directions when emitters are diluted in a liquid solution, which severely limits the amount of collected light. Making use of the directional manipulation of the SP-inspired metasurface, Aouani et al. [168] successfully controlled the radiation properties for nanoemitters, as shown in Figure 30. Enhancing the fluorescence intensity and narrowing the emission directivity were simultaneously obtained, and a full control of fluorescence was achieved. However this control is static. In 2011, active control over fluorescent emission was also reported by electrically pumping the similar light-emitting device [169]. This type of device facilitates the realization of a new class of active manipulation for use in new optical sources and a wide range of nanoscale optical spectroscopy applications.

In addition to the directional manipulating and transmission enhancing, the applications of groove type SP-inspired metasurface were greatly expanded recently. Orbital angular momentum (OAM) transfer [170] and wavefront shaping [171] were experimentally demonstrated. Chiral plasmonic

grooves defined on a metallic film would transform a normal plane wave to the vortex beams with tunable topological charge, as shown in Figures 31(a)–31(c). By surface-wave-holography method, Chen et al. shaped the wavefront of the incident near-infrared light into predesignated complex patterns such as Latin letters, after passing through a  $180\text{ nm}$  radius hole that is surrounded by well-designed groove patterns, as depicted in Figures 31(d)–31(g).

More recently, we provided a scheme to guide and collimate OAM at the micro- and nanolevels [172]. The coaxial plasmonic waveguide is exploited as a naturally occurring medium for light carrying OAM to transfer. The guided OAM wave is coupled to free space through corrugated grooves surrounding the coaxial waveguide, where coherent scattering of spiral surface plasmon was demonstrated to be responsible for the huge enhancement of beam directivity. Experimental results at  $\lambda = 532\text{ nm}$  validated the near-field transportation of OAM beams, where the topological charge is tunable via the modulation of a liquid crystal spatial light modulator (SLM).

**3.7. Passive Metasurface Antennas and Generalized Snell's Law.** In many cases, metasurfaces can be considered as passive antennas array. By tuning the geometries and material parameters, the amplitude, phase, and polarization state of the reradiation of these antennas can be fully controlled. In this section, we first review two kinds of phase-type metasurfaces, where only the phase is tuned. Then, the possibility of full control over the phase, polarization, and amplitude is discussed.

**3.7.1. Passive Antenna Array Based on Impedance Transition.** The impedance boundary conditions of metasurfaces can be utilized to tailor the phase delay within one single layer regardless of its thickness. This means that, theoretically, there exists no thickness limit for this problem. Based on the rigorous form of Huygens' principle developed by Love and Schelkunoff [173, 174], it has been demonstrated that the transmitted or reflected phase shift can vary between 0 and  $2\pi$  to provide complete phase coverage by adjusting the magnitude of the impedance [19, 175, 176].

As depicted in Figure 32, the concept of Huygens' metasurface was proposed by Pfeiffer and Grbic in 2013 [176] and realized with two-dimensional arrays of subwavelength structures that provide both electric and magnetic polarization currents to generate the prescribed wavefronts. The applications of the metasurfaces in a beam-refracting surface and a Gaussian-to-Bessel beam transformer were discussed.

As an attempt to increase the energy efficiency and bandwidth, we presented an efficient approach, as depicted in Figure 33, to extend the bandwidth of phase modulation by utilizing the broadband characteristic of low-quality factor (Q-factor) metasurface in the reflection mode [177]. The dispersion of the metasurface was engineered to achieve phase modulation within  $[0, 360^\circ]$ . Anomalous nearly perfect reflection with relative bandwidth near 40% was demonstrated in the microwave regime. Similar designs in reflection geometry have also been validated by other authors [178–180].

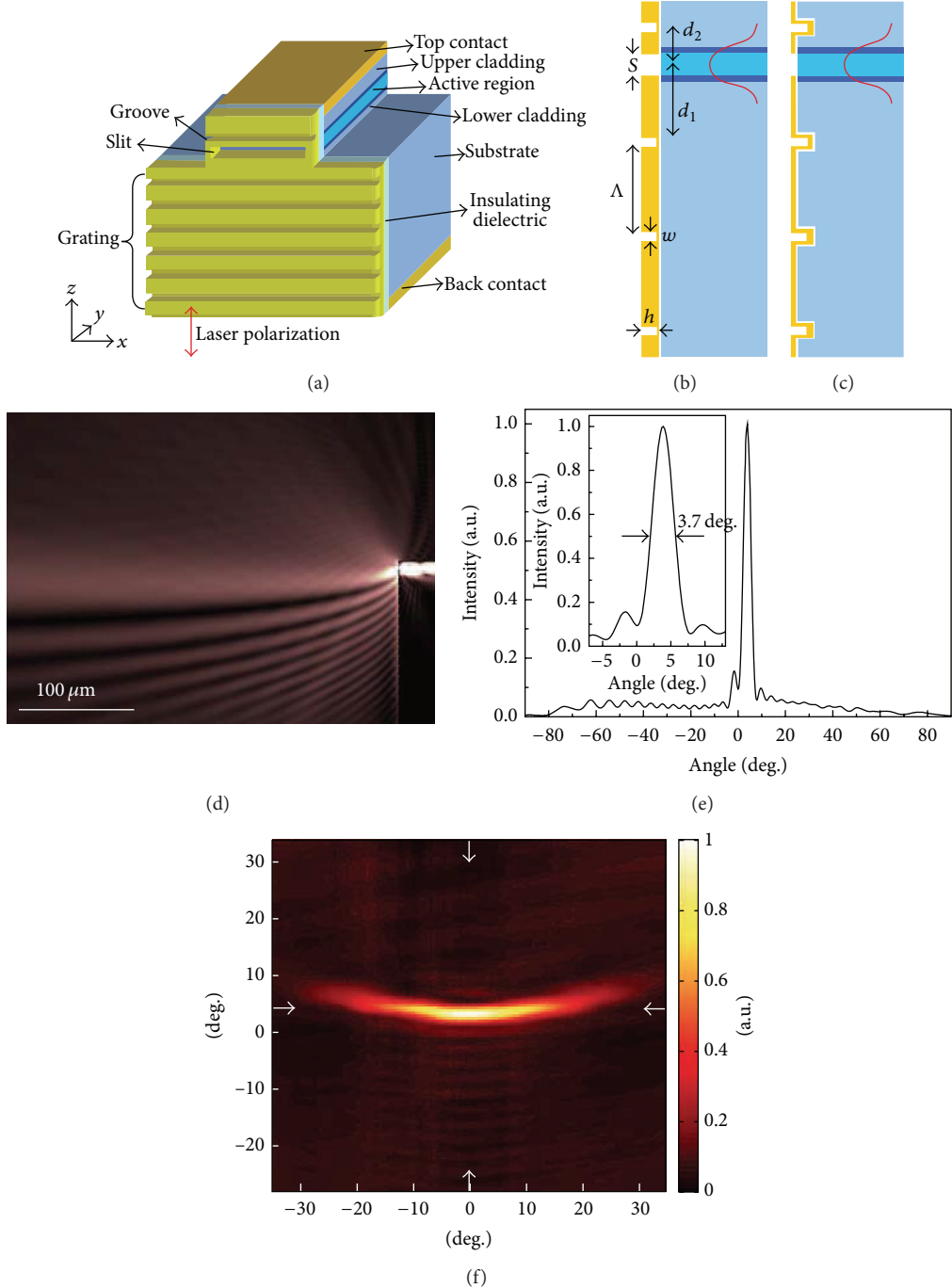


FIGURE 29: (a) Schematic of the small-divergence laser, which comprises a QCL and a metallic slit-grating structure defined on its facet. (b, c) Cross sections of the two device designs. (d) 2D simulation of the intensity distribution of a small-divergence QCL of the second design lasing at  $\lambda = 9.9 \mu\text{m}$ . (e) Calculated far-field intensity distribution of the device shown in (d); inset: enlarged view of the central lobe. (f) Measured 2D far-field intensity of device B patterned with the slit-grating structure. Figures are reproduced from [165].

**3.7.2. Passive Antenna Array Based on Ultrathin Resonators.** In the phase-engineering regime, one interesting but sometimes neglected phenomenon is that a rotation of electric field of circular polarized electromagnetic wave results in a corresponding phase shift. As early as 1955, the rotatory phase shifter was proposed by Sichak and Levine [182]. They

showed that the phase of the output voltage of a circularly polarized antenna was proportional to the angle of rotation of the antenna about its longitudinal axis. Two circularly polarized antennas with a proper rotation angle between each other were mounted in a circular waveguide to construct a phase shifter. In 1961, this rotatory phase was utilized in

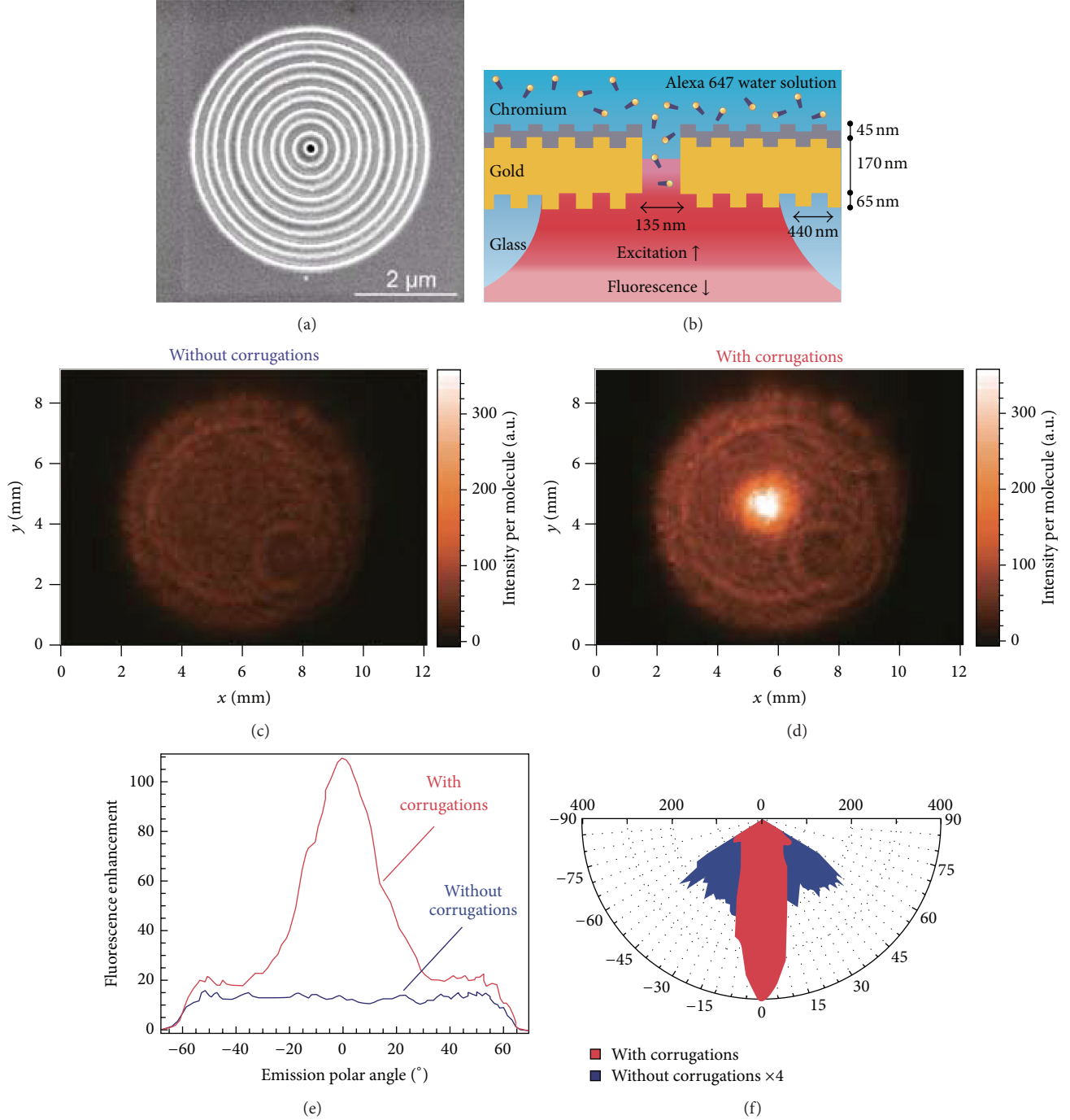


FIGURE 30: Directional radiation of fluorescent molecules. (a) SEM image of the fabricated nanoaperture with five corrugations. (b) Configuration to enhance and control the fluorescence emission of molecules diffusing in the central aperture. (c, d) Radiation patterns (intensity distribution in the back focal plane of the 1.2 NA objective) for a single nanoaperture without (a) and with (b) periodic corrugations. (e) Fluorescence intensity enhancement per single molecule as function of the emission polar angle, relative to the open solution reference case. (f) Angular radiation patterns in the polar angle. Figures are reproduced from [168].

the construction of large radio telescope in the University of Illinois [183]. Subsequently, similar phase shifting results were demonstrated for passive reflectarray antennas [184].

In 1984, Berry proposed that an adiabatic polarization can introduce a phase shift [43], which was further experimentally demonstrated in 1988 [185]. Since the phase is associated

with circular polarization, it can be termed as one kind of optical spin-orbit interaction. In 1999, polarization gratings were proposed [186]. This idea was further developed by Hasman et al., with various kinds of applications, such as beam splitter, optical vortex generation, and focusing lens [44, 187–189]. In 2006, the famous q-plates were proposed to

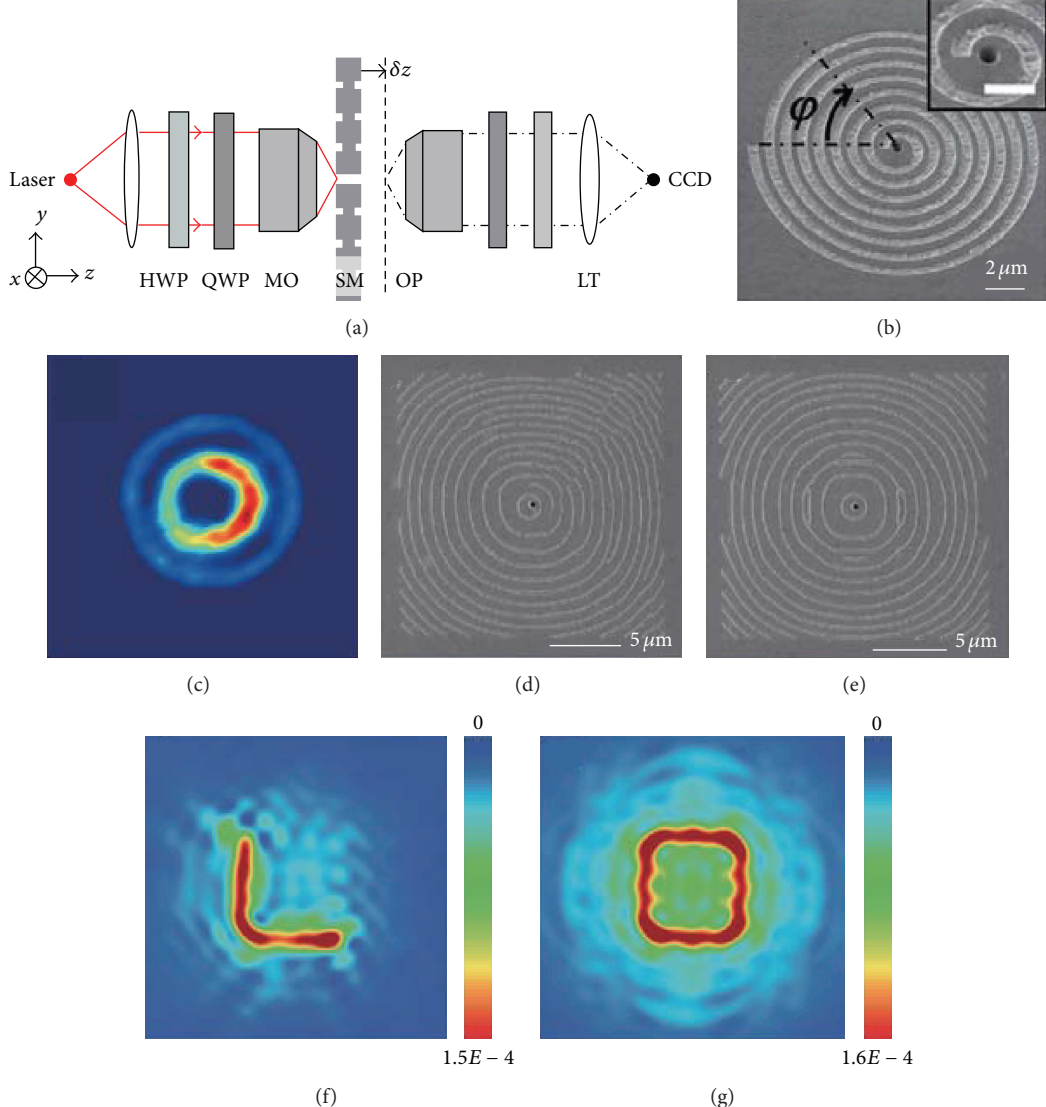


FIGURE 31: OAM generation and wavefront shaping by groove type SP-inspired metasurface. (a) Experimental setup of the OAM generation. (b) SEM image of the sample. (c) Intensity distribution imaged through the sample. (d, e) SEM images of the holographic metasurfaces. (f, g) Simulated images of the holographic images. Figures are reproduced from (a)–(c) [170] and (d)–(g) [171].

realize spin-to-orbital angular momentum conversion [190]. These q-plates can also be used as polarization converters [191]. In recent years, nanoantennas were widely adopted to control circularly polarized waves [192–195].

In 2011, Yu et al. proposed another phase shifting mechanism with linearly polarized illumination. As shown in Figure 34, by varying the angle and length of V-shaped nanoantennas, arbitrary modulation of phase shift and amplitude transmission were demonstrated. The operational principle of such V-shaped antennas relies on the asymmetric transmission enabled by the nanoantennas. Similar to the case of circular polarization, such antennas have low energy efficiency because there always exists one component with the same polarization as the incident beam. Based on this abrupt phase change, they proposed the so-called “generalized Snell’s law.” By properly tuning the geometrical parameters of

each antenna, broadband phase change could be achieved, although the phase was not rigorously achromatic [134, 138, 196].

After the pioneering work by Capasso, much work was devoted to the design of phase-discontinuity metasurfaces. Many optical devices were subsequently designed and experimentally demonstrated. For example, Zhang et al. proposed that C-shape metallic elements can also be utilized to tune the amplitude and phase of cross-polarized scattering for linear polarization incidence [196]. In addition to the simple phase-engineering, other applications, such as spiral phase plates and wave plates, were also demonstrated [197, 198].

Based on the locality of the phase shift [199], Lin et al. extended the V-shaped antennas in the near-infrared bands. The focus length was also decreased to a large extent to obtain a focus spot close to the diffraction limit. Jiang et al.

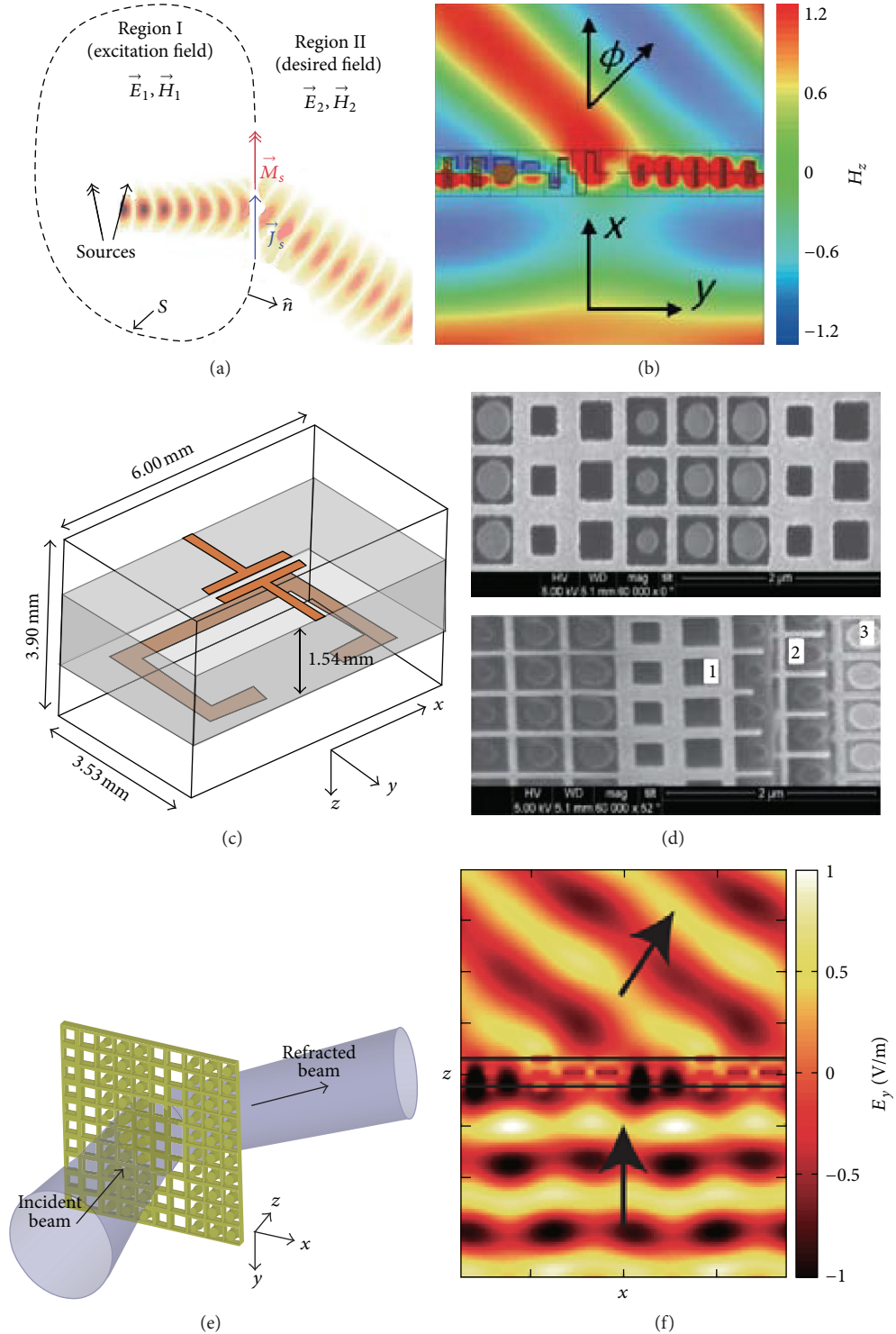


FIGURE 32: (a) Principle of the Huygens metasurface. The fields in regions I and II are defined independently of each other, and the surface equivalence principle is employed to find the fictitious electric and magnetic surface currents that satisfy the boundary conditions at the metasurfaces. (b) Simulated time snapshot of the magnetic field ( $\text{Hz}$ ) of a  $y$ -polarized plane wave, normally incident upon the designed Huygens' surface. (c) Dimensions of the unit cells comprising Huygens' metasurface. (d) SEM images of the optical Huygens' surfaces. (e) Perspective view of an optically thin, isotropic Huygens' metasurface that efficiently refracts a normally incident beam at telecommunication wavelengths. (f) Time snapshot of the steady-state,  $y$ -polarized electric field when a plane wave is normally incident from the bottom at a wavelength of 1.5  $\mu\text{m}$ . The incident electric field has an amplitude of 1 V/m. Figures are reproduced from [176, 181].

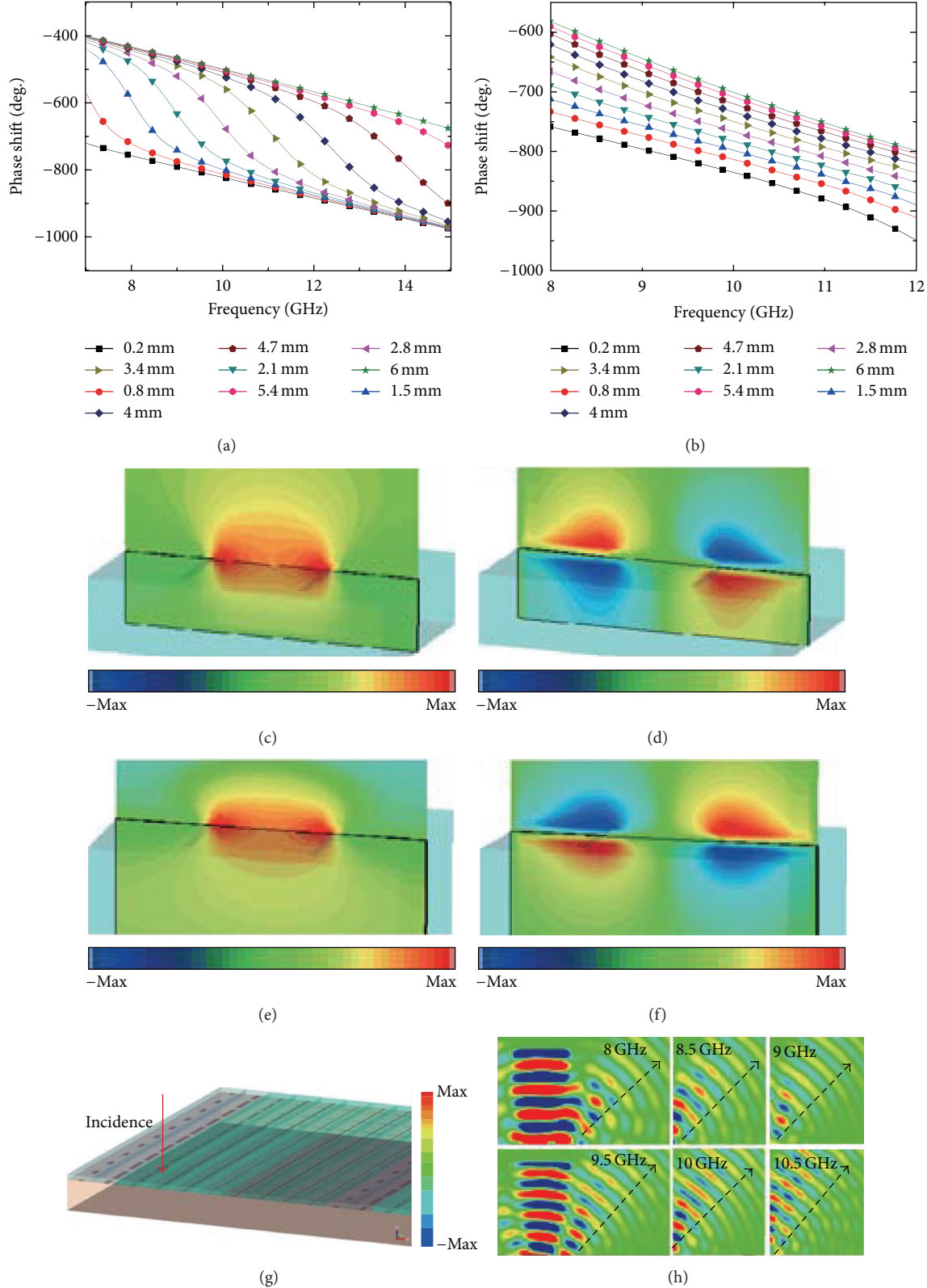


FIGURE 33: Reflection phases for different values of gap width  $g$  for thickness of (a)  $d = 2$  mm and (b)  $d = 6$  mm. The other geometrical parameters are chosen as  $l = 4$  mm and  $w = 0.2$  mm. (c)  $y$ -component and (d)  $z$ -component of electric fields for  $d = 2$  mm,  $g = 2.8$  mm, and  $f = 10$  GHz. (e)  $y$ -component and (f)  $z$ -component of electric fields for  $d = 6$  mm,  $g = 2.8$  mm, and  $f = 10$  GHz. (g) Schematic of the gradient metasurface. (h) Electric field  $E_y$  distribution in the scattering region at normal incidence for 8, 8.5, 9, 9.5, 10, and 10.5 GHz. The dashed black arrows indicate the propagation direction evaluated by  $\sin^{-1}(kx/k)$ . Figures are reproduced from [19].

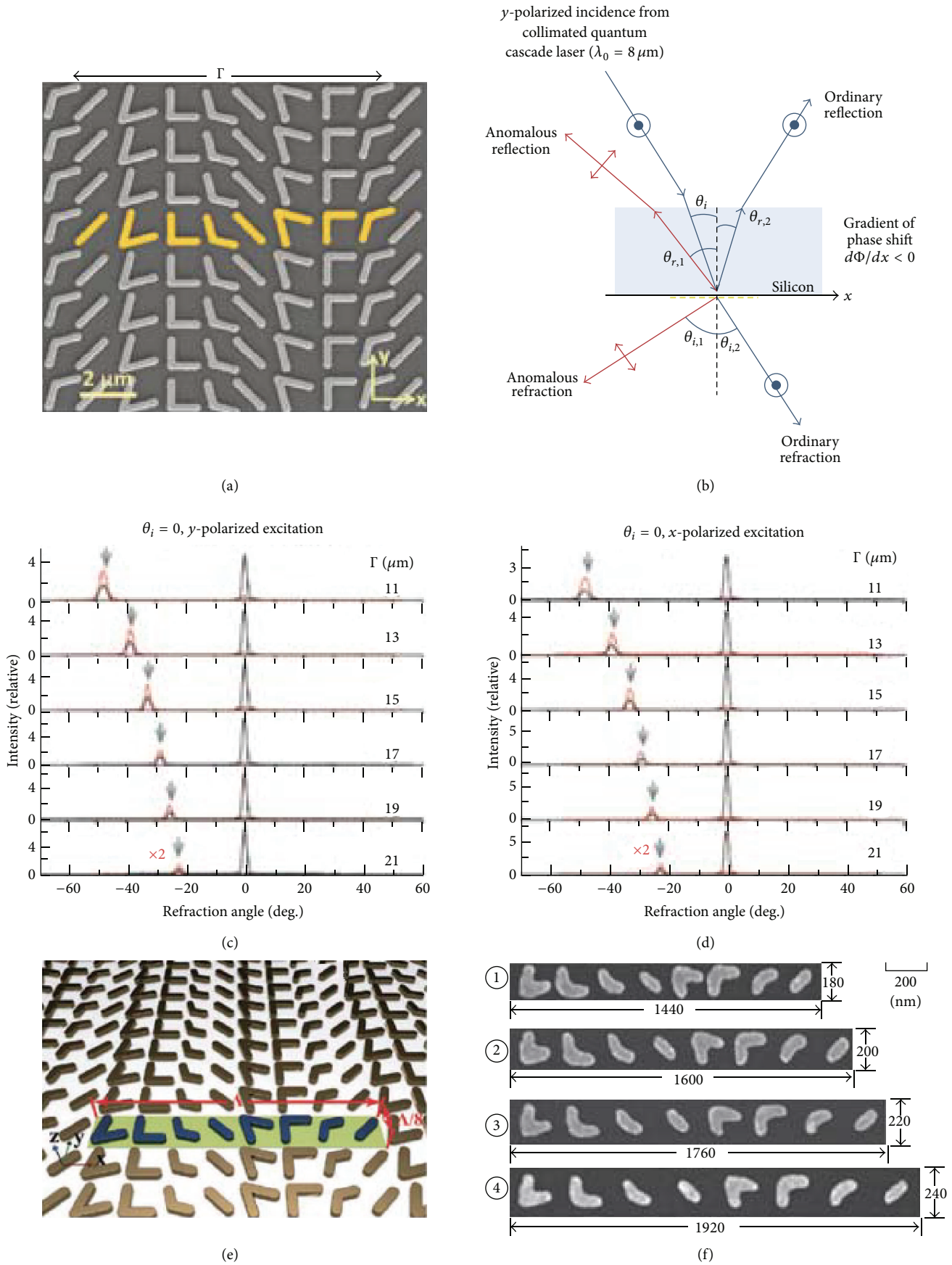


FIGURE 34: Continued.

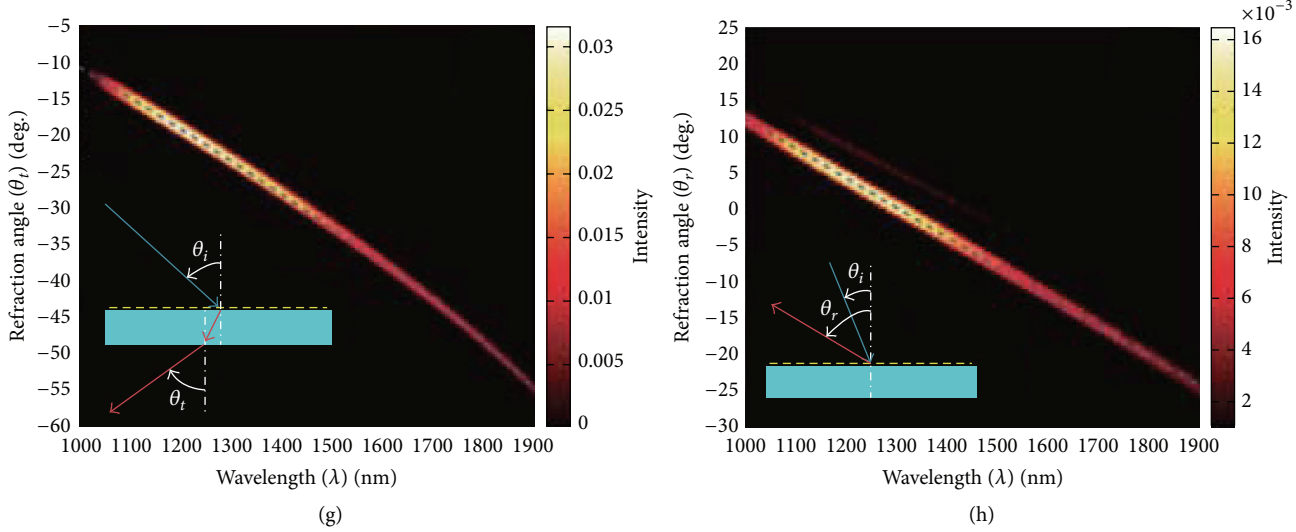


FIGURE 34: (a) SEM image of a representative antenna array fabricated on a silicon wafer. (b) Schematic experimental setup for  $y$ -polarized excitation. ((c) and (d)) Measured far-field intensity profiles for the  $y$ - and  $x$ -polarized excitations, respectively. (e) Schematic view of a representative antenna array. (f) Scanning electron microscope images of the unit cells of four antenna arrays with different periodicities fabricated on a single silicon wafer. ((g) and (h)) The false-color maps indicate the experimentally measured relative intensity profiles for the antenna array. Figures are reproduced from [134, 138].

demonstrated similar effect in the terahertz regime [200]. More recently, Ma et al. used a metasurface to focus vortex beam into a nanodoughnut [201]. As shown in Figures 35(a)–35(d), the proposed metasurface has good performance close to the ideal case. The metasurface tuned the phase distribution of the incident beam based on the concept of discontinuous phase modulation. Consequently, the proposed metasurface has two main functions. Firstly, with a circularly polarized incident beam, the metasurface converts it into a beam carrying OAM. Secondly, the incident field can be focused into a point with a certain focus length. The total energy coefficient of this metasurface exceeds 40%. By properly designing the phase modulation distribution, the copolarized component of the incident field does not participate in the focusing process. Therefore, only optical vortex can be observed in the focused field. The thickness of this planar chiral metasurface is much less than the operational wavelength and thus has potential application in compact integrated optical systems.

The geometric phase in aperture array has direct application in holography. As demonstrated in Figures 35(e)–35(h), metasurface with metallic square apertures was constructed in our lab to form a hologram image of a China map based on the concept of discontinuous phase modulation in visible band.

Since only part of the transmitted light takes geometric phase, single layered metasurfaces are often characterized by low efficiency. In principle, the efficiency could be increased dramatically with the help of a reflective layer. Taking the circularly polarized geometric phase as an example, the combination of an anisotropic metasurface with a reflective layer would form a reflective wave plate. By rotating the main axis of the embedded antennas, gradient phase could be directly

obtained. This technique was utilized in reflectarray to increase the gain of antenna while keeping the reflective surface to be flat [184]. In the optical regime, the reflective nanoantennas array was used as building blocks of high efficient holograms [202]. The metasurface has an ultrathin and uniform thickness of 30 nm and is compatible with scalar diffraction theory, even with subwavelength pixel sizes, thus simplifying the design of holograms.

Another important application of the metasurface relies on the fact that phase shifting metasurfaces placed at the optical pupil plane can increase the resolution of telescopes, which means that the far-field diffraction limit can be overcome [203]. As shown in Figure 36, the designed metasurface has several rings, which exert phase shift of 0 and  $\pi$  on the incoming light and change the corresponding spatial frequency [2]. To characterize the performance, we measured the images of two circular and triangular holes with and without the metasurface. After the insertion of the metasurface, the resolution is decreased to 0.625 times of the original value, implying that a 10-meter telescope could have the same resolution as that of a 16-meter one (i.e., a 1.6 times improvement in the resolution power).

Very recently [204], we proposed and demonstrated the concept of broadband virtual shaping at the visible, infrared, and microwave spectrum by tailoring the spatiotemporal property of spin-orbit interaction in cascaded metasurfaces. When electromagnetic waves impinge on the designed metasurface, they are reflected to predefined directions to avoid being detected by unwanted antennas. Resorting to the dispersion engineering techniques in metasurface-based polarizers, the bandwidth was dramatically enhanced, although the thickness-to-bandwidth ratio may be analogous to that of broadband absorber. The design principle provided a new

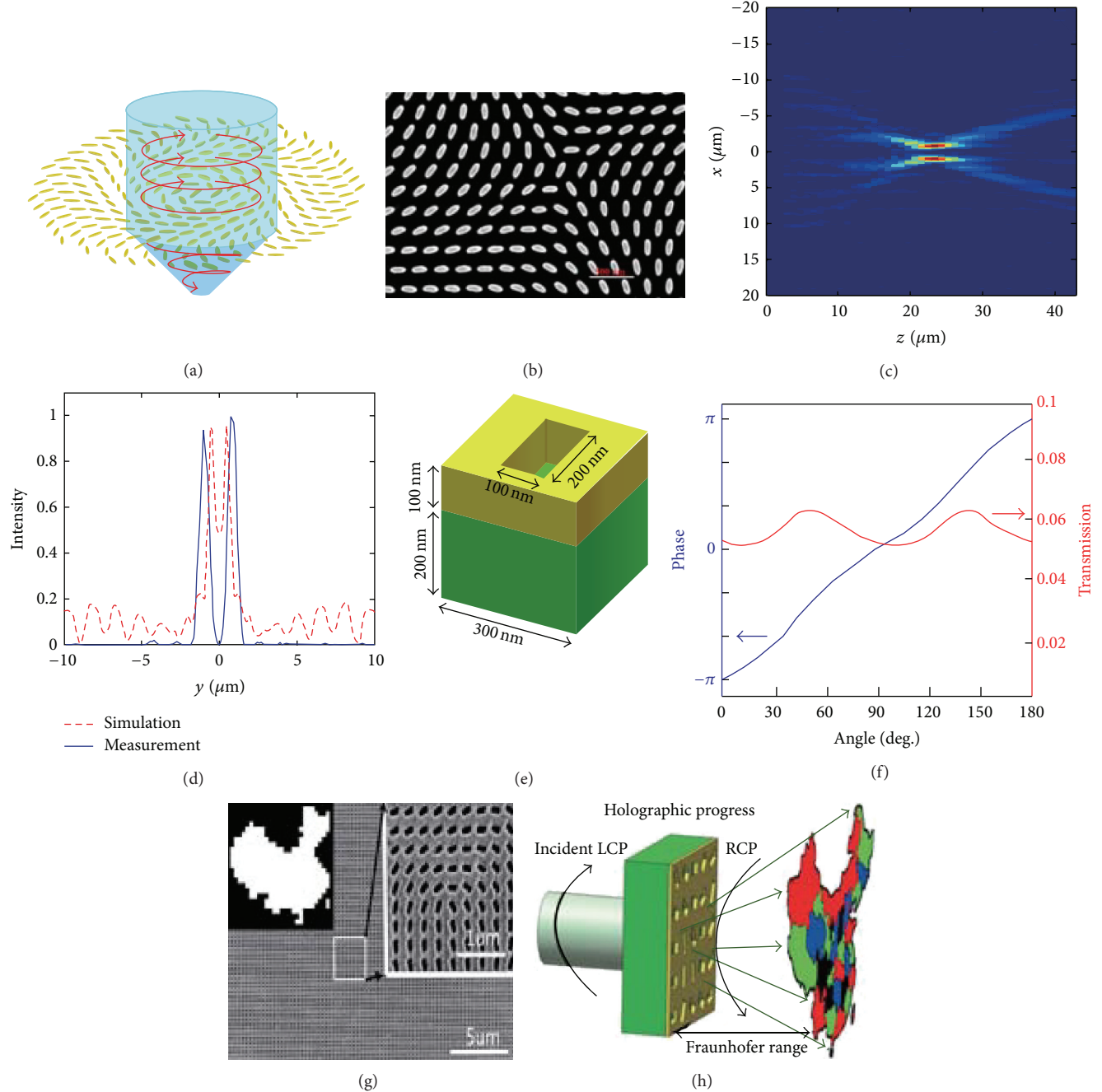


FIGURE 35: (a) Schematic of the 2D elliptic antennas array. (b) SEM image of the elliptic antennas. (c) Measured power intensity profile of the focused field in the  $xz$ -plane. (d) The simulated (dashed lines) and measured (solid lines) intensity spectra of the focused field, respectively, along the  $y$ -direction. (e) Schematic of the unit cell of rectangular aperture in metallic screen for holography. (f) Amplitude and phase transmission for various rotation angles. (g) SEM image of the sample. (h) Schematic of the measurement setup. Figures are reproduced from [201].

route for the control of electromagnetic wave for applications ranging from laser beam shaping to 3D holographic display and conformal camouflage [205].

As shown in Figures 37(a) and 37(b), we measured the specular reflection of an inhomogeneous metasurface. Since the reflected light was designed to depart from its original direction via the metasurface-assisted law reflection, only

a small reflection echo was measured. Owing to the flexibility of the metasurface, this approach could be utilized in complex objects. For example, the RCS of a cylinder can be dramatically reduced by covering our metasurfaces on it (Figure 37(c)). The metallic cylinder in our design has a radius of  $R = 90$  mm and height of  $h = 360$  mm. The geometric phase distribution on the metasurface was designed to be

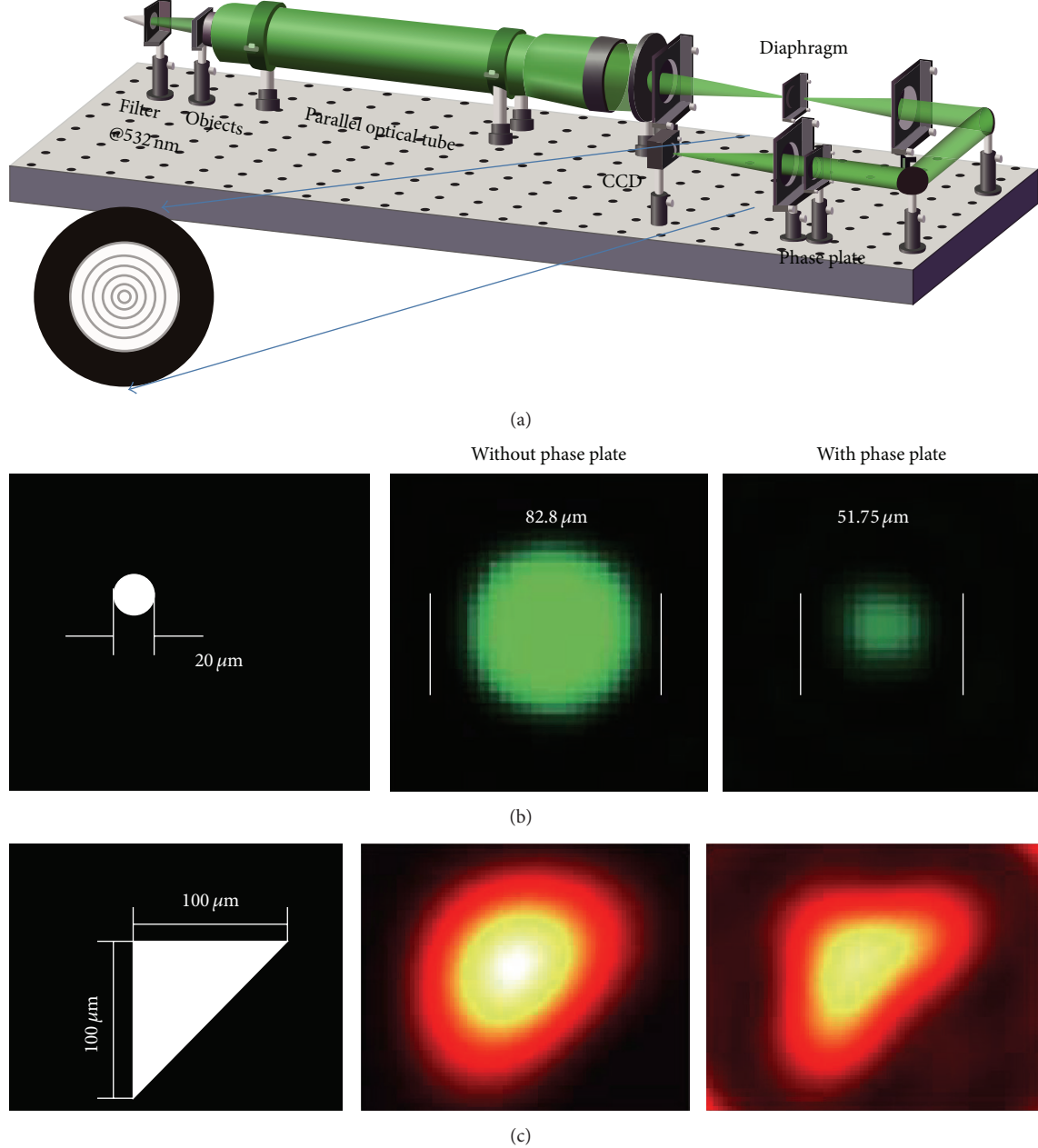


FIGURE 36: Far-field superresolution based on metasurface. (a) Schematic of the experimental setup. The inset shows the phase distribution of the metasurface. Gray regions and white regions indicate 0 and  $\pi$ , respectively. (b) Experimental results for a circular hole at wavelength of  $\lambda = 532$  nm. (c) Simulation results for a triangular hole. Figures are reproduced from [2].

$\Phi = k_z z + k_\varphi \varphi$ , where  $k_z = k_\varphi = 104.7$  rad/m. As shown in Figure 37(d), the RCS reductions for TE polarization and TM polarization were calculated under normal incidence along the  $y$ -direction. We noted that the reduction amount is a bit smaller than the planar case, which possibly stems from the nonoptimized phase profile and the fact that the RCS of a cylinder itself is smaller than its planar counterpart. Nevertheless, the conformal metasurfaces provide a new sight into the virtual shaping of nonplanar objects. In addition, this approach can be exploited to increase or decrease the RCS.

In general, the metallic metasurfaces suffer from low efficiency due to the intrinsic ohmic loss and the limited scattering cross sections of the antennas, which is not anticipated in many realms. Recently, dielectric metasurfaces based on geometric phase were presented to control the phase [44]. Nevertheless, the discrete phases lead to degradation of the performance. To overcome this issue, we proposed a semicontinuous structure to increase the continuity of phase shift. The metasurfaces consist of high-refractive-index and low-loss silicon annual ring gratings. Ohmic loss is avoided compared

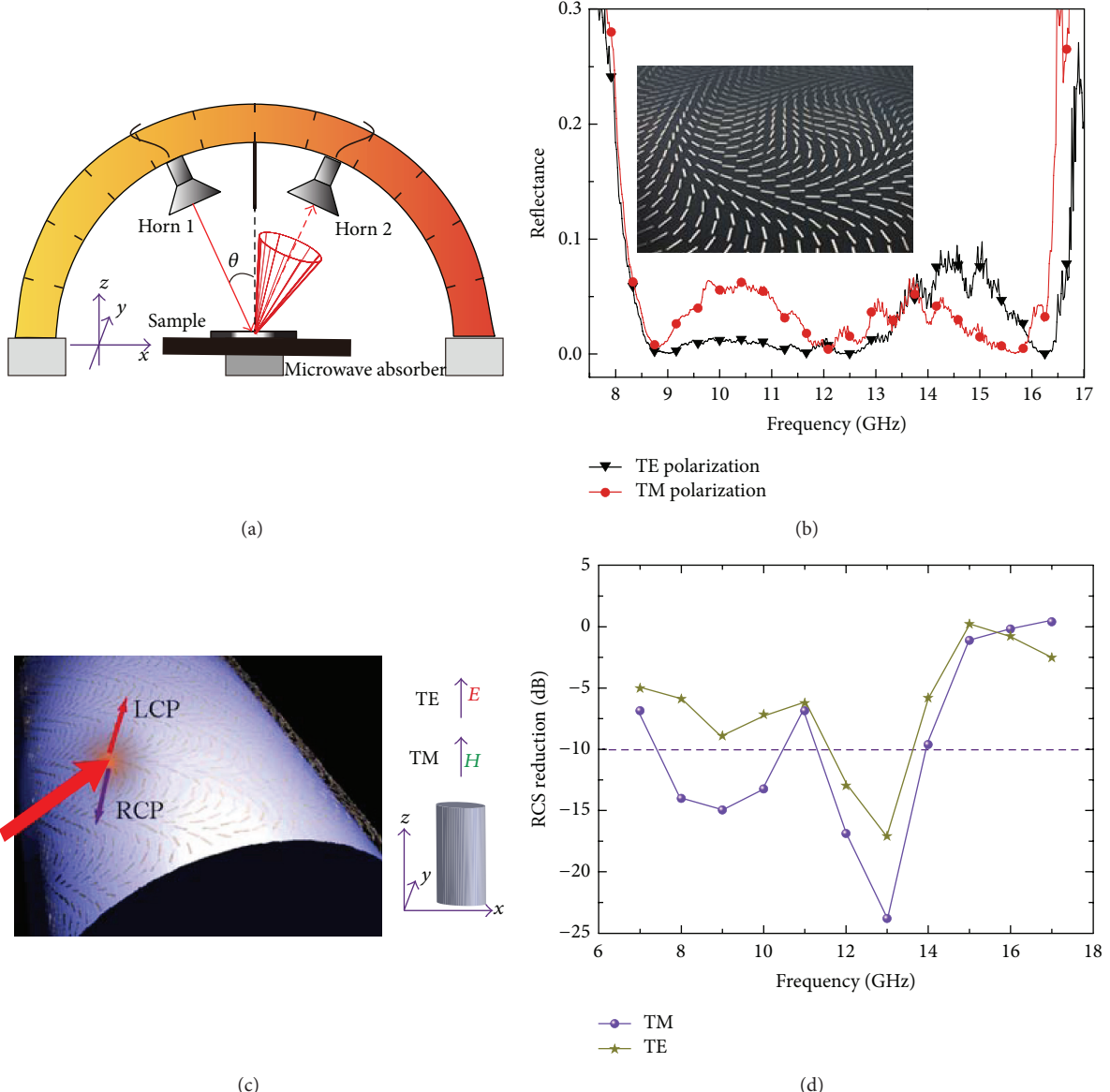


FIGURE 37: (a) Schematic of the measurement setup. (b) Measured results for both TE polarization and TM polarization. The inset shows the photography of the fabricated sample. (c) Schematic of the spin-orbit conversion in the curved metasurface on a metallic cylinder. The insets show the definitions of TE polarization and TM polarization. (d) Calculated broadband RCS reduction for TE polarization and TM polarization at normal incidence along  $y$ -direction. Figures are reproduced from [204].

to its metallic counterpart. The continuity of annual ring grating ensures the continuity of the transmitted field, thus suppressing high order diffraction effects that may arise from discontinuity.

At the end of this section, we would like to comment that metasurface with geometric phase could enable many applications in distinct disciplines. In general, traditional refractive, reflective, and diffractive devices could be replaced by metasurfaces. These elements include the spherical lenses, aspherical lenses, parabolic reflectors, fan-out grating, and laser beam shapers. In the microwave regime, metasurfaces could also be utilized to substitute traditional phased-array antenna. Furthermore, this kind of metasurface is also able to

shift the momentum of scanning beam to extend the scanning range of phased array antennas, when it is integrated in radar radomes [206].

**3.7.3. Full Control of Phase, Polarization, and Amplitude.** In many applications, the phase, polarization state, and amplitude are all important for the manipulation of electromagnetic waves. For example, a low side-lobe phased array antenna needs the full control of phase and amplitude [207], while a planar lens with large longitudinal fields in the focus spots requires that the polarization and phase be simultaneously controlled [208].

In order to achieve complete modulation of phase and polarization, Pfeiffer and Grbic proposed a four-layer cascaded metasurface lens that can focus light and control its polarization [209]. By adjusting the dimensions of structure, one can independently adjust the inductance and capacitance in the  $x$ - and  $y$ -directions so that the phase and polarization can be completely controlled.

Kim et al. demonstrated that the local reflection coefficients of gap-plasmon resonators can be independently tailored in both magnitude and phase [181]. Using an array of nanorods closely placed on a metallic layer, it was shown that the magnitude and phase of the surface's local reflection coefficients can be simultaneously tuned, with a magnitude range of [0, 0.67] and a phase range of  $360^\circ$ . The power efficiency can reach 45% for an operational wavelength of 800 nm. This method was utilized in the design of a Dolph-Tschebyscheff array, with equal-amplitude sidelobes of prescribed magnitude, as represented in Figures 38(a)–38(d).

More recently, Li et al. proposed and validated another metasurface that can provide simultaneous manipulation of the phase and polarization of the transmitted light [210]. SPPs were adopted to obtain a  $\pi$  phase shift when the top and bottom nanoapertures are laterally translated by a distance in the  $y$ -direction. Hence, the phase difference can cover 0 to  $2\pi$  by varying the parameters of nanoaperture for normally incident light polarized in the  $y$ -direction. The metasurface enabled anomalous refraction with efficiency of about 21.4% for linearly polarized incident light (Figures 38(c)–38(g)).

It also should be noted that the phase over the surface of micro- and nanoantennas can also be measured with the help of scattering near-field techniques [211, 212], which provide a way to further understand the physical processes of these antennas.

**3.8. Active Metasurfaces.** Although passive metasurfaces have been proved to be useful in many applications, the dynamic tuning of performance is always desired in practical applications. Most of the metasurfaces have fixed electromagnetic properties when the structures are designed or fabricated. Nevertheless, there is a type of “reconfigurable” metasurface which is able to tune the electromagnetic response with an outside stimulus [213–217]. The general way to obtain the tunable phase modulation is by loading active devices in its unit cells, such as varactor diodes [218], liquid crystals, and ferroelectric and microelectromechanical switch (MEMS) [219], as can be seen in Figure 39.

These reconfigurable or tunable metasurfaces efficiently broaden the application range of metamaterial and simplify the optical and communication systems. According to the particular applications, active metasurfaces can be classified into three main subdomains. In the following, we would give a brief review on these novel metasurfaces.

**3.8.1. Active Phase Modulation.** Aiming at satisfying the requirement of modern communication systems and solving the disadvantages of traditional phased array antenna, metasurfaces with phase-tuned ability have been introduced to construct novel beam scanning antennas. The principle

of beam steering for this metasurface is illustrated in Figure 40(a). The designed active metasurface is divided into  $N$  regions, which can be regarded as a linear array with a period of  $l/N$ . When a plane wave transmits through these  $N$  regions, the phase difference between adjacent regions would be  $\alpha$ . As a result, the angle of beaming direction is  $\theta$  deviated from the normal direction, which is determined by  $\alpha$ .

In Figure 40(a), the transmission phase  $\varphi_i$  of region  $i$  can be shown as

$$\varphi_i = -\zeta_i + \varphi_0 + 2k\pi, \quad (41)$$

where  $\varphi_0$  is a constant and  $k$  is an integer. The phase shift  $\zeta_i$  and the phase difference  $\alpha$  can be expressed as

$$\begin{aligned} \zeta_i &= \frac{\beta il}{N \sin \theta}, \\ \alpha &= \varphi_i - \varphi_{i-1} = -\frac{\beta l}{N \sin \theta}, \end{aligned} \quad (42)$$

where  $\beta$  is the wave number. The beam steering angle  $\theta$  can be then written as

$$\theta = \arcsin \left( -\frac{N\alpha}{\beta l} \right). \quad (43)$$

Clearly, (43) is one particular case of the metasurface-assisted Snell's law, based on which the beaming direction can be tuned by changing the phase difference  $\alpha$  between adjacent elements. In 2012, Jiang et al. [206] introduced an active cascaded metasurface for phase manipulation by tuning varactor-diodes loaded in the unit cell. The tunable metasurface was employed as the radome to tune the  $E$ -plane radiation pattern of the antenna array. However, the loss of this active phase modulation metasurface is relatively large due to its eight layered structure.

Based on the phase modulation property of the metasurface, we have proposed an active phase modulation metasurface to manipulate the phase of the incident wave and to achieve beam steering of a horn antenna [221], as depicted in Figure 40(d). The unit is composed of a metallic rectangular ring and a patch, with a pair of microwave varactor diodes inserted in between along incident electric field polarization direction. Transmission phase of the emitted wave can be tuned by changing the bias voltage applied to the varactor diodes, and  $360^\circ$  phase difference can be obtained at 5.3 GHz as the capacitance value is tuned from 0.65 pF to 2.6 pF.

Through different configurations of the bias voltages, one can obtain the gradient phase distribution of the emitted wave along  $E$ -plane and  $H$ -plane. This metasurface loaded antenna can steer the directive beam with an angle of  $\pm 30^\circ$  in both  $E$ -plane and  $H$ -plane at 5.3 GHz with a bandwidth of 180 MHz. Using an improved approach, the scanning range can also be increased to  $\pm 360^\circ$  in both  $E$ -plane and  $H$ -plane [2].

In previous works, the polarization state and beam direction are not simultaneously controlled. In order to achieve this goal, a novel transmitarray element was proposed, which achieved 1-bit phase shifting at two orthogonal linear polarization modes. The phase tuning and polarization reconfiguration can be independently controlled based on PIN diodes.

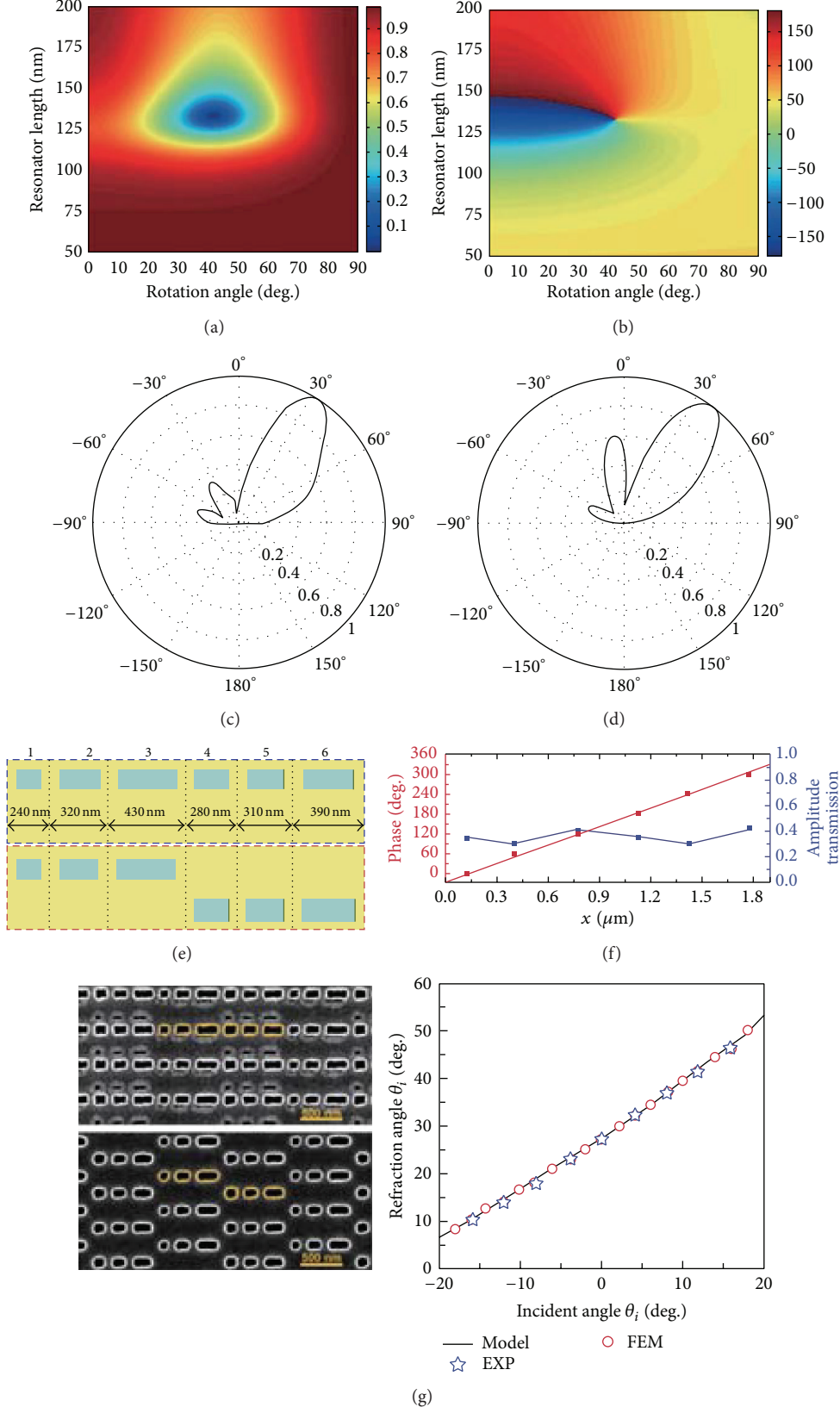


FIGURE 38: (a) Magnitude and (b) phase of  $S_{11}$  in degrees for different resonator lengths and rotation angles. (c, d) Radiation patterns of (a) Dolph-Tschebyscheff and (b) uniform arrays. Both arrays redirect the normally incident plane wave at  $33^\circ$ . (e) Schematics of the top and bottom nanoapertures forming the super-unit-cell in the plasmonic metasurfaces for the demonstration of anomalous refraction. (f) The transmission phase and amplitude of each nanoaperture pair, calculated under  $y$ -polarized incident light at  $900\text{ nm}$ . (g) SEM image of the sample (left panel) and measured refraction angle (right panel). Figures are reproduced from [181, 210].

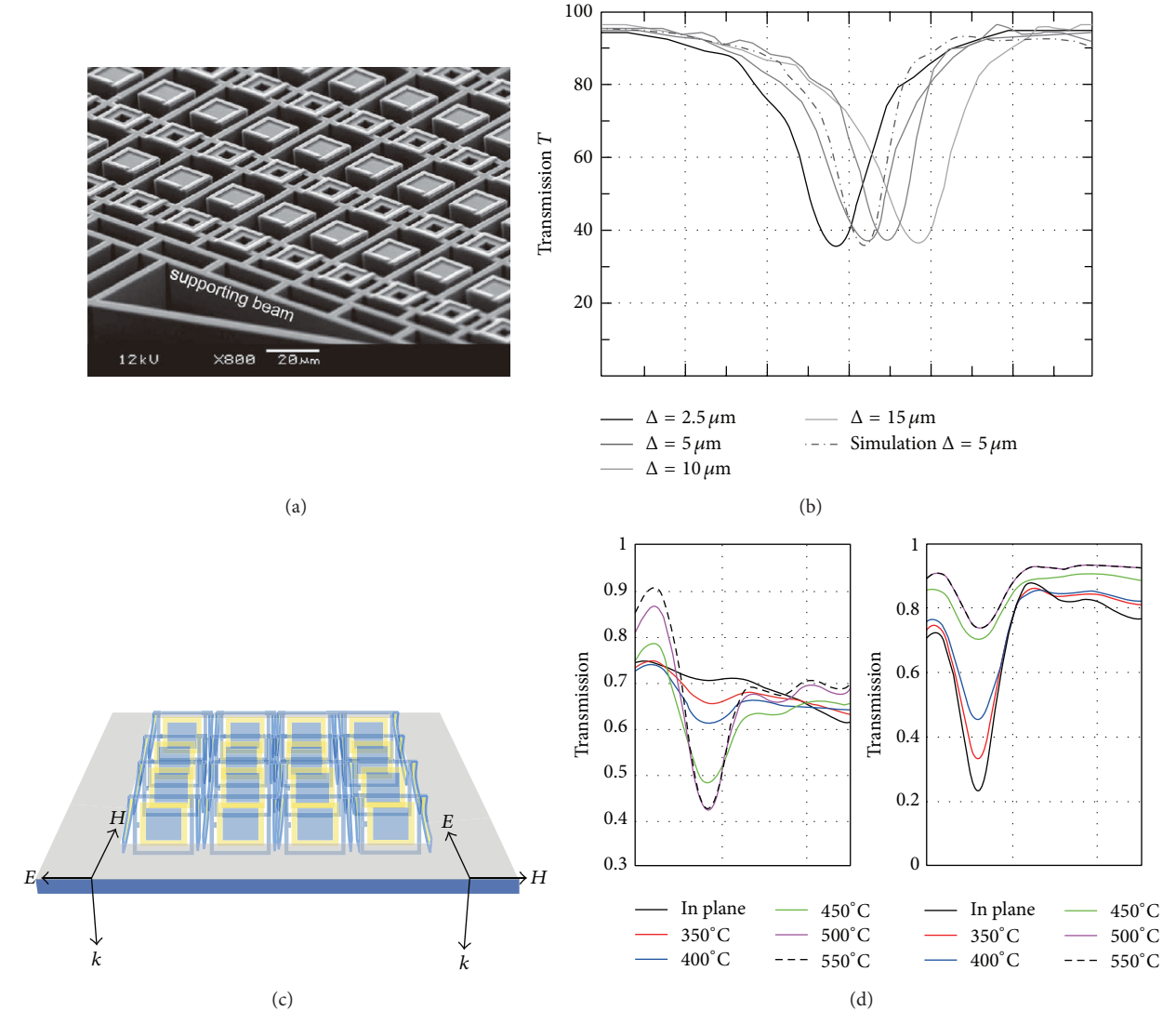


FIGURE 39: Examples of active metasurfaces. (a) SEM image (b) transmission spectra for a MEMS-based metasurface. (c) Schematic and (d) transmission spectra for magnetic resonance (left panel) and electric resonance (right panel). Figures are reproduced from [219, 220].

The unit cell of the dual linearly polarized metasurface consists of two-layer metallic patterns connected by a metalized via-hole. One-layer metallic pattern is a rectangular patch with two PIN diodes loaded in O-slot along electric field polarization direction, which is utilized as a receiver-antenna to achieve 1-bit phase tuning. The other metallic pattern is a dual linearly polarized transmitter-antenna that adopts a square ring patch with two PIN diodes distributed at the cross-polarization directions. The simulation results show that the designed antenna can achieve 1-bit phase tuning and linear polarization reconfiguration at 10.5 GHz with insertion loss of about 1.1 dB. This kind of the metasurface-based antenna has the advantages of low cost and simple implementation, which could be developed for possible applications in some communication and radar systems, especially in the area where high-gain beam steering and the anti-interference capabilities are urgently required.

**3.8.2. Active Polarization Modulation.** The polarization states can also be dynamically tuned by active metasurfaces. Zhang et al. [215] proposed a reconfigurable chiral metasurface, which switched its handedness when the semiconductor region was illuminated by external light, as shown in Figure 41. This reconfigurable or tunable property efficiently broadens the application range of metasurface and simplifies the optical and communication systems.

In order to achieve polarization conversion with simple metasurface, Ma et al. [92] demonstrated a double-layered active metasurface which changes the structure between chiral and isotropic by tuning the working states of the PIN diodes in its unit cells. When it presented chirality, the handedness could also be tuned. As shown in Figures 42(a) and 42(b), the designed metasurface could convert the incident linearly polarized wave into RCP or LCP one. Furthermore, it could also be switched to be isotropic and keep

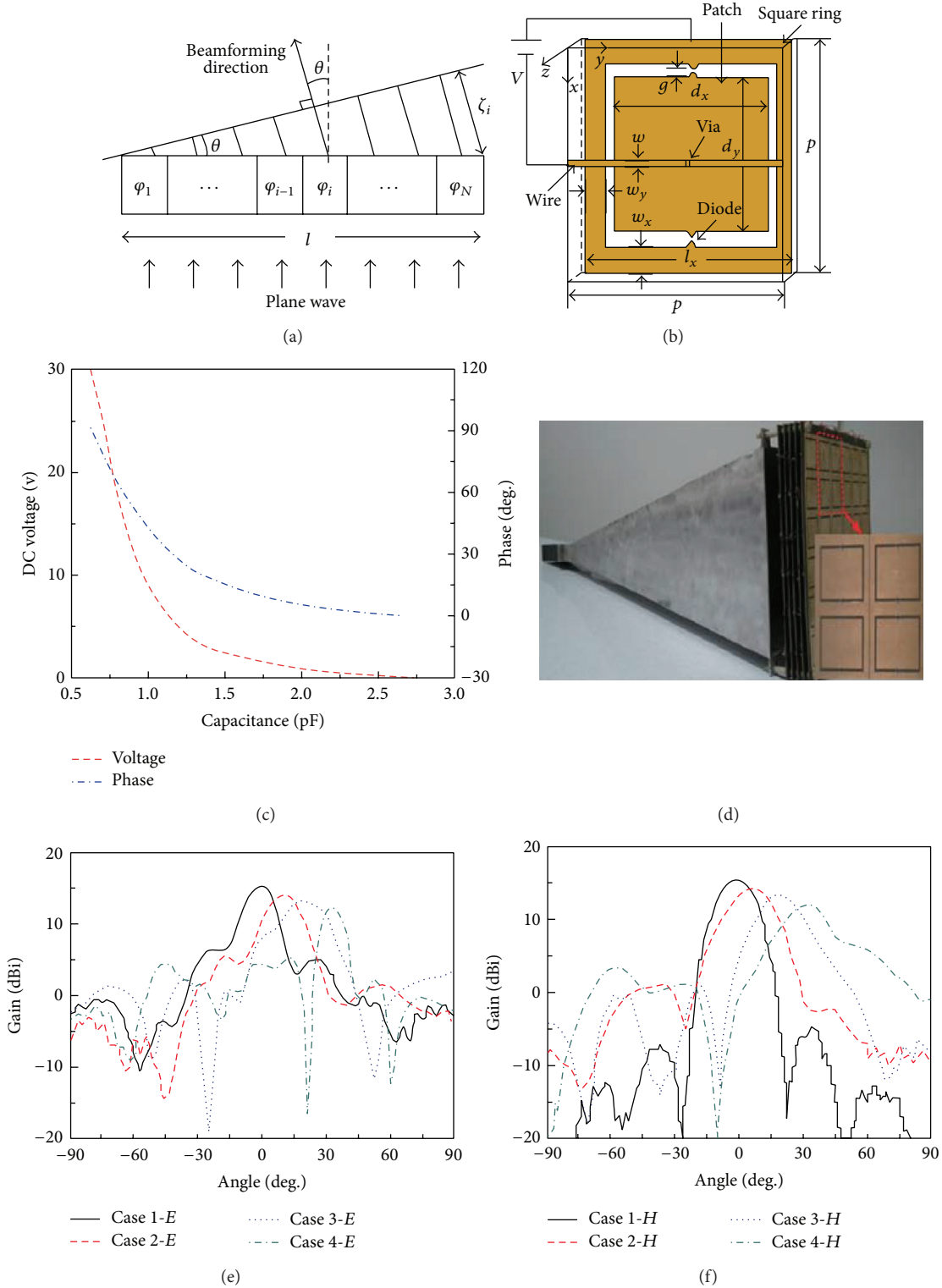


FIGURE 40: (a) Principle of beam steering. (b) Unit cell of the phase reconfigurable metasurface. (c) Phase manipulation results of the active metasurface. (d) Photography of the horn antenna with the active FSS. (e, f) Radiation patterns of the designed horn antenna in (e)  $E$ -plane and (f)  $H$ -plane for different phase distribution. Figures are reproduced from [221].

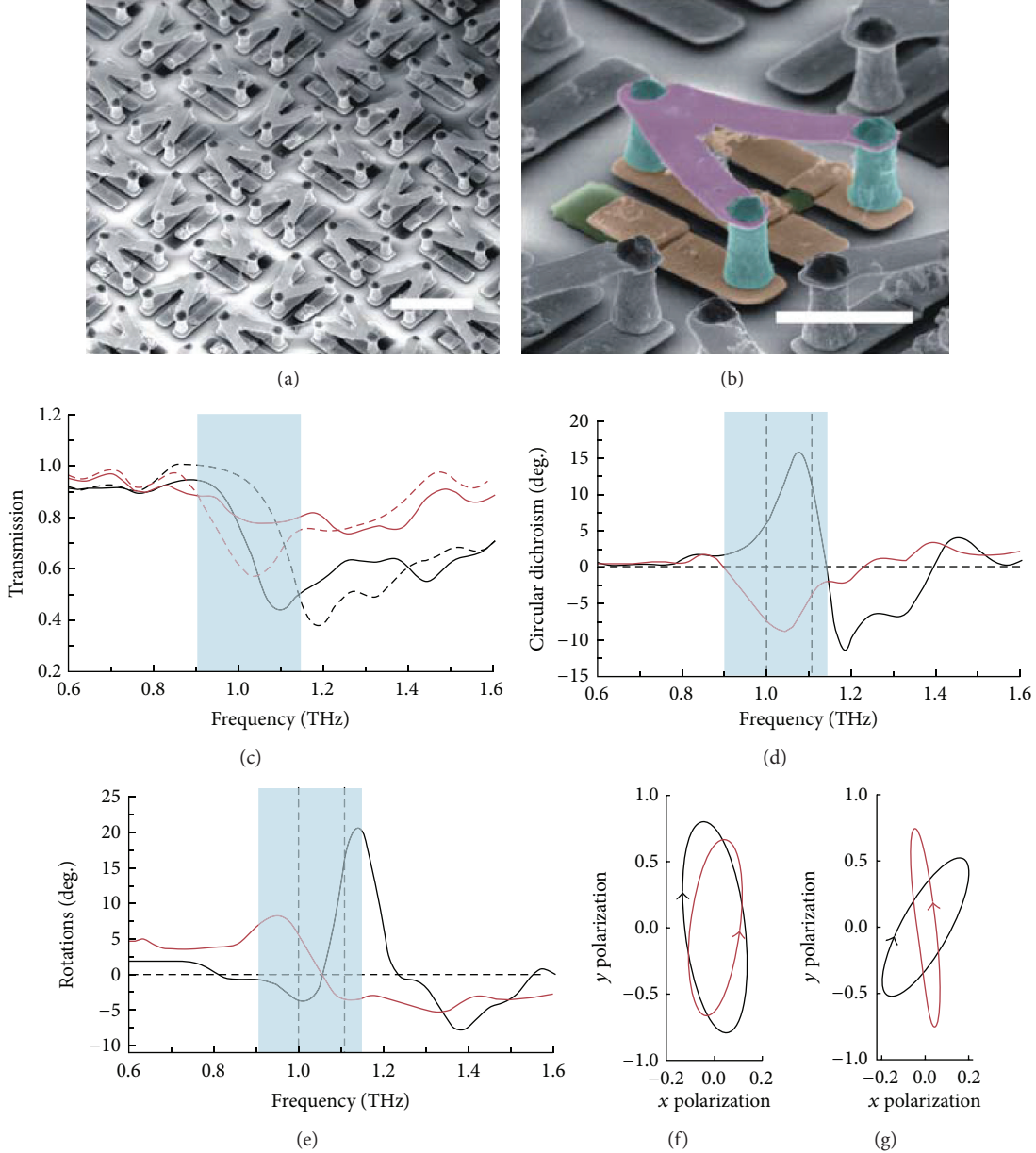


FIGURE 41: Geometry and the results of the photoinduced handedness switching metasurface. Figures are reproduced from [164].

the polarization state of the incident wave unchanged, by controlling the voltages applied on these diodes.

We have also employed this concept of active polarization manipulation into the design of antennas. As it is well known, the dipole cannot radiate efficiently near a perfect conductor due to its opposite image current; in addition, the single dipole can only produce linearly polarized waves, which cannot satisfy the requirement in many communication fields. To address the above issues, the anisotropic metasurface was proposed as the ground plane for the dipole. This novel reflective metasurface not only reduces the profile of the dipole but also assists it to achieve emission of circularly polarized wave. Through adjusting the PIN diodes loaded on the unit cell of the metasurface, the polarization states of the emitted

wave from the dipole, including RHCP, LHCP, and LP waves, can be dynamically tuned.

The tunable metasurface can make the dipole antenna work at four states. For states 1 and 2, as seen in Figure 42(d), the emitted waves with left- and right-hand circular polarization are produced at 4.6 GHz, and the AR is 1.2 and 0.3 dB, respectively. For states 3 and 4, the dipole antenna radiates the linearly polarized waves with the gains of about 6 dB at 4.6 and 4.25 GHz (see Figure 42(f)), respectively. This kind of the polarization reconfigurable antenna has a strong environmental adaptability, which may find many potential applications in the communication field.

Recently, Wang et al. demonstrated a coherent perfect polarization transformer [76]. It was proved that the phase

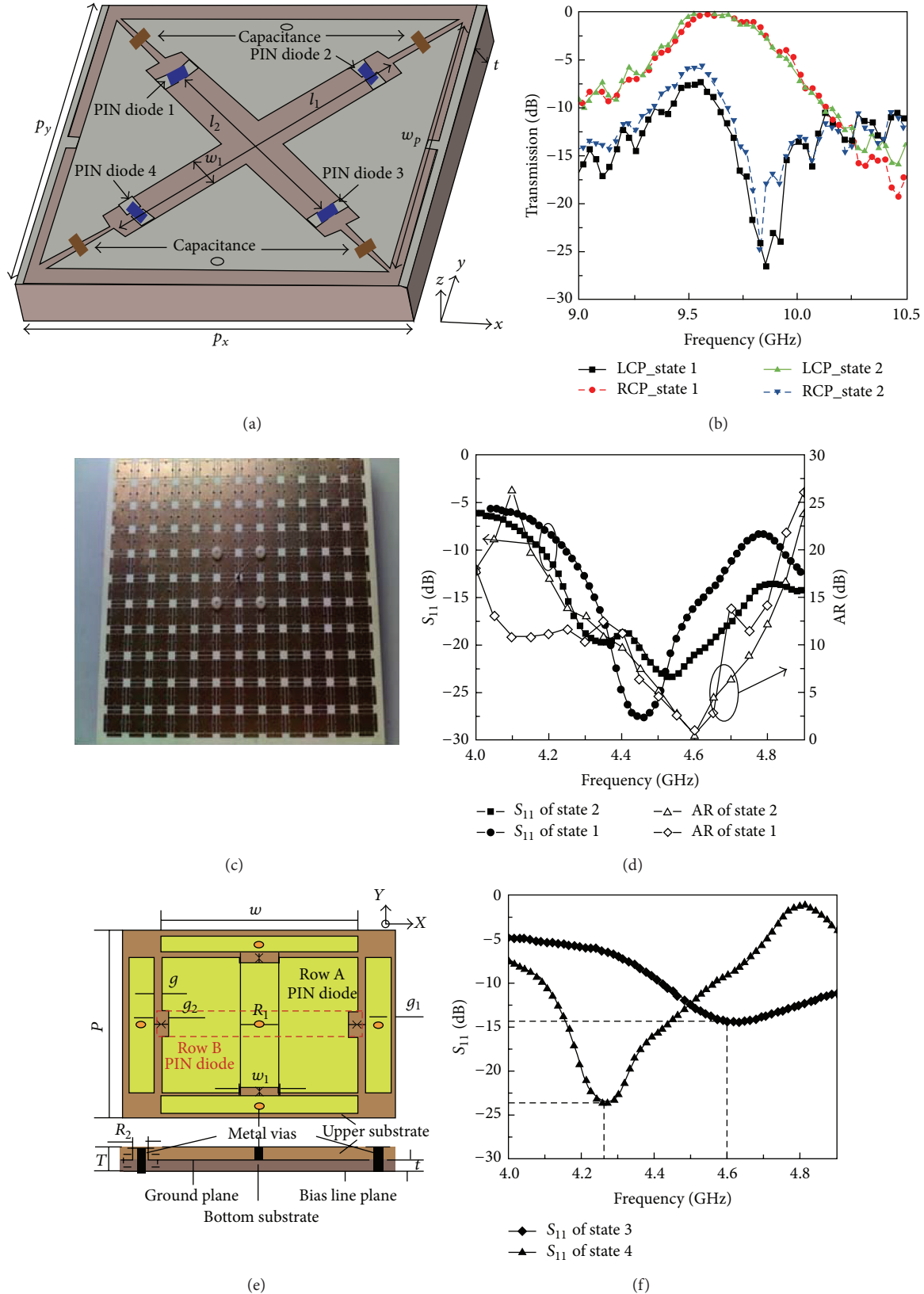


FIGURE 42: (a) Schematic of the metamolecule of the active metasurface for polarization manipulation, and the transmission spectra are shown in (b). (c) Photography of the fabricated dipole antenna using tunable metasurface with its unit cell in (e), and the measured  $S_{11}$  and AR of the designed dipole antenna for different working states are shown in (d) and (f). Figures are reproduced from [92].

shift between two coherent inputs could be utilized to dynamically tune the polarization states of output waves. Depending on the phase difference, the outputs could be  $y$  polarization, LCP, and RCP for  $x$ -polarized inputs.

**3.8.3. Active Amplitude Modulation.** Besides the phase property of the incident electromagnetic wave, the amplitude can also be modulated. As analyzed in the effective impedance theory, the transmitted amplitude and the phase of the incident wave are modulated by the effective impedance of the metasurface. Therefore, the element loading method in metasurface allows the control of the amplitude and hence provides new applications in microwave communication systems, such as controlling the sidelobe and beamwidth of the radiation antennas.

Lim et al. [222] had designed a kind of composite right-/left-handed microstrip antenna in which varactors were used to tune the amplitude of each element for achieving dynamic control of the beamwidth. Recently, a partially reflective surface (PRS) was utilized to actively change the beamwidth of the emitted waves by tuning its reflection through the varactors mounted on each element of the PRS [223].

Antennas with low side-lobe level (SLL) are urgently required since it can efficiently reduce the electromagnetic interference and improve the ability of signal capture. However, traditional approaches to achieve low SLL are mainly realized by modifying the elements weighting or spacing distribution in antenna array. In comparison, metasurfaces with amplitude tunability were employed to reduce the SLL of antennas since the radiation pattern can be reformed by metasurfaces.

Our team proposed an approach to reduce the SLL of antenna array to a desired value by utilizing amplitude modulated metasurface, as shown in Figure 43. By manipulating the structure parameters and the PIN diodes loaded in the unit cells, the transmission amplitude of each unit can be distinctly controlled. Then, the metasurface was utilized as the superstrate of the horn antenna array, and the superstrate was divided into several regions with different transmission amplitudes along the electric field polarization direction. With a plane wave illustrated on the superstrate, the transmission amplitudes were designed as Taylor distribution while the transmission phases were equal, which resulted in a tapered amplitude distribution of the output beam. An  $H$ -plane sectorial horn array is adopted as a plane wave source to verify the performance of the SLL reduction. The SLL was reduced from  $-12.4$  to  $-25.9$  dB at the desired frequency, while not influencing the gain of the antenna array.

Wang et al. proposed a kind of metasurface superstrate to control the beamwidth of horn antenna array based on the concept of amplitude modulation [225], as depicted in Figure 44. The unit cell of the metasurface was composed of two-layer periodic structures loaded with varactors. By tuning the capacitance of the varactors, the unit cell can produce two different states which are transparent and absorptive to the incident wave at a certain frequency, respectively. The whole metasurface can be divided into several groups, and each group is composed of some unit cells with the same state.

By switching the state of each group, the transparent window of the metasurface can be changed. Consequently, the emitted waves with variable beamwidth can be expected, as validated in Figure 44(c), when this metasurface was placed above the horn antenna array as superstrate.

As another method to modulate the amplitude, metasurfaces partially absorbing ability has been introduced and employed in the antenna realm. Compared to the traditional means, such as shaping of target surface and adopting radar absorbing material, such metasurface may efficiently reduce the RCS while not decreasing the radiation performance of the antenna. We proposed a design to reduce the RCS and enhance the gain of a patch antenna by using partially reflecting surface (PRS) that consists of two layers of metallic structure [58], as demonstrated in Figure 44(d). The top absorbing layer is utilized to reduce RCS, while the bottom layer was combined with the ground plane to construct the F-P cavity to achieve high gain. The antenna gain was enhanced by about 6.5 dB at 11.5 GHz, and its RCS is dramatically reduced in a broad frequency range from 6 to 14 GHz. It was fully verified that the designed PRS did not influence the radiation performance of the antenna within the bandwidth of the RCS reduction, but it also obviously improved the antenna gain. This new design provides a good method to solve the conflict between the gain enhancement and the RCS reduction.

In the above amplitude modulation metasurface, the normalized amplitude can be controlled in the range of 0-1. However, the amplitude of the incident wave can be gained above unit by utilizing amplifier in the unit cell of the metasurfaces. Recently, we also proposed an amplifying reconfigurable metasurface to achieve simultaneous control of the amplitude and phase of the incident wave. The varactor diodes were adopted to construct the reflection-type phase shifters, which achieved over  $400^\circ$  of phase shift extending the operation bandwidth beyond 10%. Most importantly, the amplifier integrated in the unit cell of the metasurface made the amplitude of the whole element simultaneously gain larger than 7 dB. In addition, the overall thickness of the proposed metasurface element is only  $0.135\lambda$  in free space, which is more compact compared to the existing metallic elements. This kind of amplifying and phase modulation metasurface could be developed to construct high-gain antenna for beam steering.

**3.8.4. Active Absorption Modulation.** In order to satisfy the requirement of modern military and civil applications, novel materials with smart absorbing characteristics are needed. In general, active metasurface absorbers have two advantages over traditional absorbers. Firstly, since traditional metamaterials absorbers are limited in the operational bandwidth, active tuning may increase the effective bandwidth in a time-diving way. Secondly, the absorption coefficients can be dynamically tuned to mimic the electromagnetic spectrum of environment, which is not obtained through traditional approaches.

The intrinsic circuit property of metasurface absorbers permits an easy way to realize active tuning. As shown in many references, the metasurface can be characterized by its equivalent resistances, inductances, and capacitances [99, 114].

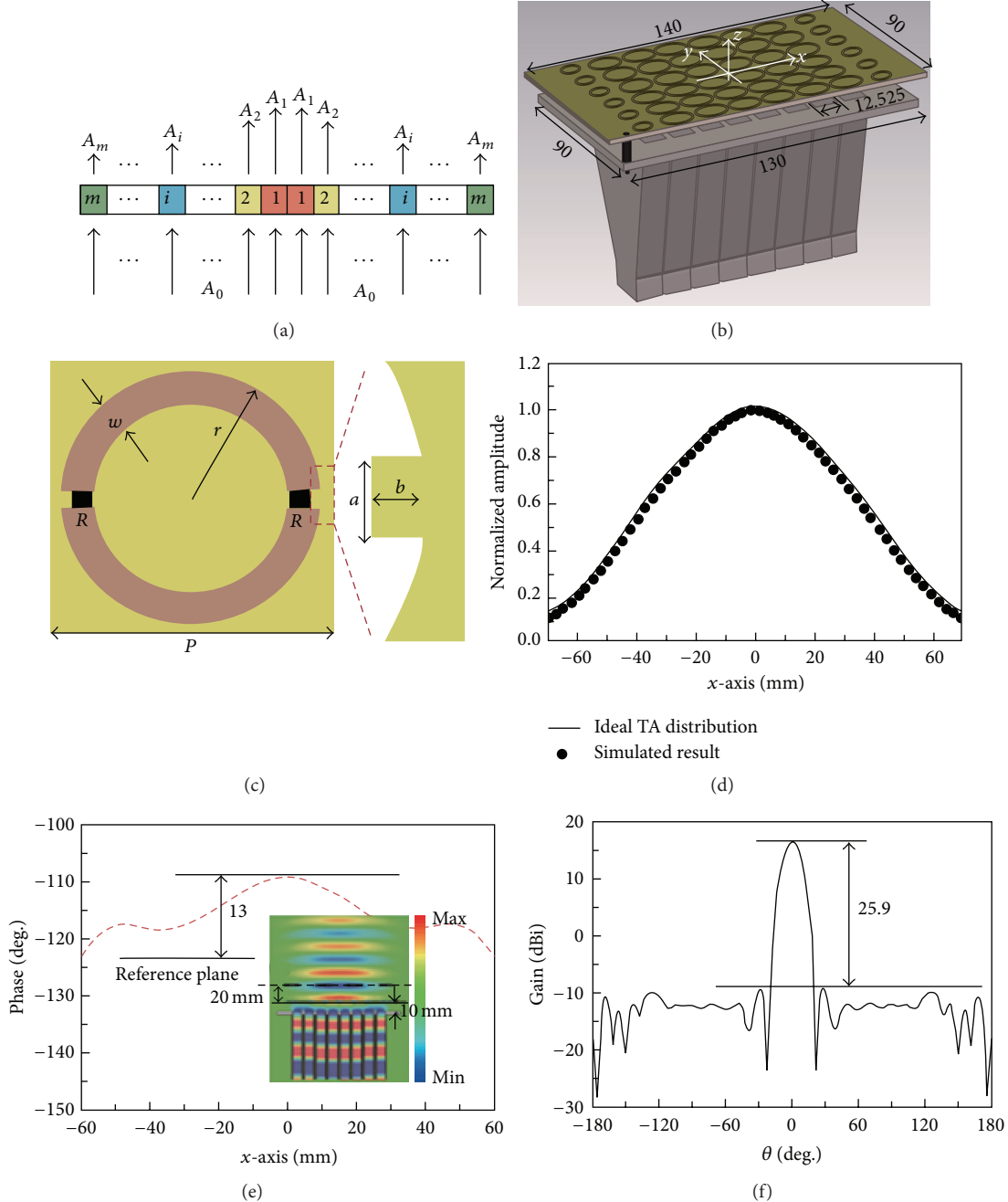


FIGURE 43: (a) Principle of the sidelobe reduction with the metasurface superstrate. (b) The geometry of the amplitude tunable metasurface to reduce the sidelobe of the horn antenna array. (c) Schematic of the unit cell of the metasurface. (d) Comparison of the normalized transmission amplitude distribution of the proposed antenna composite and the ideal Taylor amplitude distribution. (e) Phase distributions at the reference plane. The inset figure shows the electric field distribution at  $xz$ -plane. (f) Radiation pattern in the  $E$ -plane of the antenna composite at 10.3 GHz with sidelobe level of  $-25.9$  dB.

When lumped circuit devices, such as resistors, inductors, capacitors, and various kinds of diodes, are integrated in the metasurface, the electromagnetic response can be greatly improved.

Early in 2004, Tennant and Chambers presented an adaptive absorber by controlling the bias voltage of PIN diodes loaded between adjacent metallic bow ties [213]. The

absorber was similar with the topology of a Salisbury screen, but in which the conventional resistive layer was replaced by an active metasurface controlled by PIN diodes. The resulting structure had superior absorption characteristics compared to conventional passive absorbers of corresponding thickness. Measured results showed that the reflectivity response of the absorber can be controlled over the frequency band from

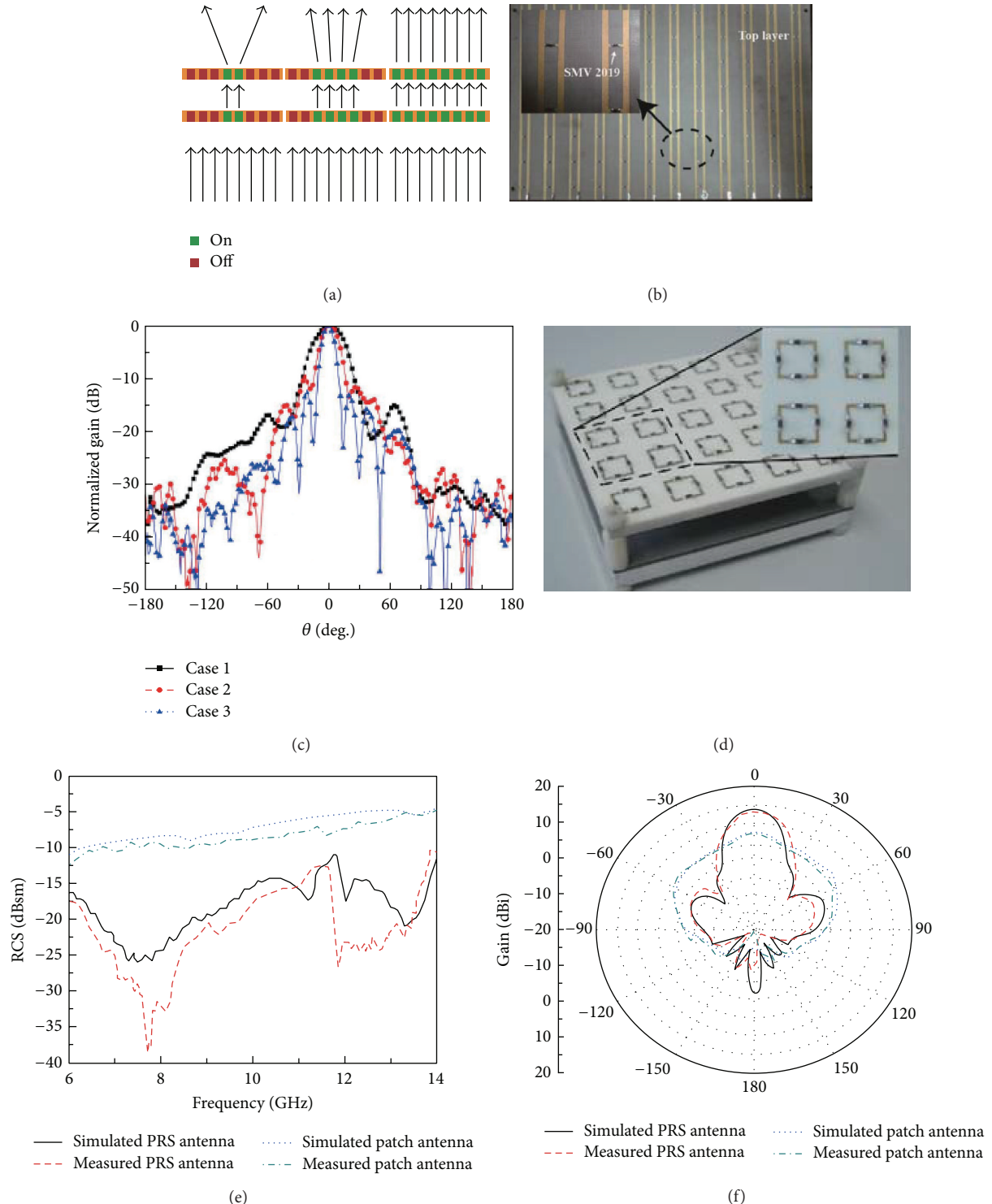


FIGURE 44: (a) Schematic of the beamwidth controlling using metasurface. (b) Photographs of the fabricated FSS for beamwidth controlling. (c) Response of reflection and transmission coefficients to different capacitance values at the interesting frequency region. (d) Photograph of the low RCS antenna loading partially absorbing metasurface. (e) The RCS results for the PRS antenna with and without PRS. (f) Measured *E*-plane far-field patterns for the beamwidth manipulation antenna at 5.5 GHz. Figures are reproduced from [224].

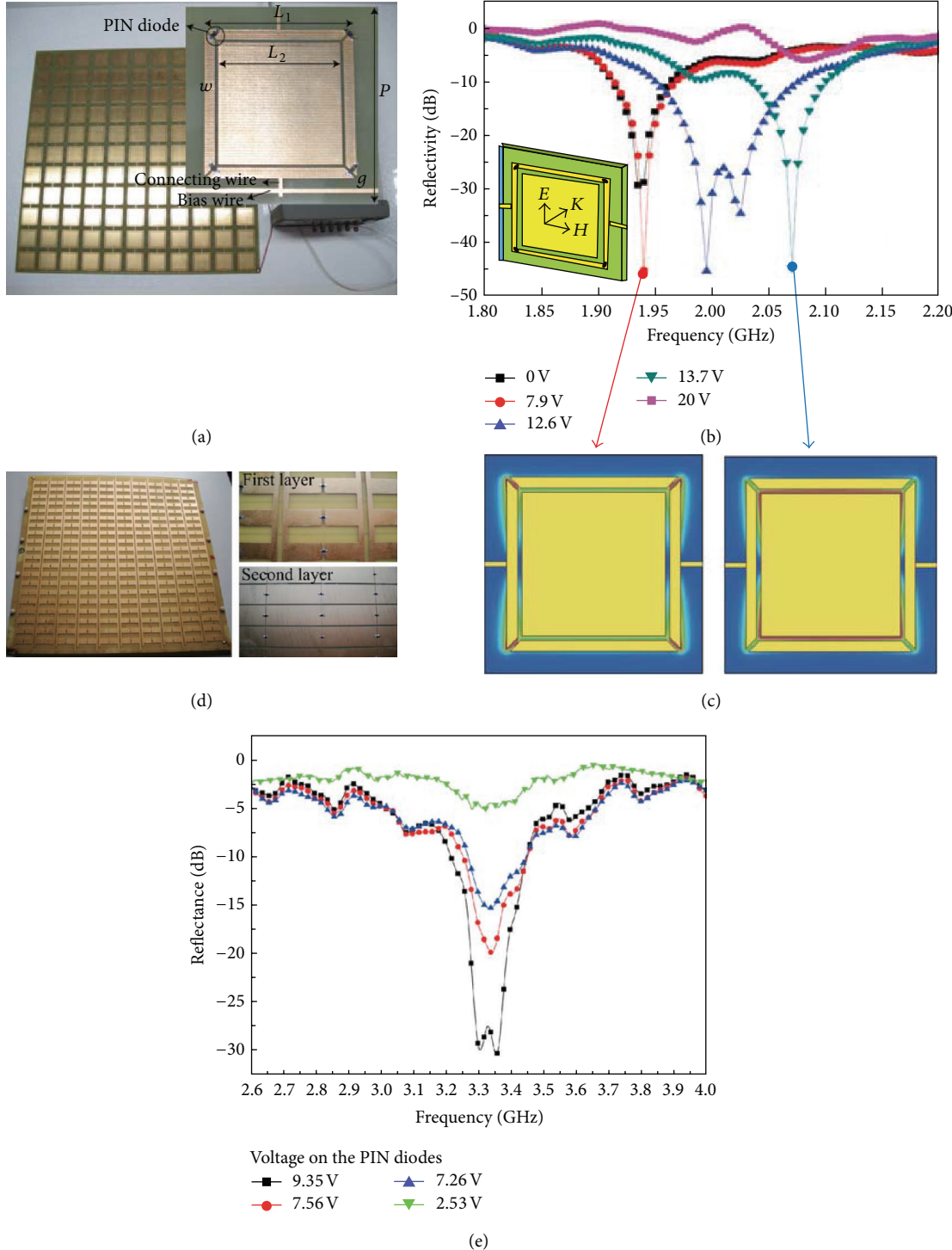


FIGURE 45: (a) Configuration of tunable absorbing material. (b) Measured reflectivity at different bias voltages under incident angle of  $15^\circ$ , and the power loss density at two frequencies is shown in (c). (d) Photograph of the fabricated active absorber; the measured sample has an area of  $340 \times 340 \text{ mm}^2$ , consisting of 200 units. Varactor and pin diodes are assembled through hand-soldering techniques. (e) Measured reflectance spectra of the active absorber with different bias voltages applied upon PIN diode. Figures are reproduced from [228, 229].

9 to 13 GHz. In a similar way, other circuit elements, such as varactors [226, 227], were introduced to change impedance of the metasurfaces.

In 2012, an electrical tunable L-band absorbing material for two polarization types was presented by Wang et al. [228].

As shown in Figures 45(a)–45(c), the proposed absorber consisted of a metal resonator and four surrounding metal lines which were connected by pin diodes and exhibited the tunable range of reflectivity reaching  $-40 \text{ dB}$  for both polarization types. Later [227], Zhao et al. demonstrated a tunable

absorber with a measured bandwidth of 1.5 GHz (or relative bandwidth of 30%). Since the units are placed along two orthogonal directions, the absorber is insensitive to the polarization of incident waves.

In principle, an active absorber should have the ability of controlling echo characteristics in both aspects of frequency and intensity. However, few active absorbers simultaneously considered the two issues in a single device. As an attempt to accomplish this purpose, Wu et al. demonstrated an electrically active absorber in which the working frequency and absorbing intensity could be separately controlled by the PIN and varactor diodes [229]. The structures and measured results are presented in Figures 45(d) and 45(e). Compared with those metasurfaces proposed before, although at the expense of increased complexity, the interesting characteristic of the absorber designed here is that it contains a special designed active magnetic resonator in which both the resonant frequency and amplitude can be, respectively, tuned and therefore shows separable modulation of absorbing frequency and peak intensity. Both simulation and experimental results revealed that the active absorber simultaneously contains such two working models. Further theoretical analysis based on LC theory also confirmed this dual ability.

Along with the increase of working frequency, sealed semiconductor devices become unsuitable due to the limited frequency response. In millimeter wave and terahertz, absorption behaviors can be tuned by modulating the relative position of cells on the top layer [230]. In 2013, Shrekenhamer et al. presented an active absorber in the terahertz regime [231]. By incorporation of liquid crystal into strategic locations within the unit cell, they were able to modify the absorption by 30% at 2.62 THz and also tune the resonant absorption over 4% in bandwidth. Other tunable metasurface absorbers adopted materials, such as vanadium oxide [232] and semiconductors [233].

Recently, we constructed self-tuning metasurface absorbers with capability of self-adaptively tracing and absorbing the incident wave with relatively narrow bandwidth. As depicted in Figure 46, the operational principle includes two main steps. Firstly, the central frequency of the incident wave was detected by a detection circuit. Secondly, a voltage bias is added to the active metasurface to achieve high efficient absorption of the incident wave. The experimental results show that the echo attenuation within the frequency region of 2.8~3.2 GHz is all larger than 10 dB; for some frequency it even reaches 35 dB.

**3.9. Flexible and Stretchable Metasurfaces.** One advantage of metasurfaces over traditional 3D materials is its flexibility which is stemming from the ultrathin thickness. Flexible metasurfaces also provide a route to actively tune the performances. In traditional active metasurfaces, the electromagnetic response can be dynamically manipulated by tuning the constitutive parameters of the related optical materials. However, the mechanical properties, such as shape and geometrical size of these metasurfaces, are invariable during the tuning process. Even for MEMS-based metasurface, the macroscopic geometry is not changed in practical operation.

In recent years, the concept of flexible and stretchable metasurfaces has accepted particular attention, as inspired by the development of flexible electronic devices. For these metasurfaces, the key properties are determined by the substrate. For most metasurfaces except for some free-standing structures, the substrate not only provides a mechanical support for the metallic or dielectric structures but also offers an additional degree of freedom for the design of metasurface. Up to date, the most commonly used flexible substrates for metasurfaces are polydimethylsiloxane (PDMS), polyimide, metaflex, polyethylene naphthalene (PEN) [234–236], polyethylene terephthalate (PET), polymethylmethacrylate (PMMA), and polystyrene [237].

One particular application of flexible metasurface is the conformal devices such as conformal antennas, conformal lenses, and conformal absorbers [238–240]. For nonplanar metasurface absorbers, different areas experience different incident angles. As a result, the large-angle stability is required. Fortunately, it was found that metasurface absorber can have good absorption for large incidence angle by proper design [241]. As a result, conformal absorbers may maintain its absorption. However, earlier designs of metasurface absorbers suffer from the strong polarization dependence [36]. In 2011, we designed and fabricated a polarization-independent wide-angle absorber, following the design principle we established [37]. As shown in Figure 47(a), the absorption does not change dramatically when the metasurface is bent as a cylinder.

In 2013, a conformal absorber was designed by utilizing nonuniform metasurface [239]. The authors designed three different unit cells, which are optimized at 0°, 30°, and 45° incident angles, respectively. As illustrated in Figure 47(b), the proposed concept was demonstrated by EM simulation and experiments. The RCS reduction with nonuniform unit cells was compared with that of the conventional planar metamaterial absorber with uniform unit cells and superior results were demonstrated.

Regarding the wavefront engineering device (Figure 48), Aieta et al. designed a conformal metasurface lens to eliminate the off-axis aberration [240]. It was found that aberration-free focusing is possible under axial illumination but off-axis aberrations appear when the excitation is not normal to the interface. An alternative design for an aplanatic metasurface on a curved substrate was proposed to focus light without coma and spherical aberrations.

The flexible property of PDMS has direct applications in other optical systems. For example, when a metallic grating was fabricated on PDMS, the period could be changed dynamically by stretching the substrate. As illustrated in Figure 49(a), the fabricated metasurface in our experiment looks orange and green, respectively, when stretched properly. Figure 49(b) shows the diffraction angle versus the overall length of the substrate when illuminated by a laser source at  $\lambda = 405$  nm. The diffraction angle can be dynamically steered between 70 and 46 degrees.

In a similar way, Shen et al. proposed a color generation mechanism that produces colors by the Fano resonance effect on thin PMMA metasurface. The metasurface consists of a periodic array of cylinder of nanorods and the resonant

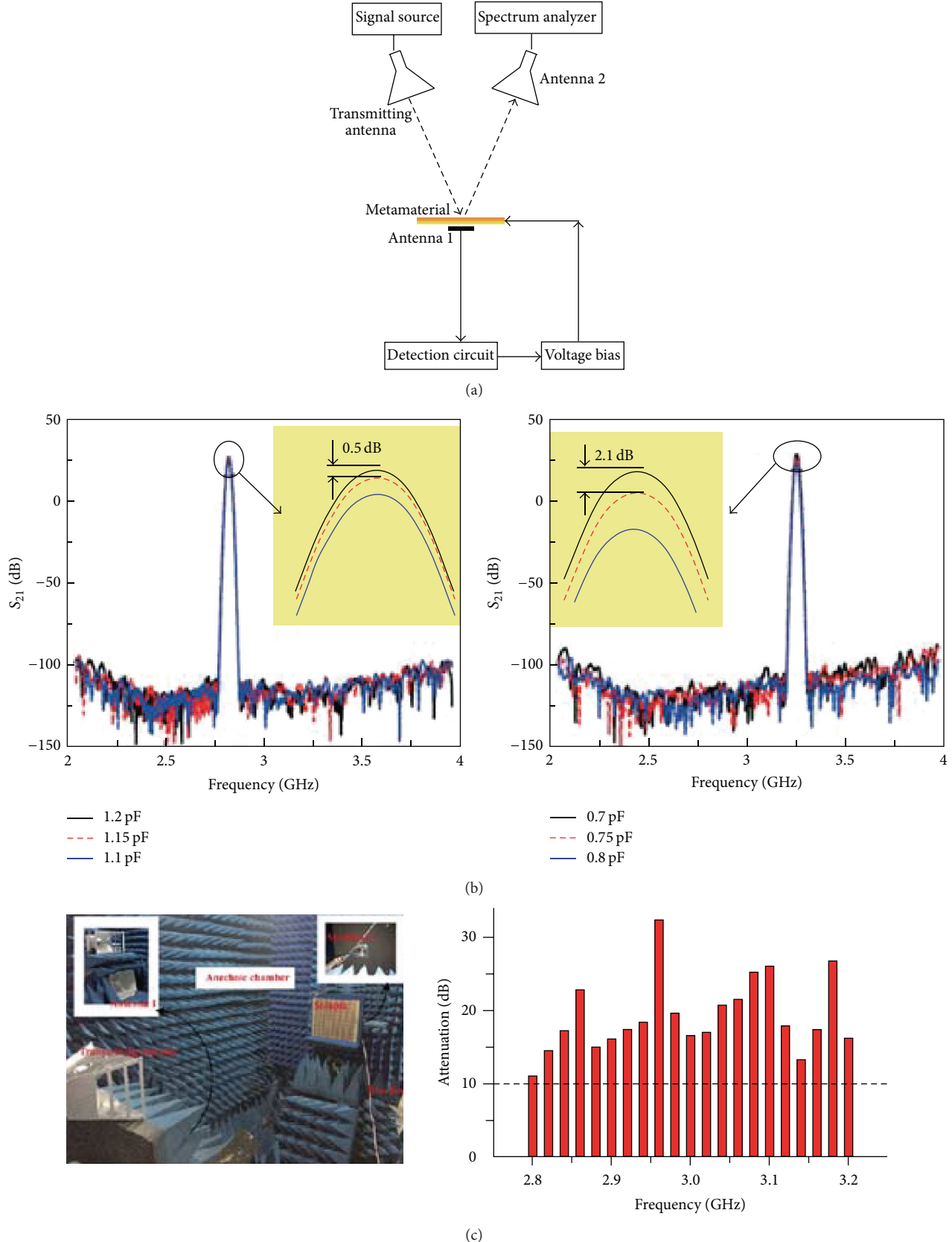


FIGURE 46: Self-tuning smart absorber. (a) Schematic of the operational principle. (b) Transmission coefficient of the absorber for a narrow incident wave for various capacitances at 2.75 GHz (left panel) and 3.25 GHz (right panel). (c) Experimental setup (left panel) and measured attenuation of the reflection wave when the incident wave is swept from 2.8 to 3.2 GHz (right panel).

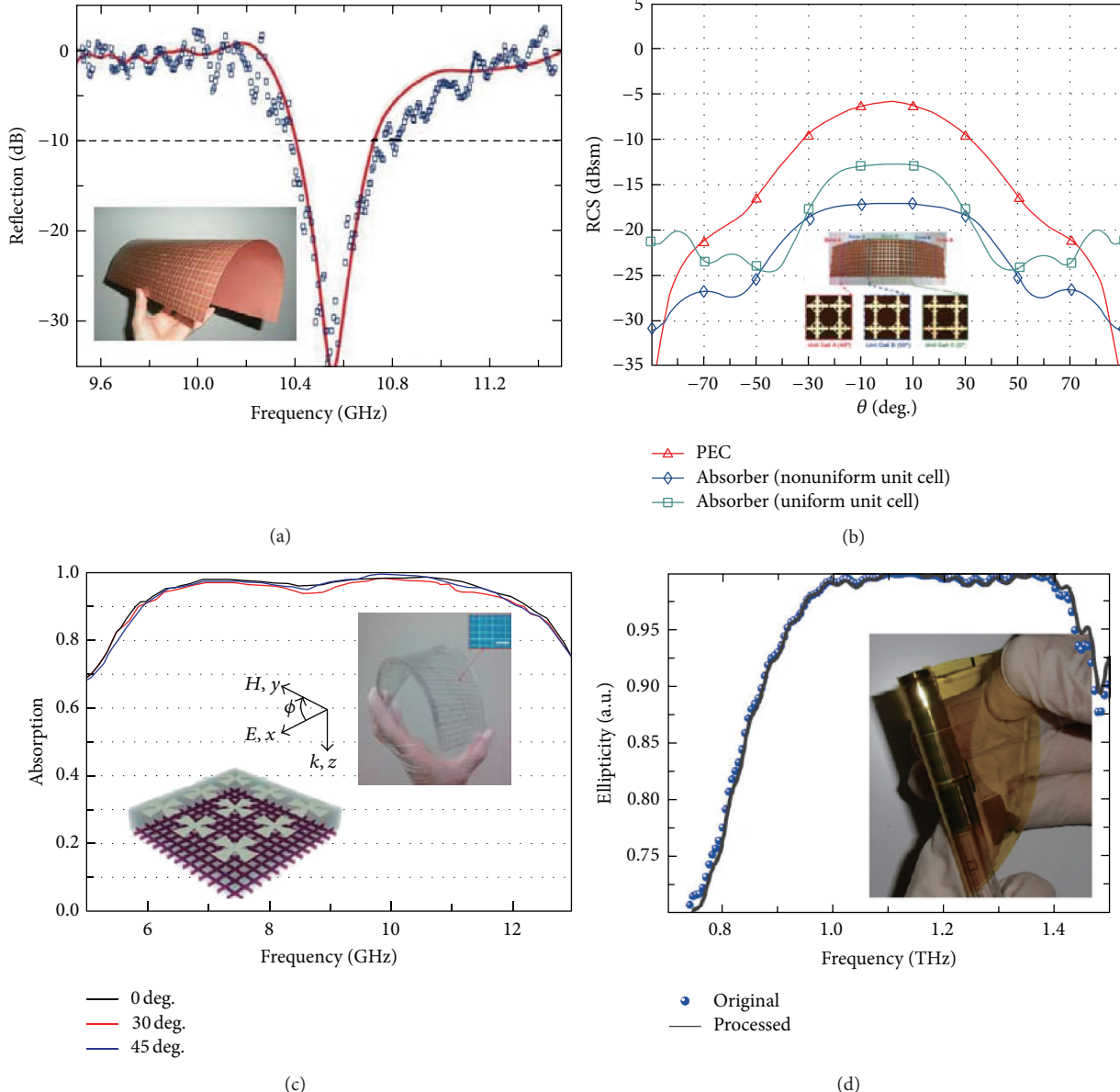


FIGURE 47: (a) Experimental results for a flexible metasurface absorber. (b) RCS reduction properties of nonuniform conformal metasurfaces. (c) Absorption of flexible absorbers fabricated on a PDMS substrate. (d) Elasticity of a flexible terahertz wave plate fabricated on polyimide. Figures are reproduced from (b)–(d) [239, 242, 243].

frequency was tuned from 400 to 600 nm, as shown in Figures 49(c) and 49(d).

**3.10. Graphene Metasurfaces.** Current metasurfaces are often limited to dielectric and metallic structured thin film. In recent years, graphene has attracted special attention owing to its exotic electronic and optical properties. Not surprisingly, graphene has been widely utilized as one kind of metasurfaces or as a key component of functional metasurfaces.

Graphene is  $sp^2$ -hybridized monolayer of carbon atoms densely packed into a honeycomb lattice, which was firstly experimentally isolated from graphite in the lab in 2003 [247]. In 2004, Geim et al. demonstrated that the carrier density in the graphene sheet can be controlled by a gate voltage,

paving the way of graphene-based electronic devices. Subsequently, after the magnetic field response of graphene was validated, the studies on graphene's electrooptics magnetooptics features increased dramatically. Moreover, the approach of growing large-scale pattern graphene film makes the practical applications of such devices possible.

Indeed, the unique structural element of graphene gives rise to many excellent electromagnetic properties, permitting various important applications. For example, a single sheet of homogeneous graphene was found to be able to absorb only a little (~2.3%) fraction of incident white light at Dirac point, making it possible to be used as transparent conducting electrodes [248]. Besides, graphene exhibits ultrahigh electron mobility, anomalous quantum Hall effect, ambipolar electric

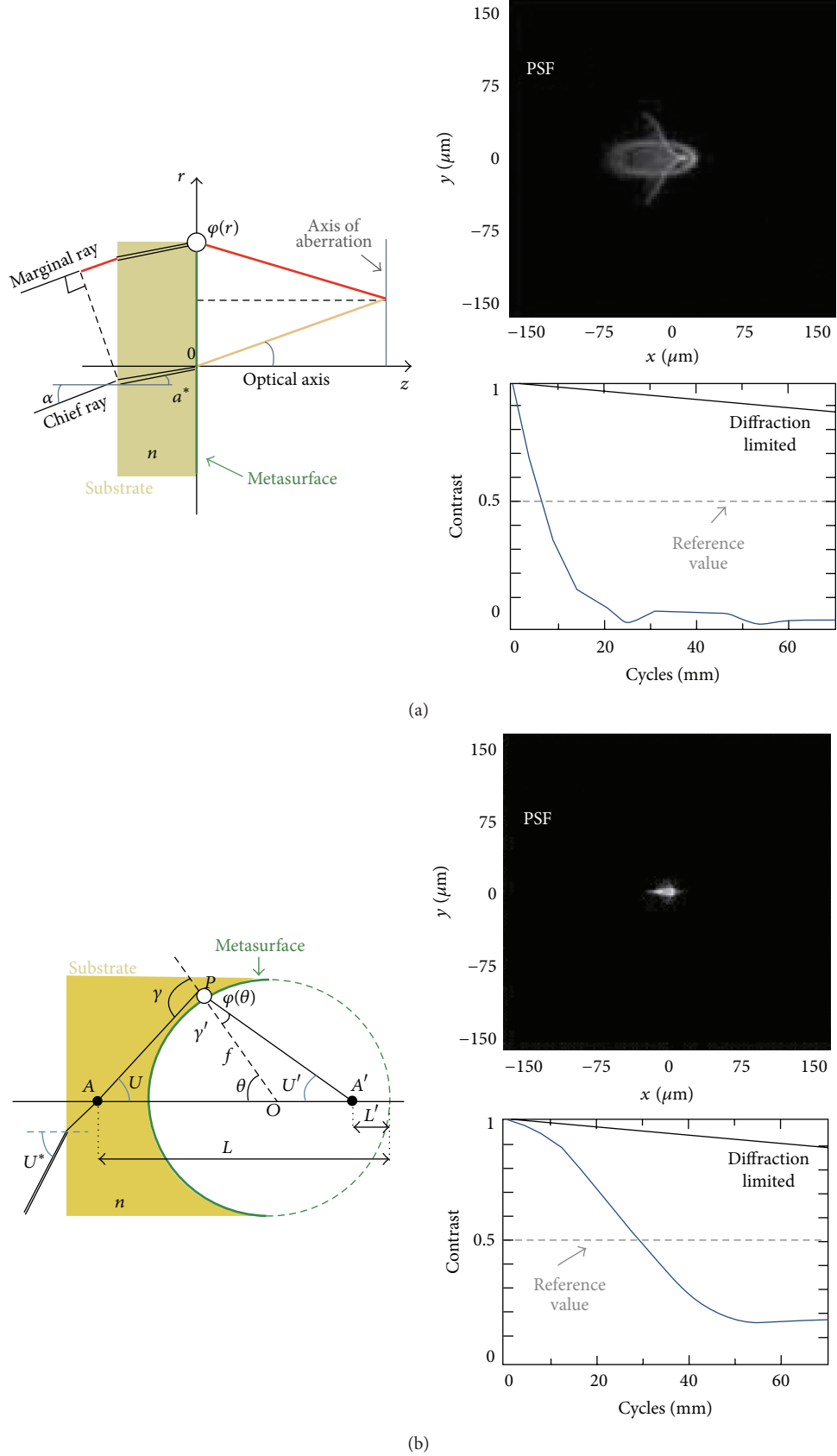


FIGURE 48: (a) Schematic, PSF, and MTF of a flat metasurface lens. (b) Schematic, PSF, and MTF of a conformal metasurface lens. Figures are reproduced from [240].

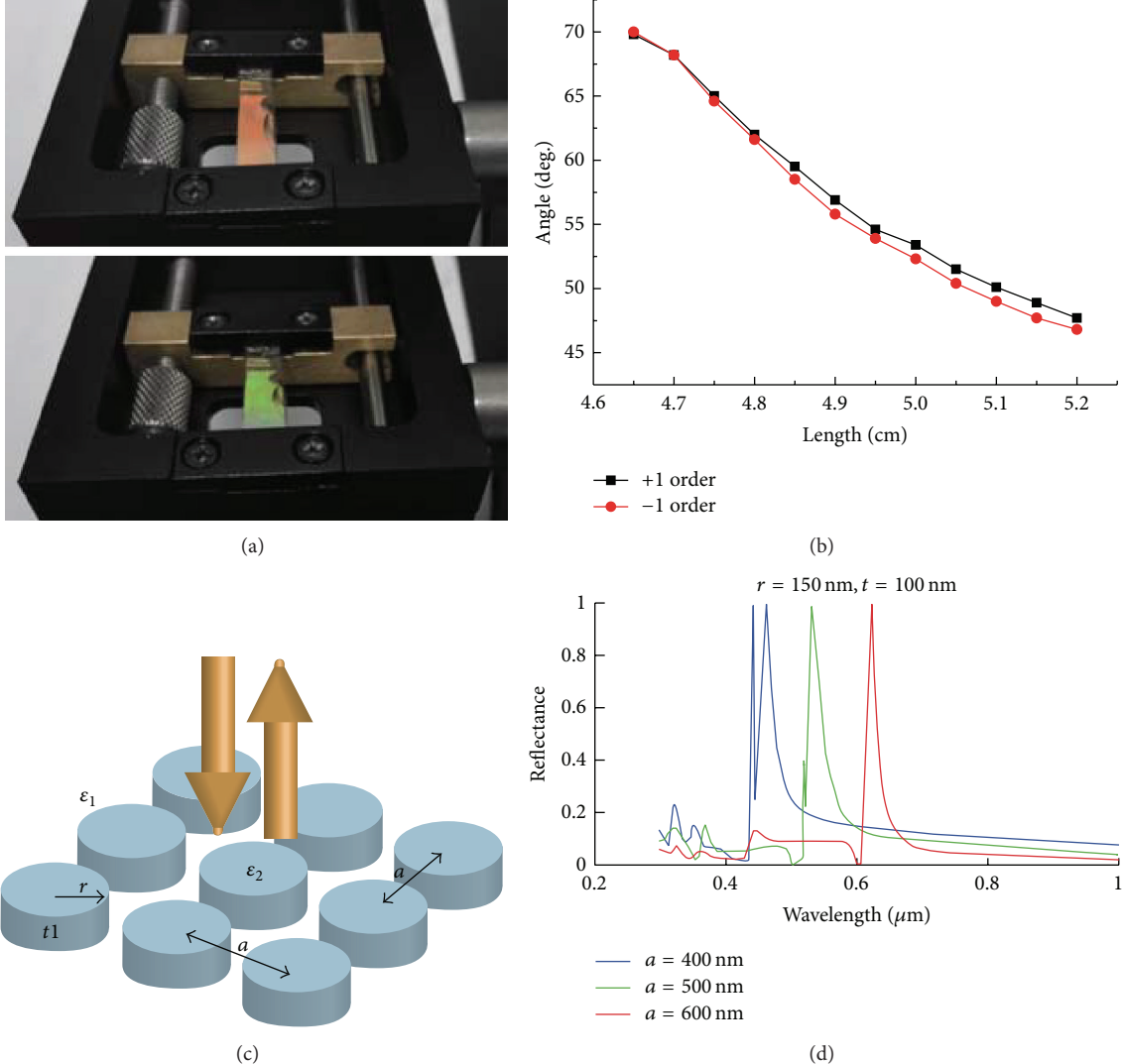


FIGURE 49: (a) Optical images of a flexible metasurface when stretched. (b) Diffract angle of the metasurface grating for different length of the PDMS substrate. (c) Schematic of a flexible color-filtering metasurface. (d) Measured reflectance spectrum when the substrate is uniformly stretched. (c, d) Figures are reproduced from [244].

field effect, massless relativistic carriers, over micrometer-scale spin coherence length, highly confined plasmonic propagation, and large nonlinear Kerr effect. Thanks to these properties, graphene, up to now, has been widely used to fabricate field-effect transistors, electrochemical biosensor, solar cells, super capacitors, lithium ion batteries, catalyst carriers, electromagnetic absorber, and so on [247].

Surface conductivity is usually adopted to describe the electromagnetic characteristic of 2D graphene. If there is no external magnetostatic bias going through the graphene, the local conductivity is isotropic and can be approximately calculated using the Kubo formula on condition that  $K_B T \ll \mu_c, \hbar\omega$  [249]:

$$\sigma_{2D}(\omega)$$

$$\approx \frac{ie^2}{4\pi\hbar} \ln \left[ \frac{2|\mu_c| - (\omega + i2\Gamma)\hbar}{2|\mu_c| + (\omega + i2\Gamma)\hbar} \right]$$

$$+ \frac{ie^2 k_B T}{\pi\hbar^2(\omega + i2\Gamma)} \left[ \frac{\mu_c}{k_B T} + 2 \ln \left( e^{-\mu_c/k_B T} + 1 \right) \right], \quad (44)$$

where  $k_B T$  is the thermal energy,  $\mu_c$  is the chemical potential,  $\Gamma$  is the scattering rate, and  $e$ ,  $k_B$ , and  $\hbar$  are electron charge, Boltzmann constant, and reduced Plank constant (Dirac constant), respectively. Two inequivalent pairs of cones with apex at the Brillouin zone corners constitute graphene's band structure; thus, two kinds of electron transition exist: interband and intraband transition. The first term in (44) is due to the contribution of interband transition and the second term arises for intraband transition. From the equation we know that the chemical potential governs the transition frequency of electrons. Further, if the frequency satisfies the condition

of  $\hbar\omega < 2\mu_c$ , the interband transitions can be neglected and (44) is simplified as Drude formula:

$$\sigma_{GR}(\omega) = \frac{2D}{\pi} \frac{i}{(\omega + i2\Gamma)}, \quad (45)$$

where  $D$  is a Drude weight. Owing to the mapping relation between gate voltage and chemical potential, the two equations are fairly enough to describe the conductivity of gate voltage-biased graphene.

Moreover, if the graphene sheet is present in a perpendicular magnetostatic bias, owing to the cyclotron motion of charge carriers, a nondiagonal component is introduced, namely, Hall conductivity. In low frequency (<10 THz usually), graphene is represented by full tensor conductivity:

$$\sigma_{GR} = \begin{pmatrix} \sigma_{xx} & \sigma_{xy} \\ \sigma_{yx} & \sigma_{yy} \end{pmatrix}, \quad (46)$$

with

$$\begin{aligned} \sigma_{xx}(\omega, B) = \sigma_{yy}(\omega, B) &= \frac{2D}{\pi} \cdot \frac{2\Gamma - i\omega}{\omega_c^2 - (\omega + i2\Gamma)^2}, \\ \sigma_{xy}(\omega, B) = -\sigma_{yx}(\omega, B) &= -\frac{2D}{\pi} \cdot \frac{\omega_c}{\omega_c^2 - (\omega + i2\Gamma)^2}, \end{aligned} \quad (47)$$

where  $\omega_c = eBv_f^2/\mu_c$  is the cyclotron frequency,  $B$  is the amplitude of magnetostatic bias, and  $v_f$  is the Fermi velocity of the Dirac fermions in graphene. Thus, the conductivities for the RCP light and the LCP light can be derived as  $\sigma_{\pm} = \sigma_{xx} \pm i\sigma_{xy}$ , where sign “+” stands for RCP light and “-” stands for LCP light.

More efforts have been devoted to the investigation of graphene in recent years [250]. Some works were focused on enhancing the Faraday rotation angle in the microwave, THz, and infrared region. Meanwhile, graphene as a component of ultrathin electromagnetic absorber has drawn great attention. It is reported that the monolayer graphene is an effective saturable absorber for mode-locking fiber lasers. As illustrated in Figures 50(a) and 50(b), it was demonstrated that complete optical absorption can take place in a single patterned sheet of doped graphene [251]. One interesting phenomenon shows that monolayer graphene shows highly directive comb-like thermal radiation at near-infrared frequency [249]. With the layer number increases, the radiation angle and beamwidth would be changed, as shown in Figures 50(c) and 50(d).

To increase the freedom degree of design, subwavelength structures have been proposed to change of electromagnetic response of graphene. Consequently, the effective conductivity of patterned graphene was investigated. In 2012, effective impedance for a patch patterned graphene sheet was proposed. It can be considered as a combination of two parts: impedance of unpatterned graphene produced by a scaling factor and capacitance caused by the gaps. The accuracy of the proposed impedance is debatable, because the capacitance is originated from the electronic motion which is relative to the magnetic responsible conductivity of graphene. In 2014, we [252] presented an approach for calculating the effective impedance for a hole-patterned graphene sheet based on

equivalent surface RLC impedance model. The impedance caused by periodic hole was obviously relative to the magnetostatic bias. Utilizing the model, authors well explained the magnetic circular dichroism of the hole-patterned graphene absorber in a varying bias within 0~7 Tesla.

Graphene can also be utilized in plasmonic metasurface to increase the performance of traditional plasmonic devices. It is well known that traditional plasmonic materials do not work well in the infrared band, owing to the significant loss. In 2011, Engheta's theoretical study showed that one can engineer the patch of surface wave on graphene by varying the chemical potential, making it a new platform of transformation optics [54]. Owing to its complex conductivity, graphene supports surface plasmon modes, accompanied with extremely short effective wavelength. Based on the exotic electronic transfer properties, graphene-based plasmonic waveguide devices and even Luneburg lens were constructed (see Figures 51(a) and 51(b)).

Very recently, we demonstrated that spiral surface plasmon could be utilized to transfer orbital angular momentum (OAM) [253]. Graphene-based microtube was demonstrated to be able to accomplish this goal perfectly. When a graphene tube is coated on the dielectric cylinder, the whole structure can also steadily support the steady propagation of light carrying OAM with different topological charges, as shown in Figures 51(c)–51(g). Furthermore, as the effective wavelength of the SPP induced in the graphene is much shorter than that in vacuum, the graphene-based microtube is suitable for the propagation of subwavelength of OAM.

**3.11. Nonlinear Metasurfaces.** Metasurfaces can also be utilized to enhance the nonlinear effect [254]. Different from other broadband applications, the nonlinear process requires strong increase of the local fields, which is only obtainable for resonant metasurface. One of the most important applications of nonlinear metasurface is the harmonic generation, such as second harmonic generation (SHG) and third harmonic generation (THG).

One way to enhance SHG is to engineer the metasurface so that they resonate at both the fundamental frequency (FF) and the harmonic frequency (HF) [255–257]. In 2014, Lee et al. proposed and experimentally realized metasurfaces with a record-high nonlinear response based on the coupling of electromagnetic modes in plasmonic metasurfaces with quantum engineered electronic intersubband transitions in semiconductor heterostructures [258]. It was stated that the obtained susceptibility is many orders of magnitude larger than any second-order nonlinear response in optical metasurfaces measured up to then.

To obtain stronger nonlinear response, it is critical to understand the intrinsic relation between the linear and nonlinear processes. Fortunately, it was also demonstrated that the nonlinear response can also be predicted by using the information of linear response [259].

## 4. Fabrication Techniques of Metasurface

Up to date, there are many fabrication techniques available for the physical realization of metasurface. In microwave

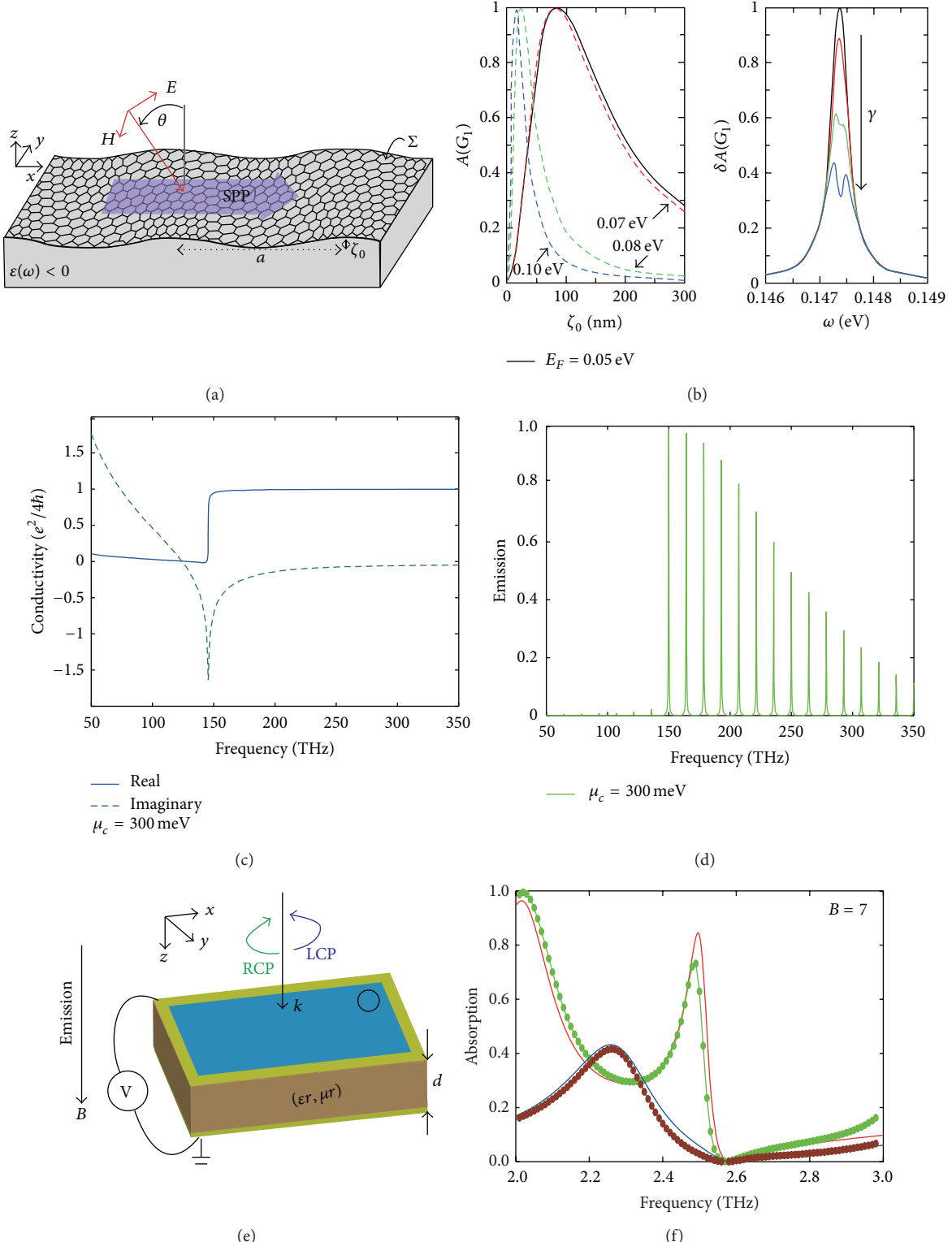


FIGURE 50: (a) Schematic picture showing transverse magnetic light impinging on graphene placed on a periodically structured conducting substrate. The light is converted into surface plasmonic waves and subsequently absorbed in graphene. (b) Dependence of the absorption at resonance on the corrugation height (left panel) for different graphene Fermi energies,  $E_F$ , and relative absorption for a nonzero metamaterial relaxation's rate. (c) Optical conductivity of graphene under electric bias. (d) Thermal emission property of the grapheme layer obtained from Kirchhoff's law. (e) Schematic of the graphene absorber under both electric bias and magnetic bias. (f) Absorption of the dual-biased absorber. Figures are reproduced from [249, 251, 252].

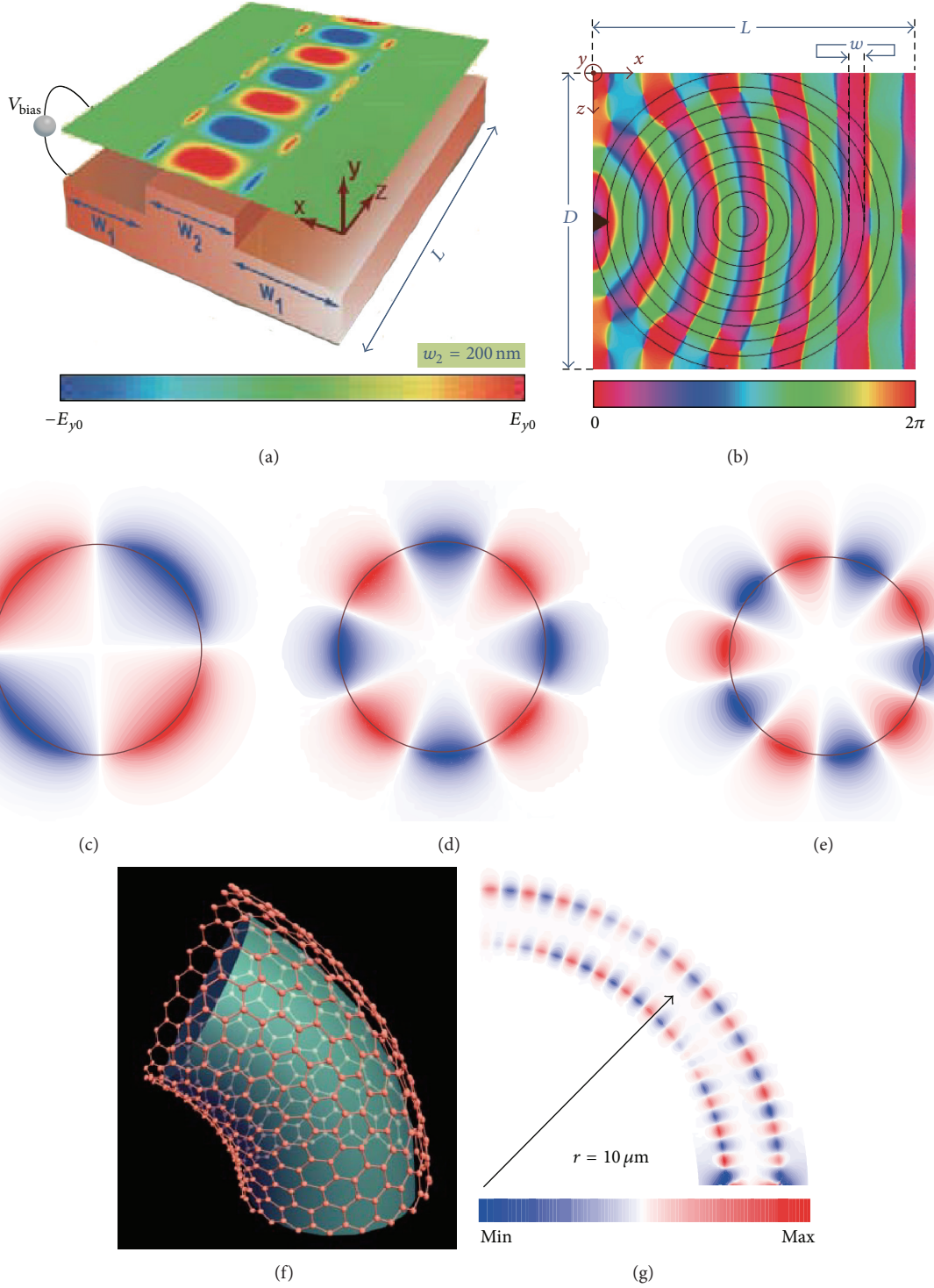


FIGURE 51: (a) Simulation results of  $E_y$  (snapshot in time) for a guided wave at  $f = 30 \text{ THz}$  along the ribbon-like section of graphene. (b) One atom-thick Luneburg lens. (c)–(e) Electric fields for the eigenmodes at a graphene microtube. (f) Schematic of a bent microtube. (g) Simulated electric field distribution on the graphene microtube. (a, b) Figures are reproduced from [54].

frequencies, since the line width of metasurface is larger than ten microns, traditional optical or mechanical approaches could be used, such as printed circuit board (PCB)

technologies based on mechanical milling, chemical etching, and laser ablation. In terahertz to mid-infrared region, the typical feature size of the metasurface structure is around

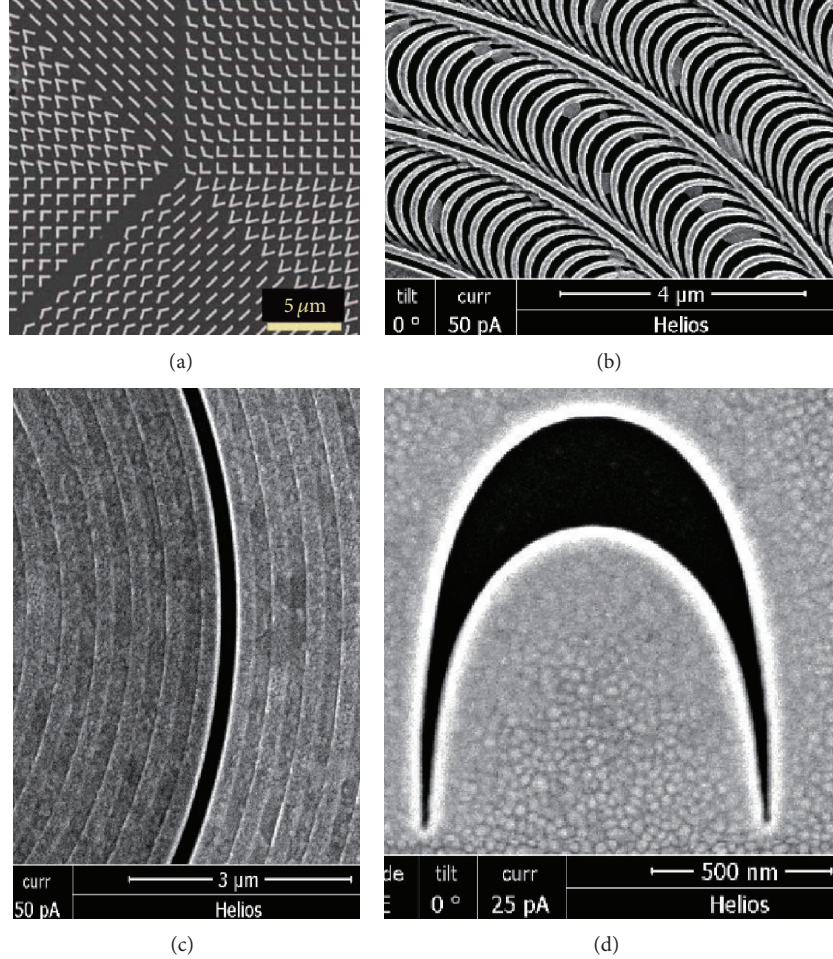


FIGURE 52: Typical fabricated metasurfaces at optical frequencies via EBL and FIB. Figures are reproduced from (a) [134], (b) [172], and (c) and (d) [2].

1~100  $\mu\text{m}$ . Traditional optical lithography and laser direct writing are commonly used for the structure fabrication in this frequency region.

However, when the working frequency range goes into the near-infrared and visible spectra, the fine features of metasurfaces generally could not be realized by traditional mechanical or optical methods. Instead, electron beam or ion beams are required to accomplish the fabrication goal. Electron beam lithography (EBL) and focused ion beam milling (FIB) are frequently adopted to make the related structures working in this wavelength range, as shown in Figure 52. Nevertheless, the fabrication processes of both of these techniques are based on the moving of the beam or stage, which makes them of slow speed and high cost, thus limiting their practical applications in metasurfaces fabrication in a certain extent.

Recently, some novel techniques are proposed in the fabrications of specific design of metasurfaces. Interference lithography is a very useful strategy in the fabrication of regular periodic patterns, such as grating and dot array. Periodic structures with feature size of hundred nanometers are easily realized by using UV laser. In order to further shrink the

fabrication size of interference lithography, surface plasmon interference technique was developed. Subdiffraction limit patterns were obtained by employing the interference effect of SPPs [31, 260, 261]. The surface plasmon interference technique is considered to be the most promising plasmonic lithography technique for fabricating large-area simple periodic structures. However, it is difficult to generate complex and nonperiodic structures due to the limited propagating space for evanescent waves. More recently, reflective plasmonic slab or SPP cavity was proposed to improve the aspect profile and contrast of imaging pattern [32, 132], with experimentally reported 22 nm line width. As shown in Figures 53(a) and 53(b), it was shown that surface plasmon could be utilized to achieve line width of 50 nm. Very recently, hyperbolic metasurfaces composed of  $\text{SiO}_2/\text{Al}$  films are explored to squeeze out bulk plasmon polaritons (BPPs) to produce large-area and uniform deep subwavelength interference patterns. As examples, two and four bulk plasmon polaritons (BPPs) interference lithography with a half pitch of 45 nm ( $\sim\lambda/8$ ) were demonstrated in experiments. Much deeper resolution up to 22.5 nm ( $\sim\lambda/16$ ) and variety of BPPs interference patterns are feasible.

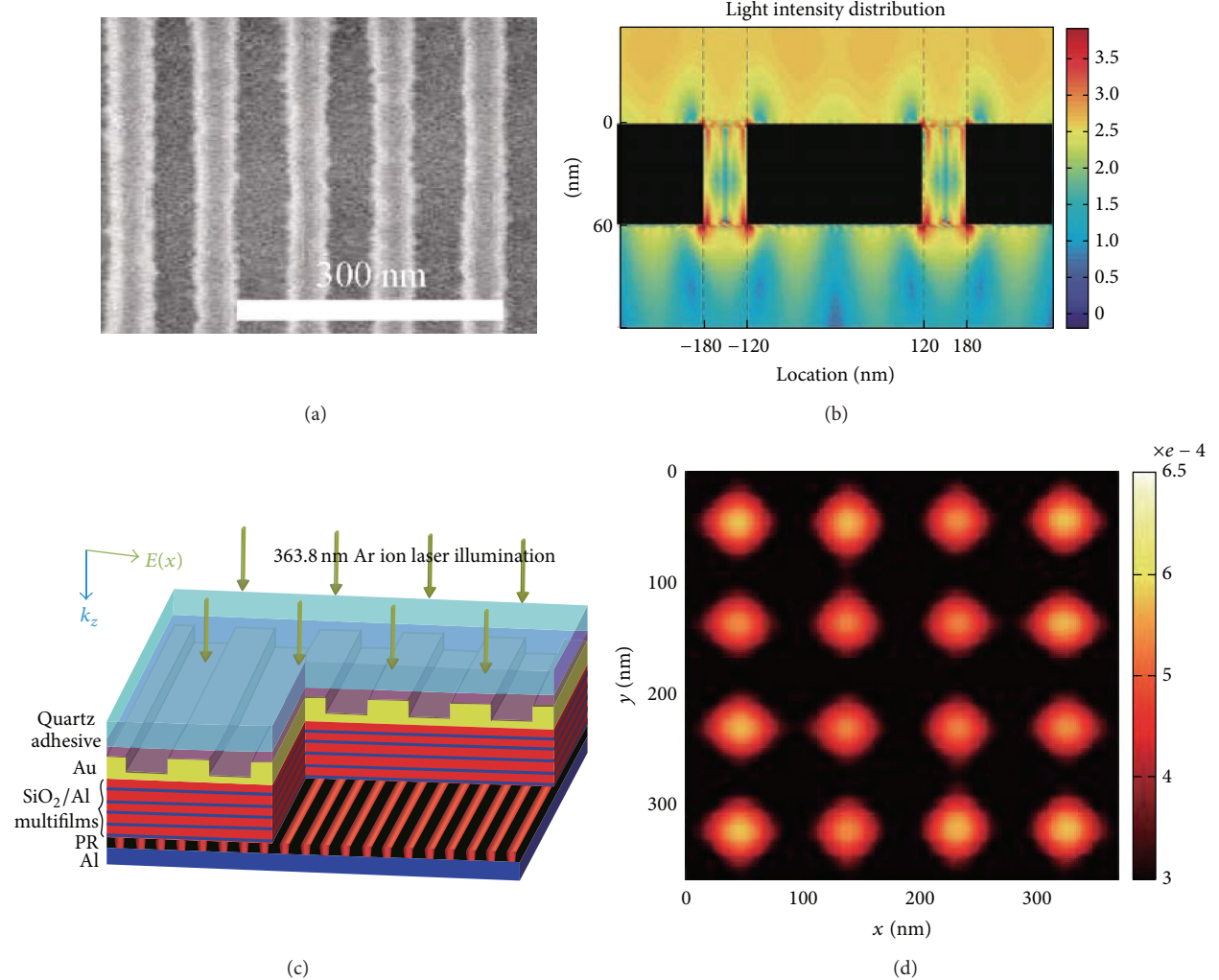


FIGURE 53: Interference lithography by surface plasmon polariton. (a) SEM image of the fabricated sample. (b) Simulated electric field distribution. (c) Schematic of the improved lithography technique. (d) Two-dimensional interference patterns. Figures are reproduced from [31, 260].

With the purpose of achieving high efficient, large-area fabrication of the nanoscale metasurfaces with arbitrary shape, we propose to utilize surface plasmon imaging lithography to transfer the patterns on mask. As shown in Figures 54(a) and 54(b), a Babinet-inverted plasmonic gradient metlens was fabricated. The metlens consists of anisotropic nanohole arrays with parabolic phase distributions. The size of approximate elliptic nanohole is  $75 \text{ nm} \times 140 \text{ nm}$ . We characterized the focusing property of metlens at visible light with wavelengths of 633 nm and 532 nm. The results of simulations show good agreement with the measured results. The results of experiment demonstrate that surface plasmonic lithography not only offers the ability of transfer pattern with nanoscale resolution but also could be applied in the fabrication of planar metasurface devices.

Nanosphere lithography (NSL) is another promising technology in fabrication of metasurface with nanoscale feature size. The NSL was primely developed in the 1995, which was also referred to colloidal lithography. When NSL

was just invented, only simple periodic nanoparticles could be produced. In recent years, the power of NSL was improved greatly. As shown in Figures 54(c) and 54(d), Nemirovski et al. showed that the parameter space of shadow-derived shapes could enable a substantial expansion of the power of NSL [262]. They used custom-designed software to engineer compositions of shadows that guide multiangled deposition of one or multiple materials through a plasma-etched monolayer colloidal crystal (MCC). Meanwhile, Zhao et al. demonstrated multiple repetitions of hole-mask colloidal nanolithography to create single-layer metasurfaces with complex, multishape plasmonic nanostructures that exhibit desired optical functionalities [263]. This fabrication method is particularly suited for the creation of large-area, single-layer C3-rotationally symmetric, 3D chiral metasurfaces. It should be noted that a similar glancing angle deposition technique with shadowing effect is able to produce 3D film structures with fine control on a scale less than 10 nm [264].

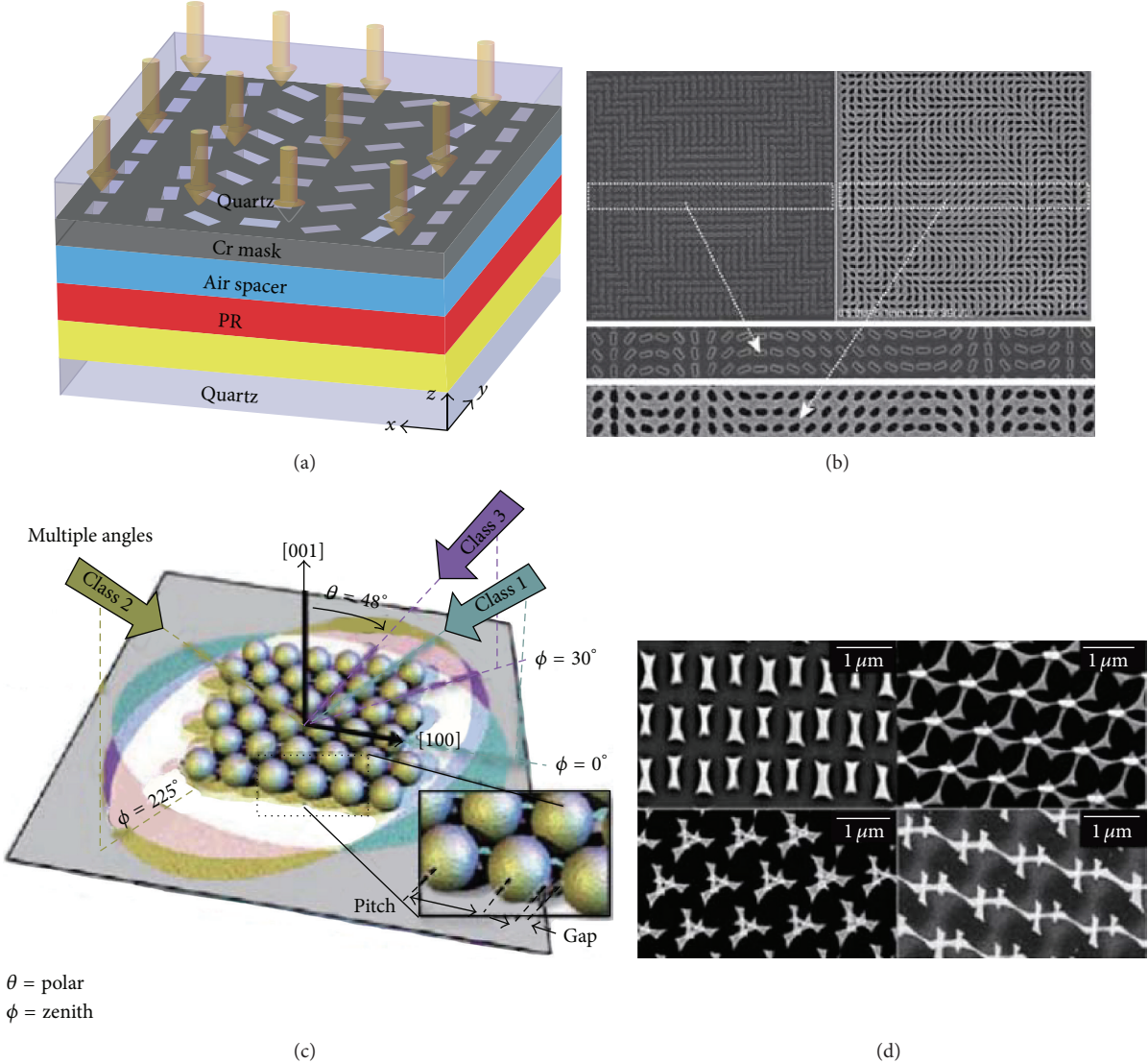


FIGURE 54: Novel fabrication techniques for optical metasurfaces. (a) Schematic of the surface plasmon lithography and simulated intensity distributions for a metasurface lens. (b) SEM images of the mask (left) and fabricated sample (right). (c) Schematic of the multiangled NSL. (d) SEM images of fabricated samples. (c, d) Figures are reproduced from [262].

In addition to the fabrication technologies aforementioned, some other methods are introduced in some special situations. The capacity of nanoimprinting, multiple photons polymerization, microsphere lithography, and so forth [265] are also demonstrated in making the structures of metasurfaces. To overview, one should choose the proper fabrication method based on the corresponding requirement of specific structures which are designed.

## 5. Discussion

**5.1. Unified Bandwidth Limit of Broadband Metasurfaces.** As shown in the above discussion, the metasurfaces have many different applications depending on their constitutive materials and geometry. Nevertheless, all these devices can be

classified as broadband, wideband, and narrowband according to their frequency responses. In this section, we would give a unified theory for the bandwidth limit of these metasurfaces, especially regarding the absorbers and polarizers. For the simplification of the discussion, we would like to consider only the narrowband and broadband cases.

The typical case of narrowband application is the Fano resonance. One of the most important aspects of Fano resonance is the sharp resonance peak accompanied with strong local field enhancement, which is the basis of many applications, such as biological sensing and nonlinear photonics [21]. Unfortunately, ultrahigh Q-factor is difficult to be realized for two-dimensional metasurfaces due to the lack of large volume confinement of electromagnetic fields and strong coupling to free space [20]. Recently, we showed that there is fundamentally no limit for the bandwidth when no absorption loss is

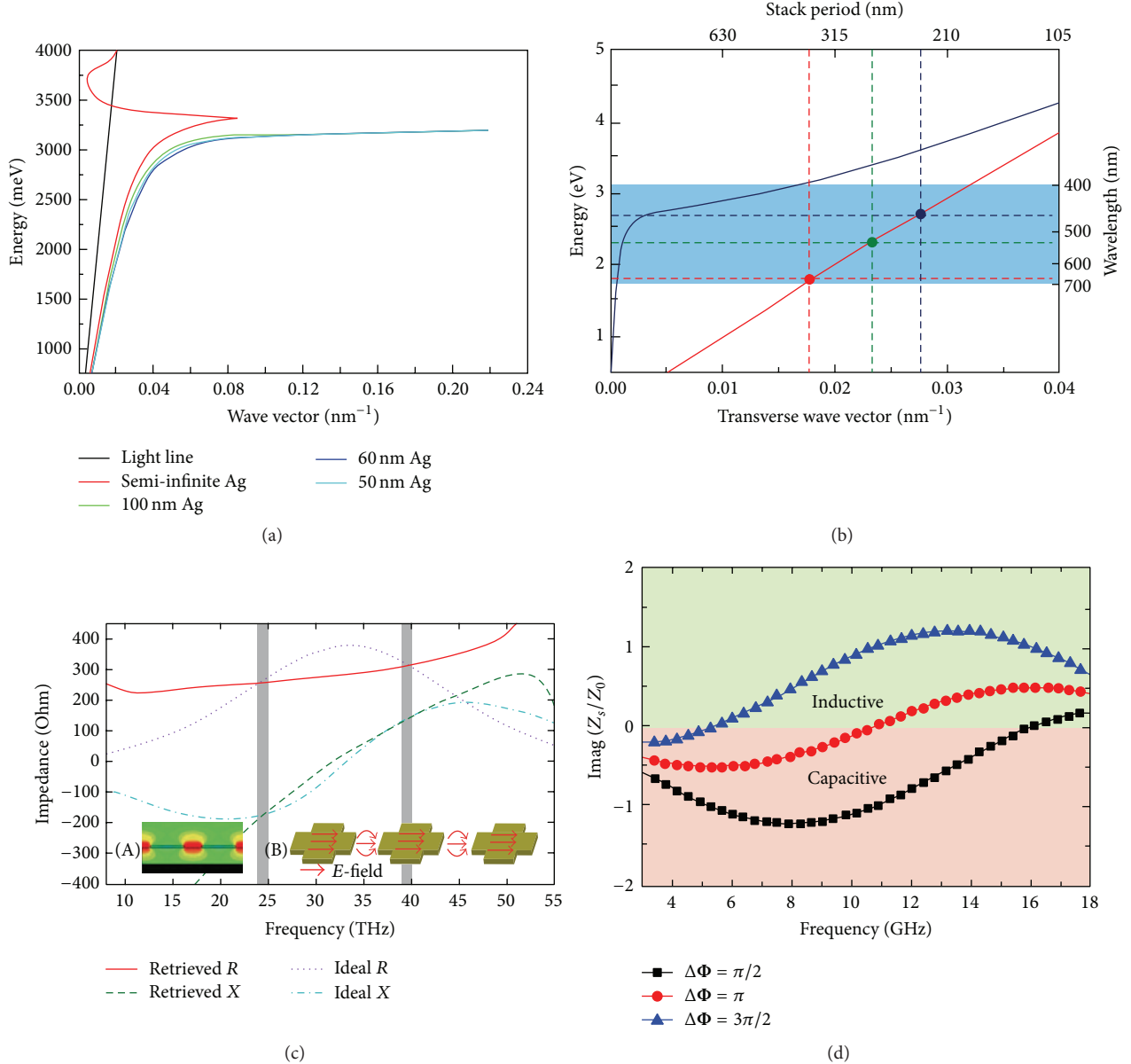


FIGURE 55: (a) Dispersion of an ultrathin metallic film with ultrasmall effective wavelength. (b) Dispersion of a metasurface consisting of metal-insulator-metal (MIM) structure, which acts as a high efficient color filter. (c) Lorentz dispersion for broadband metasurface absorber. (d) Lorentz-type dispersion for broadband polarization control. Figures are reproduced from (a) [55], (b) [17], (c) [114], and (d) [81].

considered and the metasurface is infinite in the horizontal plane [19]. However, a further study is needed to show the limit for the finite metasurface.

For broadband and multiband applications, the dispersion of metasurfaces can be exploited. As illustrated in Figure 55, it is shown that the dispersion of metasurface can enable superresolution imaging beyond the diffraction limit, high performance color filter, broadband absorbers, and polarizers.

Most importantly, the results on coherent perfect absorber and coherent perfect rotation have shown that there is also no bandwidth limit for these applications [38, 76]. However, for noncoherent absorbers and polarizers,

the classic limits are still applicable [100, 266], if we do not consider the case of non-Foster and active devices [267]. It is important to note that the bandwidth limits for the absorbers and polarizers have the same origin, and both of them can be deduced from the concept of artificial magnetic conductor (AMC). For AMC, there is a fundamental limit on the bandwidth [266]

$$h \geq \frac{\lambda_{\max} - \lambda_{\min}}{\pi^2} \ln \left( \frac{2}{\Delta\phi} \right), \quad (48)$$

where  $\Delta\phi$  is the reflective phase shift, which should be 0 for perfect magnetic conductor and  $\pi$  for perfect electric conductor.

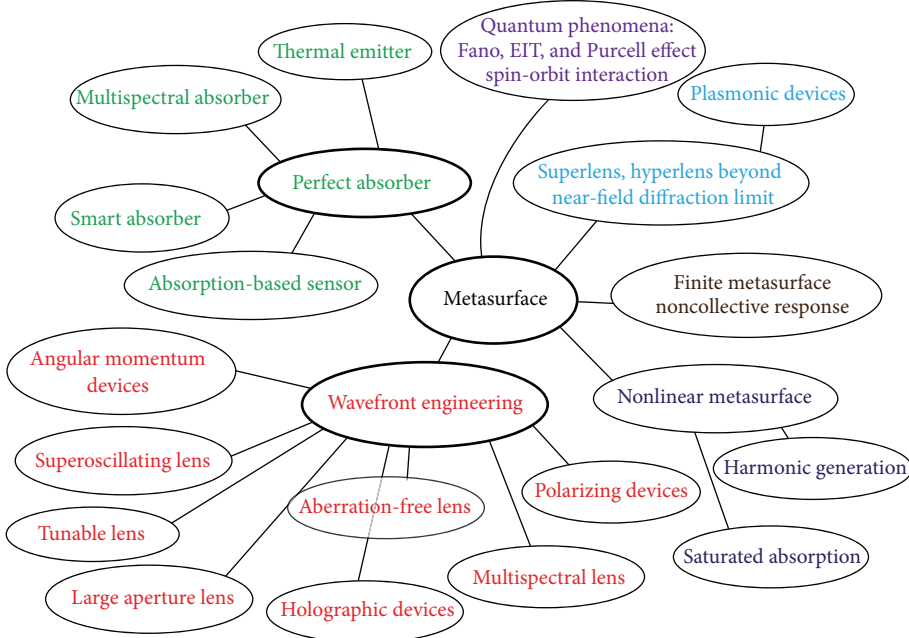


FIGURE 56: Outlook of the future trends of metasurface and metadevices. Figures are reproduced from [2].

For perfect absorber comprised of a resistive sheet on a lossless AMC, the relation between the absorption and phase shift can be written as

$$r = \frac{\exp(i\Delta\phi) - 1}{\exp(i\Delta\phi) + 3}. \quad (49)$$

The 10 dB and 20 dB copolarized reflection coincides with  $\Delta\phi = 1.176$  and  $0.4$ . The thickness limit can be written as  $0.054\Delta\lambda$  and  $0.163\Delta\lambda$ . From Rozanov's theory, this limit should be written as

$$h \geq \frac{(\lambda_{\max} - \lambda_{\min})\Gamma}{172}, \quad (50)$$

where  $\Gamma$  is the reflectance in dB. For 10 dB and 20 dB reflectance, the thickness limits are  $0.058\Delta\lambda$  and  $0.116\Delta\lambda$ , agreeing well with the above results. As shown in Table 1, the thickness ratios of all the current available absorbers except the thin film CPA are smaller than the ideal case.

For perfect reflective half-wave plate, the copolarized reflection can be written as

$$r = \frac{1 - \exp(i\Delta\phi)}{2}. \quad (51)$$

The 10 dB and 20 dB copolarized reflection coincides with  $\Delta\phi = 0.6435$  and  $0.2$ . The thickness limit can be written as  $0.115\Delta\lambda$  and  $0.233\Delta\lambda$ . In this regard, our recent results have given an approach to overcome this limitation [81, 82].

In addition, we would like to comment that the thickness-bandwidth limitation of perfect absorbers can also be extended to the broadband antireflection coatings. Considering light passing from a medium with high refractive index  $\epsilon$  to air, the energy can be nearly perfectly absorbed if a resistive

layer with frequency-independent resistance  $R$  is added at the boundary [39]. As a result, the maximum thickness for the antireflection coating is that of the perfect absorbers.

**5.2. Future Trends of Metasurfaces.** In summary, the area of metasurfaces has become a cutting-edge and promising researching direction in recent years, although long histories can be found in almost any of their branches. In general, there is an obvious trend to extend the researching frequency regime from microwave to optical regime or the new emerging terahertz region. One may wonder that the extension of frequency range is straightforward and thus not so physically meaningful. However, we must note that the materials properties would change dramatically at different frequencies. The fabrication techniques and measurement equipment will also vary. At optical frequencies, even quantum phenomena would play an important role [21].

As illustrated in Figure 56, in the next few years, the researches in metasurfaces will be focused on the aspects including but not limited to [2] the following.

**Functional Metasurfaces with Better Performances.** For example, current flat lenses suffered from the strong chromatic dispersion. Although these devices are thin, lightweight, and capable of working at a wide range of frequencies, the focus lengths would vary as the change of operational wavelength. Recently, some works have been devoted to solving this problem, but the performance is still far from perfect [268]. Another drawback of these metasurfaces is that efficiencies are typically very low, especially for the devices based on geometric phase [134, 193]. As a result, much work should be paid to enhance the efficiency [204].

TABLE 1: Overview of the bandwidth limit for metasurface-based absorbers.

| Journal and time                          | Thickness          | $\Delta\lambda$ (20 dB) | Ratio (limit: 0.163) |
|---|--------------------|-------------------------|----------------------|
| IEEE Trans. Antennas Propagat. 2011 [110] | 14.5 mm            | 83.4 mm                 | 0.174                |
| Opt. Express, 2011 [245]                  | 4.5 mm             | 25.7 mm                 | 0.175                |
| Opt. Lett., 2012 [114]                    | 1.5 $\mu\text{m}$  | 8.72 $\mu\text{m}$      | 0.172                |
| Opt. Express, 2012 [38]                   | 0.3 nm             | $\infty$                | 0                    |
| Appl. Phys. Lett., 2012 [102]             | 5 mm               | 13.86 mm                | 0.36                 |
| ACS Nano, 2014 [105]                      | 0.86 $\mu\text{m}$ | 3.57 $\mu\text{m}$      | 0.24                 |
| Phys. Rev. Lett., 2013 [246]              | 40 mm              | 80.2 mm                 | 0.498                |

*Fabrication Technologies for Large-Area Metasurfaces.* One of the huge challenges for the successful application of metasurfaces is how to fabricate these metasurfaces fast and low-costly. With these fabrication techniques [269], a bright future of metasurfaces and metasurface-based devices can be envisioned.

## Conflict of Interests

The authors declare that there is no conflict of interests regarding the publication of this paper.

## Acknowledgments

This work was supported by the 973 Program of China under Grant 2013CBA01700 and by the National Natural Science Funds under Grant 61138002. The authors also thank Z. Y. Zhao, C. T. Wang, C. Huang, C. G. Hu, Y. Q. Wang, and P. Gao for their helpful suggestions.

## References

- [1] N. Yu and F. Capasso, "Flat optics with designer metasurfaces," *Nature Materials*, vol. 13, no. 2, pp. 139–150, 2014.
- [2] X. Luo, "Principles of electromagnetic waves in metasurfaces," *Science China Physics, Mechanics & Astronomy*, vol. 58, no. 9, Article ID 594201, pp. 1–18, 2015.
- [3] J. B. Pendry, D. Schurig, and D. R. Smith, "Controlling electromagnetic fields," *Science*, vol. 312, no. 5781, pp. 1780–1782, 2006.
- [4] J. B. Pendry, "Negative refraction makes a perfect lens," *Physical Review Letters*, vol. 85, no. 18, pp. 3966–3969, 2000.
- [5] N. Meinzer, W. L. Barnes, and I. R. Hooper, "Plasmonic meta-atoms and metasurfaces," *Nature Photonics*, vol. 8, no. 12, pp. 889–898, 2014.
- [6] C. L. Holloway, E. F. Kuester, J. A. Gordon, J. O'Hara, J. Booth, and D. R. Smith, "An overview of the theory and applications of metasurfaces: the two-dimensional equivalents of metamaterials," *IEEE Antennas and Propagation Magazine*, vol. 54, no. 2, pp. 10–35, 2012.
- [7] J. D. Jackson, *Classical Electrodynamics*, Wiley, Hoboken, NJ, USA, 3rd edition, 1999.
- [8] D. Schurig, J. J. Mock, B. J. Justice et al., "Metamaterial electromagnetic cloak at microwave frequencies," *Science*, vol. 314, no. 5801, pp. 977–980, 2006.
- [9] T. Ergin, N. Stenger, P. Brenner, J. B. Pendry, and M. Wegener, "Three-dimensional invisibility cloak at optical wavelengths," *Science*, vol. 328, no. 5976, pp. 337–339, 2010.
- [10] A. V. Kildishev, A. Boltasseva, and V. M. Shalaev, "Planar photonics with metasurfaces," *Science*, vol. 339, no. 6125, Article ID 1232009, 2013.
- [11] R. W. Wood, "On a remarkable case of uneven distribution of light in a diffraction grating spectrum," *Proceedings of the Physical Society of London*, vol. 18, no. 1, article 325, 1901.
- [12] T. Senior, "Approximate boundary conditions," *IEEE Transactions on Antennas and Propagation*, vol. 29, no. 5, pp. 826–829, 1981.
- [13] K. Yao and Y. Liu, "Plasmonic metamaterials," *Nanotechnology Reviews*, vol. 3, no. 2, pp. 177–210, 2014.
- [14] B. A. Munk, *Frequency Selective Surfaces*, Wiley, New York, NY, USA, 2000.
- [15] D. Van Labeke, D. Gérard, B. Guizal, F. I. Baida, and L. Li, "An angle-independent Frequency Selective Surface in the optical range," *Optics Express*, vol. 14, no. 25, pp. 11945–11951, 2006.
- [16] A. H. Abdelrahman, A. Z. Elsherbeni, and F. Yang, "Transmission phase limit of multilayer frequency-selective surfaces for transmitarray designs," *IEEE Transactions on Antennas and Propagation*, vol. 62, no. 2, pp. 690–697, 2014.
- [17] T. Xu, Y.-K. Wu, X. Luo, and L. J. Guo, "Plasmonic nanoresonators for high-resolution colour filtering and spectral imaging," *Nature communications*, vol. 1, p. 59, 2010.
- [18] A. E. Miroshnichenko, S. Flach, and Y. S. Kivshar, "Fano resonances in nanoscale structures," *Reviews of Modern Physics*, vol. 82, no. 3, pp. 2257–2298, 2010.
- [19] M. Pu, C. Hu, C. Huang et al., "Investigation of Fano resonance in planar metamaterial with perturbed periodicity," *Optics Express*, vol. 21, no. 1, pp. 992–1001, 2013.
- [20] V. A. Fedotov, M. Rose, S. L. Prosvirnin, N. Papasimakis, and N. I. Zheludev, "Sharp trapped-mode resonances in planar metamaterials with a broken structural symmetry," *Physical Review Letters*, vol. 99, no. 14, Article ID 147401, 2007.
- [21] B. Luk'yanchuk, N. I. Zheludev, S. A. Maier et al., "The Fano resonance in plasmonic nanostructures and metamaterials," *Nature Materials*, vol. 9, no. 9, pp. 707–715, 2010.
- [22] M. Rahmani, B. Luk'yanchuk, and M. Hong, "Fano resonance in novel plasmonic nanostructures," *Laser and Photonics Reviews*, vol. 7, no. 3, pp. 329–349, 2013.
- [23] M. Rahmani, T. Tahmasebi, Y. Lin, B. Lukiyanchuk, T. Y. F. Liew, and M. H. Hong, "Influence of plasmon destructive interferences on optical properties of gold planar quadrupoles," *Nanotechnology*, vol. 22, no. 24, Article ID 245204, 2011.
- [24] M. Rahmani, B. Lukiyanchuk, B. Ng, K. G. A. Tavakkoli, Y. F. Liew, and M. H. Hong, "Generation of pronounced Fano resonances and tuning of subwavelength spatial light distribution in plasmonic pentamers," *Optics Express*, vol. 19, no. 6, pp. 4949–4956, 2011.

- [25] J. Yang, M. Rahmani, J. H. Teng, and M. H. Hong, "Magnetic-electric interference in metal-dielectric-metal oligomers: generation of magneto-electric fano resonance," *Optical Materials Express*, vol. 2, no. 10, pp. 1407–1415, 2012.
- [26] C. S. Lim, M. H. Hong, Z. C. Chen, N. R. Han, B. Luk'Yanchuk, and T. C. Chong, "Hybrid metamaterial design and fabrication for terahertz resonance response enhancement," *Optics Express*, vol. 18, no. 12, pp. 12421–12429, 2010.
- [27] Z. C. Chen, M. H. Hong, H. Dong et al., "Parallel laser micro-fabrication of terahertz metamaterials and its polarization-dependent transmission property," *Applied Physics A: Materials Science and Processing*, vol. 101, no. 1, pp. 33–36, 2010.
- [28] D. Wang, C. Qiu, and M. Hong, "Coupling effect of spiral-shaped terahertz metamaterials for tunable electromagnetic response," *Applied Physics A: Materials Science and Processing*, vol. 115, no. 1, pp. 25–29, 2014.
- [29] D. Wang, Q. Huang, C. Qiu, and M. Hong, "Selective excitation of resonances in gammadion metamaterials for terahertz wave manipulation," *Science China Physics, Mechanics & Astronomy*, vol. 58, no. 8, Article ID 084201, 2015.
- [30] N. Fang, H. Lee, C. Sun, and X. Zhang, "Sub-diffraction-limited optical imaging with a silver superlens," *Science*, vol. 308, no. 5721, pp. 534–537, 2005.
- [31] X. Luo and T. Ishihara, "Surface plasmon resonant interference nanolithography technique," *Applied Physics Letters*, vol. 84, no. 23, pp. 4780–4782, 2004.
- [32] C. Wang, P. Gao, Z. Zhao et al., "Deep sub-wavelength imaging lithography by a reflective plasmonic slab," *Optics Express*, vol. 21, no. 18, pp. 20683–20691, 2013.
- [33] Z. Liu, H. Lee, Y. Xiong, C. Sun, and X. Zhang, "Far-field optical hyperlens magnifying sub-diffraction-limited objects," *Science*, vol. 315, no. 5819, p. 1686, 2007.
- [34] X. Luo and L. Yan, "Surface plasmon polaritons and its applications," *IEEE Photonics Journal*, vol. 4, no. 2, pp. 590–595, 2012.
- [35] H. Severin, "Nonreflecting absorbers for microwave radiation," *IRE Transactions on Antennas and Propagation*, vol. 4, no. 3, pp. 385–392, 1956.
- [36] N. I. Landy, S. Sajuyigbe, J. J. Mock, D. R. Smith, and W. J. Padilla, "Perfect metamaterial absorber," *Physical Review Letters*, vol. 100, no. 20, Article ID 207402, 2008.
- [37] M. Pu, C. Hu, M. Wang et al., "Design principles for infrared wide-angle perfect absorber based on plasmonic structure," *Optics Express*, vol. 19, no. 18, pp. 17413–17420, 2011.
- [38] M. Pu, Q. Feng, M. Wang et al., "Ultrathin broadband nearly perfect absorber with symmetrical coherent illumination," *Optics Express*, vol. 20, no. 3, pp. 2246–2254, 2012.
- [39] A. Thoman, A. Kern, H. Helm, and M. Walther, "Nanostructured gold films as broadband terahertz antireflection coatings," *Physical Review B*, vol. 77, no. 19, Article ID 195405, 2008.
- [40] Y. Zhou, X. Xu, F. Hu et al., "Graphene as broadband terahertz antireflection coating," *Applied Physics Letters*, vol. 104, no. 5, Article ID 051106, 2014.
- [41] L. Ding, Q. Y. S. Wu, and J. H. Teng, "Polarization independent broadband terahertz antireflection by deep-subwavelength thin metallic mesh," *Laser & Photonics Reviews*, vol. 8, no. 6, pp. 941–945, 2014.
- [42] J. Yang, F. Luo, T. S. Kao et al., "Design and fabrication of broadband ultralow reflectivity black Si surfaces by laser micro/nanoprocessing," *Light: Science and Applications*, vol. 3, article e185, 2014.
- [43] M. V. Berry, "Quantal phase factors accompanying adiabatic changes," *Proceedings of the Royal Society of London. Series A. Mathematical, Physical and Engineering Sciences*, vol. 392, no. 1802, pp. 45–57, 1984.
- [44] D. Lin, P. Fan, E. Hasman, and M. L. Brongersma, "Dielectric gradient metasurface optical elements," *Science*, vol. 345, no. 6194, pp. 298–302, 2014.
- [45] X. Ma, C. Huang, M. Pu, C. Hu, Q. Feng, and X. Luo, "Single-layer circular polarizer using metamaterial and its application in antenna," *Microwave and Optical Technology Letters*, vol. 54, no. 7, pp. 1770–1774, 2012.
- [46] L. Verslegers, P. B. Catrysse, Z. Yu et al., "Planar lenses based on nanoscale slit arrays in a metallic film," *Nano Letters*, vol. 9, no. 1, pp. 235–238, 2009.
- [47] R. C. Hadarig, M. E. De Cos, and F. Las-Heras, "Microstrip patch antenna bandwidth enhancement using AMC/EBG structures," *International Journal of Antennas and Propagation*, vol. 2012, Article ID 843754, 6 pages, 2012.
- [48] H.-X. Xu, G.-M. Wang, and C.-X. Zhang, "Fractal-shaped metamaterials and applications to enhanced-performance devices exhibiting high selectivity," *International Journal of Antennas and Propagation*, vol. 2012, Article ID 515167, 14 pages, 2012.
- [49] F. Yang, Z. L. Mei, and T. J. Cui, "Control of the radiation patterns using homogeneous and isotropic impedance metasurface," *International Journal of Antennas and Propagation*, vol. 2015, Article ID 917829, 7 pages, 2015.
- [50] M. Tauseef Asim and M. Ahmed, "Metamaterial inspired microstrip antenna investigations using metascreens," *International Journal of Antennas and Propagation*, vol. 2015, Article ID 236136, 9 pages, 2015.
- [51] X. Chen, T. M. Grzegorczyk, B.-I. Wu, J. Pacheco Jr., and J. A. Kong, "Robust method to retrieve the constitutive effective parameters of metamaterials," *Physical Review E—Statistical, Nonlinear, and Soft Matter Physics*, vol. 70, no. 1, Article ID 016608, 2004.
- [52] A. Vora, J. Gwamuri, N. Pala, A. Kulkarni, J. M. Pearce, and D. O. Güney, "Exchanging ohmic losses in metamaterial absorbers with useful optical absorption for photovoltaics," *Scientific Reports*, vol. 4, article 4901, 2014.
- [53] A. Karlsson, "Approximate boundary conditions for thin structures," *IEEE Transactions on Antennas and Propagation*, vol. 57, no. 1, pp. 144–148, 2009.
- [54] A. Vakil and N. Engheta, "Transformation optics using graphene," *Science*, vol. 332, no. 6035, pp. 1291–1294, 2011.
- [55] X. Luo and T. Ishihara, "Subwavelength photolithography based on surface-plasmon polariton resonance," *Optics Express*, vol. 12, no. 14, pp. 3055–3065, 2004.
- [56] J. B. Pendry, L. Martín-Moreno, and F. J. Garcia-Vidal, "Mimicking surface plasmons with structured surfaces," *Science*, vol. 305, no. 5685, pp. 847–848, 2004.
- [57] X. Li, L. Yang, C. Hu, X. Luo, and M. Hong, "Tunable bandwidth of band-stop filter by metamaterial cell coupling in optical frequency," *Optics Express*, vol. 19, no. 6, pp. 5283–5289, 2011.
- [58] K. Sarabandi and N. Behdad, "A frequency selective surface with miniaturized elements," *IEEE Transactions on Antennas and Propagation*, vol. 55, no. 5, pp. 1239–1245, 2007.
- [59] Y. Yang, I. I. Kravchenko, D. P. Briggs, and J. Valentine, "All-dielectric metasurface analogue of electromagnetically induced transparency," *Nature Communications*, vol. 5, article 5753, 2014.
- [60] J. Gu, R. Singh, X. Liu et al., "Active control of electromagnetically induced transparency analogue in terahertz metamaterials," *Nature Communications*, vol. 3, article 1151, 2012.

- [61] J. Kim, R. Soref, and W. R. Buchwald, "Multi-peak electromagnetically induced transparency (EIT)-like transmission from bull's-eye-shaped metamaterial," *Optics Express*, vol. 18, no. 17, pp. 17997–18002, 2010.
- [62] S. H. Mousavi, A. B. Khanikaev, and G. Shvets, "Optical properties of Fano-resonant metallic metasurfaces on a substrate," *Physical Review B*, vol. 85, no. 15, Article ID 155429, 2012.
- [63] M. Pu, M. Song, H. Yu et al., "Fano resonance induced by mode coupling in all-dielectric nanorod array," *Applied Physics Express*, vol. 7, no. 3, Article ID 032002, 2014.
- [64] S. Fan and J. D. Joannopoulos, "Analysis of guided resonances in photonic crystal slabs," *Physical Review B*, vol. 65, no. 23, Article ID 235112, 8 pages, 2002.
- [65] C. Genet and T. W. Ebbesen, "Light in tiny holes," *Nature*, vol. 445, no. 7123, pp. 39–46, 2007.
- [66] C. M. Horwitz, "A new solar selective surface," *Optics Communications*, vol. 11, no. 2, pp. 210–212, 1974.
- [67] M. Song, H. Yu, C. Hu et al., "Conversion of broadband energy to narrowband emission through double-sided metamaterials," *Optics Express*, vol. 21, no. 26, pp. 32207–32216, 2013.
- [68] L. Young, L. A. Robinson, and C. Hacking, "Meander-line polarizer," *IEEE Transactions on Antennas and Propagation*, vol. 21, no. 3, pp. 376–378, 1973.
- [69] S. L. Wadsworth and G. D. Boreman, "Broadband infrared meanderline reflective quarter-wave plate," *Optics Express*, vol. 19, no. 11, pp. 10604–10612, 2011.
- [70] D. Wang, Y. Gu, Y. Gong, C.-W. Qiu, and M. Hong, "An ultrathin terahertz quarter-wave plate using planar babinet-inverted metasurface," *Optics Express*, vol. 23, no. 9, pp. 11114–11122, 2015.
- [71] M. Euler, V. Fusco, R. Cahill, and R. Dickie, "325 GHz single layer sub-millimeter wave FSS based split slot ring linear to circular polarization convertor," *IEEE Transactions on Antennas and Propagation*, vol. 58, no. 7, pp. 2457–2459, 2010.
- [72] W. Sun, Q. He, J. Hao, and L. Zhou, "A transparent metamaterial to manipulate electromagnetic wave polarizations," *Optics Letters*, vol. 36, no. 6, pp. 927–929, 2011.
- [73] D. L. Markovich, A. Andryieuski, M. Zalkovskij, R. Malureanu, and A. V. Lavrinenko, "Metamaterial polarization converter analysis: limits of performance," *Applied Physics B: Lasers and Optics*, vol. 112, no. 2, pp. 143–152, 2013.
- [74] A. Pors, M. G. Nielsen, G. D. Valle, M. Willatzen, O. Albrektsen, and S. I. Bozhevolnyi, "Plasmonic metamaterial wave retarders in reflection by orthogonally oriented detuned electrical dipoles," *Optics Letters*, vol. 36, no. 9, pp. 1626–1628, 2011.
- [75] J. Hao, Y. Yuan, L. Ran et al., "Manipulating electromagnetic wave polarizations by anisotropic metamaterials," *Physical Review Letters*, vol. 99, no. 6, Article ID 063908, 2007.
- [76] Y. Wang, M. Pu, C. Hu, Z. Zhao, C. Wang, and X. Luo, "Dynamic manipulation of polarization states using anisotropic metasurface," *Optics Communications*, vol. 319, pp. 14–16, 2014.
- [77] N. K. Grady, J. E. Heyes, D. R. Chowdhury et al., "Terahertz metamaterials for linear polarization conversion and anomalous refraction," *Science*, vol. 340, no. 6138, pp. 1304–1307, 2013.
- [78] S.-C. Jiang, X. Xiong, Y.-S. Hu et al., "Controlling the polarization state of light with a dispersion-free metastructure," *Physical Review X*, vol. 4, no. 2, Article ID 021026, 2014.
- [79] Z. H. Jiang, L. Lin, D. Ma et al., "Broadband and wide field-of-view plasmonic metasurface-enabled waveplates," *Scientific Reports*, vol. 4, article 7511, 2014.
- [80] J. Hao, Q. Ren, Z. An et al., "Optical metamaterial for polarization control," *Physical Review A: Atomic, Molecular, and Optical Physics*, vol. 80, no. 2, Article ID 023807, 2009.
- [81] M. Pu, P. Chen, Y. Wang et al., "Anisotropic meta-mirror for achromatic electromagnetic polarization manipulation," *Applied Physics Letters*, vol. 102, no. 13, Article ID 131906, 2013.
- [82] Y. Guo, Y. Wang, M. Pu et al., "Dispersion management of anisotropic metasurface for super-octave bandwidth polarization conversion," *Scientific Reports*, vol. 5, p. 8434, 2015.
- [83] J. E. Roy and L. Shafai, "Reciprocal circular-polarization-selective surface," *IEEE Antennas and Propagation Magazine*, vol. 38, no. 6, pp. 18–32, 1996.
- [84] J. K. Gansel, M. Thiel, M. S. Rill et al., "Gold helix photonic metamaterial as broadband circular polarizer," *Science*, vol. 325, no. 5947, pp. 1513–1515, 2009.
- [85] J. K. Gansel, M. Wegener, S. Burger, and S. Linden, "Gold helix photonic metamaterials: a numerical parameter study," *Optics Express*, vol. 18, no. 2, pp. 1059–1069, 2010.
- [86] X. Ma, C. Huang, M. Pu, C. Hu, Q. Feng, and X. Luo, "Multi-band circular polarizer using planar spiral metamaterial structure," *Optics Express*, vol. 20, no. 14, pp. 16050–16058, 2012.
- [87] M. Mutlu, A. E. Akosman, A. E. Serebryannikov, and E. Ozbay, "Asymmetric chiral metamaterial circular polarizer based on four U-shaped split ring resonators," *Optics Letters*, vol. 36, no. 9, pp. 1653–1655, 2011.
- [88] C. Menzel, C. Helgert, C. Rockstuhl et al., "Asymmetric transmission of linearly polarized light at optical metamaterials," *Physical Review Letters*, vol. 104, no. 25, Article ID 253902, 2010.
- [89] X. Ma, C. Huang, M. Pu et al., "Dual-band asymmetry chiral metamaterial based on planar spiral structure," *Applied Physics Letters*, vol. 101, no. 16, Article ID 161901, 2012.
- [90] X. Ma, C. Huang, W. Pan, B. Zhao, J. Cui, and X. Luo, "A dual circularly polarized horn antenna in Ku-band based on chiral metamaterial," *IEEE Transactions on Antennas and Propagation*, vol. 62, no. 4, pp. 2307–2311, 2014.
- [91] C. Huang, X. Ma, M. Pu, G. Yi, Y. Wang, and X. Luo, "Dual-band 90° polarization rotator using twisted split ring resonators array," *Optics Communications*, vol. 291, pp. 345–348, 2013.
- [92] X. Ma, W. Pan, C. Huang et al., "An active metamaterial for polarization manipulating," *Advanced Optical Materials*, vol. 2, no. 10, pp. 945–949, 2014.
- [93] X. Ma, C. Huang, M. Pu, W. Pan, Y. Wang, and X. Luo, "Circular dichroism and optical rotation in twisted Y-shaped chiral metamaterial," *Applied Physics Express*, vol. 6, no. 2, Article ID 022001, 2013.
- [94] H. K. Raut, V. A. Ganesh, A. S. Nair, and S. Ramakrishna, "Anti-reflective coatings: a critical, in-depth review," *Energy and Environmental Science*, vol. 4, no. 10, pp. 3779–3804, 2011.
- [95] J.-Q. Xi, M. F. Schubert, J. K. Kim et al., "Optical thin-film materials with low refractive index for broadband elimination of Fresnel reflection," *Nature Photonics*, vol. 1, no. 3, pp. 176–179, 2007.
- [96] B. Zhang, J. Hendrickson, N. Nader, H.-T. Chen, and J. Guo, "Metasurface optical antireflection coating," *Applied Physics Letters*, vol. 105, no. 24, Article ID 241113, 2014.
- [97] Y.-F. Huang, S. Chattopadhyay, Y.-J. Jen et al., "Improved broadband and quasi-omnidirectional anti-reflection properties with biomimetic silicon nanostructures," *Nature Nanotechnology*, vol. 2, no. 12, pp. 770–774, 2007.

- [98] L. Ding, Q. Y. S. Wu, J. F. Song, K. Serita, M. Tonouchi, and J. H. Teng, "Perfect broadband Terahertz antireflection by deep-subwavelength, thin, lamellar metallic gratings," *Advanced Optical Materials*, vol. 1, no. 12, pp. 910–914, 2013.
- [99] E. F. Knott, J. F. Shaeffer, and M. T. Tuley, *Radar Cross Section*, SciTech Publishing, Raleigh, NC, USA, 2nd edition, 2004.
- [100] K. N. Rozanov, "Ultimate thickness to bandwidth ratio of radar absorbers," *IEEE Transactions on Antennas and Propagation*, vol. 48, no. 8, pp. 1230–1234, 2000.
- [101] M. Planck and M. Masius, *The Theory of Heat Radiation*, P. Blakiston's Son & Co, Philadelphia, Pa, USA, 1914.
- [102] F. Ding, Y. Cui, X. Ge, Y. Jin, and S. He, "Ultra-broadband microwave metamaterial absorber," *Applied Physics Letters*, vol. 100, no. 10, Article ID 103506, 2012.
- [103] Y. Cui, K. H. Fung, J. Xu et al., "Ultrabroadband light absorption by a sawtooth anisotropic metamaterial slab," *Nano Letters*, vol. 12, no. 3, pp. 1443–1447, 2012.
- [104] X. Zang, C. Shi, L. Chen, B. Cai, Y. Zhu, and S. Zhuang, "Ultra-broadband terahertz absorption by exciting the orthogonal diffraction in dumbbell-shaped gratings," *Scientific Reports*, vol. 5, article 8901, 2015.
- [105] J. A. Bossard, L. Lin, S. Yun, L. Liu, D. H. Werner, and T. S. Mayer, "Near-ideal optical metamaterial absorbers with super-octave bandwidth," *ACS Nano*, vol. 8, no. 2, pp. 1517–1524, 2014.
- [106] L. K. Sun, H. F. Cheng, Y. J. Zhou, and J. Wang, "Broadband metamaterial absorber based on coupling resistive frequency selective surface," *Optics Express*, vol. 20, no. 4, pp. 4675–4680, 2012.
- [107] K. V. Nerkararyan, S. K. Nerkararyan, and S. I. Bozhevolnyi, "Plasmonic black-hole: broadband omnidirectional absorber of gap surface plasmons," *Optics Letters*, vol. 36, no. 22, pp. 4311–4313, 2011.
- [108] J. Grant, Y. Ma, S. Saha, A. Khalid, and D. R. S. Cumming, "Polarization insensitive, broadband terahertz metamaterial absorber," *Optics Letters*, vol. 36, no. 17, pp. 3476–3478, 2011.
- [109] E. E. Narimanov and A. V. Kildishev, "Optical black hole: broadband omnidirectional light absorber," *Applied Physics Letters*, vol. 95, no. 4, Article ID 041106, 2009.
- [110] A. Kazemzadeh, "Nonmagnetic ultrawideband absorber with optimal thickness," *IEEE Transactions on Antennas and Propagation*, vol. 59, no. 1, pp. 135–140, 2011.
- [111] A. K. Zadeh and A. Karlsson, "Capacitive circuit method for fast and efficient design of wideband radar absorbers," *IEEE Transactions on Antennas and Propagation*, vol. 57, no. 8, pp. 2307–2314, 2009.
- [112] J. Hao, J. Wang, X. Liu, W. J. Padilla, L. Zhou, and M. Qiu, "High performance optical absorber based on a plasmonic metamaterial," *Applied Physics Letters*, vol. 96, no. 25, Article ID 251104, 2010.
- [113] N. Liu, M. Mesch, T. Weiss, M. Hentschel, and H. Giessen, "Infrared perfect absorber and its application as plasmonic sensor," *Nano Letters*, vol. 10, no. 7, pp. 2342–2348, 2010.
- [114] Q. Feng, M. Pu, C. Hu, and X. Luo, "Engineering the dispersion of metamaterial surface for broadband infrared absorption," *Optics Letters*, vol. 37, no. 11, pp. 2133–2135, 2012.
- [115] A. Moreau, C. Ciraci, J. J. Mock et al., "Controlled-reflectance surfaces with film-coupled colloidal nanoantennas," *Nature*, vol. 491, no. 7427, pp. 86–89, 2012.
- [116] A. J. Hoffman, L. Alekseyev, S. S. Howard et al., "Negative refraction in semiconductor metamaterials," *Nature Materials*, vol. 6, no. 12, pp. 946–950, 2007.
- [117] M. Pu, M. Wang, C. Hu et al., "Engineering heavily doped silicon for broadband absorber in the terahertz regime," *Optics Express*, vol. 20, no. 23, pp. 25513–25519, 2012.
- [118] C. Shi, X. Zang, Y. Wang, L. Chen, B. Cai, and Y. Zhu, "A polarization-independent broadband terahertz absorber," *Applied Physics Letters*, vol. 105, no. 3, Article ID 031104, 2014.
- [119] Y. D. Chong, L. Ge, H. Cao, and A. D. Stone, "Coherent perfect absorbers: time-reversed lasers," *Physical Review Letters*, vol. 105, no. 5, Article ID 053901, 2010.
- [120] W. Wan, Y. Chong, L. Ge, H. Noh, A. D. Stone, and H. Cao, "Time-reversed lasing and interferometric control of absorption," *Science*, vol. 331, no. 6019, pp. 889–892, 2011.
- [121] S. Li, J. Luo, S. Anwar et al., "An equivalent realization of coherent perfect absorption under single beam illumination," *Scientific Reports*, vol. 4, p. 7369, 2014.
- [122] G. Nie, Q. Shi, Z. Zhu, and J. Shi, "Selective coherent perfect absorption in metamaterials," *Applied Physics Letters*, vol. 105, no. 20, Article ID 201909, 2014.
- [123] M. Pu, Q. Feng, C. Hu, and X. Luo, "Perfect absorption of light by coherently induced plasmon hybridization in ultrathin metamaterial film," *Plasmonics*, vol. 7, no. 4, pp. 733–738, 2012.
- [124] J. Zhang, K. F. MacDonald, and N. I. Zheludev, "Controlling light-with-light without nonlinearity," *Light: Science & Applications*, vol. 1, no. 7, article e18, 2012.
- [125] J. Shi, X. Fang, E. T. F. Rogers, E. Plum, K. F. MacDonald, and N. I. Zheludev, "Coherent control of Snell's law at metasurfaces," *Optics Express*, vol. 22, no. 17, pp. 21051–21060, 2014.
- [126] M. Crescimanno, N. J. Dawson, and J. H. Andrews, "Coherent perfect rotation," *Physical Review A—Atomic, Molecular, and Optical Physics*, vol. 86, no. 3, Article ID 031807, 2012.
- [127] H. Yao, G. Yu, P. Yan, X. Chen, and X. Luo, "Patterning sub 100 nm isolated patterns with 436 nm lithography," in *Proceedings of the International Microprocesses and Nanotechnology Conference*, Tokyo, Japan, 2003.
- [128] X. Luo and I. Teruya, "Sub 100 nm lithography based on plasmon polariton resonance," in *Proceedings of the International Microprocesses and Nanotechnology Conference*, pp. 138–139, Tokyo, Japan, 2003.
- [129] C. Park, J.-H. Park, C. Rodriguez et al., "Full-field subwavelength imaging using a scattering superlens," *Physical Review Letters*, vol. 113, Article ID 113901, 2014.
- [130] K. Aydin, I. Bulu, and E. Ozbay, "Subwavelength resolution with a negative-index metamaterial superlens," *Applied Physics Letters*, vol. 90, no. 25, Article ID 254102, 2007.
- [131] M. D. Arnold and R. J. Blaikie, "Subwavelength optical imaging of evanescent fields using reflections from plasmonic slabs," *Optics Express*, vol. 15, no. 18, pp. 11542–11552, 2007.
- [132] P. Gao, N. Yao, C. Wang et al., "Enhancing aspect profile of half-pitch 32 nm and 22 nm lithography with plasmonic cavity lens," *Applied Physics Letters*, vol. 106, no. 9, Article ID 093110, 2015.
- [133] Z. Jacob, L. V. Alekseyev, and E. Narimanov, "Optical hyperlens: far-field imaging beyond the diffraction limit," *Optics Express*, vol. 14, no. 18, pp. 8247–8256, 2006.
- [134] N. Yu, P. Genevet, M. A. Kats et al., "Light propagation with phase discontinuities: generalized laws of reflection and refraction," *Science*, vol. 334, no. 6054, pp. 333–337, 2011.
- [135] Y. Chen, X. Li, Y. Sonnefraud et al., "Engineering the phase front of light with phase-change material based planar lenses," *Scientific Reports*, vol. 5, p. 8660, 2015.
- [136] S. Ishii, V. M. Shalaev, and A. V. Kildishev, "Holey-metal lenses: sieving single modes with proper phases," *Nano Letters*, vol. 13, no. 1, pp. 159–163, 2013.

- [137] T. Xu, C. Wang, C. Du, and X. Luo, "Plasmonic beam deflector," *Optics Express*, vol. 16, no. 7, pp. 4753–4759, 2008.
- [138] X. Ni, N. K. Emani, A. V. Kildishev, A. Boltasseva, and V. M. Shalaev, "Broadband light bending with plasmonic nanoantennas," *Science*, vol. 335, no. 6067, p. 427, 2012.
- [139] C. Min, P. Wang, X. Jiao, Y. Deng, and H. Ming, "Beam manipulating by metallic nano-optic lens containing nonlinear media," *Optics Express*, vol. 15, no. 15, pp. 9541–9546, 2007.
- [140] B. Hu, Q. J. Wang, S. W. Kok, and Y. Zhang, "Active focal length control of terahertz slotted plane lenses by magnetoplasmons," *Plasmonics*, vol. 7, no. 2, pp. 191–199, 2012.
- [141] J. Sun, X. Wang, T. Xu, Z. A. Kudyshev, A. N. Cartwright, and N. M. Litchinitser, "Spinning light on the nanoscale," *Nano Letters*, vol. 14, no. 5, pp. 2726–2729, 2014.
- [142] K. A. Willets and R. P. Van Duyne, "Localized surface plasmon resonance spectroscopy and sensing," *Annual Review of Physical Chemistry*, vol. 58, pp. 267–297, 2007.
- [143] P. L. Stiles, J. A. Dieringer, N. C. Shah, and R. P. Van Duyne, "Surface-enhanced Raman spectroscopy," *Annual Review of Analytical Chemistry*, vol. 1, no. 1, pp. 601–626, 2008.
- [144] C. Wu, A. B. Khanikaev, R. Adato et al., "Fano-resonant asymmetric metamaterials for ultrasensitive spectroscopy and identification of molecular monolayers," *Nature Materials*, vol. 11, no. 1, pp. 69–75, 2012.
- [145] M. Rahmani, D. Y. Lei, V. Giannini et al., "Subgroup decomposition of plasmonic resonances in hybrid oligomers: modeling the resonance lineshape," *Nano Letters*, vol. 12, no. 4, pp. 2101–2106, 2012.
- [146] M. Rahmani, B. Lukiyanchuk, T. T. V. Nguyen et al., "Influence of symmetry breaking in pentamers on Fano resonance and near-field energy localization," *Optical Materials Express*, vol. 1, no. 8, pp. 1409–1415, 2011.
- [147] M. Rahmani, A. E. Miroshnichenko, D. Y. Lei et al., "Beyond the hybridization effects in plasmonic nanoclusters: diffraction-induced enhanced absorption and scattering," *Small*, vol. 10, no. 3, pp. 576–583, 2014.
- [148] A. A. Yanik, A. E. Cetin, M. Huang et al., "Seeing protein monolayers with naked eye through plasmonic Fano resonances," *Proceedings of the National Academy of Sciences of the United States of America*, vol. 108, no. 29, pp. 11784–11789, 2011.
- [149] A. Tittl, P. Mai, R. Taubert, D. Dregely, N. Liu, and H. Giessen, "Palladium-based plasmonic perfect absorber in the visible wavelength range and its application to hydrogen sensing," *Nano Letters*, vol. 11, no. 10, pp. 4366–4369, 2011.
- [150] G. Sarau, B. Lahiri, P. Banzer et al., "Enhanced Raman scattering of graphene using arrays of split ring resonators," *Advanced Optical Materials*, vol. 1, no. 2, pp. 151–157, 2013.
- [151] H. Aouani, H. Šípová, M. Rahmani et al., "Ultrasensitive broadband probing of molecular vibrational modes with multifrequency optical antennas," *ACS Nano*, vol. 7, no. 1, pp. 669–675, 2013.
- [152] M. König, M. Rahmani, L. Zhang et al., "Unveiling the correlation between nanometer-thick molecular monolayer sensitivity and near-field enhancement and localization in coupled plasmonic oligomers," *ACS Nano*, vol. 8, no. 9, pp. 9188–9198, 2014.
- [153] M. Rahmani, B. Lukiyanchuk, T. Tahmasebi, Y. Lin, T. Y. F. Liew, and M. H. Hong, "Polarization-controlled spatial localization of near-field energy in planar symmetric coupled oligomers," *Applied Physics A: Materials Science and Processing*, vol. 107, no. 1, pp. 23–30, 2012.
- [154] H. Aouani, M. Rahmani, H. Šípová et al., "Plasmonic nanoantennas for multispectral surface-enhanced spectroscopies," *The Journal of Physical Chemistry C*, vol. 117, no. 36, pp. 18620–18626, 2013.
- [155] Y. Xiao, Y. Francescato, V. Giannini et al., "Probing the dielectric response of graphene via dual-band plasmonic nanoresonators," *Physical Chemistry Chemical Physics*, vol. 15, no. 15, pp. 5395–5399, 2013.
- [156] J. J. Yang, M. Huang, H. Tang, J. Zeng, and L. Dong, "Metamaterial sensors," *International Journal of Antennas and Propagation*, vol. 2013, Article ID 637270, 16 pages, 2013.
- [157] T. W. Ebbesen, H. J. Lezec, H. F. Ghaemi, T. Thio, and P. A. Wolff, "Extraordinary optical transmission through sub-wavelength hole arrays," *Nature*, vol. 391, no. 6668, pp. 667–669, 1998.
- [158] H. J. Lezec, A. Degiron, E. Devaux et al., "Beaming light from a subwavelength aperture," *Science*, vol. 297, no. 5582, pp. 820–822, 2002.
- [159] Y. Poujet, J. Salvi, and F. I. Baida, "90% Extraordinary optical transmission in the visible range through annular aperture metallic arrays," *Optics Letters*, vol. 32, no. 20, pp. 2942–2944, 2007.
- [160] L. Martin-Moreno, F. J. Garcia-Vidal, H. J. Lezec, A. Degiron, and T. W. Ebbesen, "Theory of highly directional emission from a single subwavelength aperture surrounded by surface corrugations," *Physical Review Letters*, vol. 90, no. 16, Article ID 167401, 2003.
- [161] M. J. Lockyear, A. P. Hibbins, J. Roy Sambles, and C. R. Lawrence, "Enhanced microwave transmission through a single subwavelength aperture surrounded by concentric grooves," *Journal of Optics A: Pure and Applied Optics*, vol. 7, no. 2, pp. S152–S158, 2005.
- [162] S. S. Akarca-Biyikli, I. Bulu, and E. Ozbay, "Enhanced transmission of microwave radiation in one-dimensional metallic gratings with subwavelength aperture," *Applied Physics Letters*, vol. 85, no. 7, pp. 1098–1100, 2004.
- [163] C. Huang, C. Du, and X. Luo, "A waveguide slit array antenna fabricated with subwavelength periodic grooves," *Applied Physics Letters*, vol. 91, Article ID 143512, 2007.
- [164] Z. Ying and P.-S. Kildal, "Improvements of dipole, helix, spiral, microstrip patch and aperture antennas with ground planes by using corrugated soft surfaces," *IEE Proceedings—Microwaves, Antennas and Propagation*, vol. 143, no. 3, pp. 244–248, 1996.
- [165] N. Yu, J. Fan, Q. J. Wang et al., "Small-divergence semiconductor lasers by plasmonic collimation," *Nature Photonics*, vol. 2, no. 9, pp. 564–570, 2008.
- [166] N. Yu, Q. J. Wang, M. A. Kats et al., "Designer spoof surface plasmon structures collimate terahertz laser beams," *Nature Materials*, vol. 9, no. 9, pp. 730–735, 2010.
- [167] N. Yu, M. A. Kats, C. Pflugl et al., "Multi-beam multi-wavelength semiconductor lasers," *Applied Physics Letters*, vol. 95, Article ID 161108, 2009.
- [168] H. Aouani, O. Mahboub, N. Bonod et al., "Bright unidirectional fluorescence emission of molecules in a nanoaperture with plasmonic corrugations," *Nano Letters*, vol. 11, no. 2, pp. 637–644, 2011.
- [169] Y. C. Jun, K. C. Y. Huang, and M. L. Brongersma, "Plasmonic beaming and active control over fluorescent emission," *Nature Communications*, vol. 2, article 283, 2011.
- [170] Y. Gorodetski, A. Drezet, C. Genet, and T. W. Ebbesen, "Generating far-field orbital angular momenta from near-field optical chirality," *Physical Review Letters*, vol. 110, Article ID 203906, 2013.

- [171] Y.-H. Chen, L. Huang, L. Gan, and Z.-Y. Li, "Wavefront shaping of infrared light through a subwavelength hole," *Light: Science & Applications*, vol. 1, article e26, 5 pages, 2012.
- [172] M. Pu, X. Ma, Z. Zhao et al., "Near-field collimation of light carrying orbital angular momentum with bull's-eye-assisted plasmonic coaxial waveguides," *Scientific Reports*, vol. 5, Article ID 12108, 2015.
- [173] A. E. H. Love, "The integration of the equations of propagation of electric waves," *Philosophical Transactions of the Royal Society of London Series A*, vol. 68, no. 442–450, pp. 19–21, 1901.
- [174] S. A. Schelkunoff, "Some equivalence theorems of electromagnetics and their application to radiation problems," *Bell System Technical Journal*, vol. 15, no. 1, pp. 92–112, 1936.
- [175] S. Sun, K.-Y. Yang, C.-M. Wang et al., "High-efficiency broadband anomalous reflection by gradient meta-surfaces," *Nano Letters*, vol. 12, no. 12, pp. 6223–6229, 2012.
- [176] C. Pfeiffer and A. Grbic, "Metamaterial Huygens' surfaces: tailoring wave fronts with reflectionless sheets," *Physical Review Letters*, vol. 110, no. 19, Article ID 197401, 2013.
- [177] M. Pu, P. Chen, C. Wang et al., "Broadband anomalous reflection based on gradient low-Q meta-surface," *AIP Advances*, vol. 3, no. 5, Article ID 052136, 2013.
- [178] S. Sun, Q. He, S. Xiao, Q. Xu, X. Li, and L. Zhou, "Gradient-index meta-surfaces as a bridge linking propagating waves and surface waves," *Nature Materials*, vol. 11, no. 5, pp. 426–431, 2012.
- [179] X. Li, S. Xiao, B. Cai, Q. He, T. J. Cui, and L. Zhou, "Flat metasurfaces to focus electromagnetic waves in reflection geometry," *Optics Letters*, vol. 37, no. 23, pp. 4940–4942, 2012.
- [180] A. Pors, M. G. Nielsen, R. L. Eriksen, and S. I. Bozhevolnyi, "Broadband focusing flat mirrors based on plasmonic gradient metasurfaces," *Nano Letters*, vol. 13, no. 2, pp. 829–834, 2013.
- [181] M. Kim, A. M. H. Wong, and G. V. Eleftheriades, "Optical huygens' metasurfaces with independent control of the magnitude and phase of the local reflection coefficients," *Physical Review X*, vol. 4, no. 4, Article ID 041042, 2014.
- [182] W. Sichak and D. J. Levine, "Microwave high-speed continuous phase shifter," *Proceedings of the IRE*, vol. 43, no. 11, pp. 1661–1663, 1955.
- [183] G. W. Swenson and Y. Lo, "The University of Illinois radio telescope," *IRE Transactions on Antennas and Propagation*, vol. 9, no. 1, pp. 9–16, 1961.
- [184] J. Huang, "Bandwidth study of microstrip reflectarray and a novel phased reflectarray concept," in *Proceedings of the Antennas and Propagation Society International Symposium. AP-S. Digest*, vol. 1, pp. 582–585, IEEE, Newport Beach, Calif, USA, June 1995.
- [185] R. Bhandari and J. Samuel, "Observation of topological phase by use of a laser interferometer," *Physical Review Letters*, vol. 60, no. 13, pp. 1211–1213, 1988.
- [186] F. Gori, "Measuring Stokes parameters by means of a polarization grating," *Optics Letters*, vol. 24, no. 9, pp. 584–586, 1999.
- [187] Z. Bomzon, V. Kleiner, and E. Hasman, "Pancharatnam-Berry phase in space-variant polarization-state manipulations with subwavelength gratings," *Optics Letters*, vol. 26, no. 18, pp. 1424–1426, 2001.
- [188] A. Niv, G. Biener, V. Kleiner, and E. Hasman, "Propagation-invariant vectorial Bessel beams obtained by use of quantized Pancharatnam-Berry phase optical elements," *Optics Letters*, vol. 29, no. 3, pp. 238–240, 2004.
- [189] N. Shitrit, I. Bretner, Y. Gorodetski, V. Kleiner, and E. Hasman, "Optical spin Hall effects in plasmonic chains," *Nano Letters*, vol. 11, no. 5, pp. 2038–2042, 2011.
- [190] L. Marrucci, C. Manzo, and D. Paparo, "Optical spin-to-orbital angular momentum conversion in inhomogeneous anisotropic media," *Physical Review Letters*, vol. 96, no. 16, Article ID 163905, 2006.
- [191] M. Stalder and M. Schadt, "Linearly polarized light with axial symmetry generated by liquid-crystal polarization converters," *Optics Letters*, vol. 21, no. 23, pp. 1948–1950, 1996.
- [192] M. Kang, T. Feng, H.-T. Wang, and J. Li, "Wave front engineering from an array of thin aperture antennas," *Optics Express*, vol. 20, no. 14, pp. 15882–15890, 2012.
- [193] X. Chen, L. Huang, H. Mühlenbernd et al., "Dual-polarity plasmonic metalens for visible light," *Nature Communications*, vol. 3, article 1198, 2012.
- [194] L. Huang, X. Chen, H. Mühlenbernd et al., "Dispersionless phase discontinuities for controlling light propagation," *Nano Letters*, vol. 12, no. 11, pp. 5750–5755, 2012.
- [195] W. Luo, S. Xiao, Q. He, S. Sun, and L. Zhou, "Photonic spin Hall effect with nearly 100% efficiency," *Advanced Optical Materials*, 2015.
- [196] X. Zhang, Z. Tian, W. Yue et al., "Broadband terahertz wave deflection based on C-shape complex metamaterials with phase discontinuities," *Advanced Materials*, vol. 25, no. 33, pp. 4567–4572, 2013.
- [197] N. Yu, F. Aieta, P. Genevet, M. A. Kats, Z. Gaburro, and F. Capasso, "A broadband, background-free quarter-wave plate based on plasmonic metasurfaces," *Nano Letters*, vol. 12, no. 12, pp. 6328–6333, 2012.
- [198] P. Genevet, N. Yu, F. Aieta et al., "Ultra-thin plasmonic optical vortex plate based on phase discontinuities," *Applied Physics Letters*, vol. 100, no. 1, Article ID 013101, 2012.
- [199] J. Lin, S. Wu, X. Li, C. Huang, and X. Luo, "Design and numerical analyses of ultrathin plasmonic lens for subwavelength focusing by phase discontinuities of nanoantenna arrays," *Applied Physics Express*, vol. 6, no. 2, Article ID 022004, 2013.
- [200] X.-Y. Jiang, J.-S. Ye, J.-W. He et al., "An ultrathin terahertz lens with axial long focal depth based on metasurfaces," *Optics Express*, vol. 21, no. 24, pp. 30030–30038, 2013.
- [201] X. Ma, M. Pu, X. Li et al., "A planar chiral meta-surface for optical vortex generation and focusing," *Scientific Reports*, vol. 5, Article ID 10365, 2015.
- [202] G. Zheng, H. Mühlenbernd, M. Kenney, G. Li, T. Zentgraf, and S. Zhang, "Metasurface holograms reaching 80% efficiency," *Nature Nanotechnology*, vol. 10, no. 4, pp. 308–312, 2015.
- [203] G. T. di Francia, "Super-gain antennas and optical resolving power," *Il Nuovo Cimento*, vol. 9, no. 3, pp. 426–438, 1952.
- [204] M. Pu, Z. Zhao, Y. Wang et al., "Spatially and spectrally engineered spin-orbit interaction for achromatic virtual shaping," *Scientific Reports*, vol. 5, article 9822, 2015.
- [205] W. X. Jiang, C.-W. Qiu, T. Han, S. Zhang, and T. J. Cui, "Creation of ghost illusions using wave dynamics in metamaterials," *Advanced Functional Materials*, vol. 23, no. 32, pp. 4028–4034, 2013.
- [206] T. Jiang, Z. Wang, D. Li et al., "Low-DC voltage-controlled steering-antenna radome utilizing tunable active metamaterial," *IEEE Transactions on Microwave Theory and Techniques*, vol. 60, no. 1, pp. 170–178, 2012.
- [207] F. Monticone, N. M. Estakhri, and A. Alù, "Full control of nanoscale optical transmission with a composite metascreen," *Physical Review Letters*, vol. 110, no. 20, Article ID 203903, 2013.
- [208] R. Dorn, S. Quabis, and G. Leuchs, "Sharper focus for a radially polarized light beam," *Physical Review Letters*, vol. 91, no. 23, Article ID 233901, 2003.

- [209] C. Pfeiffer and A. Grbic, "Cascaded metasurfaces for complete phase and polarization control," *Applied Physics Letters*, vol. 102, no. 23, Article ID 231116, 2013.
- [210] J. Li, S. Chen, H. Yang et al., "Simultaneous control of light polarization and phase distributions using plasmonic metasurfaces," *Advanced Functional Materials*, vol. 25, no. 5, pp. 704–710, 2015.
- [211] P. Alonso-Gonzalez, M. Schnell, P. Sarriugarte et al., "Real-space mapping of Fano interference in plasmonic metamolecules," *Nano Letters*, vol. 11, no. 9, pp. 3922–3926, 2011.
- [212] M. Rahmani, E. Yoxall, B. Hopkins et al., "Plasmonic nanoclusters with rotational symmetry: polarization-invariant far-field response vs changing near-field distribution," *ACS Nano*, vol. 7, no. 12, pp. 11138–11146, 2013.
- [213] A. Tenant and B. Chambers, "A single-layer tuneable microwave absorber using an active FSS," *IEEE Microwave and Wireless Components Letters*, vol. 14, no. 1, pp. 46–47, 2004.
- [214] H.-T. Chen, W. J. Padilla, J. M. O. Zide, A. C. Gossard, A. J. Taylor, and R. D. Averitt, "Active terahertz metamaterial devices," *Nature*, vol. 444, no. 7119, pp. 597–600, 2006.
- [215] S. Zhang, J. Zhou, Y.-S. Park et al., "Photoinduced handedness switching in terahertz chiral metamolecules," *Nature Communications*, vol. 3, article 942, 2012.
- [216] T. Debogovic and J. Perruisseau-Carrier, "MEMS-reconfigurable metamaterials and antenna applications," *International Journal of Antennas and Propagation*, vol. 2014, Article ID 138138, 8 pages, 2014.
- [217] J. P. Turpin, J. A. Bossard, K. L. Morgan, D. H. Werner, and P. L. Werner, "Reconfigurable and tunable metamaterials: a review of the theory and applications," *International Journal of Antennas and Propagation*, vol. 2014, Article ID 429837, 18 pages, 2014.
- [218] B. O. Zhu, J. Zhao, and Y. Feng, "Active impedance metasurface with full 360° reflection phase tuning," *Scientific Reports*, vol. 3, article 3059, 2013.
- [219] Y. H. Fu, A. Q. Liu, W. M. Zhu et al., "A micromachined reconfigurable metamaterial via reconfiguration of asymmetric split-ring resonators," *Advanced Functional Materials*, vol. 21, no. 18, pp. 3589–3594, 2011.
- [220] H. Tao, A. C. Strikwerda, K. Fan, W. J. Padilla, X. Zhang, and R. D. Averitt, "Reconfigurable terahertz metamaterials," *Physical Review Letters*, vol. 103, no. 14, Article ID 147401, 2009.
- [221] W. Pan, C. Huang, P. Chen, M. Pu, X. Ma, and X. Luo, "A beam steering horn antenna using active frequency selective surface," *IEEE Transactions on Antennas and Propagation*, vol. 61, no. 12, pp. 6218–6223, 2013.
- [222] S. Lim, C. Caloz, and T. Itoh, "Metamaterial-based electronically controlled transmission-line structure as a novel leaky-wave antenna with tunable radiation angle and beamwidth," *IEEE Transactions on Microwave Theory and Techniques*, vol. 52, no. 12, pp. 2678–2690, 2004.
- [223] T. Debogović and J. Perruisseau-Carrier, "Array-fed partially reflective surface antenna with independent scanning and beamwidth dynamic control," *IEEE Transactions on Antennas and Propagation*, vol. 62, no. 1, pp. 446–449, 2014.
- [224] W. Pan, C. Huang, P. Chen, X. Ma, C. Hu, and X. Luo, "A low-RCS and high-gain partially reflecting surface antenna," *IEEE Transactions on Antennas and Propagation*, vol. 62, no. 2, pp. 945–949, 2014.
- [225] M. Wang, C. Huang, M. Pu, and X. Luo, "Reducing side lobe level of antenna using frequency selective surface superstrate," *Microwave and Optical Technology Letters*, vol. 57, no. 8, pp. 1971–1975, 2015.
- [226] C. Mias and J. H. Yap, "A varactor-tunable high impedance surface with a resistive-lumped-element biasing grid," *IEEE Transactions on Antennas and Propagation*, vol. 55, no. 7, pp. 1955–1962, 2007.
- [227] J. Zhao, Q. Cheng, J. Chen, M. Q. Qi, W. X. Jiang, and T. J. Cui, "A tunable metamaterial absorber using varactor diodes," *New Journal of Physics*, vol. 15, no. 4, Article ID 043049, 2013.
- [228] M. Wang, C. Hu, M. Pu, C. Huang, X. Ma, and X. Luo, "Electrical tunable L-band absorbing material for two polarisations," *Electronics Letters*, vol. 48, no. 16, pp. 1002–1003, 2012.
- [229] X. Wu, C. Hu, Y. Wang et al., "Active microwave absorber with the dual-ability of dividable modulation in absorbing intensity and frequency," *AIP Advances*, vol. 3, no. 2, Article ID 022114, 2013.
- [230] F. Hu, Y. Qian, Z. Li et al., "Design of a tunable terahertz narrow-band metamaterial absorber based on an electrostatically actuated MEMS cantilever and split ring resonator array," *Journal of Optics*, vol. 15, no. 5, Article ID 055101, 2013.
- [231] D. Shrekenhamer, W.-C. Chen, and W. J. Padilla, "Liquid crystal tunable metamaterial absorber," *Physical Review Letters*, vol. 110, no. 17, Article ID 177403, 2013.
- [232] Q.-Y. Wen, H.-W. Zhang, Q.-H. Yang et al., "A tunable hybrid metamaterial absorber based on vanadium oxide films," *Journal of Physics D: Applied Physics*, vol. 45, no. 23, Article ID 235106, 2012.
- [233] H.-T. Chen, W. J. Padilla, M. J. Cich, A. K. Azad, R. D. Averitt, and A. J. Taylor, "A metamaterial solid-state terahertz phase modulator," *Nature Photonics*, vol. 3, no. 3, pp. 148–151, 2009.
- [234] N. R. Han, Z. C. Chen, C. S. Lim, B. Ng, and M. H. Hon, "Broadband multi-layer terahertz metamaterials fabrication and characterization on flexible substrates," *Optics Express*, vol. 19, no. 8, pp. 6990–6998, 2011.
- [235] Y. Li, Q. Huang, D. C. Wang, X. Li, M. H. Hong, and X. G. Luo, "Polarization-independent broadband terahertz chiral metamaterials on flexible substrate," *Applied Physics A: Materials Science and Processing*, vol. 115, no. 1, pp. 57–62, 2014.
- [236] Z. Chen, M. Rahmani, Y. Gong, T. C. Chong, and M. Hong, "Realization of variable three-dimensional terahertz metamaterial tubes for passive resonance tunability," *Advanced Materials*, vol. 24, no. 23, pp. OP143–OP147, 2012.
- [237] S. Walia, C. M. Shah, P. Gutruf et al., "Flexible metasurfaces and metamaterials: a review of materials and fabrication processes at micro- and nano-scales," *Applied Physics Reviews*, vol. 2, no. 1, Article ID 011303, 2015.
- [238] Z. H. Jiang, S. Yun, F. Toor, D. H. Werner, and T. S. Mayer, "Conformal dual-band near-perfectly absorbing mid-infrared metamaterial coating," *ACS Nano*, vol. 5, no. 6, pp. 4641–4647, 2011.
- [239] Y. Jang, M. Yoo, and S. Lim, "Conformal metamaterial absorber for curved surface," *Optics Express*, vol. 21, no. 20, pp. 24163–24170, 2013.
- [240] F. Aieta, P. Genevet, M. Kats, and F. Capasso, "Aberrations of flat lenses and aplanatic metasurfaces," *Optics Express*, vol. 21, no. 25, pp. 31530–31539, 2013.
- [241] M. Diem, T. Koschny, and C. M. Soukoulis, "Wide-angle perfect absorber/thermal emitter in the terahertz regime," *Physical Review B*, vol. 79, no. 3, Article ID 033101, 2009.
- [242] T. Jang, H. Youn, Y. J. Shin, and L. J. Guo, "Transparent and flexible polarization-independent microwave broadband absorber," *ACS Photonics*, vol. 1, no. 3, pp. 279–284, 2014.

- [243] L. Cong, N. Xu, J. Gu, R. Singh, J. Han, and W. Zhang, "Highly flexible broadband terahertz metamaterial quarter-wave plate," *Laser and Photonics Reviews*, vol. 8, no. 4, pp. 626–632, 2014.
- [244] Y. Shen, V. Rinnerbauer, I. Wang, V. Stelmakh, J. D. Joannopoulos, and M. Soljačić, "Structural colors from fano resonances," *ACS Photonics*, vol. 2, no. 1, pp. 27–32, 2015.
- [245] J. Sun, L. Liu, G. Dong, and J. Zhou, "An extremely broad band metamaterial absorber based on destructive interference," *Optics Express*, vol. 19, no. 22, pp. 21155–21162, 2011.
- [246] D. Ye, Z. Wang, K. Xu et al., "Ultrawideband dispersion control of a metamaterial surface for perfectly-matched-layer-like absorption," *Physical Review Letters*, vol. 111, no. 18, Article ID 187402, 2013.
- [247] A. K. Geim and K. S. Novoselov, "The rise of graphene," *Nature Materials*, vol. 6, no. 3, pp. 183–191, 2007.
- [248] R. R. Nair, P. Blake, A. N. Grigorenko et al., "Fine structure constant defines visual transparency of graphene," *Science*, vol. 320, no. 5881, p. 1308, 2008.
- [249] M. Pu, P. Chen, Y. Wang et al., "Strong enhancement of light absorption and highly directive thermal emission in graphene," *Optics Express*, vol. 21, no. 10, pp. 11618–11627, 2013.
- [250] S. H. Lee, M. Choi, T.-T. Kim et al., "Switching terahertz waves with gate-controlled active graphene metamaterials," *Nature Materials*, vol. 11, no. 11, pp. 936–941, 2012.
- [251] A. Ferreira and N. M. R. Peres, "Complete light absorption in graphene-metamaterial corrugated structures," *Physical Review B*, vol. 86, no. 20, Article ID 205401, 2012.
- [252] M. Wang, Y. Wang, M. Pu et al., "Circular dichroism of graphene-based absorber in static magnetic field," *Journal of Applied Physics*, vol. 115, no. 15, Article ID 154312, 2014.
- [253] Y. Wang, X. Ma, M. Pu et al., "Transfer of orbital angular momentum through sub-wavelength waveguides," *Optics Express*, vol. 23, no. 3, pp. 2857–2862, 2015.
- [254] A. E. Minovich, A. E. Miroshnichenko, A. Y. Bykov, T. V. Murzina, D. N. Neshev, and Y. S. Kivshar, "Functional and nonlinear optical metasurfaces," *Laser & Photonics Reviews*, vol. 9, no. 2, pp. 195–213, 2015.
- [255] H. Aouani, M. Navarro-Cia, M. Rahmani et al., "Multiresonant broadband optical antennas as efficient tunable nanosources of second harmonic light," *Nano Letters*, vol. 12, no. 9, pp. 4997–5002, 2012.
- [256] G. Grinblat, M. Rahmani, E. Cortés et al., "High-efficiency second harmonic generation from a single hybrid ZnO nanowire/Au plasmonic nano-oligomer," *Nano Letters*, vol. 14, no. 11, pp. 6660–6665, 2014.
- [257] H. Aouani, M. Rahmani, M. Navarro-Cía, and S. A. Maier, "Third-harmonic-upconversion enhancement from a single semiconductor nanoparticle coupled to a plasmonic antenna," *Nature Nanotechnology*, vol. 9, no. 4, pp. 290–294, 2014.
- [258] J. Lee, M. Tymchenko, C. Argyropoulos et al., "Giant nonlinear response from plasmonic metasurfaces coupled to intersubband transitions," *Nature*, vol. 511, no. 7507, pp. 65–69, 2014.
- [259] K. O'Brien, H. Suchowski, J. Rho et al., "Predicting nonlinear properties of metamaterials from the linear response," *Nature Materials*, vol. 14, no. 4, pp. 379–383, 2015.
- [260] G. Liang, C. Wang, Z. Zhao et al., "Squeezing bulk plasmon polaritons through hyperbolic metamaterial for large area deep subwavelength interference lithography," *Advanced Optical Materials*, 2015.
- [261] Z.-W. Liu, Q.-H. Wei, and X. Zhang, "Surface plasmon interference nanolithography," *Nano Letters*, vol. 5, no. 5, pp. 957–961, 2005.
- [262] A. Nemirovski, M. Gonidec, J. M. Fox, P. Jean-Remy, E. Turnage, and G. M. Whitesides, "Engineering shadows to fabricate optical metasurfaces," *ACS Nano*, vol. 8, no. 11, pp. 11061–11070, 2014.
- [263] J. Zhao, S. Jaber, P. Mulvaney, P. V. Braun, and H. Giessen, "Repetitive hole-mask colloidal lithography for the fabrication of large-area low-cost plasmonic multishape single-layer metasurfaces," *Advanced Optical Materials*, vol. 3, no. 5, pp. 680–686, 2015.
- [264] K. Robbie, M. J. Brett, and A. Lakhtakia, "Chiral sculptured thin films," *Nature*, vol. 384, no. 6610, p. 616, 1996.
- [265] Y.-L. Zhang, Q.-D. Chen, H. Xia, and H.-B. Sun, "Designable 3D nanofabrication by femtosecond laser direct writing," *Nano Today*, vol. 5, no. 5, pp. 435–448, 2010.
- [266] C. R. Brewitt-Taylor, "Limitation on the bandwidth of artificial perfect magnetic conductor surfaces," *IET Microwaves, Antennas and Propagation*, vol. 1, no. 1, pp. 255–260, 2007.
- [267] P.-Y. Chen, C. Argyropoulos, and A. Alù, "Broadening the cloaking bandwidth with non-foster metasurfaces," *Physical Review Letters*, vol. 111, no. 23, Article ID 233001, 2013.
- [268] F. Aieta, M. A. Kats, P. Genevet, and F. Capasso, "Multiwavelength achromatic metasurfaces by dispersive phase compensation," *Science*, vol. 347, no. 6228, pp. 1342–1345, 2015.
- [269] W. Chen, M. D. Thoreson, S. Ishii, A. V. Kildishev, and V. M. Shalaev, "Ultra-thin ultra-smooth and low-loss silver films on a germanium wetting layer," *Optics Express*, vol. 18, no. 5, pp. 5124–5134, 2010.

## Research Article

# Resonances in Reverse Vavilov-Cherenkov Radiation Produced by Electron Beam Passage over Periodic Interface

**Gerard Granet,<sup>1</sup> Petr Melezhik,<sup>2</sup> Anatoliy Poyedinchuk,<sup>2</sup> Seil Sautbekov,<sup>3</sup> Yuriy Sirenko,<sup>2,3</sup> and Nataliya Yashina<sup>2</sup>**

<sup>1</sup>*Universite Blaise Pascal, Avenue des Landais 24, 63177 Clermont-Ferrand, France*

<sup>2</sup>*A.Ya. Usikov Institute of Radiophysics and Electronics, National Academy of Sciences of Ukraine, 12 Ak. Proskury Street, Kharkov 61085, Ukraine*

<sup>3</sup>*L.N. Gumilyov Eurasian National University, 2 Mirzoyana Street, Astana 010000, Kazakhstan*

Correspondence should be addressed to Yuriy Sirenko; [yks@bk.ru](mailto:yks@bk.ru)

Received 12 March 2015; Revised 11 July 2015; Accepted 14 July 2015

Academic Editor: Weiren Zhu

Copyright © 2015 Gerard Granet et al. This is an open access article distributed under the Creative Commons Attribution License, which permits unrestricted use, distribution, and reproduction in any medium, provided the original work is properly cited.

Resonances in reverse Vavilov-Cherenkov radiation produced by the charged particles beam passage over periodic boundary of dispersive left-handed medium are found out and studied. Analysis and modeling are performed on the base of rigorous mathematical approaches. For the first time, several physical peculiarities owing to these effects are considered in the conditions of possible resonant scattering of electromagnetic waves.

## 1. Introduction

Vavilov-Cherenkov radiation is appreciated as one of the greatest discoveries of the 20th century. The modern history of Vavilov-Cherenkov radiation (VChR) goes back to Cherenkov's experiments, 1934–1937 [1]. Tamm and Frank developed this radiation theory in 1937 [2]. In 1958, the work was awarded a Nobel Prize in physics. Since then, VChR has been extensively used in physics and engineering [3]. As materials science and engineering advance, actual left-handed media providing qualitatively new characteristics in the implementation of well-known phenomena come and cause a fresh interest in VChR from both theoretical and applied standpoints.

The study presented in the paper considers several still poorly understood peculiarities of the diffraction radiation [4] and, in particular, the direct and reverse VChR [4–7] produced by a beam of charged particles moving above the dispersive medium surface (generally periodic). Depending on frequency, this medium can be right-handed (conventional dielectric), mononegative (either permittivity or permeability is negative), or left-handed (both permittivity and permeability are negative). Emphasis is placed on the radiation characteristics in the conditions of possible resonant scattering of

electromagnetic waves when the modulation period of the electron beam is comparable with the interface period and the excitation of eigenwaves supported by this boundary is possible. The study of resonant situations requires adequate research methods and tools that are based mainly on the idea of analytic regularization of boundary value problems in electromagnetic theory of gratings [8, 9].

## 2. Models and Characteristics

In free space ( $\epsilon(g) = \mu(g) = 1$ ), the eigenfield  $\{\vec{E}^i(g, k), \vec{H}^i(g, k)\}$  of electron beam with modulated density and the instantaneous value of the charge density given by the expression  $\rho\delta(z - a)\exp[i((k/\beta)y - kt)]$  represents the  $H$ -polarized field ( $\partial/\partial x \equiv 0, E_x^i = H_y^i = H_z^i = 0$ ) and accordingly [4]

$$H_x^i(g, k) = 2\pi\rho\beta$$

$$\cdot \exp \left\{ i \left[ \sqrt{k^2 - \left( \frac{k}{\beta} \right)^2} |z - a| + \left( \frac{k}{\beta} \right) y \right] \right\}$$

$$\begin{aligned}
& \cdot \left[ \frac{|z-a|}{(z-a)} \right]; \quad z \neq a, \\
E_y^i(g, k) &= -\left(\frac{\eta_0}{ik}\right) \frac{\partial H_x^i(g, k)}{\partial z}, \\
E_z^i(g, k) &= \left(\frac{\eta_0}{ik}\right) \frac{\partial H_x^i(g, k)}{\partial y}.
\end{aligned} \tag{1}$$

Here  $\delta(\dots)$  is Dirac's  $\delta$ -function;  $\rho$  and  $k$  are the amplitude and the modulation frequency of the electron beam and  $0 < \beta < 1$  is beam's relative velocity;  $\eta_0 = (\mu_0/\epsilon_0)^{1/2}$  is the impedance of free space;  $\epsilon_0$  and  $\mu_0$  are electric and magnetic constants of the vacuum;  $\epsilon(g)$  and  $\mu(g)$  are relative permittivity and permeability of the medium in the domain of wave propagation;  $g = \{y, z\}$  is a point in the space  $R^2$ ; time dependence of the harmonically oscillating fields is determined by the factor  $\exp(-ikt)$ . All physical quantities have the dimension of the SI, only "time" is measured in meters; it is the product of the real time on the speed of light in vacuum.

Suppose  $-2\pi\rho\beta\sqrt{l}\exp[-k(a-h)\sqrt{(1/\beta)^2-1}] = 1$ . Then, eigenfield (1) of the electron beam passing in the conventional medium (vacuum) over the periodic boundary  $S$  (see Figure 1) of the dispersive medium with constitutive parameters defined by relations

$$\begin{aligned}
\epsilon(k) &= 1 - \frac{k_\epsilon^2}{k^2}, \\
\mu(k) &= 1 - \frac{k_\mu^2}{k^2}
\end{aligned} \tag{2}$$

generates in the domains  $z \geq h$  and  $z \leq 0$  the  $H$ -polarized field  $\{\vec{E}^s(g, k), \vec{H}^s(g, k)\}$  with nonzero components represented as follows [8]:

$$\begin{aligned}
H_x^s(g, k) &= \sum_{n=-\infty}^{\infty} \mu_n(y) \begin{cases} R_n(k) \exp[i\Gamma_n(z-h)]; & z \geq h \\ T_n(k) \exp[-i\Gamma_n^{\epsilon,\mu} z]; & z \leq 0, \end{cases} \\
E_y^s(g, k) &= -\frac{\eta_0}{ik\epsilon(g)} \frac{\partial H_x^s(g, k)}{\partial z} = \frac{\eta_0}{k} \sum_{n=-\infty}^{\infty} \mu_n(y) \\
&\cdot \begin{cases} -R_n(k) \Gamma_n \exp[i\Gamma_n(z-h)]; & z \geq h \\ T_n(k) \Gamma_n^{\epsilon,\mu} \epsilon^{-1}(k) \exp[-i\Gamma_n^{\epsilon,\mu} z]; & z \leq 0, \end{cases} \\
E_z^s(g, k) &= \frac{\eta_0}{ik\epsilon(g)} \frac{\partial H_x^s(g, k)}{\partial y} = \frac{\eta_0}{k} \sum_{n=-\infty}^{\infty} \Phi_n \mu_n(y) \\
&\cdot \begin{cases} R_n(k) \exp[i\Gamma_n(z-h)]; & z \geq h \\ T_n(k) \epsilon^{-1}(k) \exp[-i\Gamma_n^{\epsilon,\mu} z]; & z \leq 0. \end{cases}
\end{aligned} \tag{3}$$

Here,  $l$  and  $0 \leq h < a$  are the period length and height of the corrugation mounts  $S = \{g : z = f(y), 0 \leq f(y) \leq h\}$ ;

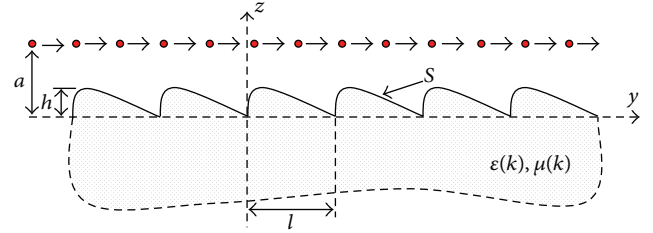


FIGURE 1: Geometry of the problem of diffraction radiation.

$k = 2\pi/\lambda$  and  $\lambda$  is the length of the electromagnetic waves in free space;  $k_\epsilon$  and  $k_\mu$  are the characteristic frequencies of dispersive medium;  $\mu_n(y) = l^{-1/2} \exp(i\Phi_n y)$ ,  $\Phi_n = 2\pi n/l + \Phi_0$ , and  $\Phi_0 = k/\beta$ ;  $\Gamma_n = \sqrt{k^2 - \Phi_n^2}$  and  $\operatorname{Re} \Gamma_n \geq 0$ ,  $\operatorname{Im} \Gamma_n \geq 0$ . Signs of real and imaginary parts of the root  $\Gamma_n^{\epsilon,\mu} = \sqrt{k^2 \epsilon(k) \mu(k) - \Phi_n^2}$  are given so that all partial components  $U_n^T(g, k) = T_n(k) \exp[-i\Gamma_n^{\epsilon,\mu} z] \mu_n(y)$  (spatial harmonics) of the field  $\{\vec{E}^s(g, k), \vec{H}^s(g, k)\}$  in the domain  $z \leq 0$  are the outgoing plane waves, that is, homogeneous waves ( $\operatorname{Im} \Gamma_n^{\epsilon,\mu} = 0$ ), transferring energy in the direction towards  $z = -\infty$  or the inhomogeneous waves ( $\operatorname{Re} \Gamma_n^{\epsilon,\mu} = 0$ ), exponentially decaying when moving in the same direction.

Amplitude coefficients  $R_n(k)$  and  $T_n(k)$  are complicated function of frequency and geometric and constitutive parameters of the media of wave propagation. We find them by solving numerically the following boundary value problem [8] in the strip  $0 \leq y \leq l$ :

$$\left[ \frac{\partial^2}{\partial y^2} + \frac{\partial^2}{\partial z^2} + k^2 \epsilon(g) \mu(g) \right] H_x(g, k) = 0; \quad 0 \leq z \leq h, \tag{4a}$$

$$\begin{aligned}
H_x \left\{ \frac{\partial H_x}{\partial y} \right\} (l, z, k) &= \exp(i\Phi_0 l) H_x \left\{ \frac{\partial H_x}{\partial y} \right\} (0, z, k); \\
0 \leq z \leq h,
\end{aligned} \tag{4b}$$

$$\begin{aligned}
H_x(g, k) &= \sum_{n=-\infty}^{\infty} \mu_n(y) \\
&\cdot \begin{cases} \delta_m^n \exp[-i\Gamma_n(z-h)] + R_n(k) \exp[i\Gamma_n(z-h)]; & z \geq h \\ T_n(k) \exp[-i\Gamma_n^{\epsilon,\mu} z]; & z \leq 0, \end{cases} \tag{4c}
\end{aligned}$$

$$H_x(g, k), E_{tg}(g, t)$$

$$\begin{aligned}
&\text{are continuous across } S \text{ and virtual boundaries } z = 0, z = h. \tag{4d}
\end{aligned}$$

Here,  $\delta_m^n$  is the Kronecker symbol and  $H_x(g, k)$  is one of the three nonzero components of the total field

$$\begin{aligned}
&\{\vec{E}(g, k), \vec{H}(g, k)\} \\
&= \begin{cases} \{\vec{E}^i(g, k), \vec{H}^i(g, k)\} + \{\vec{E}^s(g, k), \vec{H}^s(g, k)\}; & z \geq h \\ \{\vec{E}^s(g, k), \vec{H}^s(g, k)\}; & z < h. \end{cases} \tag{5}
\end{aligned}$$

This problem allows determining (within the approximation of a given current) the electromagnetic field (field

of diffraction radiation) generated by density modulated electron beam [4, 8]. The method, usually called as a method of analytic regularization [8, 9], was used for numerical solving of the problem of interest. The application of this method provided already the majority of the physical and applied results of the electromagnetic theory of gratings associated with resonant and anomalous spatial-frequency and spatial-time transformations of electromagnetic fields in periodic structures [8, 10–13].

The energy characteristics of diffraction radiation are given by the relation [8]

$$\begin{aligned} & \sum_{n=-\infty}^{\infty} \left[ |R_n|^2 \operatorname{Re} \Gamma_n + |T_n|^2 \operatorname{Re} \Gamma_n^{\varepsilon, \mu} \varepsilon^{-1}(k) \right] \\ & = 2 \operatorname{Im} R_0 \operatorname{Im} \Gamma_0, \end{aligned} \quad (6)$$

obtained by the application of the Poynting theorem for complex power to the field  $\{\vec{E}(g, k), \vec{H}(g, k)\}$  within the domain  $[0 \leq y \leq l] \times [0 \leq z \leq h]$ . The term in the left part in (6) is the total electromagnetic energy  $W = W^\uparrow + W^\downarrow$  radiated into the half-spaces  $z \geq h$  and  $z \leq 0$ . In the approximation of the given current, it is determined by the expression  $2 \operatorname{Im} R_0 \operatorname{Im} \Gamma_0$ . The values  $W_n^R = |R_n|^2 \operatorname{Re} \Gamma_n$  and  $W_n^T = |T_n|^2 \operatorname{Re} \Gamma_n^{\varepsilon, \mu} \varepsilon^{-1}(k)$  characterize the distribution of the energy, lost by the electrons beam, between the channels open for radiation, that is, between the harmonics of the spatial spectrum such that  $\operatorname{Re} \Gamma_n \geq 0$  and/or  $\operatorname{Re} \Gamma_n^{\varepsilon, \mu} \varepsilon^{-1}(k) > 0$ . The last inequality and the relationship  $\operatorname{Re} P_y(k) = \varepsilon^{-1}(k) \sum_{n: \operatorname{Im} \Gamma_n^{\varepsilon, \mu} = 0} |T_n|^2 \Phi_n$  ( $P_y(k)$  is the  $y$ -component of the Poynting vector  $\vec{P}(k)$  for field  $\{\vec{E}(g, k), \vec{H}(g, k)\}$  in the plane  $z = 0$  averaged over the period  $l$ ) allow determining unambiguously and quite rigorously the direction of the phase velocity of propagating in the half-space  $z > 0$  harmonic  $U_n^T(g, k)$  and the direction in which this harmonic carries the energy. In conventional media, these directions coincide and are given by the vector  $\Phi_n \vec{y} - \Gamma_n^{\varepsilon, \mu} \vec{z}$ ,  $\Gamma_n^{\varepsilon, \mu} > 0$ . In binegative media  $\Gamma_n^{\varepsilon, \mu} < 0$ , the phase velocity is oriented along the vector  $\Phi_n \vec{y} - \Gamma_n^{\varepsilon, \mu} \vec{z}$ , and the energy transfer holds along the vector  $-\Phi_n \vec{y} + \Gamma_n^{\varepsilon, \mu} \vec{z}$ . In media with only one negative constitutive parameter the harmonics  $U_n^T(g, k)$  carrying the energy in the direction  $z = -\infty$  are forbidden and cannot be excited.

For  $\{\vec{E}'(g, k), \vec{H}'(g, k)\} \equiv 0$  and  $k > 0$  fixed, the homogeneous (spectral) problem is obtained from (4a)–(4c). Its nontrivial solutions  $H_x(g, \overline{\Phi}_{0(m)})$  exist for no more than a countable set of eigenvalues  $\{\overline{\Phi}_{0(m)}\}_m \in F$  and define the field of eigenwaves  $\{\vec{E}(g, \overline{\Phi}_{0(m)}), \vec{H}(g, \overline{\Phi}_{0(m)})\}$  of the periodic interface [8, 10]. If several eigenvalues belong to the real axis  $\operatorname{Re} \Phi_0$  of the first physical sheet of the surface  $F$  (i.e., a Riemann surface onto which the solution of the problem (4a)–(4c) can be analytically continued from the domain of real values of the spectral parameter  $\Phi_0$ ), then we are dealing with conventional surface (or regular) waves propagating near the interface without attenuation. Otherwise, leaky waves, piston-type waves, and so forth do exist [8].

### 3. Physical Results: Plane Boundary

A flat boundary separating a conventional environment (vacuum) and a nonabsorbing dispersion medium (the medium sort discussed below) is able to support direct (or forward) surface waves in the frequency range [10]

$$K_2 = \frac{k_\varepsilon k_\mu}{\sqrt{k_\varepsilon^2 + k_\mu^2}} < k < \frac{k_\varepsilon}{\sqrt{2}} = K_1; \quad k_\varepsilon > k_\mu. \quad (7)$$

These waves correspond to the propagation constants  $\overline{\Phi}_0^{\text{direct}} = kk_\varepsilon^{-1} \sqrt{(k_\varepsilon^2 - k^2)(k_\varepsilon^2 - k_\mu^2)(k_\varepsilon^2 - 2k^2)^{-1}}$  and velocity  $\beta = \beta^{\text{direct}} = k/\overline{\Phi}_0^{\text{direct}}$  of synchronously moving electron beam.

Within the range

$$\frac{k_\varepsilon}{\sqrt{2}} < k < \frac{k_\varepsilon k_\mu}{\sqrt{k_\varepsilon^2 + k_\mu^2}}; \quad k_\varepsilon < k_\mu, \quad (8)$$

this boundary can support backward waves having phase and group velocities oppositely directed and characterized by anomalous dispersion. For such waves, the velocity of the synchronously moving beam is  $\beta = \beta^{\text{back}} = k/\overline{\Phi}_0^{\text{back}}$  and  $\overline{\Phi}_0^{\text{back}} = kk_\varepsilon^{-1} \sqrt{(k_\varepsilon^2 - k^2)(k_\mu^2 - k_\varepsilon^2)(2k^2 - k_\varepsilon^2)^{-1}}$ .

Figure 2 shows  $\varepsilon(k)$  and  $\mu(k)$ , propagation constants of eigensurface waves and velocity of electron beam synchronized with these waves versus frequency  $k$ . All these dependencies are presented within the ranges defined by (7) and (8). For  $k_\mu = 0.5$ ,  $k_\varepsilon = 1.0$ , and  $0.4472 < k < 0.7071$ , we have the forward waves (Figure 2(b)). For  $k_\mu = 1.0$ ,  $k_\varepsilon = 0.5$ , and  $0.3536 < k < 0.4472$ , the backward waves (Figure 2(a)).

Principal differences in the behavior of these characteristics for forward and backward surface waves are rather obvious. In the frequency range  $K_1 < k < K_2$  where the backward waves exist, the medium is binegative:  $\varepsilon(k) < 0$  and  $\mu(k) < 0$ . At the same time in the domain of the forward waves existence, the binegative medium transforms into a medium with  $\varepsilon(k) < 0$  and  $\mu(k) > 0$ . Naturally, these differences also affect the characteristics of the field excited by the electron beam.

The VChR into the lower half-space filled with the dispersive medium is possible under the condition  $\beta^2 > [\varepsilon(k)\mu(k)]^{-1}$ , which can be satisfied only for the bipositive (conventional medium, direct VChR) or binegative (reverse VChR) media. The dispersion law given by (2) yields the following frequency restriction:

$$k < K_0 = \frac{\sqrt{2}k_\varepsilon k_\mu}{\sqrt{k_\varepsilon^2 + k_\mu^2 + \sqrt{(k_\varepsilon^2 - k_\mu^2)^2 + 4k_\varepsilon^2 k_\mu^2 / \beta^2}}}. \quad (9)$$

It can be shown that the inequality  $K_0 < k_\varepsilon k_\mu / \sqrt{k_\varepsilon^2 + k_\mu^2}$  always holds if  $0 < \beta < 1$ . And as  $\beta \rightarrow 0$ , then  $K_0 \rightarrow 0$ . As  $\beta \rightarrow 1$ ,  $K_0 \rightarrow k_\varepsilon k_\mu / \sqrt{k_\varepsilon^2 + k_\mu^2}$ . In Figure 2, the VChR domain is darkened.

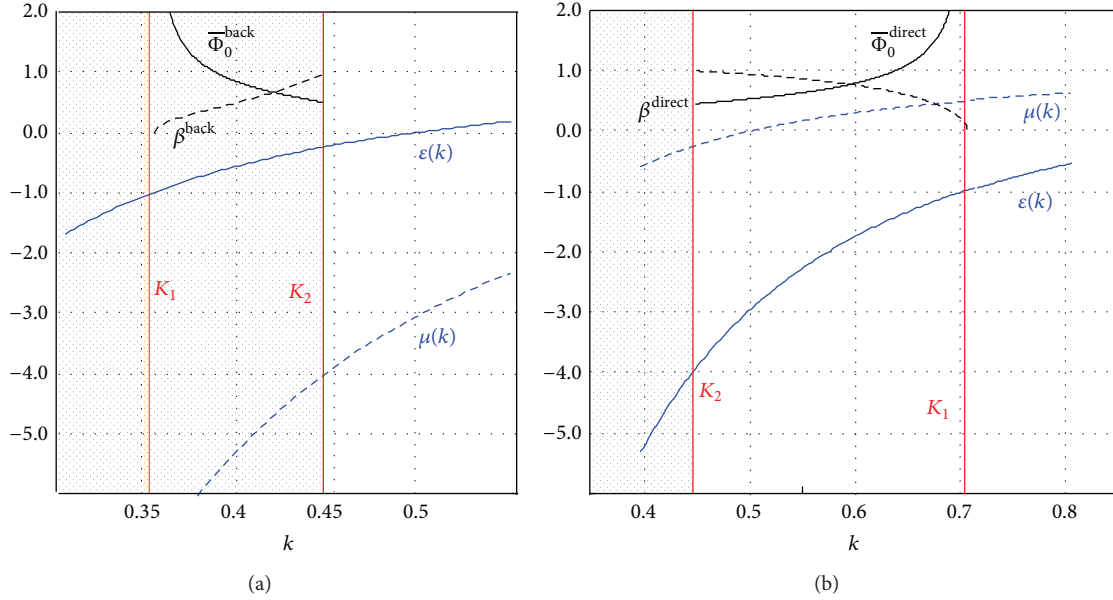


FIGURE 2: Curves of  $\varepsilon(k)$ ,  $\mu(k)$ ,  $\overline{\Phi}_0^{\text{back}}$ ,  $\overline{\Phi}_0^{\text{direct}}$ ,  $\beta^{\text{back}}$ , and  $\beta^{\text{direct}}$ .

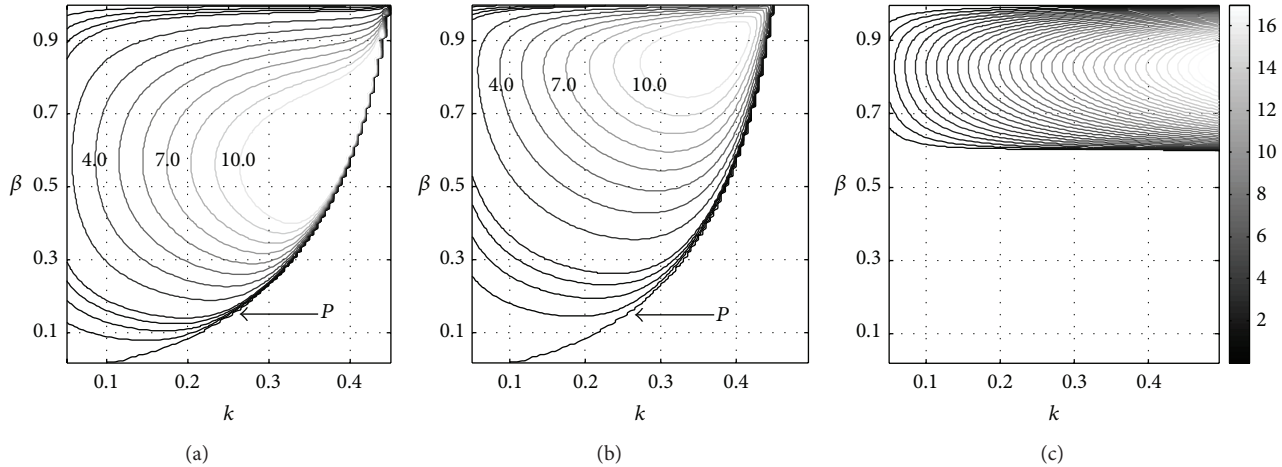


FIGURE 3: Contour plots of  $W_0^T(k, \beta) = \text{const}$ , characterizing the radiation intensity in the half-space  $z < 0$ : (a)  $k_e = 0.5$  and  $k_\mu = 1.0$ ; (b)  $k_e = 1.0$  and  $k_\mu = 0.5$ ; (c)  $\varepsilon = -2.24$ ,  $\mu = -1.24$ , and  $\beta = (\varepsilon\mu)^{-1/2} \approx 0.6$ .

In the case  $k_e < k_\mu$ , the frequency region of the VChR and the backward surface wave region overlap. On the contrary, when  $k_e > k_\mu$ , the domain of the forward surface waves is beyond the domain of possible observation of the VChR.

At  $h = 0$ , only zeroth spatial harmonics with amplitudes  $R_0(k)$  and  $T_0(k)$  remain in (4a)–(4c). The zeroth spatial harmonic in the dispersive material becomes propagating, that is, transferring the energy infinitely far in the direction  $z = -\infty$  provided  $\text{Im } \Gamma_n^{\varepsilon, \mu}(k) = 0$ , or what is the same, provided  $\beta^2 > [\varepsilon(k)\mu(k)]^{-1}$ , which is necessary for the VChR existence. Both the diffraction radiation and the VChR are associated with the transfer of electromagnetic energy in the same direction. Therefore, following [4], we identify the Vavilov-Cherenkov radiation with the diffraction radiation

on the fundamental (zeroth) spatial harmonic of the periodic interface.

Figure 3 shows the contour plots  $W_0^T(k, \beta) = \text{const}$ , describing the radiation intensity of VChR in the half-space  $z < 0$ . Various fragments correspond to the media with different parameters  $\varepsilon(k)$  and  $\mu(k)$ . And everywhere, as one would expect, the range of values  $k$  and  $\beta$  in which  $W_0^T(k, \beta) > 0$  is bounded by curves  $P : \beta = [\varepsilon(k)\mu(k)]^{-1/2}$  restricting the domain of VChR existence.

In the case  $k_e > k_\mu$  (Figure 3(b)), a maximum VChR intensity region is shifted towards higher  $\beta$  ( $0.75 < \beta < 0.95$ ) and it is concentrated in the vicinity of the curve  $P$ . In the case  $k_e < k_\mu$  (Figure 3(a)), a similar area is again located near  $P$ , but shifted towards  $0.4 < \beta < 0.75$ . These

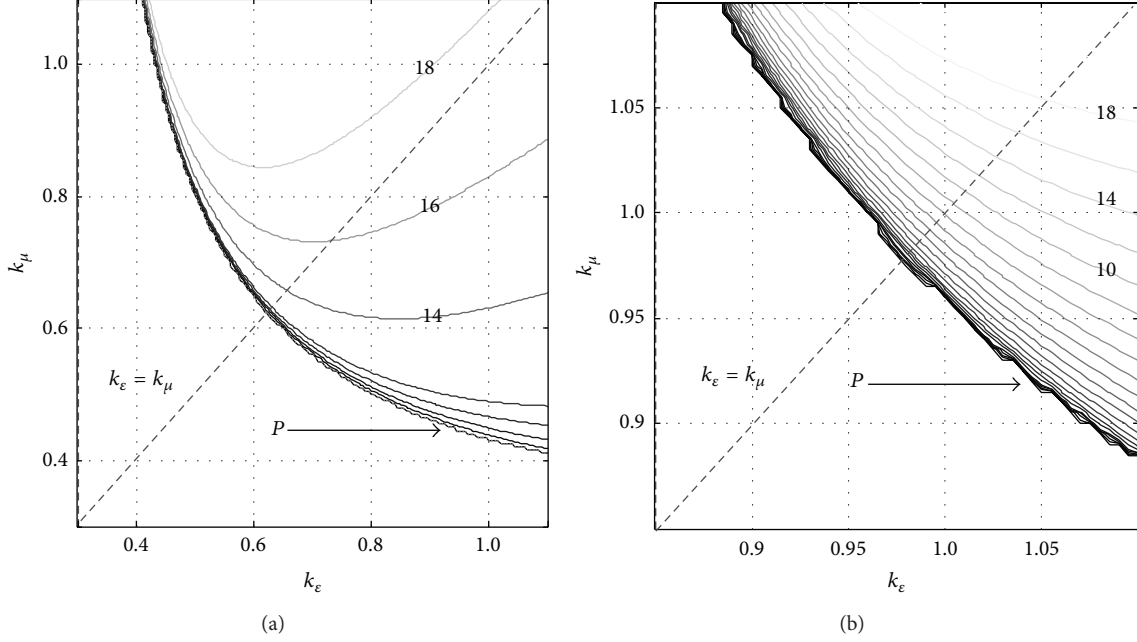


FIGURE 4: Contour plots for  $W_0^T(k_e, k_\mu) = \text{const}$ : (a)  $k = 0.3$  and  $\beta = 0.3$ ; (b)  $k = 0.6$  and  $\beta = 0.6$ .

behavioral features of energy characteristics are observed only in the dispersive medium. For a dispersion-free medium (Figure 3(c))  $\max_{(\varepsilon\mu)^{-1/2} < \beta < 1} W_0^T(k, \beta)$  is attained at any  $k$ , but  $\beta \approx 0.83$  keeps unchanged. The value  $\max_{(\varepsilon\mu)^{-1/2} < \beta < 1} W_0^T(k, \beta)$  grows with  $k$ .

The contour plots  $W_0^T(k_e, k_\mu) = \text{const}$  in Figure 4 give a fairly complete picture of the influence of the constitutive parameters of the dispersive medium with a plane boundary on the VChR energy characteristics. Interestingly, in the case of large  $k$  and  $\beta$  (in Figure 4(b)), the lines  $W_0^T(k_e, k_\mu) = \text{const}$  intersect with straight line  $k_e = k_\mu$  (the most rapid variation of VChR intensity) at an almost right angle, while for smaller  $k$  and  $\beta$  (see Figure 4(a)) and  $k_e > 0.8$  the passage along the line  $k_e = k_\mu$  does not lead to a noticeable change in the VChR intensity.

#### 4. Physical Results: Periodically Rough Boundary

In the case of a periodically rough boundary  $S$  (further on we assume  $l = 2\pi$ ), the radiation field in the domain  $z \geq h$  ( $z < 0$ ) consists of spatial harmonics  $U_n^R(g, k) = R_n(k) \exp[i\Gamma_n(z - h)]\mu_n(y)(U_n^T(g, k))$  propagating without attenuation. So, it is represented by harmonics with such  $n$  that  $\text{Im } \Gamma_n = 0$  ( $\text{Im } \Gamma_n^{\varepsilon, \mu} = 0$ ). Obviously, when  $\Phi_0 = k/\beta$  only harmonics with negative  $n$  can propagate without attenuation in the domain  $z \geq h$ . In a dispersive medium, the range of  $k$  and  $\beta$  providing the propagation without decay of one or another spatial harmonic  $U_n^T(g, k)$  can be easily determined using the data on the configuration of their limits  $Q_n : \Gamma_n^{\varepsilon, \mu}(k, \beta) = 0$  (see, e.g., Figure 5(a)).

A periodically rough boundary supports a larger number of surface waves. Their propagation constants in the frequency range of interest ( $k < 1$ ) and small  $h$  are given by the approximate relations  $\overline{\Phi}_0^{\text{direct}, \pm, m} = \pm \overline{\Phi}_0^{\text{direct}} + m$  and  $\overline{\Phi}_0^{\text{back}, \pm, m} = \pm \overline{\Phi}_0^{\text{back}} + m$ ,  $m = 0, \pm 1, \pm 2, \dots$  [8, 10]. Accordingly, we define the sets of approximate values  $\beta^{\text{direct}, \pm, m} = k/\overline{\Phi}_0^{\text{direct}, \pm, m}$  and  $\beta^{\text{back}, \pm, m} = k/\overline{\Phi}_0^{\text{back}, \pm, m}$  (see Figures 5(b) and 5(c)). It should be pointed out that all the curves corresponding to velocities  $\beta^{\text{direct}, \pm, m}$  and  $\beta^{\text{back}, \pm, m}$  practically merge near the values of the frequency parameter  $k = k_{\text{accum}} = k_e/\sqrt{2}$ , which for the given dispersion law (2) define accumulation point of the frequency spectra of the electrodynamic structure [13]. At this point,  $\varepsilon(k) = -1$  in the vicinity of this frequency, there are an infinite number of resonances in the intensity of diffraction radiation.

Consider now the changes in the radiation field arising for  $h \neq 0$  in that case when only zeroth spatial harmonic propagates in the lower half-space without decay. Figure 6 shows the frequency dependence of the intensity of radiation in the lower half-space for the electron beam velocity  $\beta = 0.89$ . Over the whole frequency range considered here, we have  $\varepsilon(k) < 0$  and  $\mu(k) < 0$ . For parameters  $k_e = 1.0$  and  $k_\mu = 0.5$  (see Figure 6(a)), a periodic boundary within the considered frequency range and for not very large  $h$  does not support propagation of surface waves, and  $W_0^T(k)$  behaves almost in the same way as in the case  $h = 0$ .

For parameters  $k_e = 0.5$  and  $k_\mu = 1.0$  (see Figure 6(b)), the periodic boundary supports the propagation of backward surface waves (see Figure 2(a)). This fact changes significantly the  $W_0^T(k)$  behavior: at  $k \approx 0.4365$  a certain resonance appears due to the excitation of the surface wave with

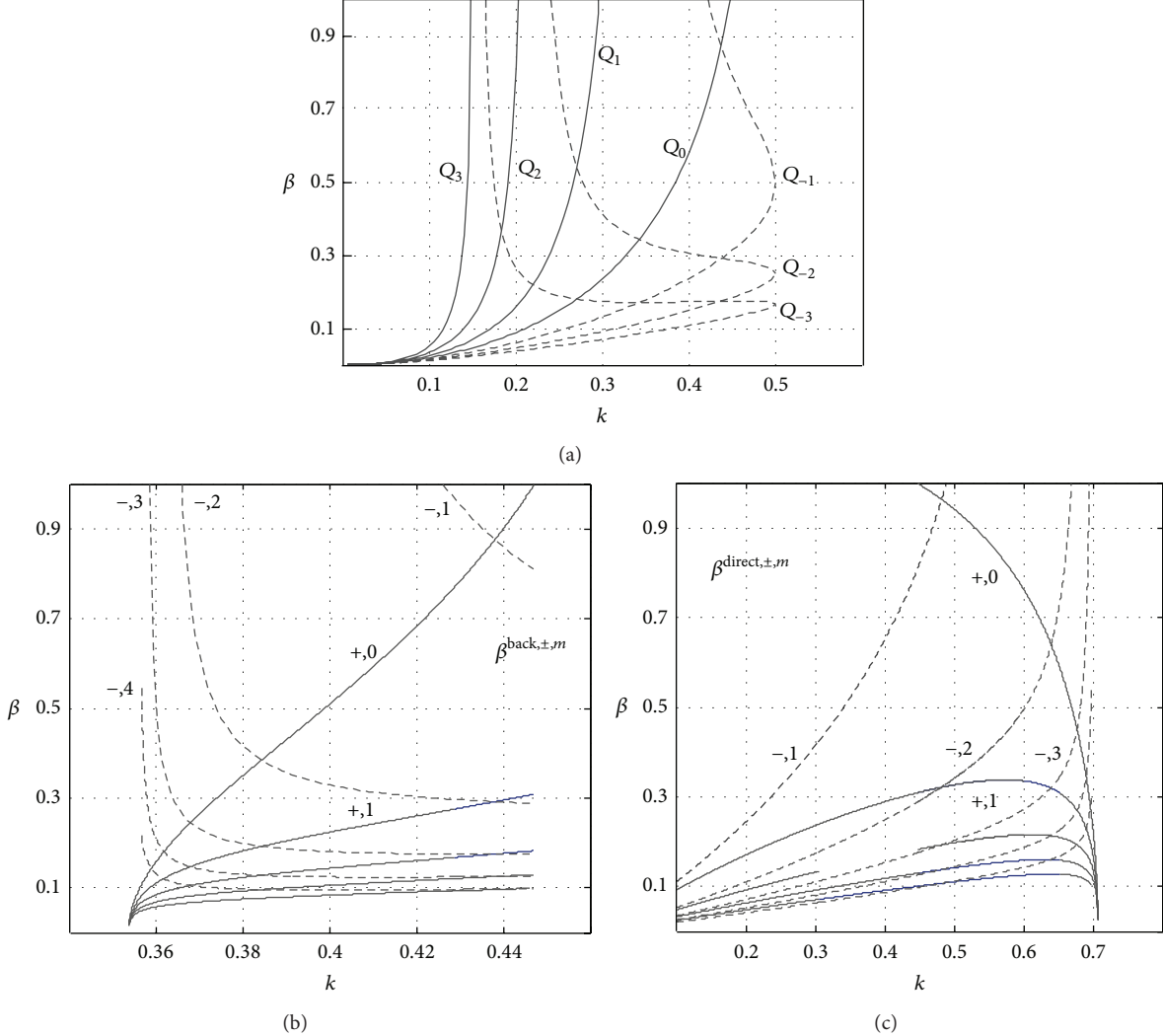


FIGURE 5: (a) Configuration of boundaries  $Q_n$ ; (b) phase velocities of backward eigenwaves,  $k_e = 0.5$  and  $k_\mu = 1.0$ ; (c) phase velocities of direct eigenwaves,  $k_e = 1.0$  and  $k_\mu = 0.5$ .

eigenpropagation constant  $\overline{\Phi}_0^{\text{back},-1} = -\overline{\Phi}_0^{\text{back}} + 1 = 0.49$ . The phase velocity of this wave is  $\beta^{\text{back},-1} = k/\overline{\Phi}_0^{\text{back},-1} = 0.89$  and coincides with the beam velocity  $\beta$ .

Resonances in reverse Vavilov-Cherenkov radiation are possible in the region of parameter values  $k$  and  $\beta$  such that  $\beta^2 > [\epsilon(k)\mu(k)]^{-1}$  and  $\text{Re } \Gamma^{\epsilon,\mu}(k, \beta) = 0$  for all  $n \neq 0$  (only the fundamental spatial harmonic propagates in the dispersive medium without decay). It is also necessary that in this domain (in the domain  $VCh_{k,\beta}$ ) the synchronism conditions  $\beta = \beta^{\text{back},\pm,m} = k/\overline{\Phi}_0^{\text{back},\pm,m}$  for certain  $m$  can be implemented.

Naturally, the selected values  $k_e$  and  $k_\mu$  should ensure the existence of such a domain. For example, when  $0.5 < k_e < k_\mu$ , the values  $\beta = \beta^{\text{back},\pm,m} = k/\overline{\Phi}_0^{\text{back},\pm,m}$  do not fall into the domain  $VCh_{k,\beta}$ ; but for  $k_e = 0.1$  and  $k_\mu = 0.55$  in the domain  $VCh_{k,\beta}$ , which is marked in Figure 7(b) with oblique hatching, the surface waves whose phase velocity coincides with the velocity of electron beam may already

exist. The latter case is particularly interesting because (i) the resonances in the reverse VChR can appear for rather small values  $\beta$  (Figure 7(c)) and thus at low velocities of the particles beam and (ii) the accumulation point of the frequency spectrum  $k_{\text{accum}} = k_e/\sqrt{2} \approx 0.0707$  falls into the region  $VCh_{k,\beta}$  and within it the existence of a large number of resonances in reverse VChR (Figures 7(a) and 7(c)) is possible. It should be pointed out once again that these resonances appeared due to the implementation of synchronism mechanism that is the coincidence of beam velocity with the phase velocity of one or another surface wave.

The data presented in Figure 8 allow us to estimate the influence of parameters of the dispersive media  $k_e$  and  $k_\mu$  on the intensity of reverse VChR. The lines  $W_0^T(k_e, k_\mu) = \text{const}$  (Figure 8(b)) are calculated for parameters  $k_e$  and  $k_\mu$  from the domain  $[0 \leq k_e \leq 0.12] \times [0.35 \leq k_\mu \leq 0.7]$  and for  $k = 0.08$ ,  $\beta = 0.2$ , and  $h = 0.4$ . Under such choice of parameters, the region bounded by the curves  $Q_0$  and  $Q_{-1}$  is the domain

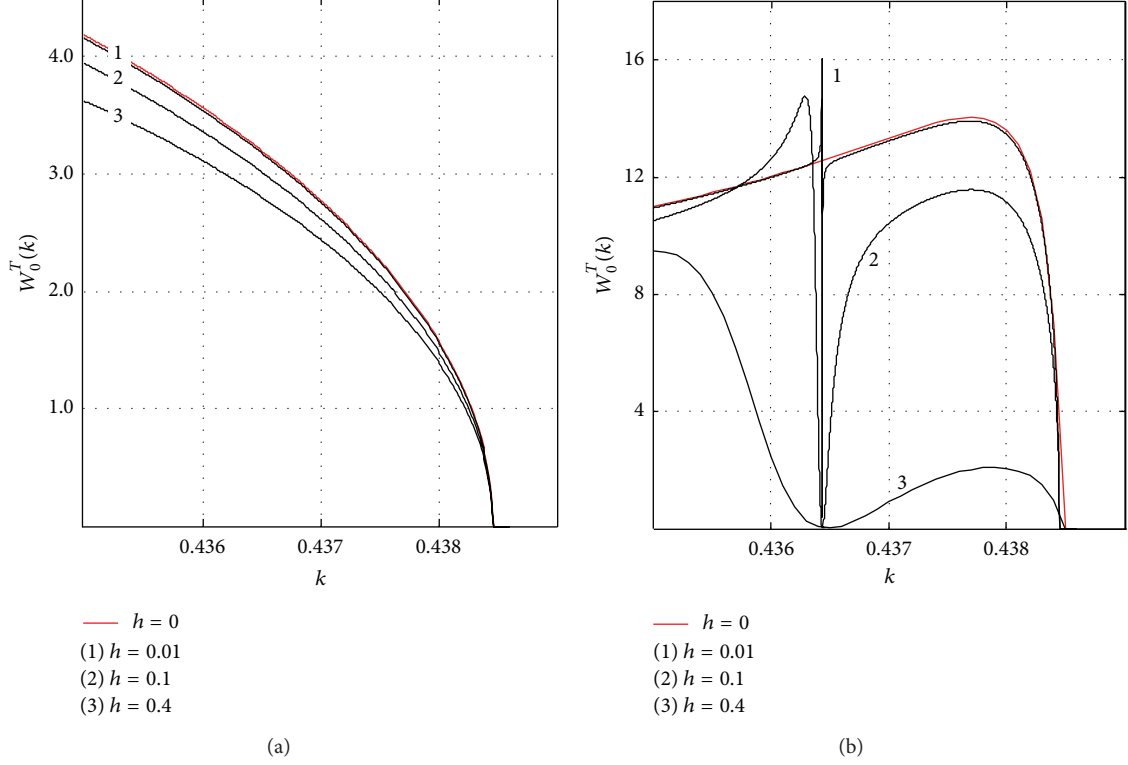


FIGURE 6: Change in frequency characteristics of radiation intensity with an increase in the height of corrugation mounts periodically rough boundary.

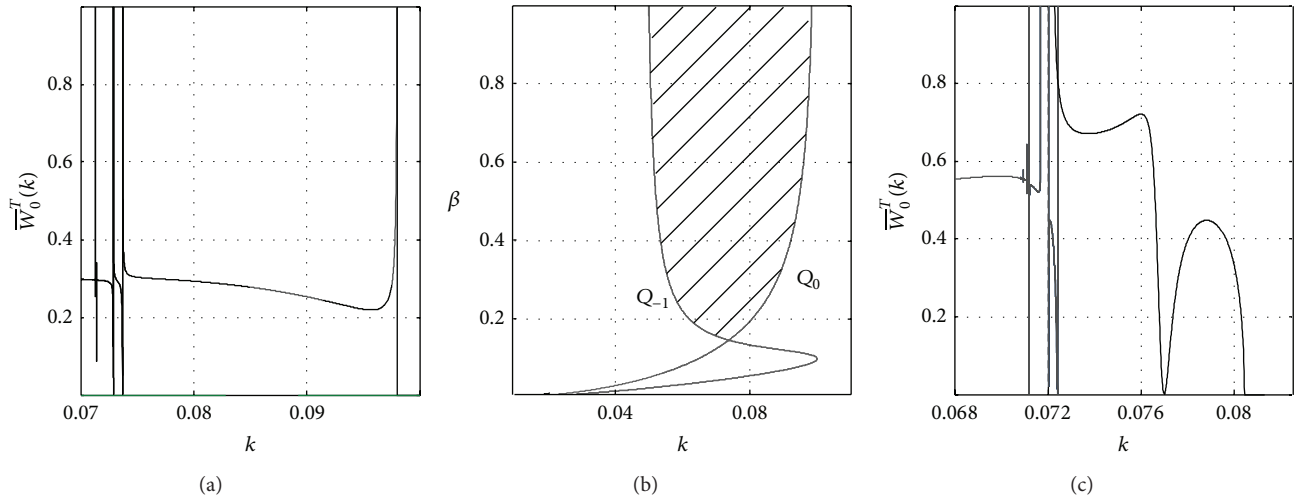


FIGURE 7: (a), (c) Dependencies  $\bar{W}_0^T(k)$ , characterizing the radiation intensity in the half-space  $z < 0$  for  $\beta = 0.89$  and  $\beta = 0.2$ ; (b) domain  $VCh_{k_\beta}$ . All for  $k_\epsilon = 0.1$ ,  $k_\mu = 0.55$ , and  $h = 0.4$ . Here and further on  $\bar{W}_0^T(\dots) = W_0^T(\dots)/\max(\dots)W_0^T(\dots)$ .

$VCh_{k_\epsilon, k_\mu}$ . The first pronounced resonant fall in the intensity of the reverse  $VChR$  (the locus of corresponding points forms the straight line in the given range of variables  $k_\epsilon$  and  $k_\mu$ ) corresponds to the synchronism of electron beam with the surface wave having phase velocity  $\Phi_0^{back,-1}$ . Sequence of resonances is clearly displayed in Figure 8(a), where a plot

$W_0^T(k_\epsilon)$  for  $k_\mu = 0.55$  is presented. The low- $Q$  resonant fall of intensity of the reverse  $VChR$  manifests itself when  $k_\epsilon$  increases and then as you get closer to the value  $k_\epsilon = 0.113$  at which the chosen frequency  $k = 0.08$  is an accumulation point. As we have mentioned above and in [13] in the vicinity of accumulation point, the number of high- $Q$  resonances,

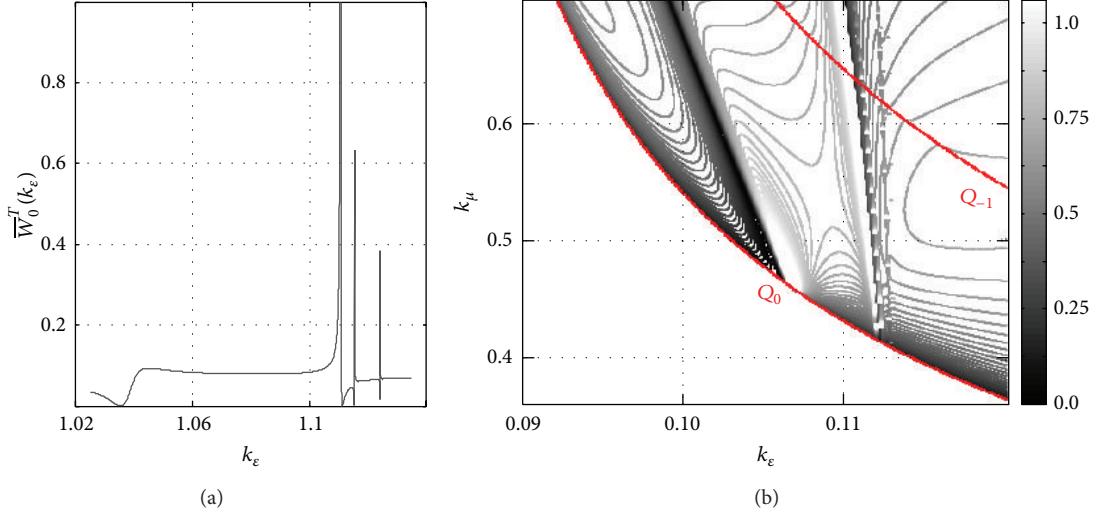


FIGURE 8: Influence of parameters  $k_e$  and  $k_\mu$  onto the intensity of the radiation in the lower half-space: (a) plot  $\bar{W}_0^T(k_e)$  for  $k_\mu = 0.55$ ; (b) contour plots  $\bar{W}_0^T(k_e, k_\mu) = \text{const}$ .

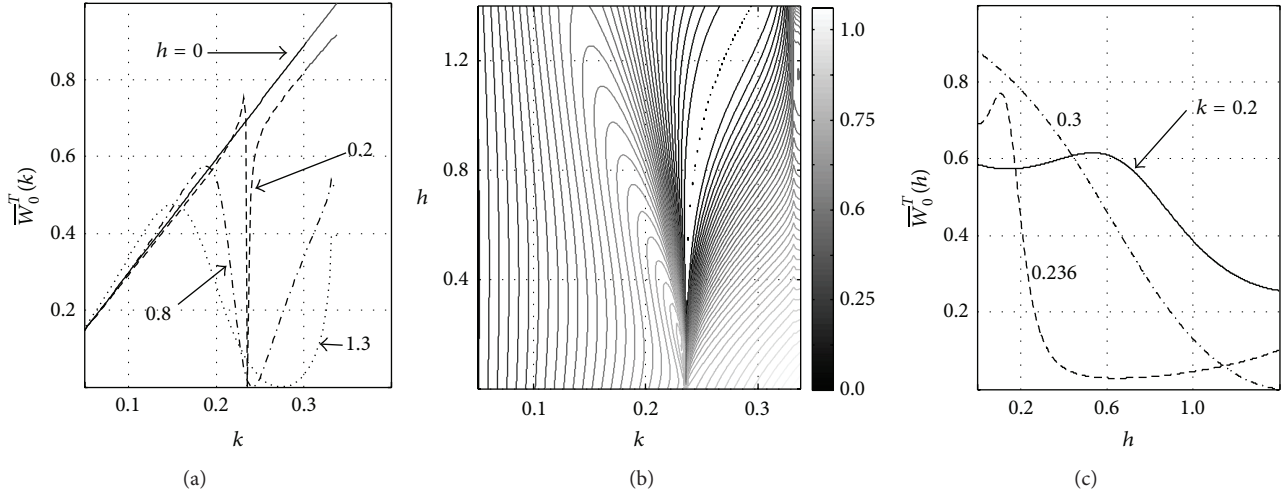


FIGURE 9: (a), (c) Plots  $\bar{W}_0^T(k)$  for several fixed values  $h$  and plots  $\bar{W}_0^T(h)$  for several fixed values  $k$ ; (b) contour plots  $\bar{W}_0^T(k, h) = \text{const}$ . All for  $\varepsilon = -0.84$ ,  $\mu = -4.84$ , and  $\beta = 0.89$ .

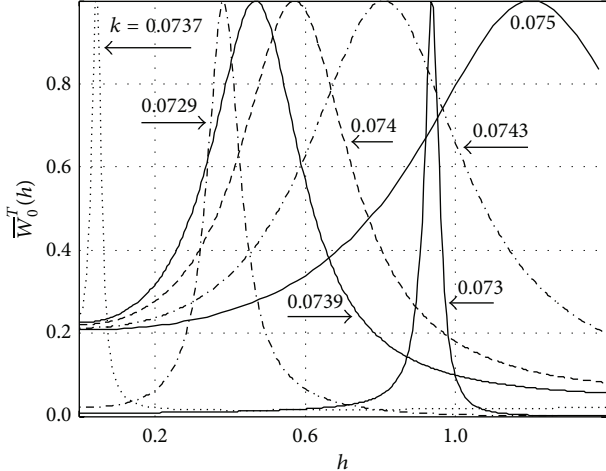
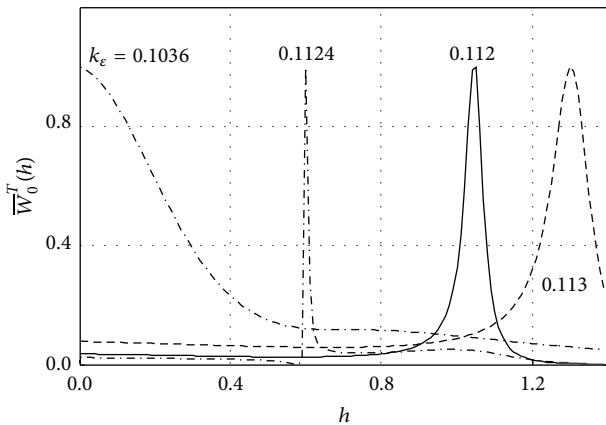
causing a sharp drop and a sharp rise in  $W_0^T(k_e)$ , increases significantly.

Influence of profiling depth  $h$  onto the intensity of VChR shows itself differently depending on the values of other parameters and, in fact, depending on whether a periodic boundary between two media at such values of parameters is able to support the propagation of forward or backward surface waves and whether the synchronization of electron beam velocity with phase velocity of these waves is possible.

Consider periodic boundary of the nondispersive left-handed medium,  $\mu = -4.84$ ,  $\varepsilon = -0.84$ , and  $\beta = 0.89$ , Figure 9. The resonance dip to zero of intensity of reverse VChR, which is clearly visible in Figure 9(b), is associated with the excitation of a surface wave, and the quality factor of the corresponding resonance is significantly reduced with

the increase of  $h$ . Two other fragments of Figure 9 allow considering the important details in the behavior of the dependencies  $W_0^T(k)$  (for some fixed values  $h$ ) and  $W_0^T(h)$  (for some fixed values  $k$ ) which may be lost in the analysis of the overall picture of the contour plots  $W_0^T(k, h) = \text{const}$  (Figure 9(b)).

In the case of the dispersive medium and the parameter values  $k_e$ ,  $k_\mu$ ,  $k$ , and  $\beta$ , guaranteeing the existence of direct surface waves, dependencies  $W_0^T(h)$  are almost monotonous. In the region of the backward surface waves, intensity of the reverse VChR varies essentially differently. For example, in the case of parameters already considered above  $k_e = 0.1$ ,  $k_\mu = 0.55$ , and  $\beta = 0.89$  ( $k_{\text{con}} \approx 0.0707$ ), functions  $W_0^T(h)$  have a pronounced peak due to the coincidence of

FIGURE 10: Curves of  $\bar{W}_0^T(h)$  for several fixed values of  $k$ .FIGURE 11: Influence of profiling depth of periodic boundary between two media onto the intensity of VChR. Plots  $\bar{W}_0^T(h)$  for various  $k_e$ .

the electrons beam velocity with phase velocity of one of the surface waves; and this maximum occurs at different values of  $h$  for different values of  $k$  from the frequency interval comprising  $k_{\text{accum}}$  (Figure 10). Also, it is possible to characterize the behavior and features of  $W_0^T(h)$  calculated for fixed  $k_\mu = 0.55$ ,  $k = 0.08$ , and  $\beta = 0.2$ , and for different values  $k_e$  (Figure 11). Location of peaks of function  $W_0^T(h)$  is quite sensitive to changes in  $k_e$  value and this fact can be used to solve problems related to the definition of parameters of dispersive materials. The results similar to that shown in Figure 10 may be useful in the selection of depth profiling of left-handed dispersive medium capable of supporting over its surface the propagation of eigenwave of a required type.

## 5. Conclusions

The resonances in reverse VChR produced by the charged particles beam passage over periodic boundary of dispersive left-handed medium are found out and studied.

Mathematical modeling and computational experiment are the main methodological components of this work devoted to the study of a series of features in the diffraction radiation generated by a flat, density modulated electron beam, moving over periodically rough boundary between conventional media and media with frequency dependent parameters. Conditions of radiation initiation, radiation intensity, and possibility of the existence of different resonance effects in reverse VChR associated with the excitation of surface waves of the periodic boundary have been studied analytically and numerically in the approximation of a given current. The possibilities and perspectives for efficient control of the characteristics of the reverse VChR, that may be performed by changing, for example, characteristic frequencies  $k_e$  and  $k_\mu$  in constitutive parameters of dispersive medium or/and the height of the corrugation mounts  $h$  of the periodic surface, are found out and examined.

The numerical results discussed in the paper concern the limited number of specific situations. But the models and algorithms created for their analysis can be used for a more detailed research into the physics of diffraction radiation, for a correct formulation and efficient solution to a number of inverse problems having considerable practical interest.

## Conflict of Interests

The authors declare that there is no conflict of interests regarding the publication of this paper.

## Acknowledgment

This work has been carried out under financial support of the Ministry of Education and Science of Kazakhstan.

## References

- [1] P. A. Cherenkov, "Visible radiation produced by electrons moving in a medium with velocities exceeding that of light," *Physical Review*, vol. 52, p. 378, 1937.
- [2] I. Y. Tamm and I. M. Frank, "Coherent visible radiation of fast electrons passing through matter," *Comptes Rendus de l'Academie Bulgare des Sciences*, vol. 14, p. 109, 1937.
- [3] J. V. Jelley, *Cherenkov Radiation and Its Applications*, Pergamon Press, London, UK, 1958.
- [4] V. P. Shestopalov, *The Smith-Purcell Effect*, Nova Science Publishers, New York, NY, USA, 1997.
- [5] Y. O. Averkov and V. M. Yakovenko, "Cherenkov radiation by an electron bunch that moves in a vacuum above a left-handed material," *Physical Review B—Condensed Matter and Materials Physics*, vol. 72, no. 20, Article ID 205110, 2005.
- [6] Z. Y. Duan, B.-I. Wu, S. Xi, H. S. Chen, and M. Chen, "Research progress in reversed cherenkov radiation in double-negative metamaterials," *Progress in Electromagnetics Research*, vol. 90, pp. 75–87, 2009.
- [7] S. Xi, H. Chen, T. Jiang et al., "Experimental verification of reversed cherenkov radiation in Left-Handed metamaterial," *Physical Review Letters*, vol. 103, no. 19, Article ID 194801, 2009.
- [8] Y. K. Sirenko and S. Strom, Eds., *Modern Theory of Gratings. Resonant Scattering: Analysis Techniques and Phenomena*, Springer, New York, NY, USA, 2010.

- [9] V. P. Shestopalov, Y. A. Tuchkin, A. Y. Poyedinchuk, and Y. K. Sirenko, *New Solution Methods for Direct and Inverse Problems of the Diffraction Theory. Analytical Regularization of the Boundary Value Problems in Electromagnetic Theory*, Osnova, Kharkov, Ukraine, 1997 (Russian).
- [10] P. Melezhik, A. Poyedinchuk, N. Yashina, and G. Granet, "Periodic boundaries of metamaterials: eigen regimes and resonant radiation," *Journal of Optics A: Pure and Applied Optics*, vol. 9, no. 9, pp. S403–S409, 2007.
- [11] V. P. Shestopalov, A. A. Kirilenko, S. A. Masalov, and Y. K. Sirenko, *Resonance Wave Scattering. Diffraction Gratings*, Naukova Dumka, Kiev, Ukraine, 1986, (Russian).
- [12] Y. K. Sirenko and L. G. Velychko, "The features of resonant scattering of plane inhomogeneous waves by gratings: model problem for relativistic diffraction electronics," *Telecommunications and Radio Engineering*, vol. 55, p. 33, 2001.
- [13] P. Melezhik, A. Poyedinchuk, N. Yashina, G. Granet, and M. Ney, "Radiation from surface with periodic boundary of metamaterials excited by a current," *Progress in Electromagnetics Research*, vol. 65, pp. 1–14, 2006.

## Research Article

# Photonic Wannier-Stark Ladder from Coupled Electromagnetic Cavities

**Shahzad Anwar, Sucheng Li, Weixin Lu, and Bo Hou**

*College of Physics, Optoelectronics and Energy and Collaborative Innovation Center of Suzhou Nano Science and Technology, Soochow University, 1 Shizi Street, Suzhou 215006, China*

Correspondence should be addressed to Bo Hou; [houbo@suda.edu.cn](mailto:houbo@suda.edu.cn)

Received 8 March 2015; Accepted 1 May 2015

Academic Editor: Weiren Zhu

Copyright © 2015 Shahzad Anwar et al. This is an open access article distributed under the Creative Commons Attribution License, which permits unrestricted use, distribution, and reproduction in any medium, provided the original work is properly cited.

We have investigated the photonic Wannier-Stark ladder in the system of coupled electromagnetic cavities, which consists of a stack of metallic plates structured with subwavelength apertures and where the tilted potential effect is mimicked by imposing the gradient variation of refractive index. Making an analogy to its quantum counterpart and assuming the translational property of its solutions, we have shown the photonic ladder has the eigenenergies, that is, frequencies, in a geometrical series. Within the approximation of small gradient, the ladder states manifest the equidistant frequency spacing in the spectrum. By both analytical derivation and numerical simulation, we have illustrated the geometrically progressed energies of the photonic Wannier-Stark ladder.

## 1. Introduction

A lot of similar physical properties have been revealed between electrons in a solid and photons in a periodic structure [1]. Besides band gap, another fascinating example is the concepts of Wannier-Stark ladder (WSL) and Bloch oscillation (BO) [2]. When a solid is biased by a static electric field, the electron eigenstates do not belong to the extended Bloch states because the linear potential imposed by the static electric field breaks the translational symmetry of the periodical crystal potential but becomes the WSL which is a family of localized wavefunctions with equidistant energies in the energy spectrum. The Bloch oscillation, in which the electrons driven by the DC bias oscillate periodically in semi-classical picture, is just the time domain counterpart of the quantum-mechanical WSL. Due to the potential applications toward high speed electronics, both WSL and BO have been theoretically investigated and experimentally observed in the semiconductor superlattices [3]. In contrast, WSL and BO in natural crystals are difficult to observe because the coherence of electron wave packets is very fragile to various decoherence processes, for example, disorder, in the crystals.

Recently, the two concepts advance to electromagnetic (EM) waves in an analogy way, driven by the physical

similarity of wave systems and the phenomenological robustness of classical waves [4]. For EM waves, the gradient refractive index or thickness of the dielectric layers introduced to a photonic structure plays the same role as the DC field in electronic cases and gives rise to both the photonic WSL in the frequency domain and the photonic BO in the time domain [5–7]. Besides the conventional photonic crystals [8–11], the microcavity systems from metamaterial with negative index have been shown to display the photonic BO [12–16]. In addition, the BO can be demonstrated equivalently inside the transversely coupled waveguide arrays undergoing the gradient modulation along the transverse direction [17, 18] and manifests the rich physics of wave propagation, such as quasi and fractional versions [19, 20]. More recently, the WSL has also been observed in acoustic/elastic systems [21–24].

In this work, we have investigated the photonic WSL in the system of coupled EM cavities, where the biased potential effect is mimicked by imposing the gradient variation of refractive index. A numerical model is constructed, using a stack of metallic plates patterned with subwavelength apertures. By calculating the transmission, we have observed that the transmission peaks of the ladder states have the equidistant frequency spacing in the spectrum, that is, their frequencies (eigenenergies) showing an arithmetical series,

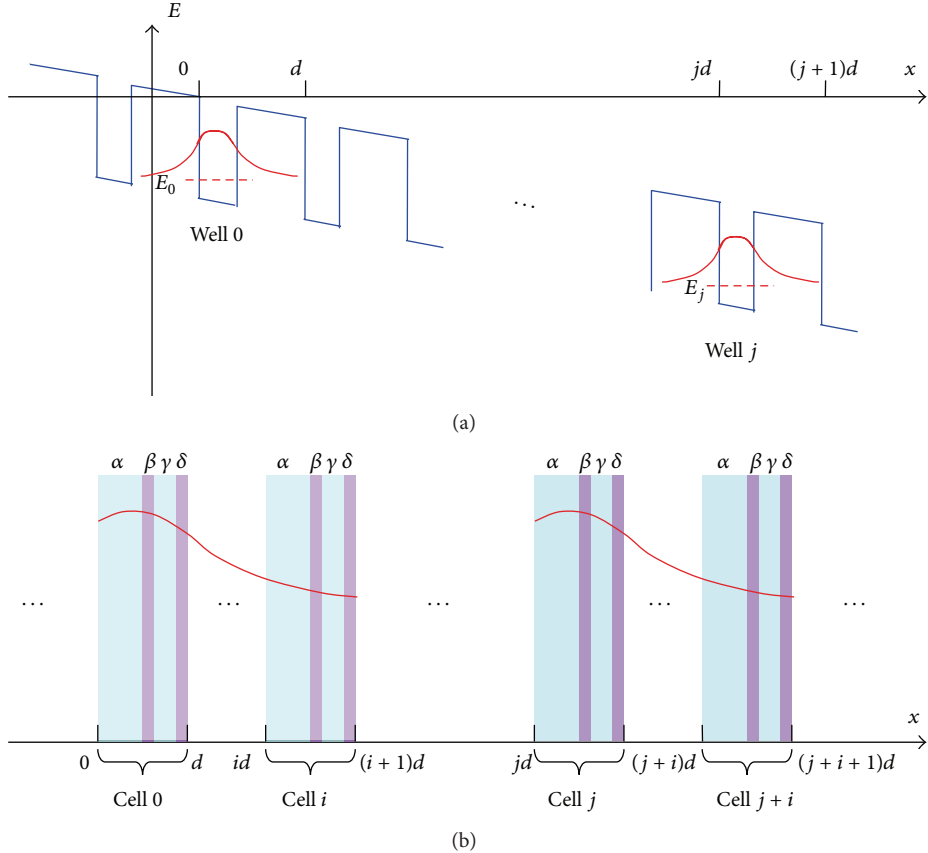


FIGURE 1: (a) The Kronig-Penney potential (coupled quantum wells) titled by a static electric field, where  $d$  is the spatial periodicity between the neighboring wells and the red line depicts schematically the quantum WSL state localized in the different well. (b) The one-dimensional coupled EM cavities, that is, “photonic wells,” with increasing the refractive indexes of the dielectric layers,  $\alpha$ ,  $\beta$ ,  $\gamma$ , and  $\delta$ , along the  $x$ -direction.

in the case of small gradient. Specifically, the frequencies of the peaks evolve into a geometrical series in the case of large gradient, which points out the generalized photonic WSL with geometrically progressed energies.

## 2. Materials and Methods

We start with the quantum WSL problem. Consider a particle of mass  $m$  and charge  $q$  moving in the simplified crystal potential of spatial periodicity  $d$  (Kronig-Penney model [25]) tilted by a static electric field  $\xi$ , as depicted in Figure 1(a). For the quantum system, the Schrodinger equation has the following expression:

$$-\frac{\hbar^2}{2m} \frac{d^2\psi(x)}{dx^2} + V(x)\psi(x) = E\psi(x), \quad (1)$$

where  $\psi(x)$  is the wavefunction,  $E$  is the eigenenergy, and the position-dependent potential has the property  $V(x) = V(x+d) + q\xi d$ . When an electron moves in the tilted periodic potential, it will localize somewhere due to the translational symmetry breaking. Assume such a state  $\psi(x)$  localized near well 0 and with energy  $E_0$ , and then the above equation reads

$$-\frac{\hbar^2}{2m} \frac{d^2\psi(x)}{dx^2} + V(x)\psi(x) = E_0\psi(x). \quad (2)$$

Change the variable  $x$  to  $x - jd$  ( $j$  being an integer), and we obtain

$$\begin{aligned} & -\frac{\hbar^2}{2m} \frac{d^2\psi(x-jd)}{dx^2} + V(x-jd)\psi(x-jd) \\ &= E_0\psi(x-jd); \end{aligned} \quad (3)$$

that is,

$$\begin{aligned} & -\frac{\hbar^2}{2m} \frac{d^2\psi(x-jd)}{dx^2} + [V(x-jd) - q\xi jd]\psi(x-jd) \\ &= (E_0 - q\xi jd)\psi(x-jd), \end{aligned} \quad (4)$$

or

$$\begin{aligned} & -\frac{\hbar^2}{2m} \frac{d^2\psi(x-jd)}{dx^2} + V(x)\psi(x-jd) \\ &= E_j\psi(x-jd), \quad \text{with } E_j = E_0 - q\xi jd. \end{aligned} \quad (5)$$

Therefore, a new solution  $\psi(x-jd)$  is localized near the well  $j$  and has the energy  $E_j$ . It is seen that a family of such states can be obtained with the consistent wavefunctions  $\psi$ , except that their locations translate with respect to each other. The family of states is just the WSL where their eigenenergies compose

an arithmetical progression,  $E_j = E_0 - q\xi jd$ , with common difference  $q\xi d$ .

The photonic WSL has been proved in one-dimensional coupled EM cavities [5, 6], where a ramp-up of the refractive index along the stacking direction is used to mimic the effect of the electric field  $\xi$  in the quantum case, as illustrated in Figure 1(b). Here, we reformulate the EM problem in the same style as solving the quantum system. For explicitness and simplification, the individual cavity is assumed including four dielectric layers, and the solution also holds for the cavity with more or less layers. The Helmholtz wave equation for the photonic system is written as

$$\frac{d^2}{dx^2} F(x) + n^2(x) \frac{\omega^2}{c^2} F(x) = 0, \quad (6)$$

where the refractive index profile

$$n(x) = \begin{cases} n_i^\alpha, & x \in [id, id + L^\alpha), \\ n_i^\beta, & x \in [id + L^\alpha, id + L^\alpha + L^\beta), \\ n_i^\gamma, & x \in [id + L^\alpha + L^\beta, id + L^\alpha + L^\beta + L^\gamma), \\ n_i^\delta, & x \in [id + L^\alpha + L^\beta + L^\gamma, (i+1)d), \end{cases} \quad (7)$$

with the integer  $i$  specifying the cavity cell and the Greek alphabet specifying the layer, and the cavity length  $d = L^\alpha + L^\beta + L^\gamma + L^\delta$  with  $L^\alpha, L^\beta, L^\gamma$ , and  $L^\delta$  being the thicknesses of the four layers,  $\alpha, \beta, \gamma$ , and  $\delta$ , respectively. Following  $n(x)$ , the photonic state,  $F(x)$ , is supposed to be sectioned. Similar to the quantum case, we hypothesize a solution,  $F(x)$ , which is centralized somewhere, to say near cell 0, and has the photon energy  $\hbar\omega_0$  and the field function:

$$F(x) = \begin{cases} F_i^\alpha(x), & x \in [id, id + L^\alpha), \\ F_i^\beta(x), & x \in [id + L^\alpha, id + L^\alpha + L^\beta), \\ F_i^\gamma(x), & x \in [id + L^\alpha + L^\beta, id + L^\alpha + L^\beta + L^\gamma), \\ F_i^\delta(x), & x \in [id + L^\alpha + L^\beta + L^\gamma, (i+1)d), \end{cases} \quad (8)$$

where the cell number  $i$  may range within the integers  $[-M, M]$ , depending on the localizing degree. In fact, the positive integer  $M$  characterizes the localization scale of the solution ( $M \rightarrow 0$  representing a state localized inside only one cell and  $M \rightarrow \infty$  meaning the weak localization). Without losing generality, the solution in the region  $x \in [id + L^\alpha, id + L^\alpha + L^\beta)$  satisfies

$$\frac{d^2}{dx^2} F_i^\beta(x) + (n_i^\beta)^2 \frac{\omega_0^2}{c^2} F_i^\beta(x) = 0. \quad (9)$$

Changing the variable, we obtain

$$\frac{d^2}{dx^2} F_i^\beta(x - jd) + (n_i^\beta)^2 \frac{\omega_0^2}{c^2} F_i^\beta(x - jd) = 0, \quad (10)$$

or

$$\frac{d^2}{dx^2} F_i^\beta(x - jd) + (n_{j+i}^\beta)^2 \frac{\omega_j^2}{c^2} F_i^\beta(x - jd) = 0, \quad (11)$$

where  $n_{j+i}^\beta \omega_j = n_i^\beta \omega_0$  and  $x \in [(j+i)d + L^\alpha, (j+i)d + L^\alpha + L^\beta)$ . With applying to the other layers and cells, we can see that the new field function,  $F(x - jd)$ , its segmented expressions being  $F_i^{\alpha,\beta,\gamma,\delta}(x - jd)$ , actually represents another state which centralizes near the cell  $j$  and has the energy  $\hbar\omega_j$ , where  $\omega_j = n_i \omega_0 / n_{j+i}$ . For the strongly localized photonic state ( $M \rightarrow 0$ ), for example, the one which allows the tight binding description of the coupling effect between the EM cavities, the energy relation  $n_i \omega_0 = n_{j+i} \omega_j$  can be simplified as  $n_0 \omega_0 = n_j \omega_j$ . This relation can also be justified directly from (6), if the photonic WSL takes a series of solutions which are spatially translational to each other, like the quantum case.

It can be proved that a geometric series,  $n_i = n_0 q^i$  and  $\omega_j = \omega_0 / q^j$  ( $q$  being the common ratio), meets exactly the relation  $n_i \omega_0 = n_{j+i} \omega_j$  or  $n_0 \omega_0 = n_j \omega_j$ . Particularly, in the case of  $q = 1 + \eta$  with the approximation  $\eta \ll 1$ ,  $n_i = n_0 (1 + \eta)^i \approx n_0 + i n_0 \eta$  and  $\omega_j = \omega_0 (1 + \eta)^{-j} \approx \omega_0 - j \omega_0 \eta$ , where  $\omega_0 \eta$  is identified as Bloch oscillation frequency  $\omega_B$  which manifests the equidistant frequency spacing in spectra.

### 3. Results and Discussion

In order to illustrate the photonic WSL states in a specific system, we employ a metallic plate patterned with narrow H-fractal slits as EM cavity. The resonant state supported by the exotic fractal pattern has been found to be responsible for transmission enhancement of EM wave through such metallic plates [26]. When a number of the metallic plates with H-fractal slits are cascaded, their resonant modes will couple together; the transmission bands would be developed in a way analog to the formation of miniband in the superlattice and furthermore comply with the photonic tight binding description [27]. Note that our fractal slits should not be considered as a sole candidate, while all other shaped apertures supporting the local resonance are applicable, too.

The coupled cavity system is 8 stacked metallic plates on which a periodic array of fractal slits was cut with lattice constant smaller than the relevant incident wavelength to avoid the grating effect, illustrated schematically in Figure 2(a). The unit cell of the array includes a five-level H-fractal slit structure where the longest slit is 10 mm and the width of each slit is 0.8 mm [26], and the plates have a thickness of 3 mm and a spacing of 9 mm. Numerically, we employ a commercial finite-difference time-domain (FDTD) software package to investigate the microwave spectra [28]. The microwave polarization was such that the electric field is perpendicular to the shortest slits of the fractal pattern. In the simulation, we assume periodic boundary condition in the transverse direction and perfect conductor approximation for metal.

To impose a tilted potential effect, we embed the plates in the dielectrics, which have the geometrically increasing refractive index,  $n_j = (1 + dn)^j$ , where the integer  $j$  denotes the plate number from 0 to 7 and the varying quantity  $dn$  tunes the magnitude of the common ratio of the geometrical series. Each structured plate is embedded inside the dielectric in a symmetrical way, as illustrated in Figure 2(b).

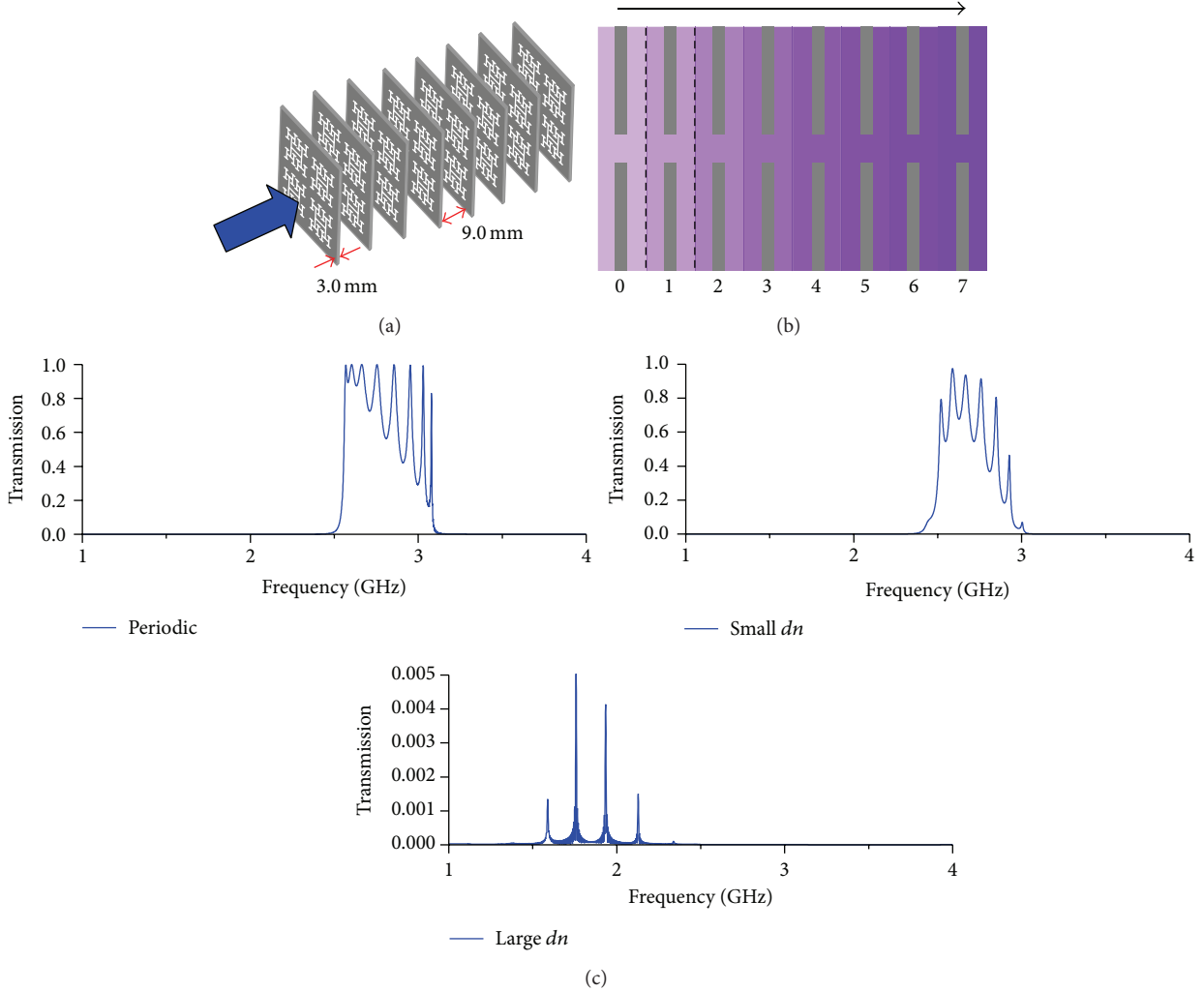


FIGURE 2: (a) The 8 stacked metallic plates on which a periodic array of fractal slits was generated. In the schematic picture, the plate has  $2 \times 2$  unit cells, each of which is a five-level H-fractal slit. (b) The 8 plates are embedded, respectively, inside 8 dielectrics, which have the refractive index,  $n_j = (1 + dn)^j$ , where  $j$  takes the denoted numbers. The index gradient is along the propagation direction, as pointed by the arrow. The dash lines depict a single EM cavity cell composed of a structured plate and a homogeneous dielectric. (c) The simulated transmissions at normal incidence of microwave, where three cases, no, small, and large gradient of refractive index, are considered.

When  $dn = 0$ , which is referred to as the periodic case because there is no refractive index gradient, the simulated result shows that a passband is formed between 2.5 and 3.1 GHz in the same physics as the miniband in the semiconductor superlattice, seeing the upper curve in Figure 2(c). The peaks originate from the coupling of the resonant modes in the plates at different phase delay, analogous to the development of energy band (or miniband) in crystal (or superlattice) within the tight binding description [25, 27]. It is seen that the peaks are more crowded at the two band edges than in the middle region, which is the typical density-of-state characteristics of the miniband.

After a small variation,  $dn = 0.01$ , is introduced, the magnitudes and positions of the peaks change drastically, seeing the middle curve in Figure 2(c). The underlying resonance states, responsible for transmission, become localized somewhere in the stacking direction. For example, the peak

at the lower band edge has degraded into a spectral shoulder ( $\sim 2.45$  GHz) with low transmission ( $\sim 10\%$ ). This is because the fractal slits which support the peak are being located at the far end plate of the stacking system, where the refractive index is highest, and the other plates with the higher resonance frequencies behave like the potential barrier. Consequently, the incident wave has to tunnel through them to excite the eigenmode of the farthest one, similar to the Zener tunneling [23, 24]. Likewise, the situation also occurs at the upper band edge, the tiny peak at 3.0 GHz. Note that the peaks' spacing in frequency begin to appear even.

While a large variation,  $dn = 0.1$ , is considered, an obvious downshift of the miniband region is seen in the spectrum, as plotted in Figure 2(c), originating from the overall increasing in the refractive index. At the same time, the transmission magnitude is suppressed significantly, as the titled potential is much steeper and the states have become

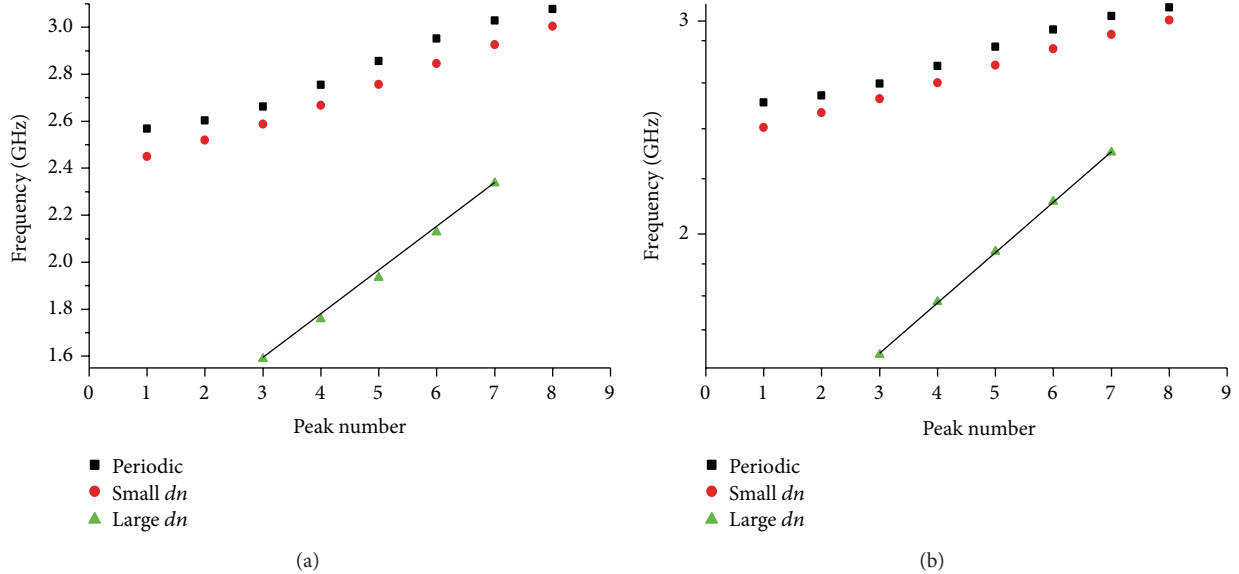


FIGURE 3: (a) The peak frequencies in the three cases, periodic, small  $dn$ , and large  $dn$ . The vertical axis is in linear scale. (b) The same as (a) but with the vertical axis being logarithmic scale. The horizontal axis in (a) and (b) represents the peak number. The numbers, 3, 4, 5, 6, and 7, of the five peaks in the case of large  $dn$  are arbitrarily assigned, being not relevant to the line shape recognition. To see the linear line shape, a straight line connecting two end points is drawn, respectively, in (a) and (b).

more localized, so that only five peaks are identified, seeing Figure 3 for their frequencies. The decrease of the number of spectra peaks is a consequence of larger  $dn$  or steeper titled potential, because a few of WSL states (e.g., the farthest one) cannot be efficiently excited any more via the tunneling. Likewise, the spectra spacing of the peaks become wider with increasing  $dn$ , due to the larger eigenenergy differences between neighboring WSL states under steeper potential.

We have labeled the frequency values of all identified peaks from Figure 2(c) and plotted them in Figure 3. With the linearly scaled frequency axis, as shown in Figure 3(a), the frequency dots in the periodic case display a curved trend, consistent with the tight binding description of the miniband [27]. In contrast, the line shapes of the latter two cases can be approximately regarded as being linear. However, if the axis is switched to be logarithmic scale, seeing Figure 3(b), the frequency dots of the gradient cases are more close to a linear curve, especially for the large  $dn$  case, where the dots of peaks 4, 5, and 6 fall completely on the straight line connecting two end points (the dots of peaks 3 and 7). The linear line shape in logarithmic scale reveals that these frequency values are actually in a geometric sequence, which is consistent with the analytical derivation.

From the experimental perspective, the critical requirement for observing the proposed WSL is to fabricate the dielectrics with designed refractive index  $n_j = (1 + dn)^j$ . The feasible technique route of well-controlling refractive index or dielectric constant is to employ composite material whose permittivity can be fine-tuned by the component concentration according to effective medium theory [29–31]. The composite suitable to our model may be the plastic foam where the porosity (air concentration) can be engineered to realize the desired dielectrics. We will conduct

the experimental investigation along with this technique consideration in the future.

## 4. Conclusions

In conclusion, by making an analogy to the quantum counterpart and assuming the translational properties of the solution  $F(x)$ , we have shown the photonic WSL in the system of coupled EM cavities, where the tilted potential effect is mimicked by imposing the gradient variation of refractive index along the propagation direction, may have the eigenenergies (frequencies) in geometrical progression. Within the approximation of small gradient, the WSL states have the equidistant frequency spacing in the spectrum. The numerical simulations of the model system, the stack of structured plates, have illustrated the generalized photonic WSL state with geometrically progressed energies.

## Conflict of Interests

The authors declare that there is no conflict of interests regarding the publication of this paper.

## Acknowledgments

This work was supported by the National Natural Science Foundation of China (Grant nos. 11104198 and 11474212), the Natural Science Foundation of Jiangsu Province (Grant no. BK20141191), and a Project Funded by the Priority Academic Program Development (PAPD) of Jiangsu Higher Education Institutions. The authors thank Professors Gang Wang and Zhi Hong Hang for the beneficial discussions.

## References

- [1] J. D. Joannopoulos, R. D. Meade, and J. N. Winn, *Photonic Crystals: Molding the Flow of Light*, Princeton University Press, Princeton, NJ, USA, 1995.
- [2] G. H. Wannier, "Dynamics of band electrons in electric and magnetic fields," *Reviews of Modern Physics*, vol. 34, pp. 645–655, 1962.
- [3] E. E. Mendez and G. Bastard, "Wannier-stark ladders and bloch oscillations in superlattices," *Physics Today*, vol. 46, no. 6, pp. 34–42, 1993.
- [4] G. Monsivais, M. del Castillo-Mussot, and F. Claro, "Stark-ladder resonances in the propagation of electromagnetic waves," *Physical Review Letters*, vol. 64, no. 12, pp. 1433–1436, 1990.
- [5] R. Sapienza, P. Costantino, D. Wiersma, M. Ghulinyan, C. J. Oton, and L. Pavesi, "Optical analogue of electronic Bloch oscillations," *Physical Review Letters*, vol. 91, no. 26, Article ID 263902, 2003.
- [6] V. Agarwal, J. A. Del Río, G. Malpuech et al., "Photon bloch oscillations in porous silicon optical superlattices," *Physical Review Letters*, vol. 92, no. 9, Article ID 097401, 2004.
- [7] J. O. Estevez, J. Arriaga, A. Mendez-Blas, E. Reyes-Ayona, J. Escoria, and V. Agarwal, "Demonstration of photon Bloch oscillations and Wannier-Stark ladders in dual-periodical multilayer structures based on porous silicon," *Nanoscale Research Letters*, vol. 7, article 413, 2012.
- [8] G. Malpuech, A. Kavokin, G. Panzarini, and A. Di Carlo, "Theory of photon Bloch oscillations in photonic crystals," *Physical Review B: Condensed Matter and Materials Physics*, vol. 63, no. 3, Article ID 035108, 2001.
- [9] P. B. Wilkinson, "Photonic Bloch oscillations and Wannier-Stark ladders in exponentially chirped Bragg gratings," *Physical Review E: Statistical, Nonlinear, and Soft Matter Physics*, vol. 65, Article ID 056616, 2002.
- [10] V. Lousse and S. Fan, "Tunable terahertz Bloch oscillations in chirped photonic crystals," *Physical Review B*, vol. 72, no. 7, Article ID 075119, 2005.
- [11] G. Wang, J. P. Huang, and K. W. Yu, "Tunable photonic Bloch oscillations in electrically modulated photonic crystals," *Optics Letters*, vol. 33, no. 19, pp. 2200–2202, 2008.
- [12] X. Kang and Z. Wang, "Optical Bloch oscillation and resonant Zener tunneling in one-dimensional quasi-period structures containing single negative materials," *Optics Communications*, vol. 282, no. 3, pp. 355–359, 2009.
- [13] T.-B. Wang, C.-P. Yin, W.-Y. Liang, and H.-Z. Wang, "Bloch oscillations in one-dimensional photonic crystal coupled microcavity composed of single-negative materials," *Physics Letters A*, vol. 373, no. 45, pp. 4197–4200, 2009.
- [14] T.-B. Wang, N.-H. Liu, X.-H. Deng, and Q.-H. Liao, "Bloch oscillations in one-dimensional coupled multiple microcavities containing negative-index materials," *Journal of Optics*, vol. 13, no. 9, Article ID 095705, 2011.
- [15] Z.-H. Li, X.-N. Pang, J.-W. Dong, and H.-Z. Wang, "Electromagnetic Bloch-like oscillations in one-dimensional quasicrystal consisting of negative permeability metamaterial," *Europhysics Letters*, vol. 95, no. 3, Article ID 36004, 2011.
- [16] T.-B. Wang, N.-H. Liu, T.-B. Yu, X.-H. Deng, X.-M. Xu, and Q.-H. Liao, "Electromagnetic Bloch oscillation in one-dimensional multiple microcavities composed of metamaterials," *Chinese Physics B*, vol. 23, no. 4, Article ID 044101, 2014.
- [17] U. Peschel, T. Pertsch, and F. Lederer, "Optical Bloch oscillations in waveguide arrays," *Optics Letters*, vol. 23, no. 21, pp. 1701–1703, 1998.
- [18] W. H. Lin, X. Zhou, G. P. Wang, and C. T. Chan, "Spatial Bloch oscillations of plasmons in nanoscale metal waveguide arrays," *Applied Physics Letters*, vol. 91, no. 24, Article ID 243113, 2007.
- [19] A. Joushaghani, R. Iyer, J. K. S. Poon et al., "Quasi-bloch oscillations in curved coupled optical waveguides," *Physical Review Letters*, vol. 103, no. 14, Article ID 143903, 2009.
- [20] G. Corrielli, A. Crespi, G. Della Valle, S. Longhi, and R. Osellame, "Fractional Bloch oscillations in photonic lattices," *Nature Communications*, vol. 4, article 1555, 2013.
- [21] J. Mateos and G. Monsivais, "Stark-ladder resonances in elastic waves," *Physica A: Statistical Mechanics and Its Applications*, vol. 207, no. 1–3, pp. 445–451, 1994.
- [22] L. Gutiérrez, A. Díaz-De-Anda, J. Flores, R. A. Méndez-Sánchez, G. Monsivais, and A. Morales, "Wannier-Stark ladders in one-dimensional elastic systems," *Physical Review Letters*, vol. 97, no. 11, Article ID 114301, 2006.
- [23] H. Sanchis-Alepuz, Y. A. Kosevich, and J. Sánchez-Dehesa, "Acoustic analogue of electronic bloch oscillations and resonant zener tunneling in ultrasonic superlattices," *Physical Review Letters*, vol. 98, no. 13, Article ID 134301, 2007.
- [24] M. M. de Lima, Y. A. Kosevich, P. V. Santos, and A. Cantarero, "Surface acoustic bloch oscillations, the wannier-stark ladder, and landau-zener tunneling in a solid," *Physical Review Letters*, vol. 104, no. 16, Article ID 165502, 2010.
- [25] C. Kittel, *Introduction to Solid State Physics*, John Wiley & Sons, New York, NY, USA, 1996.
- [26] W. J. Wen, L. Zhou, B. Hou, C. T. Chan, and P. Sheng, "Resonant transmission of microwaves through subwavelength fractal slits in a metallic plate," *Physical Review B*, vol. 72, no. 15, Article ID 153406, 2005.
- [27] B. Hou, X. Xiao, and W. Wen, "Photonic bands from cascaded metallic plates with subwavelength slits," *Journal of Optics*, vol. 14, no. 5, Article ID 055102, 2012.
- [28] Simulations were performed using the commercial package QuickWave developed by QWED, Poland, <http://www.qwed.com.pl>.
- [29] W. Cai and V. M. Shalaev, *Optical Metamaterials: Fundamentals and Applications*, Springer, New York, NY, USA, 2010.
- [30] Z. L. Mei, J. Bai, and T. J. Cui, "Gradient index metamaterials realized by drilling hole arrays," *Journal of Physics D: Applied Physics*, vol. 43, no. 5, Article ID 055404, 2010.
- [31] H. Han, L. Wu, X. Tian, D. Li, M. Yin, and Y. Wang, "Broadband gradient refractive index planar lens based on a compound liquid medium," *Journal of Applied Physics*, vol. 112, no. 11, Article ID 114913, 2012.

## Review Article

# Recent Advances in the Modeling of Transmission Lines Loaded with Split Ring Resonators

Jordi Naqui, Lijuan Su, Javier Mata, and Ferran Martín

GEMMA/CIMITEC, Departament d'Enginyeria Electrònica, Universitat Autònoma de Barcelona, 08193 Bellaterra, Spain

Correspondence should be addressed to Jordi Naqui; [jordi.naqui@uab.cat](mailto:jordi.naqui@uab.cat)

Received 19 December 2014; Accepted 23 April 2015

Academic Editor: Ivan D. Rukhlenko

Copyright © 2015 Jordi Naqui et al. This is an open access article distributed under the Creative Commons Attribution License, which permits unrestricted use, distribution, and reproduction in any medium, provided the original work is properly cited.

This paper reviews the recent advances in the modeling of transmission lines loaded with split ring resonators (SRRs). It is well known that these artificial lines can exhibit a negative effective permeability in a narrow band above the SRR fundamental resonance, providing stopband functionality. By introducing shunt inductive elements to the line, the stopband can be switched to a pass band with left-handed (LH) wave propagation. For the design of microwave circuits based on these artificial lines, accurate circuit models are necessary. The former circuit model of SRR-loaded lines was presented more than one decade ago and is valid under restrictive conditions. This paper presents the progress achieved in the modeling of these artificial lines during the last years. The analysis, restricted to coplanar waveguide (CPW) transmission lines loaded only with SRRs (negative permeability transmission lines), includes the effects of SRR orientation, the coupling between adjacent resonators, and the coupling between the two SRRs constituting the unit cell. The proposed circuit models are validated through electromagnetic simulation and experimental data. It is also pointed out that the analysis can be easily extended to negative permittivity transmission lines based on complementary split ring resonators (CSRRs).

## 1. Introduction

The topic of metamaterials has attracted the interest of researchers since 2000 when the first left-handed (LH) metamaterial structure was synthesized [1]. These artificial media exhibit unusual electromagnetic properties, derived from the simultaneous negative effective permeability and permittivity, as predicted by Veselago in 1968 [2]. After the seminal work [1], various papers have experimentally confirmed the properties of LH media. Among them, the experimental verification of negative refraction [3] and the demonstration of backward leaky wave radiation in one-dimensional LH media, that is, the analogous of backward Cherenkov radiation in bulk LH media, are worth mentioning [4]. There are many books devoted to the topic of metamaterials among the available literature [5–13]. The unusual (or exotic) properties of metamaterials can be applied to the design of microwave circuits and antennas. In particular, by replacing the ordinary transmission lines in distributed circuits by artificial lines based on metamaterial concepts, it is possible to implement microwave devices with reduced size, enhanced performance,

and novel functionalities on the basis of impedance and dispersion engineering [5, 6, 8]. These artificial lines based on (or inspired by) metamaterials have been designated as metamaterial transmission lines, consisting of a host line loaded with reactive elements (inductors, capacitors, and/or resonators), and can be considered to be one-dimensional metamaterials (sometimes these lines are also referred to as transmission line metamaterials [14–16]). By loading appropriately the host lines, it is possible to achieve negative effective permeability ( $\mu_{\text{eff}} < 0$ ), permittivity ( $\epsilon_{\text{eff}} < 0$ ), or both negative parameters simultaneously ( $\mu_{\text{eff}}, \epsilon_{\text{eff}} < 0$ ). (Despite the fact that the permittivity and permeability are parameters of bulk media, the effective permeability and permittivity in transmission lines can be defined from the equivalence between plane wave propagation in source-free, isotropic, linear, and homogenous media and TEM wave propagation in transmission lines. The wave equations are identical if the permeability and permittivity are given by  $Z'_s(\omega) = j\omega\mu_{\text{eff}}$  and  $Y'_p(\omega) = j\omega\epsilon_{\text{eff}}$ , respectively, where  $Z'_s$  and  $Y'_p$  are the per-unit-length impedance (series branch)

and admittance (shunt branch), respectively, of the equivalent T- or  $\pi$ -circuit model (unit cell) of the considered line.) In the last case, wave propagation is allowed, and it is backward (i.e., the phase and group velocities are antiparallel). If only one of the constitutive parameters is negative, wave propagation is not allowed. One of the most interesting properties of metamaterials and metamaterial transmission lines is the controllability (of course within certain limits) of the effective permeability and permittivity. In metamaterial transmission lines, this controllability is equivalent to the controllability of the characteristic impedance and dispersion (or phase constant), which are the parameters of interest in circuit or antenna design.

From the unit cell model of the considered metamaterial transmission line, the characteristic impedance and dispersion are given by [17]

$$\begin{aligned} Z_B^\pm &= -\frac{2B}{A - D \mp \sqrt{(A + D)^2 - 4}}, \\ \cosh(\gamma l) &= \frac{A + D}{2}, \end{aligned} \quad (1)$$

where,  $A$ ,  $B$ , and  $D$  are elements of the  $ABCD$  matrix of the unit cell,  $l$  is the unit cell length, and  $\gamma$  is the complex propagation constant; that is,  $\gamma = \alpha + j\beta$ , where  $\alpha$  and  $\beta$  are the attenuation and the phase constant, respectively. If the unit cell is symmetric with regard to the ports and it is described by a T-model, the previous expressions can be written as

$$\begin{aligned} Z_{B,T} &= \sqrt{Z_s(Z_s + 2Z_p)}, \\ \cosh(\gamma l) &= 1 + \frac{Z_s}{Z_p}, \end{aligned} \quad (2)$$

whereas if the considered model is the  $\pi$ -model, the dispersion is given by the same expression, and the characteristic impedance is

$$Z_{B,\pi}(\omega) = \sqrt{\frac{Z_s(\omega)Z_p(\omega)/2}{1 + Z_s(\omega)/2Z_p(\omega)}}, \quad (3)$$

where  $Z_s = j\chi_s$  and  $Z_p = 1/jB_p$  are the impedance of the series and shunt branch, respectively, of the T- or  $\pi$ -circuit models, with  $\chi_s$  and  $B_p$  being the series reactance and shunt susceptance, respectively (it is assumed that losses are negligible).

In the propagation regions,  $\alpha = 0$  and  $\beta \neq 0$ , and the dispersion relation in those regions can be expressed as

$$\cos(\beta l) = 1 + \frac{Z_s}{Z_p} = 1 - \chi_s B_p. \quad (4)$$

According to the dispersion relation, a necessary (although not sufficient) condition for wave propagation is an identical sign for the series reactance ( $\chi_s$ ) and shunt susceptance ( $B_p$ ). Moreover, if both signs are positive, wave propagation is forward, whereas it is backward (LH) if the signs of  $\chi_s$  and  $B_p$

are negative. To demonstrate this, we calculate the product  $(\beta l) \cdot d(\beta l)/d\omega$  using expression (4). The following result is obtained:

$$(\beta l) \cdot \frac{d(\beta l)}{d\omega} = \frac{\beta l}{\sin(\beta l)} \left( \chi_s \frac{dB_p}{d\omega} + B_p \frac{d\chi_s}{d\omega} \right). \quad (5)$$

Since, according to the Foster reactance theorem, the slope of the reactance/susceptance of a lossless network must be always positive, it follows that if  $\chi_s, B_p > 0$ , then  $\beta l \cdot d(\beta l)/d\omega > 0$ , corresponding to forward wave propagation. Conversely, if  $\chi_s, B_p < 0$ , then  $\beta l \cdot d(\beta l)/d\omega < 0$ , and wave propagation is backward (note that  $(\beta l)/\sin(\beta l) > 0$ ).

Depending on the complexity of the loading elements of the host line, it is possible to achieve not only either forward or backward wave transmission but also a composite right-/left-handed (CRLH) behavior, namely, LH wave propagation at certain frequency bands and forward (or right-handed (RH)) wave propagation in other frequency regions. There are two main approaches for the implementation of metamaterial transmission lines: (i) the CL-loaded approach [14–16] and (ii) the resonant-type approach [18, 19]. In the first case, the host line is loaded with series capacitors and shunt inductors. At low frequencies, the loading elements are dominant and wave propagation is backward; at high frequencies, the host line dominates over the loading elements, and wave propagation is forward. Thus CL-loaded lines actually exhibit a CRLH behavior. In the resonant-type approach, a host line is loaded with electrically small resonators, such as split ring resonators (SRRs) [20], or complementary split ring resonators (CSRRs) [21] and other reactive elements. CPWs loaded with pairs of SRRs and shunt inductive elements exhibit a CRLH behavior [18]. Similarly, microstrip lines loaded with CSRRs and series capacitive gaps support the propagation of backward (low frequencies) and forward (high frequencies) waves [22]. Obviously, CRLH lines can also be implemented by combining the CL-loaded and the resonant-type approach (hybrid approach [23]) or by using multiple reactive elements and/or resonators in many different configurations loading the host line. By increasing the degrees of freedom, it is possible to obtain circuit functionalities not easily achievable by using ordinary lines, for example, the multiband functionality attainable by means of generalized (or extended) metamaterial transmission lines [24–27].

In this paper, the focus is on the modeling of metamaterial transmission lines based on SRRs. The aim is to analyze in detail some effects related to the resonant elements (SRRs) which are not usually taken into account but that may be important under certain conditions, namely, the coupling between SRRs and the SRR orientation with regard to the transmission line. For this reason, the analysis is restricted to SRR-loaded lines without the presence of shunt inductive elements or other elements loading the line. Thus, the considered structures exhibit stopband functionality and provided that the number of unit cells is high enough, such structures are one-dimensional negative permeability metamaterials. These structures have found applications as bandstop filters [28], multiband devices, including dual-band matching networks [29] and dual-band printed dipole antennas [30] and sensors [31].

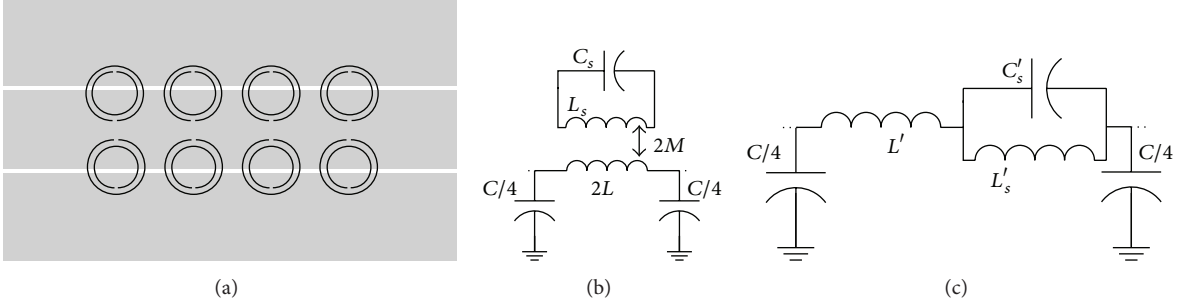


FIGURE 1: Typical topology (a) and circuit model (b) of a CPW loaded with SRRs. The model of (b) can be transformed to the one depicted in (c). The magnetic wall concept has been considered.

## 2. Structure under Study and Former Circuit Model

The typical topology of an SRR-loaded metamaterial transmission line, based on CPW technology, is depicted in Figure 1(a). The line is loaded with an array of SRR pairs etched in the back substrate side, with their centers roughly aligned with the slots of the line and their symmetry planes orthogonal to the line axis. With this configuration, the magnetic field generated by the line is able to excite the SRRs, and the structure exhibits a stopband in the vicinity of the SRR fundamental resonance frequency. This stopband has been interpreted as due to the negative effective permeability of the line just above the SRR resonance and to the high positive permeability below it (causing a strong mismatch); that is, the effective permeability is resonant and is described by the Lorentz model [1]. However, the stopband can also be explained from the lumped element equivalent circuit model of the unit cell of the structure, depicted in Figure 1(b). According to this model, firstly reported in [18], the SRRs are described by the resonant tank  $L_s-C_s$ ; the CPW line section is described by the series inductance  $L$  and the shunt capacitance  $C$ , and  $M$  accounts for the magnetic coupling between the line and the SRRs. This model can be transformed to the model depicted in Figure 1(c), where the following transformations apply

$$\begin{aligned} C'_s &= \frac{L_s}{4M^2\omega_o^2}, \\ L'_s &= 4M^2C_s\omega_o^2, \\ L' &= 2L - L'_s \end{aligned} \quad (6)$$

with

$$\omega_o^2 = \frac{1}{L_s C_s} = \frac{1}{L'_s C'_s}. \quad (7)$$

It should be noted that interresonator coupling (i.e., the coupling between resonators of different cells as well as between the pair of resonators forming the unit cell) is neglected in that model.

According to the model of Figure 1, a transmission zero (notch) is expected at the resonance frequency of the SRRs.

Since the presence of many SRR pairs tends to obscure the position of the transmission zero, it is convenient to consider a single cell structure, like the one shown in Figure 2(a). The simulated response (using the *Agilent Momentum* commercial software) is depicted in Figure 2(b). This response can be used to extract the parameters of the circuit model of Figure 1(c), following the procedure reported in [32]. The extracted circuit elements are those indicated in the caption of Figure 2. By using these reactive parameters, the circuit response can be inferred. The results, also depicted in Figure 2(b) [33], validate the circuit model of Figure 1 (note that the agreement between the circuit and electromagnetic simulation is very good).

The model of Figure 2 provides accurate results of the electromagnetic response of SRR-loaded lines. However, this model includes neither the coupling between SRRs (potentially possible when the resonators are closely spaced) nor the effects of SRR rotation (with regard to the topology shown in Figures 1 and 2). In the next section, interresonator coupling and its effects on the response of the structures are studied in detail on the basis of more elaborated circuit models that incorporate such electromagnetic interaction. Afterwards, the analysis of SRR-loaded CPW structures with arbitrarily oriented SRRs is carried out, and it is demonstrated that mixed (electric and magnetic) coupling between the line and the resonators must be considered for an accurate description of the structures.

## 3. Interresonator Coupling

With a view to studying interresonator coupling, let us consider the SRR orientation of Figures 1 and 2, namely, with the symmetry plane of the SRR orthogonal to the line axis. As is well known, if the structure is made of multiple unit cells, coupling between resonators belonging to different cells may exist. In addition, when the SRRs of the same unit cell are close to one another, interresonator coupling within the same unit cell may also arise. Therefore, there are two possible coupling contributions between the resonant elements: (i) interunit cell coupling and (ii) intraunit cell coupling. Both couplings will be studied, assuming that the coupling type is magnetic. Note that the magnetic coupling between coplanar SRRs of adjacent cells is negative [8, 12], whereas that between

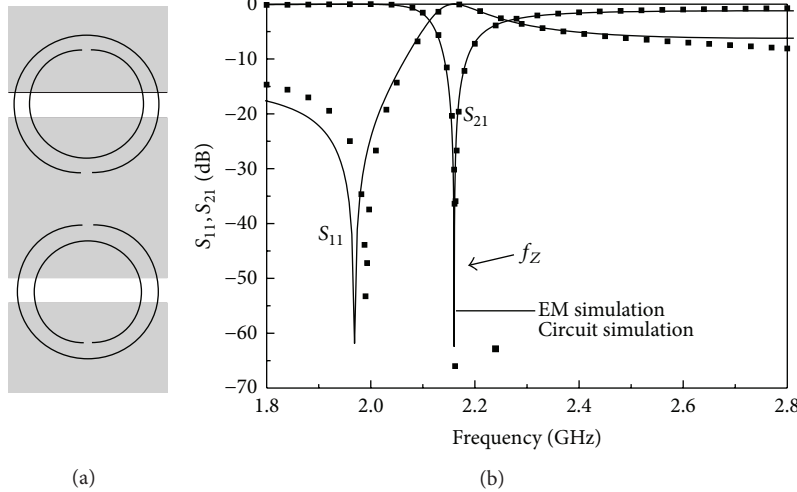


FIGURE 2: Layout (a) and electromagnetic response (b) of an SRR-loaded CPW unit cell. The considered substrate throughout this paper is *Rogers RO3010* with dielectric constant  $\epsilon_r = 11.2$  and thickness  $h = 1.27$  mm. CPW dimensions are central strip width  $W = 8$  mm, width of the slots  $G = 1.43$  mm, and length of the line  $l = 8$  mm. SRR dimensions are outer ring width  $c_{\text{out}} = 0.36$  mm, inner ring width  $c_{\text{inn}} = 0.37$  mm, distance between the rings  $d = 0.24$  mm, and internal radius  $r = 2.69$  mm. The extracted circuit parameters are  $L' = 1.91$  nH,  $C = 2.07$  pF,  $L'_s = 0.24$  nH, and  $C'_s = 23.01$  pF. From [33], reprinted with permission.

SRRs is positive [34]. The proper modeling of the magnetic coupling sign is mandatory; that is, the sign cannot be disregarded. Otherwise, the frequency response predicted by the circuit will not be able to describe correctly the behavior of the SRR-loaded lines. Let us now study these coupling mechanisms separately.

**3.1. Interunit Cell Coupling.** Let us consider that the magnetic coupling between adjacent resonators is accounted for by means of mutual inductances denoted as  $M_R$ . The circuit model is therefore the one depicted in Figure 3(a) [34]. In this model, losses are neglected, and the nearest-neighbor approximation in the interunit cell coupling is considered, so that interresonator interaction is modeled only between adjacent resonant elements. By using the T-circuit equivalence of magnetically coupled inductors, the circuit model of Figure 3(a) can be redrawn as depicted in Figure 3(b), from which it is possible to identify the four-port unit cell of Figure 3(c). Qualitatively, this unit cell is composed of a conventional transmission line-type circuit magnetically coupled to a secondary propagating structure. The latter structure supports a kind of backward waves that have been studied in depth in [35–38] and have been called magnetoinductive waves (MIWs). MIWs propagate within a narrow frequency band in the vicinity of SRR resonance, and the associated bandwidth is dependent on how strongly the resonators are coupled to each other. The stronger the interaction between the resonant elements, the wider the passband of the MIWs. Since multiconductor theory predicts that the resulting unit cell can propagate two modes [39], forward and backward waves are expected to coexist at some frequency band.

For the purpose of obtaining the dispersion characteristics of these SRR-loaded lines with interresonator coupling,

we apply Bloch mode analysis to the four-port circuit of Figure 3(c). Let us denote  $V_{Li}$  and  $I_{Li}$  as the voltages and currents at the ports ( $i = 1, 2$ ) of the left-hand side of the unit cell and  $V_{Ri}$  and  $I_{Ri}$  as the variables at the right-hand side ports. The variables at both sides of the network are linked through a generalized order-4 transfer matrix, according to

$$\begin{pmatrix} \mathbf{V}_L \\ \mathbf{I}_L \end{pmatrix} = \begin{pmatrix} \mathbf{A} & \mathbf{B} \\ \mathbf{C} & \mathbf{D} \end{pmatrix} \begin{pmatrix} \mathbf{V}_R \\ \mathbf{I}_R \end{pmatrix}, \quad (8)$$

where  $\mathbf{V}_L$ ,  $\mathbf{I}_L$ ,  $\mathbf{V}_R$ , and  $\mathbf{I}_R$  are column vectors composed of the pair of port variables, and  $\mathbf{A}$ ,  $\mathbf{B}$ ,  $\mathbf{C}$ , and  $\mathbf{D}$  are order-2 matrices. The dispersion relation is obtained from the eigenmodes of the system (8); that is

$$\det \begin{pmatrix} \mathbf{A} - e^{\gamma l} \cdot \mathbf{I} & \mathbf{B} \\ \mathbf{C} & \mathbf{D} - e^{\gamma l} \cdot \mathbf{I} \end{pmatrix} = 0, \quad (9)$$

where  $\mathbf{I}$  is the identity matrix and the propagation factor  $e^{\gamma l}$  is the eigenvalue. For reciprocal, lossless, and symmetric networks, the eigenvalues can be simplified to the solutions of [40, 41]:

$$\det (\mathbf{A} - \cosh(\gamma l) \cdot \mathbf{I}) = 0, \quad (10)$$

which gives

$$\begin{aligned} & \cosh(\gamma l) \\ &= \frac{1}{2} \left( A_{11} + A_{22} \pm \sqrt{(A_{11} - A_{22})^2 + 4A_{12}A_{21}} \right), \end{aligned} \quad (11)$$

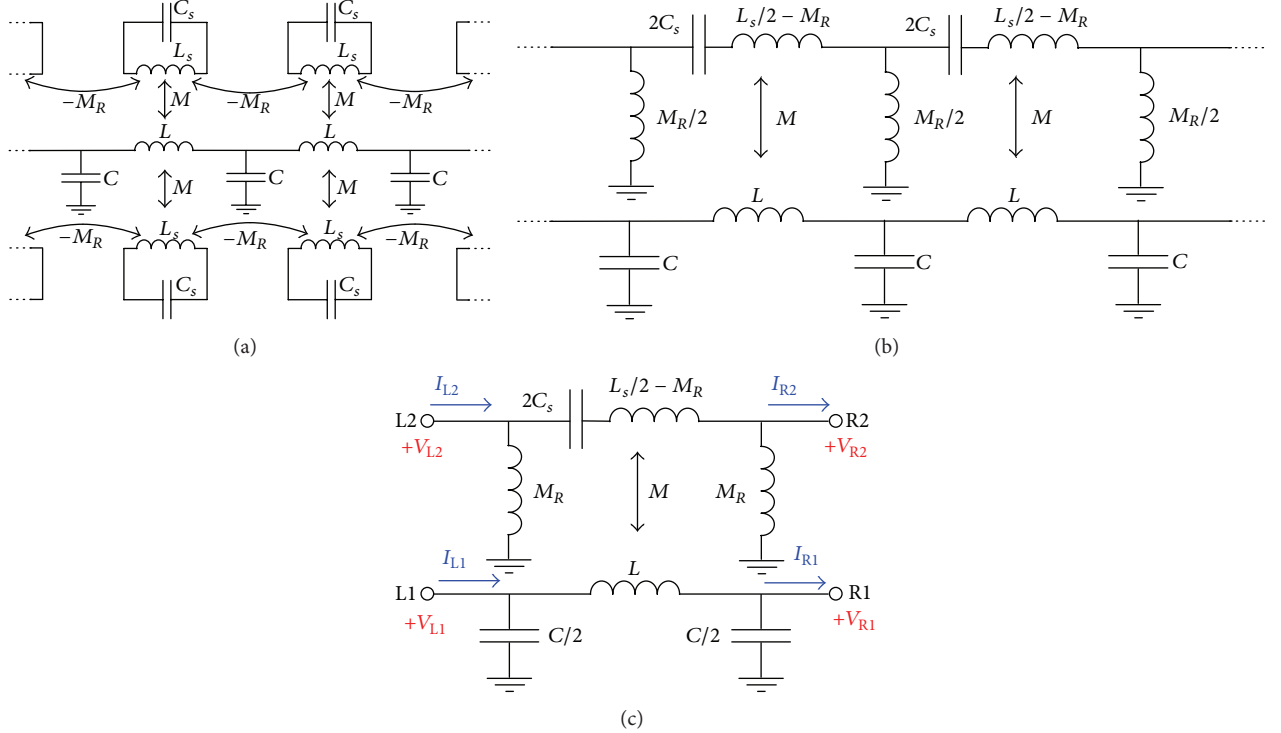


FIGURE 3: Lumped element equivalent circuit model of a periodic structure composed of a cascade of SRR-loaded CPW unit cells, including magnetic coupling between resonators of adjacent cells; model with mutual inductance between resonators (a), transformed model (b), and four-port unit cell model indicating the port voltages and currents relative to the calculation of the transfer  $ABCD$  matrix. From [34], reprinted with permission.

where the elements of  $\mathbf{A}$  matrix (inferred from the network of Figure 3(c)) are [34]

$$\mathbf{A} = \mathbf{D}^t = \begin{pmatrix} 1 - \frac{LC}{2}\omega^2 & \frac{M}{M_R} \\ -\frac{MC}{2}\omega^2 & \frac{1}{2M_R} \left( L_s - \frac{1}{C_s\omega^2} \right) \end{pmatrix}. \quad (12)$$

Since the network of Figure 3(c) is lossless, the elements of  $\mathbf{A}$  ( $A_{ij}$ ) are real numbers. Hence, if the radicand of the square root in (11) is positive, the propagation constant is either purely real ( $\alpha \neq 0, \beta = 0$ ) or purely imaginary ( $\alpha = 0, \beta \neq 0$ ), corresponding to evanescent or propagating modes, respectively. However, if the radicand in (11) is negative, the two solutions are of the form  $\gamma = \alpha \pm j\beta$ , corresponding to complex modes [42]. The frequency band that supports complex modes is thus obtained by forcing the radicand in (11) to be negative. Since complex modes do not carry net power, the frequency band supporting such modes is a rejection band, despite being of different nature from that associated to evanescent modes (where  $\alpha \neq 0, \beta = 0$ ).

Inspection of (11) and (12) reveals that a necessary condition for the presence of complex modes is the fact that  $M$  is different from zero (this is always the case, unless the substrate of the considered CPW is extremely thick). The two modal solutions for  $M = 0$  (meaning that the host line and the SRR array are decoupled) are simply the dispersion relation of a lossless transmission line described by the well-known LC ladder network and the dispersion of an array of

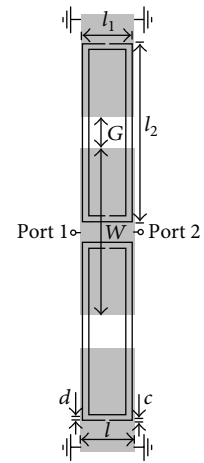
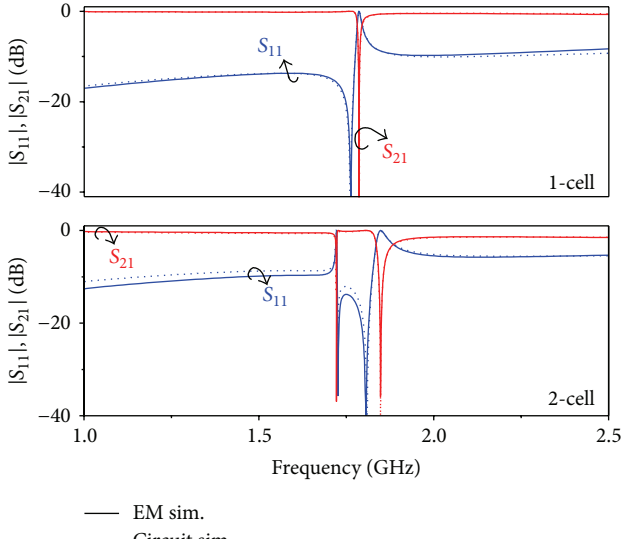


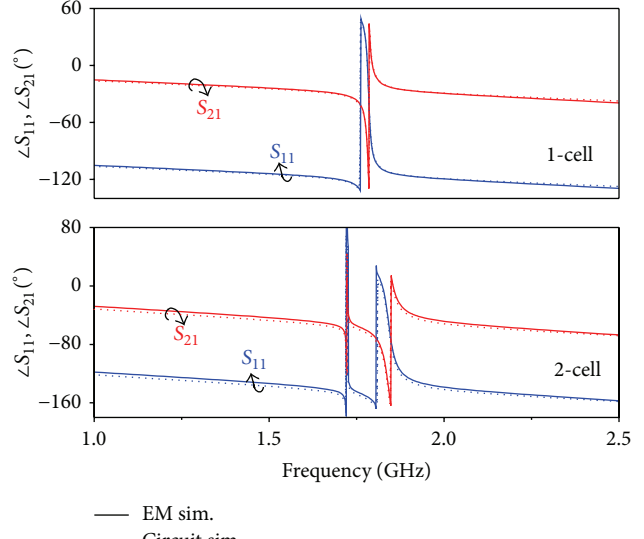
FIGURE 4: Unit cell of a CPW transmission line loaded with a pair of SRRs designed to enhance coupling between resonators of neighboring cells. Dimensions are  $W = 9.1$  mm,  $G = 1.7$  mm,  $l = 3$  mm,  $c = d = 0.15$  mm,  $l_1 = 2.8$  mm, and  $l_2 = 9.8$  mm. The Bloch waves propagate from port 1 to port 2. From [34], reprinted with permission.

inductively (edge) coupled SRRs, where backward MIWs in a narrow frequency band in the vicinity of SRR resonance are supported [34].

To validate the model of Figure 3, the unit cell of Figure 4 has been considered [34]. In this unit cell, the resonators



(a)



(b)

FIGURE 5: Magnitude (a) and phase (b) of the lossless transmission ( $S_{21}$ ) and reflection ( $S_{11}$ ) coefficients for a unit cell and for two cascaded unit cells of the structure in Figure 4. The extracted circuit parameters are  $L = 1.01 \text{ nH}$ ,  $C = 1.40 \text{ pF}$ ,  $L_s = 17.66 \text{ nH}$ ,  $C_s = 0.45 \text{ pF}$ ,  $M = 0.72 \text{ nH}$ , and  $M_R = 1.17 \text{ nH}$ . From [34], reprinted with permission.

are rectangular in order to enhance interresonator coupling. The circuit parameters have been extracted according to the general method reported in [32] (which ignores interresonator coupling) and the specific procedure (to determine  $M_R$ ) thoroughly described in [34]. Figure 5 depicts the circuit and electromagnetic simulations of the frequency response of a single unit cell and two unit cells, where the good agreement between circuit and electromagnetic simulations can be appreciated. The well-known frequency-splitting phenomenon as a consequence of the interresonator coupling should be noticed.

Once the circuit parameters have been extracted, the pair of modal propagation constants given by (11) can be inferred. The results are depicted in Figure 6. In the first allowed band there is a region with bi-valued propagation constant: one (forward) corresponding to transmission-line type propagation and the other (backward) related to magnetoinductive waves. Then, a region with a pair of conjugate complex propagation constants (complex modes) appears where forward and backward waves interfere with each other, followed by a region of evanescent waves. Finally, a forward wave transmission band emerges again. Hence, the enhancement of the stopband due to interresonator coupling is explained by the appearance of complex waves in the lower frequency region of that stopband (the complex modes exist from 1.843 GHz to 1.961 GHz, and the evanescent modes extend up to 1.977 GHz). However, the magnetic coupling between SRRs of adjacent cells is limited in practice and, hence, bandwidth broadening is also limited. The dispersion relation of a periodic structure composed of a cascade of the unit cells of Figure 4, obtained by means of the full-wave eigenmode solver of *CST Microwave Studio*, is also depicted in Figure 6. There is good agreement with the analytical

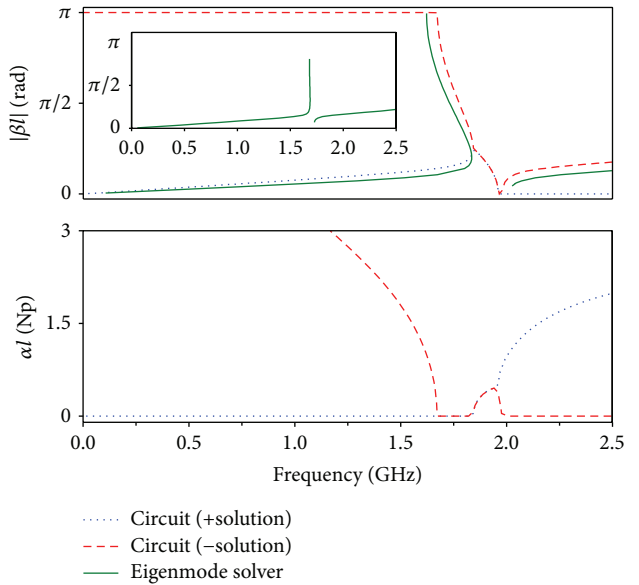


FIGURE 6: Dispersion relation for the structure of Figure 4 inferred from an eigenmode solver and from its equivalent circuit model of Figure 3(c). The circuit parameters are those indicated in the caption of Figure 5. The dispersion relation for the structure of Figure 4 with  $l = 4.8 \text{ mm}$  is depicted in the inset. The attenuation constant  $\alpha$  is not provided by the eigenmode solver. From [34], reprinted with permission.

dispersion curve predicted by the circuit model. That is, the bi-valued region is perfectly predicted by the eigenmode solver. Nevertheless, since there is no electromagnetic field pattern with net current transfer in the stopband, the tool is

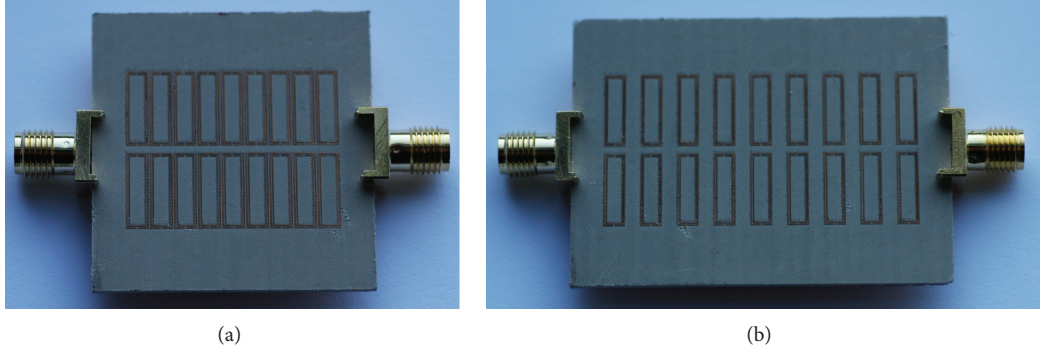


FIGURE 7: Photograph of the bottom face of the fabricated order-9 structures composed of the unit cell in Figure 4 with (a)  $l = 3$  mm and (b)  $l = 4.8$  mm. From [34], reprinted with permission.

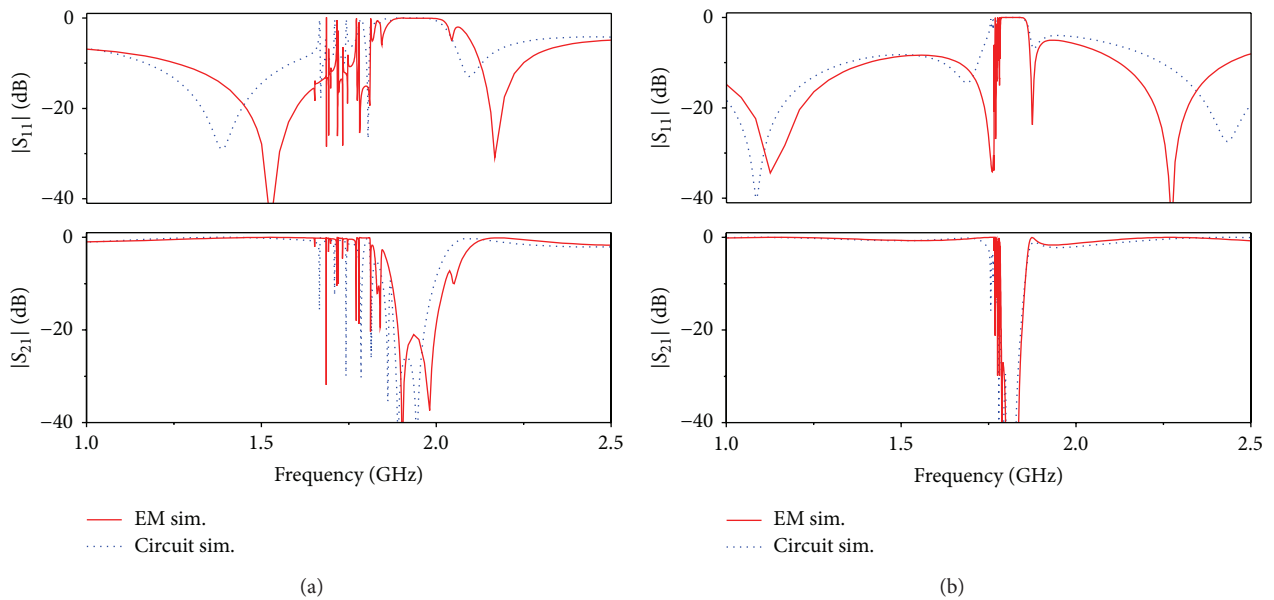


FIGURE 8: Lossless electromagnetic and circuit simulations of the transmission and reflection coefficients (magnitude) for nine cascaded cells of the structure in Figure 4 for (a)  $l = 3$  mm and (b)  $l = 4.8$  mm (the interresonator separation has been increased from 0.2 mm to 2 mm). The circuit parameters are those indicated in the caption of Figure 5, with the exception of  $M_R = 0.22$  nH in (b). Furthermore, in (b), a CPW section of 1.8 mm length has been cascaded between the port R1 and the port L1 of the contiguous cell in the circuit model. From [34], reprinted with permission.

not able to provide the dispersion curves in that region. For comparison purposes, we have also considered a structure whose resonators are spaced further apart providing much weaker coupling. The dispersion diagram, depicted in the inset of Figure 6, reveals that the stopband bandwidth is significantly narrower. Therefore, the dispersion diagrams indicate that most of the stopband in the structure of Figure 4 is related to the presence of complex modes rather than evanescent modes. In other words, as long as interresonator coupling is significant, complex modes may be the dominant mechanism of signal rejection (in the vicinity of SRR fundamental resonance) of these SRR-loaded structures.

The experimental validation has been carried out by considering two 9-cell structures, one with  $l = 3$  and the other one with  $l = 4.8$  (corresponding to tightly and weakly coupled resonators, resp.), in coherence with the two

considered structures of which the dispersion relation was determined. The photographs of these SRR-loaded lines are shown in Figure 7. Figure 8 shows the comparison between the lossless electromagnetic simulation and circuit simulation for both structures, whereas Figure 9 compares the lossy electromagnetic simulation and measurement. As expected, interresonator coupling enhances the stopband bandwidth. The measured stopbands are also in accordance with those obtained from the dispersion relation. Hence, the dispersion relation inferred from the multiterminal circuit model is a powerful tool to gain insight into the stopband and the effects of interresonator coupling in SRR-loaded lines.

**3.2. Intraunit Cell Coupling.** In the previous subsection, the coupling between the two resonators of the unit cell was neglected, and this is reasonable if the resonators are not

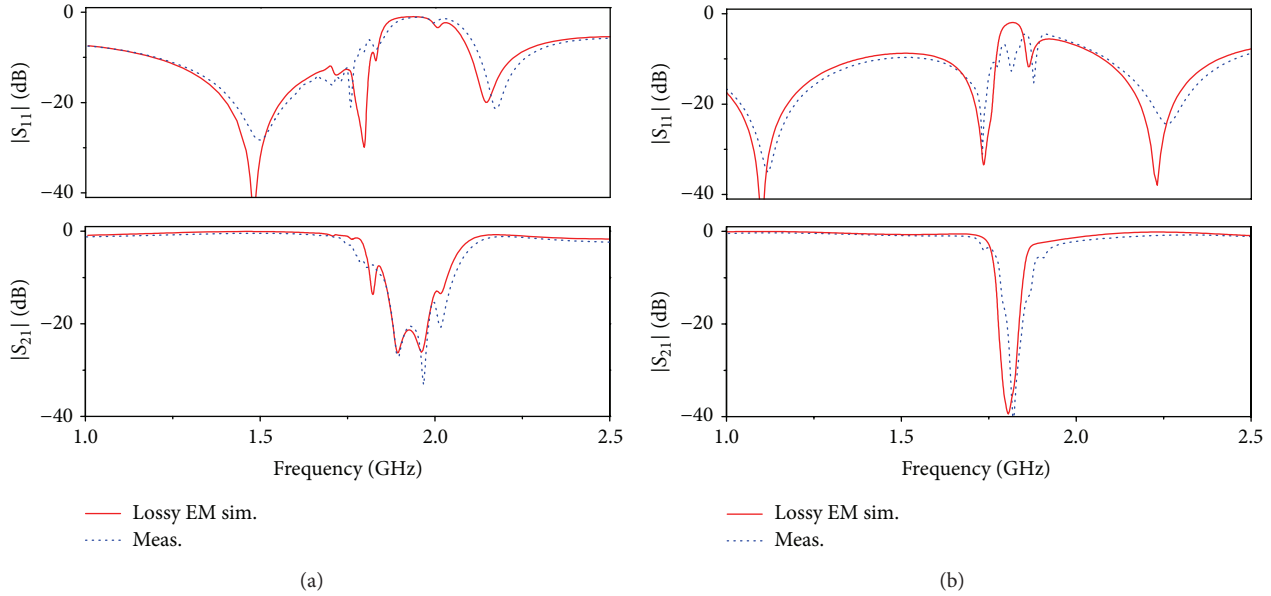


FIGURE 9: Measurement and lossy electromagnetic simulation of the transmission and reflection coefficients of the structures in Figure 7; (a)  $l = 3 \text{ mm}$  and (b)  $l = 4.8 \text{ mm}$ . The loss tangent in *Rogers RO3010* is  $\tan \delta = 0.0023$ . From [34], reprinted with permission.

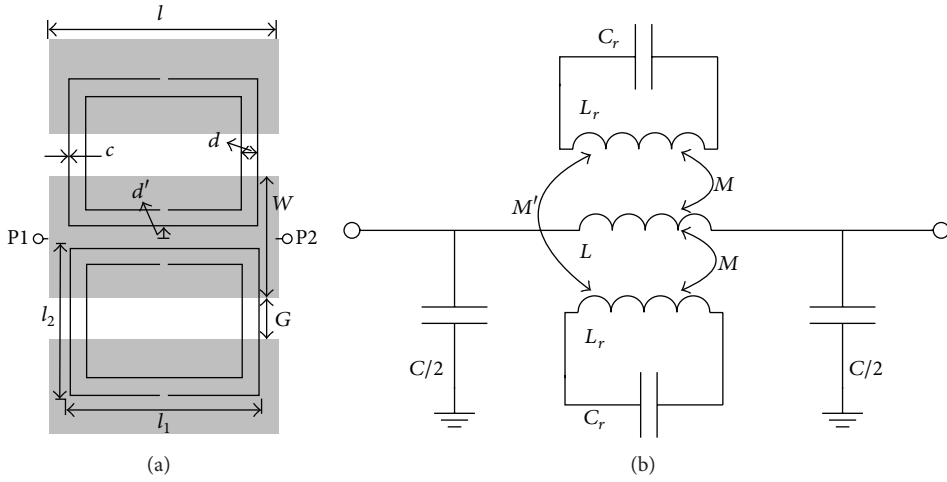


FIGURE 10: Typical topology of a CPW loaded with a pair of square-shaped SRRs (a) and lumped element equivalent circuit model considering magnetic coupling between SRRs (b).

closely spaced. If this is not the case, as is in general, interresonator coupling emerges. To gain insight into the effects of such a coupling, we consider the structure in Figure 10(a) where the interresonator magnetic coupling is included in the circuit model of the unit cell (through  $M'$ ), whilst the coupling between adjacent resonators is neglected (i.e.,  $M_R = 0$ ). The resulting model (unit cell) is depicted in Figure 10(b) [43] (for coherence with [43],  $L_r$  and  $C_r$  stand for the SRR inductance and capacitance, resp.). The magnetic coupling between the resonators of the unit cell shifts the transmission zero frequency as compared to the structure with negligible coupling. To demonstrate this, it suffices to apply the T-circuit equivalence of a pair of magnetically coupled inductors (Figure 11(a)) [44]. Since

there is a magnetic wall across the symmetry plane of the structure, it follows that the circuit model of Figure 10(b) can be transformed as shown in Figure 11(b), and by applying the magnetic wall concept, the circuit of Figure 11(c) results. By comparing this latter circuit model to the one depicted in Figure 1(b), it is clear that  $M'$  modifies the transmission zero frequency, which is now given by

$$\omega'_o = \frac{\omega_o}{\sqrt{1 + M'/L_r}} = \frac{\omega_o}{\sqrt{1 + k_m}}, \quad (13)$$

where  $k_m$  is the magnetic coupling coefficient between the resonators [44] and  $\omega_o$  is the intrinsic resonance frequency of the SRRs, defined in (7). According to the model of

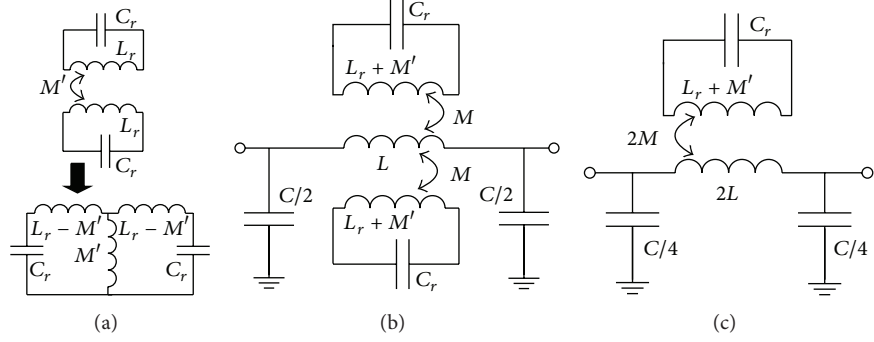


FIGURE 11: Equivalent T-circuit model of a pair of magnetically coupled inductors (a), circuit model of the structure of Figure 10(a) with the inductive coupling between resonators transformed to the equivalent T-model (b), and circuit that results by applying the magnetic wall concept (c). From [43], reprinted with permission.

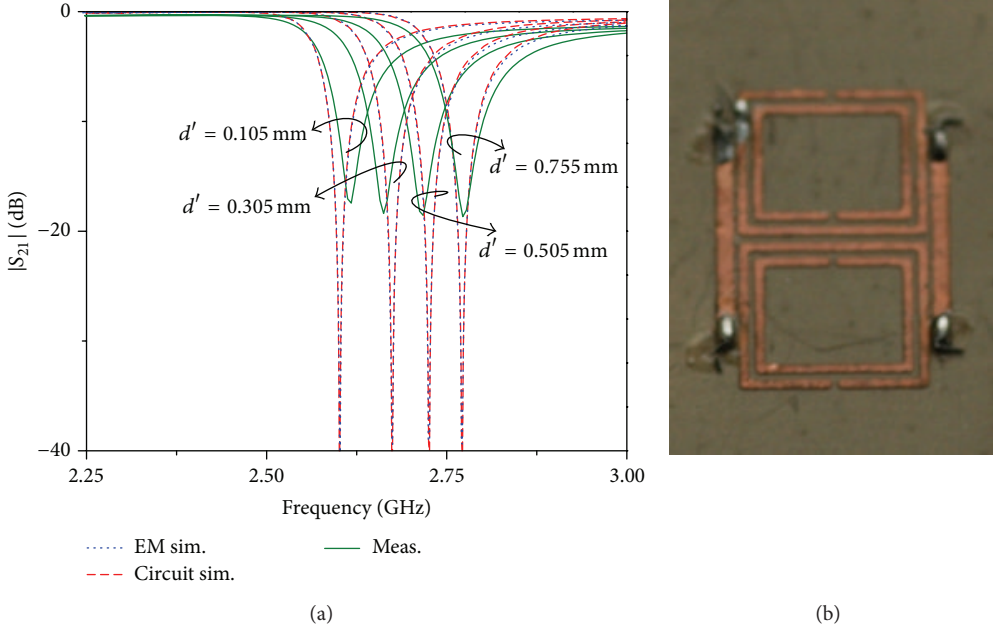


FIGURE 12: Frequency response for different values of  $d'$  (a) and detail of the bottom side of one of the fabricated samples (b). In reference to Figure 10(a), dimensions are  $l_1 = 4.8$  mm,  $l_2 = 3.8$  mm,  $c = d = 0.2$  mm,  $l = 5.6$  mm,  $W = 3$  mm, and  $G = 1.01$  mm. The circuit parameters are listed in Table 1. From [43], reprinted with permission.

Figure 11(c), the effects of magnetic coupling between the resonators of the unit cell can be accounted for by simply modifying the SRR inductance and considering the former circuit model of Figure 1(b). As a result of the positive sign in  $M'$ , this mutual inductance shifts the resonance frequency downwards. However, this is usually ignored regardless of the distance (and hence coupling) between the SRRs. It is worth mentioning that if SRRs with different dimensions (and hence different coupling to the line) are considered, interresonator coupling also modifies the position of the transmission zero frequencies (with regard to the intrinsic resonance frequency of the individual resonators). Analytical expressions are given in [43]. Nevertheless, in contrast to the symmetric case, mutual coupling cannot be neglected in CPWs asymmetrically loaded with pairs of SRRs. Furthermore, in the most

general asymmetric case, it is not easy to identify a simplified equivalent circuit similar to the one of Figure 1(c), that is, without mutual inductances.

To validate the models in Figures 10 and 11 of a CPW symmetrically loaded with a pair of magnetically coupled SRRs and the effects of coupling, four different structures with identical SRRs but with different interresonator distance have been considered. The lossless electromagnetic simulations of the structure ( $S_{21}$ ), assuming different values of interresonator distance,  $d'$ , are depicted in Figure 12(a). The circuit parameters for the four considered cases are indicated in Table 1. As  $d'$  increases, the mutual coupling  $M'$  decreases, and the resonance frequency increases. Note that the other circuit parameters do not significantly vary, and the agreement between circuit and electromagnetic simulations

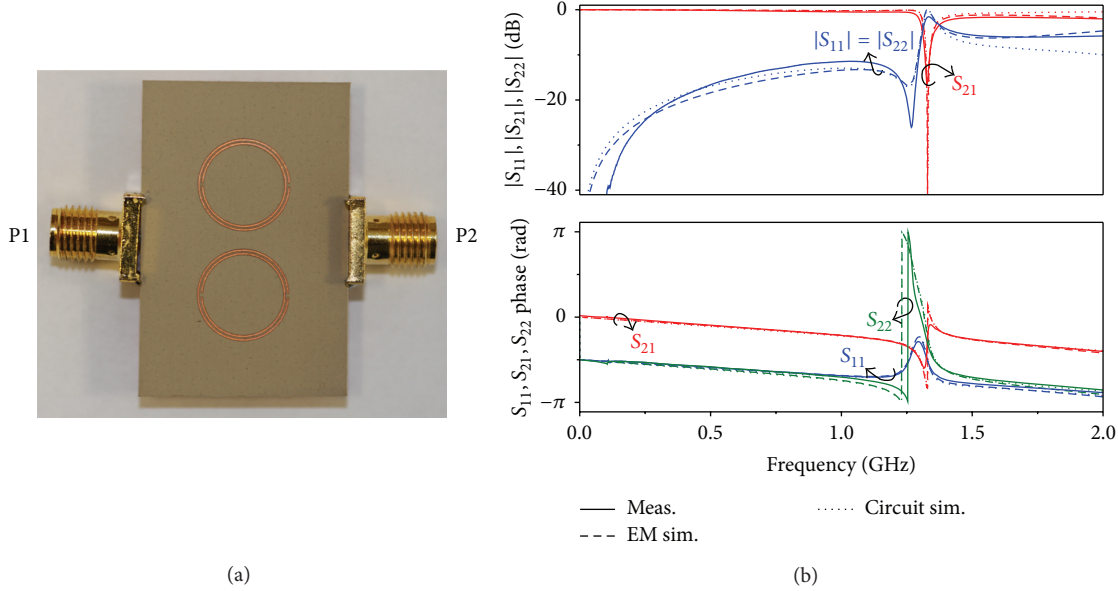


FIGURE 13: Bottom side photograph of the fabricated SRR-loaded CPW with  $\phi = 90^\circ$  (a) and frequency response (b). Dimensions are  $W = 10.4$  mm,  $G = 1.6$  mm, external radius  $r_{\text{ext}} = 5$  mm, and  $c = d = 0.2$  mm. The extracted circuit parameters are  $L = 1.5$  nH,  $C = 6.1$  pF,  $L_s = 28.2$  nH,  $C_s = 0.43$  pF,  $M = 1.35$  nH, and  $C_a = 0.08$  pF. From [46], reprinted with permission.

TABLE 1: Extracted circuit parameters for different values of  $d'$ .

| $d'$ (mm) | $L$ (nH) | $C$ (pF) | $C_r$ (pF) | $L_r$ (nH) | $M$ (nH) | $M'$ (nH) |
|-----------|----------|----------|------------|------------|----------|-----------|
| 0.105     | 1.82     | 1.58     | 0.44       | 6.85       | 0.82     | 1.74      |
| 0.305     | 1.86     | 1.58     | 0.44       | 6.85       | 0.82     | 1.29      |
| 0.505     | 1.84     | 1.57     | 0.43       | 6.85       | 0.81     | 1.02      |
| 0.755     | 1.85     | 1.55     | 0.43       | 6.85       | 0.80     | 0.80      |

in the region of interest is very good, pointing out the validity of the model. The measured responses (plotted in Figure 12(a)) are also in good agreement.

#### 4. SRR Rotation: Mixed Coupling

In the SRR-loaded CPW structures considered thus far, the slits of the SRR (aligned with the symmetry plane of the particle) are orthogonally oriented to the line axis. With this configuration, the coupling mechanism between the line and the resonators is magnetic, and the circuit models are those presented in the previous sections. By contrast, let us now consider that the SRRs are oriented with an arbitrary angle  $\phi$  (where  $\phi = 0^\circ$  corresponds to the orthogonal orientation). If  $\phi \neq 0^\circ$ , the SRR-loaded line is no longer symmetric with regard to the ports, and the circuit model must account for that asymmetry (note that any of the structures and circuit models previously presented are symmetric with regard to the ports). Moreover, since the SRR exhibits an electric dipole moment (at the fundamental resonance) in the plane of the particle and orthogonal to its symmetry plane [8, 45], it follows that, by rotating the SRR ( $\phi \neq 0^\circ$ ), electric coupling between the line and the SRR does also arise.

As a case study, consider the structure shown in Figure 13(a), where  $\phi = 90^\circ$ . The response of this structure (unit cell), shown in Figure 13(b), indicates that the phases of  $S_{11}$  and  $S_{22}$  are different, as expected on account of the asymmetry with regard to the ports. Obviously, these different phases cannot be explained by the previous circuit models. Necessarily, the circuit model describing the SRR-loaded CPW with  $\phi \neq 0^\circ$  must be asymmetric. By including electric coupling between the line and the SRRs in the model of Figure 1(b), that is, by modeling the structure through mixed magnetoelectric coupling, the resulting circuit (depicted in Figure 14) is asymmetric, and it describes very accurately the frequency response of the structure [46]. Note that the asymmetry in the circuit model (necessary to explain that  $S_{11} \neq S_{22}$ ) comes from the magnetic coupling (the dot convention for the mutual inductance is used, where the currents entering dot-marked terminals produce additive magnetic fluxes), although this is not manifested if electric coupling is not present.

From the electromagnetic response depicted in Figure 13(b), the circuit parameters of the model of Figure 14 were extracted [46]. The resulting circuit parameters are indicated in the caption of Figure 13. The agreement between the circuit simulation (also depicted in Figure 13(b)) and the electromagnetic simulation is good. The device was fabricated, and the measured response is also in good accordance with the circuit and electromagnetic simulations. These results clearly point out that, to avoid electric coupling between the line and the SRRs, it is mandatory to etch the SRRs with their symmetry plane orthogonally oriented to the line axis. Otherwise, mixed coupling appears and must be taken into account for an accurate description of

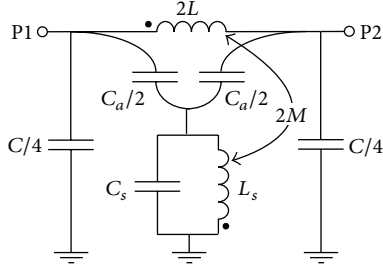


FIGURE 14: Proposed equivalent circuit model (unit cell) of the CPW loaded with arbitrarily oriented SRRs ( $C_a = 0$  for  $\phi = 0^\circ$ ). The magnetic wall concept has been applied. From [46], reprinted with permission.

the SRR-loaded line through its lumped element equivalent circuit model.

## 5. Discussion

The description of the previous SRR-loaded lines through lumped element equivalent circuits assumes that the electrical size of the unit cell is small. Under these conditions, the proposed circuits provide an accurate description of the structures up to frequencies slightly above the SRR resonance frequency. At higher frequencies, the circuit response and the electromagnetic (or measured) response progressively diverge since the SRRs dimensions are comparable or larger than the wavelength. This effect is more pronounced if the electrical size of the SRRs is not very small, as occurs in SRRs with weakly coupled loops or in SRRs consisting of a single loop. In a very recent paper [47], the model of Figure 1(b) has been improved by representing the transmission line section by two  $\pi$ -cells, keeping the same number of independent parameters. This model allows for better matching with full-wave electromagnetic simulation and measurement and is especially convenient when single-loop SRRs are considered (as is the case of the structures in [47]). By describing the line section with two cascaded  $\pi$ -cells, more accurate results can be obtained if the SRR and hence the transmission line section of the unit cell are not electrically very small. However, the penalty, from the point of view of circuit design, is a higher complexity. In other words, the circuits proposed in [47] are justified if the considered resonators have a moderate electrical size. If the electric size of the particles is small, then the circuits proposed in the previous sections suffice.

Concerning the bandwidth enhancement caused by interunit cell coupling, this effect also manifests in SRRs operating inside waveguides or free space [48].

Lastly, it is worth mentioning that similar improvements to the original model of the SRR-loaded line of Figure 1(b) can also be applied to the original model of a microstrip line loaded with complementary split ring resonators (CSRRs), formerly reported in [19]. Thus, the effects of CSRR rotation (leading to mixed coupling) have been reported in [46], and the effects of interresonator coupling between CSRRs of adjacent cells (enhancing the stopband bandwidth) were

studied in [49]. In the case of microstrip lines loaded with (electrically) coupled CSRRs, the presence of complex modes has been explained as due to the coexistence of electromagnetic and electroinductive waves [50]. Typically, microstrip lines are loaded with CSRRs including a single resonant element in the unit cell. It is for this reason that an analogous study to the one reported in Section 3.2 for CSRR-loaded lines has not been considered so far.

## 6. Conclusions

In conclusion, the recent progress in the circuit modeling of SRR-loaded CPW transmission lines has been reviewed. We have modeled three main effects not considered in the former model of the unit cell presented more than one decade ago. Specifically, we have analyzed the effects of interresonator coupling between resonators of adjacent cells and between the pair of resonators of the unit cell, and we have also studied the SRR angular orientation. All these effects have been taken into account in order to accurately describe the structure through novel lumped element equivalent circuits. In brief, coupling between adjacent resonators enhances the stopband bandwidth, and this has been found to be caused by the appearance of complex modes; coupling between the two resonators of the unit cell modifies the notch frequency and can be simply modeled by modifying the inductance of the SRR. Finally, it has been found that if the SRR symmetry plane is not orthogonal to the line axis, mixed (i.e., electric and magnetic) coupling between the line and the SRRs emerges, and both coupling mechanisms must be included in the circuit model for an accurate description of the structures.

## Conflict of Interests

The authors declare that there is no conflict of interests regarding the publication of this paper.

## Acknowledgments

This work has been supported by MINECO-Spain (Projects TEC2010-17512 METATRANSFER, CONSOLIDER EMET CSD2008-00066, EXPLORA TEC2011-13615-E, and TEC2013-40600-R COM-SEN-RFID) and by Generalitat de Catalunya (Project 2014SGR-157). Jordi Naqui and Ferran Martín have been awarded with an FPU grant (AP2010-0431) and with an ICREA Academia Award, respectively.

## References

- [1] D. R. Smith, W. J. Padilla, D. C. Vier, S. C. Nemat-Nasser, and S. Schultz, "Composite medium with simultaneously negative permeability and permittivity," *Physical Review Letters*, vol. 84, no. 18, pp. 4184–4187, 2000.
- [2] V. G. Veselago, "The electrodynamics of substances with simultaneously negative values of  $\epsilon$  and  $\mu$ ," *Soviet Physics Uspekhi*, vol. 10, no. 4, pp. 509–514, 1968.
- [3] R. A. Shelby, D. R. Smith, and S. Schultz, "Experimental verification of a negative index of refraction," *Science*, vol. 292, no. 5514, pp. 77–79, 2001.

- [4] A. Grbic and G. V. Eleftheriades, "Experimental verification of backward-wave radiation from a negative refractive index metamaterial," *Journal of Applied Physics*, vol. 92, no. 10, pp. 5930–5935, 2002.
- [5] G. V. Eleftheriades and K. G. Balmain, Eds., *Negative-Refraction Metamaterials: Fundamental Principles and Applications*, John Wiley & Sons, New York, NY, USA, 2005.
- [6] C. Caloz and T. Itoh, *Electromagnetic Metamaterials: Transmission Line Theory and Microwave Applications*, John Wiley & Sons, New York, NY, USA, 2006.
- [7] N. Engheta and R. W. Ziolkowski, *Metamaterials: Physics and Engineering Explorations*, John Wiley & Sons, New York, NY, USA, 2006.
- [8] R. Marqués, F. Martín, and M. Sorolla, *Metamaterials with Negative Parameters: Theory, Design and Microwave Applications*, John Wiley & Sons, New York, NY, USA, 2007.
- [9] A. K. Sarychev and V. M. Shalaev, *Electrodynamics of Metamaterials*, World Scientific Publishing, Singapore, 2007.
- [10] P. Markos and C. M. Sokoulis, *Wave Propagation: From Electrons to Photonic Crystals and Left-Handed Materials*, Princeton University Press, 2008.
- [11] F. Capolino, Ed., *Metamaterials Handbook*, CRC Press, New York, NY, USA, 2009.
- [12] L. Solymar and E. Shamonina, *Waves in Metamaterials*, Oxford University Press, Oxford, UK, 2009.
- [13] T. J. Cui, D. R. Smith, and R. Liu, Eds., *Metamaterials: Theory, Design and Applications*, Springer, New York, NY, USA, 2010.
- [14] A. K. Iyer and G. V. Eleftheriades, "Negative refractive index metamaterials supporting 2-D waves," in *Proceedings of the IEEE MSS-S International Microwave Symposium Digest*, pp. 412–415, Seattle, Wash, USA, June 2002.
- [15] A. A. Oliner, "A periodic-structure negative-refractive-index medium without resonant elements," in *Proceedings of the URSI Digest, IEEE-AP-S USNC/URSI National Radio Science Meeting*, p. 41, San Antonio, Tex, USA, June 2002.
- [16] C. Caloz and T. Itoh, "Application of the transmission line theory of left-handed (LH) materials to the realization of a microstrip LH transmission line," in *Proceedings of the IEEE AP-S USNC/URSI National Radio Science Meeting*, vol. 2, pp. 412–415, IEEE, San Antonio, Tex, USA, June 2002.
- [17] D. M. Pozar, *Microwave Engineering*, Addison Wesley, New York, NY, USA, 1990.
- [18] F. Martín, J. Bonache, F. Falcone, M. Sorolla, and R. Marqués, "Split ring resonator-based left-handed coplanar waveguide," *Applied Physics Letters*, vol. 83, no. 22, pp. 4652–4654, 2003.
- [19] J. D. Baena, J. Bonache, F. Martín et al., "Equivalent-circuit models for split-ring resonators and complementary split-ring resonators coupled to planar transmission lines," *IEEE Transactions on Microwave Theory and Techniques*, vol. 53, no. 4, pp. 1451–1460, 2005.
- [20] J. B. Pendry, A. J. Holden, D. J. Robbins, and W. J. Stewart, "Magnetism from conductors and enhanced nonlinear phenomena," *IEEE Transactions on Microwave Theory and Techniques*, vol. 47, no. 11, pp. 2075–2084, 1999.
- [21] F. Falcone, T. Lopetegi, J. D. Baena, R. Marqués, F. Martín, and M. Sorolla, "Effective negative- $\epsilon$  stopband microstrip lines based on complementary split ring resonators," *IEEE Microwave and Wireless Components Letters*, vol. 14, no. 6, pp. 280–282, 2004.
- [22] M. Gil, J. Bonache, J. Selga, J. García-García, and F. Martín, "Broadband resonant-type metamaterial transmission lines," *IEEE Microwave and Wireless Components Letters*, vol. 17, no. 2, pp. 97–99, 2007.
- [23] J. Bonache, M. Gil, I. Gil, J. García-García, and F. Martín, "Limitations and solutions of resonant-type metamaterial transmission lines for filter applications: the hybrid approach," in *Proceedings of the IEEE MTT-S International Microwave Symposium Digest*, pp. 939–942, San Francisco, Calif, USA, June 2006.
- [24] A. Rennings, S. Otto, J. Mosig, C. Caloz, and I. Wolff, "Extended composite right/left-handed metamaterial and its application as quadband quarter-wavelength transmission line," in *Proceedings of the Asia-Pacific Microwave Conference (APMC '06)*, pp. 1405–1408, Yokohama, Japan, December 2006.
- [25] G. V. Eleftheriades, "A generalized Negative-RefRACTive-Index Transmission-Line (NRI-TL) metamaterial for dual-band and quad-band applications," *IEEE Microwave and Wireless Components Letters*, vol. 17, no. 6, pp. 415–417, 2007.
- [26] G. Sisó, M. Gil, J. Bonache, and F. Martín, "Generalized model for multiband metamaterial transmission lines," *IEEE Microwave and Wireless Components Letters*, vol. 18, no. 11, pp. 728–730, 2008.
- [27] C. Camacho-Peña, T. M. Martín-Guerrero, J. Esteban, and J. E. Page, "Derivation and general properties of artificial lossless balanced composite right/left-handed transmission lines of arbitrary order," *Progress In Electromagnetics Research B*, no. 13, pp. 151–169, 2009.
- [28] F. Martín, F. Falcone, J. Bonache, R. Marqués, and M. Sorolla, "Miniaturized CPW stop band filters based on multiple tuned split ring resonators," *IEEE Microwave and Wireless Components Letters*, vol. 13, no. 12, pp. 511–513, 2003.
- [29] F. Paredes, G. Zamora, J. Bonache, and F. Martín, "Dual-band impedance matching networks based on split ring resonators for applications in radiofrequency identification (RFID)," *IEEE Transactions on Microwave Theory and Techniques*, vol. 58, no. 5, pp. 1159–1166, 2010.
- [30] F. J. Herraiz-Martínez, L. E. García-Muñoz, D. González-Ovejero, V. González-Posadas, and D. Segovia-Vargas, "Dual-frequency printed dipole loaded with split ring resonators," *IEEE Antennas and Wireless Propagation Letters*, vol. 8, pp. 137–140, 2009.
- [31] J. Naqui, M. Durán-Sindreu, and F. Martín, "Novel sensors based on the symmetry properties of split ring resonators (SRRs)," *Sensors*, vol. 11, no. 8, pp. 7545–7553, 2011.
- [32] F. Aznar, M. Gil, J. Bonache et al., "Characterization of miniaturized metamaterial resonators coupled to planar transmission lines through parameter extraction," *Journal of Applied Physics*, vol. 104, no. 11, Article ID 114501, 8 pages, 2008.
- [33] F. Aznar, M. Gil, J. Bonache, and F. Martín, "Modelling metamaterial transmission lines: a review and recent developments," *Opto-Electronics Review*, vol. 16, no. 3, pp. 226–236, 2008.
- [34] J. Naqui, A. Fernández-Prieto, F. Mesa, F. Medina, and F. Martín, "Effects of inter-resonator coupling in split ring resonator loaded metamaterial transmission lines," *Journal of Applied Physics*, vol. 115, no. 19, Article ID 194903, 2014.
- [35] E. Shamonina, V. A. Kalinin, K. H. Ringhofer, and L. Solymar, "Magneto-inductive waveguide," *Electronics Letters*, vol. 38, no. 8, pp. 371–373, 2002.
- [36] E. Shamonina, V. A. Kalinin, K. H. Ringhofer, and L. Solymar, "Magnetoinductive waves in one, two, three dimensions," *Journal of Applied Physics*, vol. 92, no. 10, pp. 6252–6261, 2002.
- [37] R. R. A. Syms, E. Shamonina, V. Kalinin, and L. Solymar, "A theory of metamaterials based on periodically loaded

- transmission lines: interaction between magnetoinductive and electromagnetic waves," *Journal of Applied Physics*, vol. 97, no. 6, Article ID 064909, 2005.
- [38] M. J. Freire, R. Marqués, F. Medina, M. A. G. Laso, and F. Martin, "Planar magnetoinductive wave transducers: theory and applications," *Applied Physics Letters*, vol. 85, no. 19, pp. 4439–4441, 2004.
  - [39] R. Mongia, I. Bahl, and P. Barthia, *RF and Microwave Coupled Line Circuits*, Artech House, 1999.
  - [40] J. Shekel, "Matrix analysis of multi-terminal transducers," *Proceedings of the IRE*, vol. 42, no. 5, pp. 840–847, 1954.
  - [41] R. Islam, M. Zedler, and G. V. Eleftheriades, "Modal analysis and wave propagation in finite 2D transmission-line metamaterials," *IEEE Transactions on Antennas and Propagation*, vol. 59, no. 5, pp. 1562–1570, 2011.
  - [42] T. Tamir and A. A. Oliner, "Guided complex waves," *Proceedings of the IEEE*, vol. 110, pp. 310–334, 1963.
  - [43] L. Su, J. Naqui, J. Mata-Contreras, and F. Martín, "Modeling metamaterial transmission lines loaded with pairs of coupled split-ring resonators," *IEEE Antennas and Wireless Propagation Letters*, vol. 14, pp. 68–71, 2015.
  - [44] J. Hong and M. J. Lancaster, *Microstrip Filters for RF/Microwave Applications*, John Wiley & Sons, New York, NY, USA, 2001.
  - [45] R. Marqués, F. Medina, and R. Rafii-El-Idrissi, "Role of bianisotropy in negative permeability and left-handed metamaterials," *Physical Review B*, vol. 65, no. 14, Article ID 144440, 2002.
  - [46] J. Naqui, M. Durán-Sindreu, and F. Martín, "Modeling split ring resonator (SRR) and complementary split ring resonator (CSRR) loaded transmission lines exhibiting cross polarization effects," *IEEE Antennas and Wireless Propagation Letters*, vol. 12, pp. 178–181, 2013.
  - [47] R. Bojanic, V. Milosevic, B. Jokanovic, F. Medina-Mena, and F. Mesa, "Enhanced modelling of split-ring resonators couplings in printed circuits," *IEEE Transactions on Microwave Theory and Techniques*, vol. 62, no. 8, pp. 1605–1615, 2014.
  - [48] J. Machac, J. Zehentner, and M. Blaha, "Coupling of split ring resonators in a mu-negative volumetric metamaterial," in *Proceedings of the IEEE MTT-S International Microwave Symposium Digest*, pp. 327–330, Atlanta, Ga, USA, June 2008.
  - [49] J. Naqui, M. Duran-Sindreu, A. Fernandez-Prieto, F. Mesa, F. Medina, and F. Martin, "Multimode propagation and complex waves in CSRR-based transmission-line metamaterials," *IEEE Antennas and Wireless Propagation Letters*, vol. 11, pp. 1024–1027, 2012.
  - [50] M. Beruete, F. Falcone, M. J. Freire, R. Marqús, and J. D. Baena, "Electroinductive waves in chains of complementary metamaterial elements," *Applied Physics Letters*, vol. 88, no. 8, Article ID 083503, 2006.

## Research Article

# Polarization-Independent and Angle-Insensitive Metamaterial Absorber Using 90-Degree-Rotated Split-Ring Resonators

Jia-Qi Feng,<sup>1</sup> Wei-Dong Hu,<sup>1</sup> Qing-Le Zhang,<sup>1</sup> Hua Zong,<sup>1</sup> Hui Huang,<sup>2</sup> Yu-Ting Jin,<sup>1</sup> Yu-Ming Wu,<sup>1</sup> Zhan Xu,<sup>1</sup> Xin Lv,<sup>1</sup> and Li-Ming Si<sup>1</sup>

<sup>1</sup>Beijing Key Laboratory of Millimeter Wave and Terahertz Technology, School of Information and Electronics, Beijing Institute of Technology, Beijing 100081, China

<sup>2</sup>Microwave Parameters Laboratory, Division of Electronics and Information Technology, National Institute of Metrology, Beijing 100013, China

Correspondence should be addressed to Li-Ming Si; lms@bit.edu.cn

Received 6 March 2015; Revised 24 April 2015; Accepted 24 April 2015

Academic Editor: Roman E. Noskov

Copyright © 2015 Jia-Qi Feng et al. This is an open access article distributed under the Creative Commons Attribution License, which permits unrestricted use, distribution, and reproduction in any medium, provided the original work is properly cited.

We present the design, simulation, and measurement of a polarization-independent and angle-insensitive metamaterial absorber (MA) in X-band. Since the unit cell of the MA consists of four subwavelength split-ring resonators with 4-fold symmetric rotation, the MA is insensitive to the variation of both polarization and incident angle of the planar electromagnetic wave. The electromagnetic performances of the MA are studied by full-wave simulations based on finite-element method and the Naval Research Laboratory arch experimental measurements. The electric field distributions are numerically investigated, which confirm the polarization-insensitive property of the MA, as expected from the symmetric nature of the structure. When the incident angles vary from 0 to 45 degrees, the MA remains at full width at half maximum of 0.4 GHz (0.5 GHz) with peak absorptions of 99.9% (95.2%) at 10.27 GHz (10.3 GHz) by simulations (measurements).

## 1. Introduction

Metamaterials can provide exotic and very useful electric and magnetic properties which are not readily found in nature [1, 2]. Over the past decade, a large number of metamaterials have been demonstrated at the desired regimes of electromagnetic spectrum from microwave, terahertz (THz), infrared to visible frequencies [3–6]. As metamaterials research continues to mature, they have inspired a vast amount of electromagnetic devices such as invisibility cloaks [7, 8], perfect lens [9], and novel types of circuits and antennas [10–14]. One of the most promising applications of metamaterials is the absorption of electromagnetic waves, known as metamaterial absorbers (MAs) [15–29]. MAs offer three distinct advantages—nearly perfect absorption, deeply subwavelength thickness, and tunability—compared to conventional radar absorbing materials. Potential applications of MAs include the bolometer, perfectly matched layer, and radar cross section (RCS) reduction. MA with ultrathin

structure and near-unity absorption was first introduced by Landy et al. in 2008 [15]. Since then, great efforts have been concentrated on MAs to achieve broadband, multiband, polarization-independent, or angle-insensitive absorptions from microwave, THz, to optical frequencies [16–29]. During the last few years, although some of the studies show good absorptions, experimental realization of MAs with both polarization-independent and angle-insensitive properties are still in the initial stage. In future research more unit cell structures will provide greater flexibility in MA design and practical applications.

In this study, an X-band polarization-independent and angle-insensitive MA based on 90-degree-rotated split-ring resonators (SRRs) is designed and proposed. The MA is designed and optimized by full-wave simulations using finite-element method (FEM) based commercial software ANSYS HFSS and verified by the Naval Research Laboratory (NRL) arch experimental measurements. We will show that the proposed MA yields not only a compact structure that can

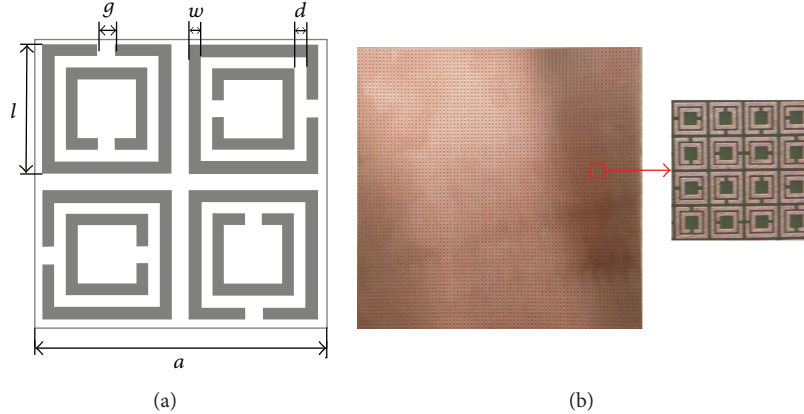


FIGURE 1: Schematic of MA: (a) unit cell with dimensions of  $a = 5$ ,  $l = 2.22$ ,  $g = 0.3$ ,  $w = 0.2$ , and  $d = 0.2$ . (b) Photograph of the fabricated MA with  $40 \times 40$  unit cells (dimension of  $200 \times 200$ ). All units are in millimeters.

be readily fabricated through standard printed circuit board (PCB) technology, but also good polarization-independent and angle-insensitive absorption characteristics from both simulation and experiment results.

## 2. MA Design

For our MA design, we chose unit cell with 4-fold rotational symmetric configuration, which leads to polarization-independent property. Meanwhile, the MA constructed with subwavelength unit cells can offer angle-insensitivity property. Figure 1(a) shows the geometry of the unit cell of the MA, and the fabricated prototype of the proposed MA is illustrated in Figure 1(b). The unit cell of the MA consists of four symmetric subwavelength 90-degree-rotated SRRs, and it is fabricated by etching an  $18 \mu\text{m}$  thick copper (conductivity  $5.8 \times 10^7 \text{ S/m}$ ) pattern on an FR4 (relative permittivity 4.4 and dielectric loss tangent 0.02) epoxy dielectric substrate with 0.8 mm thickness. The optimized geometrical parameters of the unit cell are listed in the caption of Figure 1(a).

The absorption  $A$  of the MA can be determined by the expression [30]

$$A = 1 - R - T = 1 - |S_{11}|^2 - |S_{21}|^2, \quad (1)$$

where reflection  $R = |S_{11}|^2$  and transmission  $T = |S_{21}|^2$  are obtained from simulated and measured  $S$ -parameters. From this equation, reflection  $R$  and transmission  $T$  should be minimized to achieve maximum absorption  $A$ . The transmission  $T$  of the proposed MA is equal to zero,  $S_{21} = 0$ , due to the presence of the metallic ground plane in our design. Therefore, the absorption  $A$  of the MA can be maximized by minimization of the reflection  $R$ .

To better understand the mechanism of the perfect absorption of the MA, the effective impedance of the MA can be obtained from effective medium theory [31–33]:

$$z = \sqrt{\frac{(1 + S_{11}^2)^2 - S_{21}^2}{(1 - S_{11}^2)^2 - S_{21}^2}} = \frac{1 + R}{1 - R}. \quad (2)$$

Combination of (1) and (2) results in the general expression of the absorption:

$$\begin{aligned} A &= \frac{2}{\operatorname{Re}(z) + i \operatorname{Im}(z) + 1} \\ &= \frac{2 [\operatorname{Re}(z) + 1]}{[\operatorname{Re}(z) + 1]^2 + \operatorname{Im}(z)^2} \\ &\quad - i \frac{2 \operatorname{Im}(z)}{[\operatorname{Re}(z) + 1]^2 + \operatorname{Im}(z)^2}. \end{aligned} \quad (3)$$

In case of perfect absorption,  $A = 1$ , the real part of the effective impedance should match the free-space value,  $\operatorname{Re}(z) = 1$ , and the imaginary part is supposed to be vanished,  $\operatorname{Im}(z) = 0$ , according to (3).

## 3. Simulations and Measurements

The MA with three layers is modelled with full-wave FEM solver ANSYS HFSS. The top layer is made of 90-degree-rotated SRRs in a periodic pattern. The middle layer is dielectric substrate FR4. The bottom layer is a solid metallic ground plane. The simulation is based on a MA unit cell along with Floquet ports and Master/Slave periodic boundary condition (PBC). The usage of PBC can mimic an infinite extended periodic structure.

The simulated  $S_{11}$  of the MA is shown in Figure 2. A minimal reflection of near zero is observed at 10.27 GHz. By using (1) and (2), the absorption and effective impedance can be easily calculated. The effective impedance is calculated and shown in Figure 3. The inset in Figure 3 shows the zoomed view of the effective impedance. It can be observed that the real part of the effective impedance of the MA is near unity (matched to the air),  $\operatorname{Re}(z) \approx 1$ , and imaginary part of the MA is near zero,  $\operatorname{Im}(z) \approx 0$  at 10.27 GHz, corresponding to the perfect absorption. Figure 4 shows the absorption as a function of polarization angle with step of  $10^\circ$  at 10.27 GHz. The absorption amplitude for different polarization angles

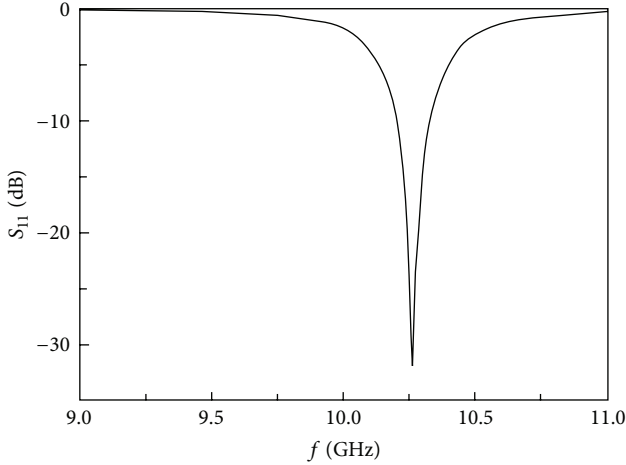


FIGURE 2: The simulated  $S_{11}$  of the proposed MA from a normal incident planar wave.

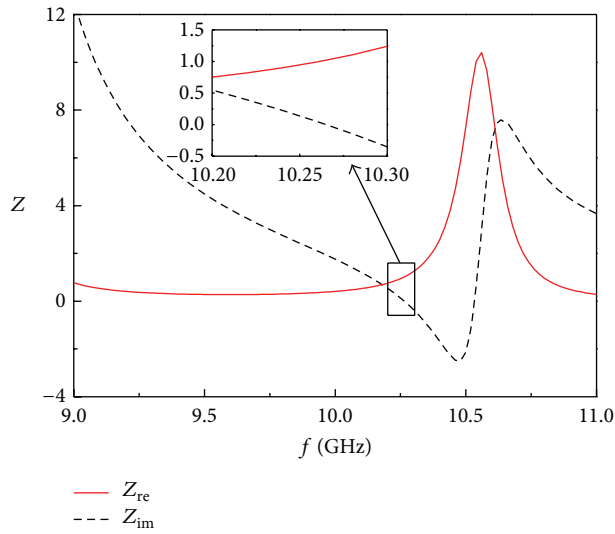


FIGURE 3: Calculated real and imaginary part of the effective impedance of the proposed MA.

varies by less than 1%. The detailed discussion on angle-insensitive property of the proposed MA is presented in the fifth paragraph of this section.

Figure 5 shows the simulated electric field distribution at 10.27 GHz for normal incident TE and TM waves, as well as the 45° condition. It is seen that the MA performs almost the same electric field distributions, except a 90-degree rotation, for normal incident TE and TM waves, as shown in Figures 5(a) and 5(b). This indicates that the symmetrical structure of the MA with the unit cell of 4-fold rotational SRRs possesses a polarization-independent performance, in accordance with our predication. In Figure 5(c), the electric field distribution for 45° incident electromagnetic waves is shown at 10.27 GHz. In this condition, we discovered that all of the incident electromagnetic waves are absorbed by the four 90-degree-rotated SRRs.

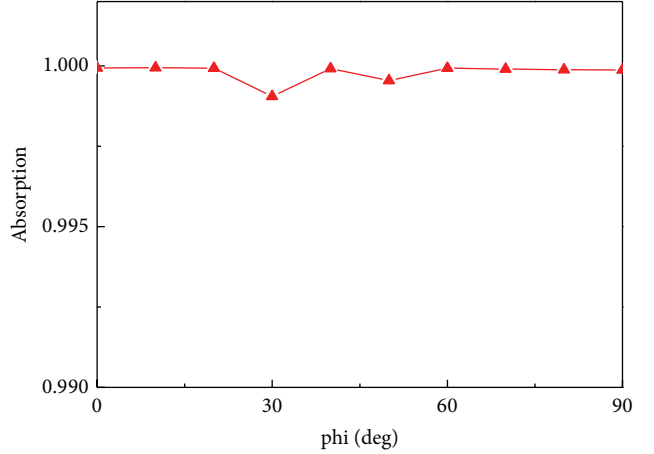


FIGURE 4: Simulated absorption as a function of polarization angle with step of 10° at 10.27 GHz.

To verify the numerical results, we fabricate the MA by using PCB technique, as shown in Figure 1(b). The absorption characteristics of the fabricated MA at different incident angles are measured with the NRL arch, as shown in Figure 6. NRL arch is a reliable standard for characterizing the reflection and absorption of materials [34]. In our measurements, a vector network analyzer (Agilent N5244A) is used to measure the reflection of the proposed MA.

Figure 7 shows the simulated and measured absorption at incident angles from 0 to 45 degrees in X-band. It can be seen that when the incident angle of the electromagnetic wave is altered from 0 to 45 degrees, the absorption does not change significantly, which proves that our proposed MA possesses angle-insensitive property. It is known that a periodic structure with subwavelength dimensions of unit cell is equivalent to a homogenous and isotropic medium. The effective impedance of a homogenous and isotropic medium is stable for wide angles of incident electromagnetic waves. Therefore, the strong subwavelength dimensions of the lattice constant of unit cell ( $a = 5$  mm) and dielectric thickness (0.8 mm) of the MA make it absorb wide angles of incident electromagnetic waves. The measured results are in good agreement with numerical simulations. The small discrepancy of the peak absorption with the change of incident angle might be due to nonidealities of fabrication, such as the surface roughness of the metal pattern and nonuniformity of the dielectric substrate.

Furthermore, the full width at half maximum (FWHM) and fractional bandwidth (FBW) are very important parameters to describe the performance of the MA. Fractional bandwidth (FBW) was calculated as

$$\text{FBW} = \frac{\text{FWHM}}{f_c}, \quad (4)$$

where  $f_c$  is the center frequency of FWHM. For incident angles varying from 0 to 45 degrees, the MA remains at the FWHM of 0.4 GHz with peak absorptions of 99.9% at 10.27 GHz in simulations, while in experiments the MA remains at an FWHM of 0.5 GHz with peak absorptions

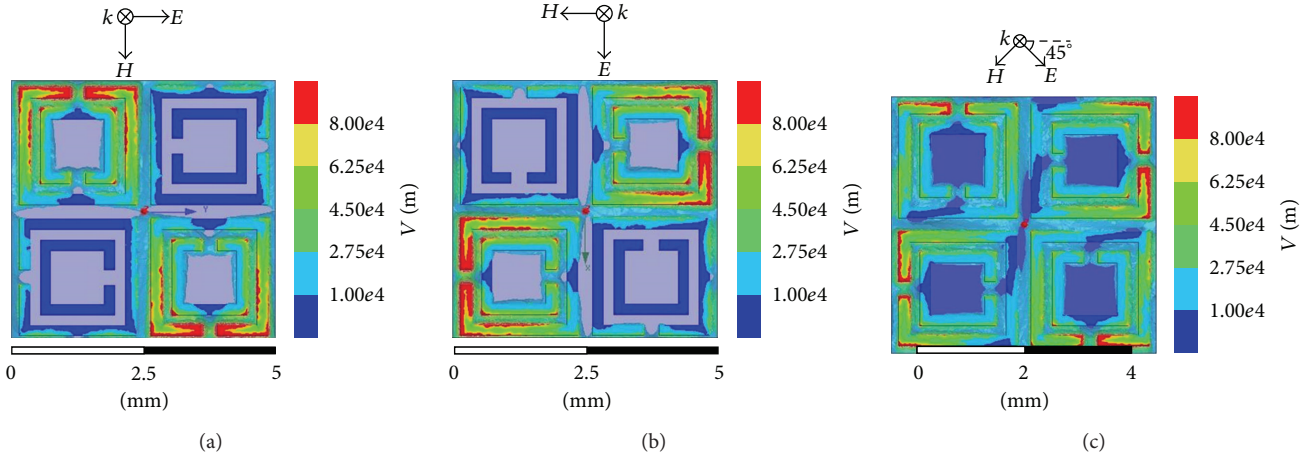


FIGURE 5: Electric field distribution at 10.27 GHz for (a) normal incident TE, (b) normal incident TM, and (c) 45° incident waves.

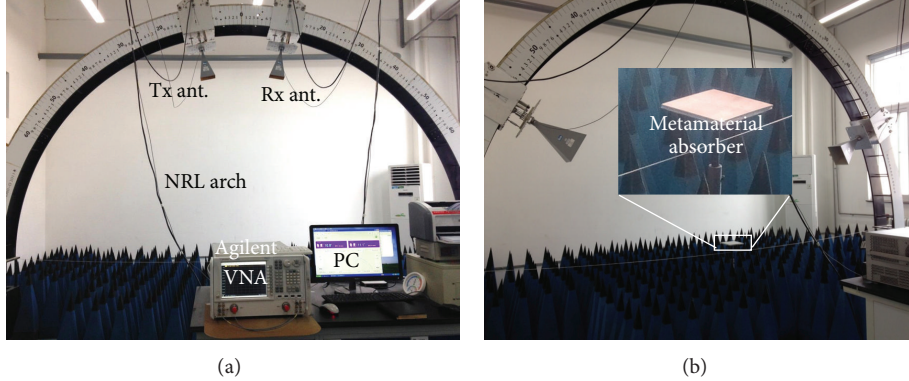


FIGURE 6: NRL arch used to measure the absorption of the MA at different incident angles. (a) Front and (b) side view of the experimental setup. The insert in (b) shows the zoomed view of the MA under measurement.

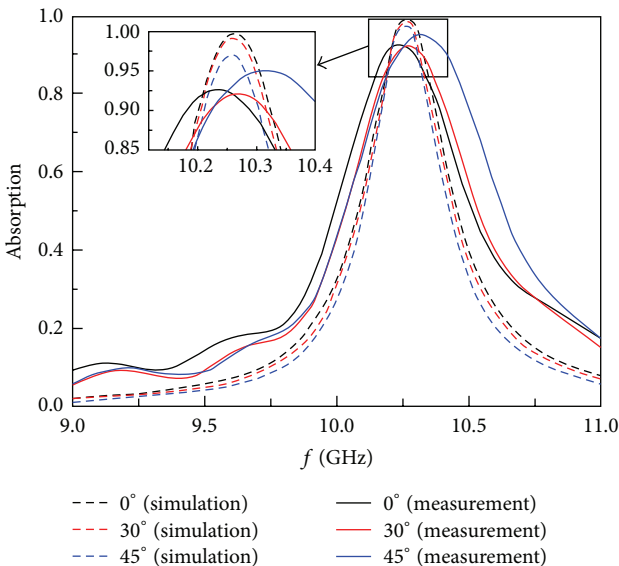


FIGURE 7: Simulated and measured absorptions at different angles (0, 30, and 45 degrees).

of 95.2% at 10.3 GHz, as shown in Figure 7. It is worth noting that the difference between the simulations and measurements can be attributed to the fabrication tolerance and measurement calibration.

The measured FBW of the MA is about 5% (FWHM  $\approx$  0.5 GHz,  $f_c \approx 10.3$  GHz), which is good enough for many practical applications. For example, both the microstrip patch antenna and the waveguide slot antenna generally need less than 3% FBW for efficient operations [35, 36]. Hence, this MA is a promising candidate for radar cross section reduction of antennas and antenna arrays.

#### 4. Conclusions

The theoretical analysis, full-wave FEM simulation, fabrication, and measurement of an X-band polarization-independent and angle-insensitive MA are demonstrated. The MA employs 90-degree-rotated SRRs as a unit cell, which shows the absorption FBW of 5% with incident angles ranging from 0 to 45 degrees by experiment. The measured results are in good agreement with the theoretical analysis.

and the full-wave FEM simulated ones, which provide effectively design guidelines for MAs. The proposed MA exhibits simple planar structure, easy fabrication using PCB technology, polarization-independence, angle-insensitiveness, and sufficient effective band. These remarkable features allow the MA to be a promising candidate for future applications, such as bolometer, perfectly matched layer, and scattering reductions.

## Conflict of Interests

The authors declare that there is no conflict of interests regarding the publication of this paper.

## Acknowledgments

This work was supported by the National Natural Science Foundation of China (Grants nos. 61307128, 61401025, 61371044, and 61275107), the Specialized Research Fund for the Doctoral Program of Higher Education of China (Grant no. 20131101120027), the Open Research Fund of The Academy of Satellite Application (Grant no. 2014\_CXJJ-TX\_03), the Beijing Natural Science Foundation (Grant no. 4154085), the Shanghai Academy of Spaceflight Technology (Grant no. SAST\_201439), and the Basic Research Foundation of Beijing Institute of Technology, China (Grants nos. 20120542015, 20130542010, 20130542016, and 20140542002).

## References

- [1] V. G. Veselago, "The electrodynamics of substances with simultaneously negative values of  $\epsilon$  and  $\mu$ ," *Soviet Physics Uspekhi*, vol. 10, no. 4, pp. 509–514, 1968.
- [2] J. B. Pendry, A. J. Holden, D. J. Robbins, and W. J. Stewart, "Magnetism from conductors and enhanced nonlinear phenomena," *IEEE Transactions on Microwave Theory and Techniques*, vol. 47, no. 11, pp. 2075–2084, 1999.
- [3] D. H. Werner and D. H. Kwon, *Transformation Electromagnetics and Metamaterials: Fundamental Principles and Applications*, Springer, London, UK, 2014.
- [4] G. V. Eleftheriades and N. Engheta, "Metamaterials: fundamentals and applications in the microwave and optical regimes," *Proceedings of the IEEE*, vol. 99, no. 10, pp. 1618–1621, 2011.
- [5] N. Engheta and R. W. Ziolkowski, *Metamaterials: Physics and Engineering Explorations*, John Wiley & Sons, New York, NY, USA, 2006.
- [6] B. Liu and C. L. Ji, "Bayesian nonparametric modeling for rapid design of metamaterial microstructures," *International Journal of Antennas and Propagation*, vol. 2014, Article ID 165102, 9 pages, 2014.
- [7] J. Li and J. B. Pendry, "Hiding under the carpet: a new strategy for cloaking," *Physical Review Letters*, vol. 101, no. 20, Article ID 203901, 2008.
- [8] Q. Wu, K. Zhang, F.-Y. Meng, and L.-W. Li, "Material parameters characterization for arbitrary N-sided regular polygonal invisible cloak," *Journal of Physics D: Applied Physics*, vol. 42, no. 3, Article ID 035408, 2009.
- [9] J. B. Pendry, "Negative refraction makes a perfect lens," *Physical Review Letters*, vol. 85, no. 18, pp. 3966–3969, 2000.
- [10] T. J. Cui, D. R. Smith, and R. P. Liu, *Metamaterials: Theory, Design and Applications*, Springer, Berlin, Germany, 2009.
- [11] W. R. Zhu, I. D. Rukhlenko, and M. Premaratne, "Graphene metamaterial for optical reflection modulation," *Applied Physics Letters*, vol. 102, no. 24, Article ID 241914, 2013.
- [12] Q.-L. Zhang, L.-M. Si, Y. Huang, X. Lv, and W. Zhu, "Low-index-metamaterial for gain enhancement of planar terahertz antenna," *AIP Advances*, vol. 4, no. 3, Article ID 037103, 2014.
- [13] W. R. Zhu, I. D. Rukhlenko, F. Xiao, and M. Premaratne, "Polarization conversion in U-shaped chiral metamaterial with four-fold symmetry breaking," *Journal of Applied Physics*, vol. 115, no. 14, Article ID 143101, 2014.
- [14] L. M. Si, Q. L. Zhang, W. D. Hu et al., "A uniplanar triple-band dipole antenna using complementary capacitively loaded loop," *IEEE Antennas and Wireless Propagation Letters*, vol. 14, pp. 743–746, 2015.
- [15] N. I. Landy, S. Sajuyigbe, J. J. Mock, D. R. Smith, and W. J. Padilla, "Perfect metamaterial absorber," *Physical Review Letters*, vol. 100, no. 20, Article ID 207402, 2008.
- [16] J. B. Sun, L. Y. Liu, G. Y. Dong, and J. Zhou, "An extremely broad band metamaterial absorber based on destructive interference," *Optics Express*, vol. 19, no. 22, pp. 21155–21162, 2011.
- [17] Y.-J. Huang, G.-J. Wen, J. Li, W.-R. Zhu, P. Wang, and Y.-H. Sun, "Wide-angle and polarization-independent metamaterial absorber based on snowflake-shaped configuration," *Journal of Electromagnetic Waves and Applications*, vol. 27, no. 5, pp. 552–559, 2013.
- [18] G. H. Yang, X. X. Liu, Y. L. Lv, J. H. Fu, Q. Wu, and X. M. Gu, "An extremely broad band metamaterial absorber based on destructive interference," *Journal of Applied Physics*, vol. 115, Article ID 17E523, 2014.
- [19] Y. J. Huang, G. J. Wen, W. R. Zhu, J. Li, L. M. Si, and M. Premaratne, "Experimental demonstration of a magnetically tunable ferrite based metamaterial absorber," *Optics Express*, vol. 22, no. 13, pp. 16408–16417, 2014.
- [20] X. L. Liu, T. Starr, A. F. Starr, and W. J. Padilla, "Infrared spatial and frequency selective metamaterial with near-unity absorbance," *Physical Review Letters*, vol. 104, Article ID 207403, 2010.
- [21] W. R. Zhu, X. P. Zhao, B. Gong, L. Liu, and B. Su, "Optical metamaterial absorber based on leaf-shaped cells," *Applied Physics A*, vol. 102, no. 1, pp. 147–151, 2011.
- [22] B. Wang, T. Koschny, and C. M. Soukoulis, "Wide-angle and polarization-independent chiral metamaterial absorber," *Physical Review B*, vol. 80, no. 3, Article ID 033108, 2009.
- [23] B. Zhu, Z. Wang, C. Huang, Y. Feng, J. Zhao, and T. Jiang, "Polarization insensitive metamaterial absorber with wide incident angle," *Progress in Electromagnetics Research*, vol. 101, pp. 231–239, 2010.
- [24] A. Dimitriadis, N. Kantartzis, and T. Tsiboukis, "A polarization-/angle-insensitive, bandwidth-optimized, metamaterial absorber in the microwave regime," *Applied Physics A*, vol. 109, no. 4, pp. 1065–1070, 2012.
- [25] K. B. Alici, A. B. Turhan, C. M. Soukoulis, and E. Ozbay, "Optically thin composite resonant absorber at the near-infrared band: a polarization independent and spectrally broadband configuration," *Optics Express*, vol. 19, no. 15, pp. 14260–14267, 2011.
- [26] X. Shen, T. J. Cui, J. Zhao, H. F. Ma, W. X. Jiang, and H. Li, "Polarization-independent wide-angle triple-band metamaterial absorber," *Optics Express*, vol. 19, no. 10, pp. 9401–9407, 2011.

- [27] F. Dincer, M. Karaaslan, E. Unal, K. Delihacioglu, and C. Sabah, "Design of polarization and incident angle insensitive dual-band metamaterial absorber based on isotropic resonator," *Progress in Electromagnetics Research*, vol. 144, pp. 123–132, 2014.
- [28] M. R. Soheilifar, R. A. Sadeghzadeh, and H. Gobadi, "Design and fabrication of a metamaterial absorber in the microwave range," *Microwave and Optical Technology Letters*, vol. 56, no. 8, pp. 1748–1752, 2014.
- [29] M. Soheilifar and R. Sadeghzadeh, "Design, simulation, and fabrication of an ultrathin planar microwave metamaterial absorber," *Microwave and Optical Technology Letters*, vol. 56, no. 12, pp. 2916–2922, 2014.
- [30] H. Tao, C. M. Bingham, A. C. Strikwerda et al., "Highly flexible wide angle of incidence terahertz metamaterial absorber: design, fabrication, and characterization," *Physical Review B*, vol. 78, no. 24, Article ID 241103, 2008.
- [31] D. R. Smith, S. Schultz, P. Markoš, and C. M. Soukoulis, "Determination of effective permittivity and permeability of metamaterials from reflection and transmission coefficients," *Physical Review B*, vol. 65, no. 19, Article ID 195104, 2002.
- [32] D. R. Smith, D. C. Vier, T. Koschny, and C. M. Soukoulis, "Electromagnetic parameter retrieval from inhomogeneous metamaterials," *Physical Review E—Statistical, Nonlinear, and Soft Matter Physics*, vol. 71, no. 3, Article ID 036617, 2005.
- [33] X. Chen, T. M. Grzegorczyk, B.-I. Wu, J. Pacheco Jr., and J. A. Kong, "Robust method to retrieve the constitutive effective parameters of metamaterials," *Physical Review E*, vol. 70, no. 1, Article ID 016608, 2004.
- [34] R. Faez, I. M. Martin, M.-A. de Paoli, and M. C. Rezende, "Influence of processing time and composition in the microwave absorption of EPDM/PAni blends," *Journal of Applied Polymer Science*, vol. 83, no. 7, pp. 1568–1575, 2002.
- [35] L.-M. Si, Y. Liu, Y. Huang, and W. Zhu, "Ka-band slot-microstrip-covered and waveguide-cavity-backed monopulse antenna array," *International Journal of Antennas and Propagation*, vol. 2014, Article ID 707491, 5 pages, 2014.
- [36] T. Liu, X. Y. Cao, J. Gao, Q. R. Zheng, W. Q. Li, and H. H. Yang, "RCS reduction of waveguide slot antenna with metamaterial absorber," *IEEE Transactions on Antennas and Propagation*, vol. 61, no. 3, pp. 1479–1484, 2013.

## Research Article

# Compact Microstrip Bandpass Diplexer Based on Twist Revised Split Ring Resonators

Jian Li,<sup>1</sup> Yongjun Huang,<sup>1</sup> Xuefeng Zhao,<sup>1,2</sup> and Guangjun Wen<sup>1</sup>

<sup>1</sup>Centre for RFIC and System Technology, School of Communication and Information Engineering, University of Electronic Science and Technology of China, Chengdu 611731, China

<sup>2</sup>School of Computer Engineering, Huaihai Institute of Technology, Lianyungang 222005, China

Correspondence should be addressed to Yongjun Huang; [yongjunh@uestc.edu.cn](mailto:yongjunh@uestc.edu.cn)

Received 19 February 2015; Accepted 30 March 2015

Academic Editor: Roman E. Noskov

Copyright © 2015 Jian Li et al. This is an open access article distributed under the Creative Commons Attribution License, which permits unrestricted use, distribution, and reproduction in any medium, provided the original work is properly cited.

Based on the twist revised split ring resonators (TR-SRRs) inspired filter unit a microstrip bandpass diplexer with highly compact size and high frequency selection and isolation properties is synthesized and systematically characterized. The proposed filter unit exhibits both electric and magnetic coupling effects and possesses two resonance modes (magnetic and electronic resonances). The two resonance modes can be flexibly controlled by adjusting the gap between the two TR-SRRs. The synthesized diplexer has very simple configuration with size of  $0.217\lambda_d \times 0.217\lambda_d$  and degree of freedom for impedance matching. Measurement and simulation demonstrations are performed in this paper and a good agreement is achieved. The measured results indicate two quite close frequency channels (centered at 2.16 GHz and 2.91 GHz) with isolation larger than 30 dB. The proposed diplexer can be easily integrated into miniaturized RF/microwave integrated circuits.

## 1. Introduction

In modern wireless communications, the obvious development tendency is to integrate more than one communication mode in a single termination. Based on this requirement, some multiband/wideband antennas have been designed and therefore we need filters following the antennas to separate the different signals toward different frequency channels and modules [1, 2]. Various dippers/triplexes have been reported in recent years based on different filter and/or resonator units, for example, parallel-coupled filter [3], T-shaped resonator [4], stub-loaded resonator [5, 6], quarter-wavelength resonator [7], dual-mode resonator [8], and common shorted stubs [9] to realize the assignments. In particular, the filter designs focusing on compact size, high isolation, and out-of-band rejection properties are developed based on stepped impedance coupled-line resonator [10, 11], double-sided parallel-strip line [12], half-wavelength open-loop resonators [13], hybrid resonators [14], series LC tanks [15], and substrate integrated waveguide resonator [16].

On the other hand, the artificial structured resonators with dimensional size much smaller than the operating wavelength have been attracting exciting interests in the designs of compact dippers/triplexes. For example, the split ring resonator (SRR) as the basic artificial unit cell has been widely used to design microwave/millimeter wave components [17] and its complementary inclusion applied to the coplanar waveguide and substrate integrated waveguide can realize high performance dippers [18, 19]. By using composite quarter-wave right/left-handed (CRLH) resonators or balanced CRLH resonators [20–23], one can obtain more compact size compared with the conventional dippers/triplexes. However, most of these archives including conventional resonators and artificial structured resonators have complex inclusions, precise-designed T-junction, and impedance circuits which will result in large size and high costs.

In this paper, a new type of diplexer is synthesized by directly using two groups of revised SRR (by electric shorting one end of the SRR to ground plane) pairs with twist arrangements. The proposed twist revised SRR (TR-SRR) inspired

filter unit exhibits both electric and magnetic coupling effects and has two resonance modes (electric and magnetic resonances) with very small electric size. Therefore the designed diplexer possesses highly compact size compared with other recently reported inclusions. The TR-SRR and filter unit are firstly analyzed, and then the synthesized diplexer is demonstrated by both experimental and numerical methods. Finally the comparisons with previously reported dplexers are presented and discussed.

## 2. Filter Design and Analysis

Figure 1(a) shows the top and side views of the proposed revised SRR configuration. Two extended microstrip lines are collected to the split of a conventional SRR and one of the extended ends is electric shorted to ground plane. Such kind of design can be considered as a new quarter-wavelength resonator from the equivalent circuit view. The new revised SRR can exhibit impedance matching to the  $50\Omega$  feed line, which connects to the shorted branch as shown in Figure 1(a), without additional complex circuits. The electric and magnetic fields at the resonance frequency for one revised SRR are shown in Figure 1(b), which indicate asymmetric field distributions and will give us abundant choices for the coupling filter design. After numerical investigations by HFSS full-wave simulations, the twist arrangement as shown in the inset of Figure 1(c) has better passband characteristics [24] and also can be easily used to synthesize the diplexer which will be discussed later. As an example, the simulated transmission and reflection properties of the designed filter unit are shown in Figure 1(c) with parameters shown as follows, in millimeter:  $a = 4$ ,  $b = 2.7$ ,  $c = 0.4$ ,  $w = 0.4$ ,  $r = 0.15$ ,  $g = 0.5$ , and  $t = 0.8$ . Rogers RO4003 substrate, which has the relative dielectric constant  $\epsilon_r = 3.55$  and loss tangent  $\tan \delta = 0.0027$ , is used in this paper and the thickness of the SRRs and ground plane is 0.03 mm. The dimension of filter unit is  $8\text{ mm} \times 12.4\text{ mm}$ . As can be seen, such filter exhibits a passband centered at 2.97 GHz with a 3 dB bandwidth of 0.46 GHz. From the reflection curve in Figure 1(c) there are two poles at 2.88 and 3.05 GHz and the surface currents on the twist SRR pairs at such two frequencies show typical electric and magnetic resonance modes. Moreover, there is a transmission zero below the passband. From the mixed coupling filter theory, the magnetic coupling for our twist SRR based filter is larger than the electric coupling, and as a result the transmission in lower band is related to strong magnetic coupling [25, 26]. It can contribute to the high isolation when synthesizing the diplexer in the next section by using the proposed filter unit.

By altering the gap values between the TR-SRR pairs, one can obtain the changing properties of the filter passband as shown in Figure 2(a). It indicates an expanded bandwidth when decreasing the gap. This is due to the enhancements of both electric and magnetic coupling in the adjacent area. Figure 2(b) shows the captured frequency shift properties of the two resonance modes as functions of gap value  $g$ . The coupling coefficient  $k$  and the external quality factors  $Q_e$  can

then be calculated from the two resonance frequencies by using coupling theory [26]:

$$\begin{aligned} k &= \frac{(f_2^2 - f_1^2)}{(f_2^2 + f_1^2)}, \\ Q_{e1} &= \frac{f_1}{\Delta f_{3\text{dB}}}, \\ Q_{e2} &= \frac{f_2}{\Delta f_{3\text{dB}}}, \end{aligned} \quad (1)$$

where  $f_1$  and  $f_2$  correspond to the lower and higher resonance frequencies and  $\Delta f_{3\text{dB}}$  is the 3 dB frequency bandwidth. In our previous work [24], it has shown that our design exhibits high external quality factors, which can contribute to low insertion loss, flat passband, and good return loss. The calculated coupling coefficient shown in Figure 2(b) indicates that when decreasing the gap values the coupling between the two SRRs will be enhanced. However, at smaller gap values, the coupling is too strong so that the two resonance modes separate far from each other and result in the dropdown within the passband as shown in Figure 2(a). Therefore, both the bandwidth and insertion loss will be considered when choosing the gap values, and the isolation will be also taken into consideration when designing the diplexer.

## 3. Diplexer Synthesis and Demonstration

Based on the above analysis for the filter unit, here the diplexer is synthesized by placing properly two filter units side by side with different sizes and connecting to the input port with a simple T-junction as shown in Figure 3(a). Such design can effectively use the limited space to achieve the highly compact inclusion. By using the same Rogers RO4003 substrate as above, the dimensional parameters are finally optimized as follows, in millimeter:  $a_1 = 5$ ,  $a_2 = 4$ ,  $b_1 = 3.7$ ,  $b_2 = 2.7$ ,  $c = 0.4$ ,  $e = 9.2$ ,  $f = 1.76$ ,  $g_1 = 0.5$ ,  $g_2 = 0.5$ ,  $w = 0.4$ , and  $r = 0.15$ . The overall dimensional size is  $d \times d = 16\text{ mm} \times 16\text{ mm}$ . The photograph of fabricated diplexer is also shown in Figure 3(b) with the definitions of the three ports. Each port is soldered with a  $50\Omega$  microminiature coaxial connectors, operated from DC to 6 GHz.

Then the scattering parameters for the diplexer are experimentally measured by a two-port vector network analyzer (Agilent N5230A). In measurements, the third port is terminated by a wide-band  $50\Omega$  load when measuring two of these three ports for the diplexer. The measured results are shown in Figure 4 and the corresponding numerical results are also presented for comparisons. As can be seen, good agreements are achieved between measurements and simulations which demonstrate the corrections of the design and synthesis. The measured two channels are located at 2.16 GHz and 2.91 GHz with 3 dB bandwidths of 0.3 GHz and 0.32 GHz, respectively. The measured insertion losses are 1.25 dB and 1.48 dB, respectively, for the two channels, which show quite low values due to the simple configuration (including the extra losses from the microminiature coaxial

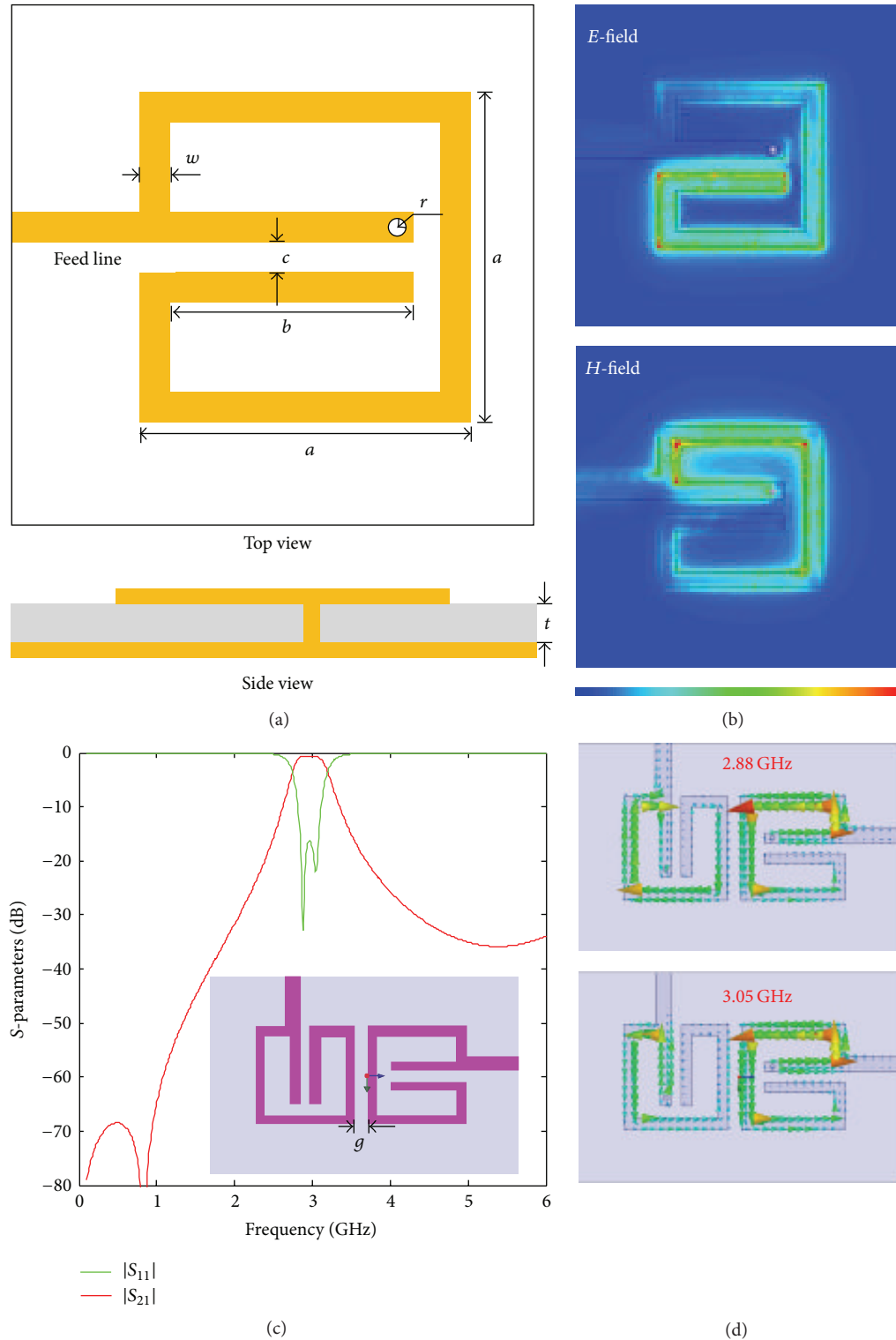


FIGURE 1: (a) The new revised SRR, (b) the electric and magnetic field distributions near the SRR at resonance frequency, (c) the twist SRRs inspired filter unit and its simulated scattering parameters, and (d) the surface current distributions at the two resonance modes.

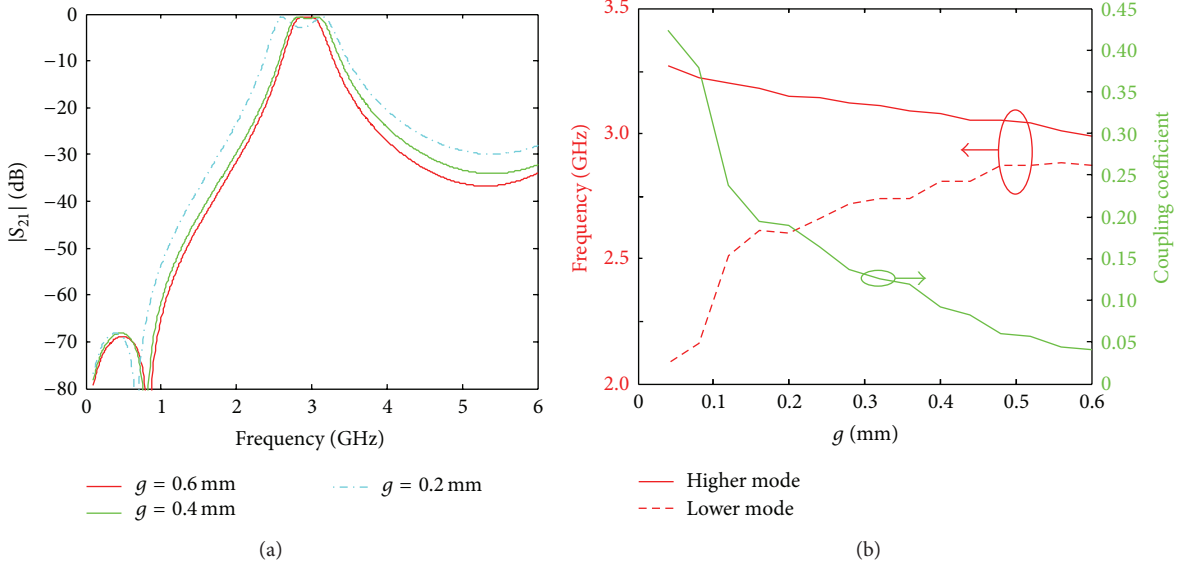


FIGURE 2: (a) Simulated transmissions for the twist SRR inspired filter unit at different gaps and (b) the changing properties for the two resonance frequencies and the calculated mix coupling coefficient as functions of gap  $g$ .

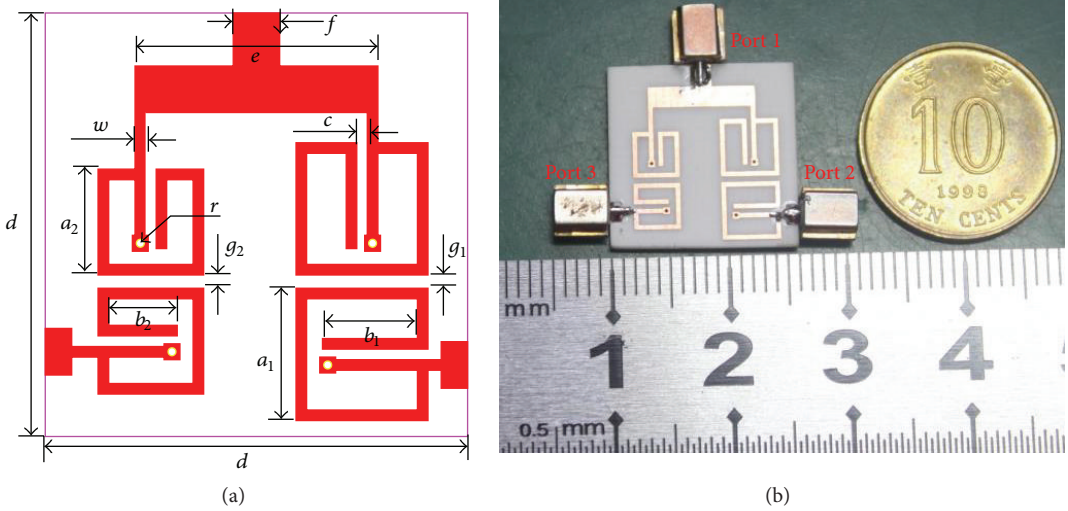


FIGURE 3: (a) The synthesized compact diplexer layout with dimensional parameters and (b) the photograph of fabricated diplexer.

connectors). The return losses for the input port (Port 1) at the two channels are 25 dB and 14 dB and for the two output ports (Ports 2 and 3) are 26 dB and 21 dB. These are quite good impedance matching properties even though they are without a carefully designed matching circuit (just conventional  $50 \Omega$  microstrip line). The out-of-band rejection is more than 30 dB and reaches up to 5 GHz for the lower channel and in the entire measured frequency region for the higher channel. Moreover, the measured isolation between the two output ports shows a value of larger than 30 dB, which is also a good isolation property for the proposed highly compact inclusion. Such isolation can be further increased by adding more SRRs in the filter units to get more transmission

zeros below and above the operating bands but will destroy the compact configuration size.

Finally, the performance comparisons for the proposed diplexer and other recently reported designs are concluded in Table 1. Here  $\lambda_d$  is the operating wavelength within the dielectric substrate defined as  $\lambda_d = c/(\sqrt{\epsilon_r}f)$ , where  $\epsilon_r$  is the relative permittivity of substrate,  $f$  is the center frequency of first channel, and  $c$  is the speed of light in free space. It can be found that the diplexer proposed in this paper has comparable frequency selection and isolation properties and almost the smallest inclusion size (except the design reported in [13] using complex series LC tanks and meander line inductors to achieve the compact resonators).

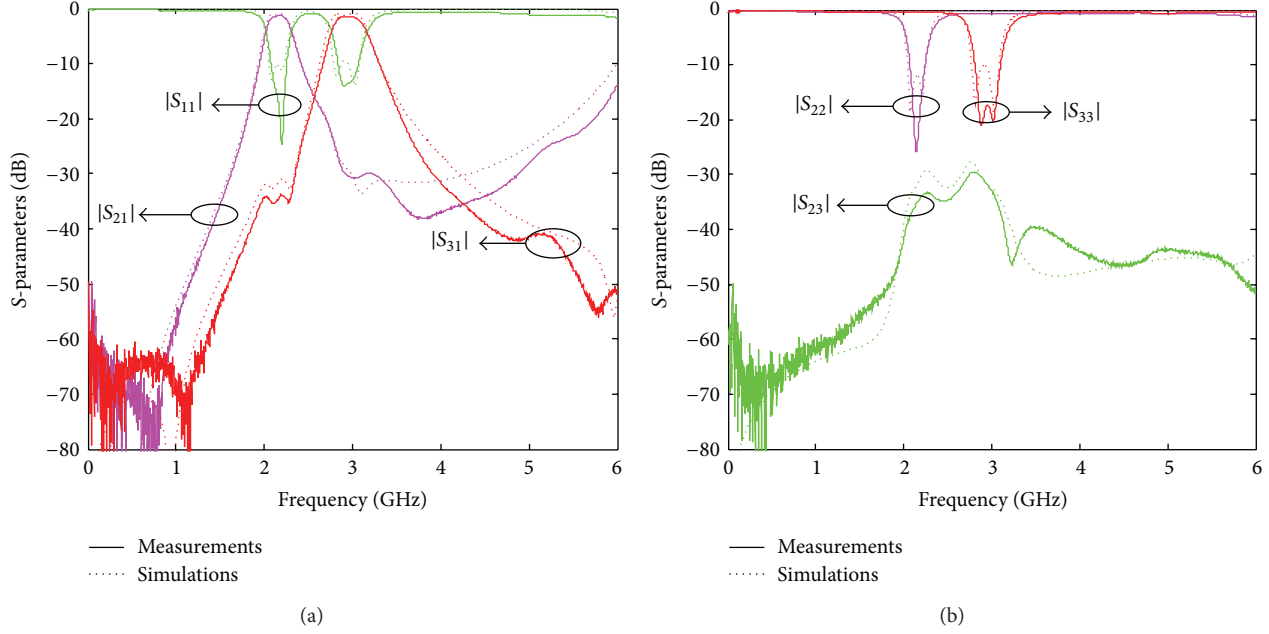


FIGURE 4: (a) The measured and simulated reflections of Port 1 and transmissions of Ports 2 and 3 from Port 1 and (b) reflection for Ports 2 and 3 and the transmission between Ports 2 and 3.

TABLE 1: Comparisons between the proposed diplexer and other compact designs.

| Designs   | $\epsilon_r$ of substrate | Frequency (GHz) | Size ( $\lambda_d^2$ ) | Insertion loss (dB) | Isolation (dB) |
|-----------|---------------------------|-----------------|------------------------|---------------------|----------------|
| [11]      | 4.5                       | 1.85, 2.5       | $0.424 \times 0.382$   | 2.05, 2.15          | >25            |
| [14]      | 2.2                       | 1.82, 2.5       | $0.193 \times 0.297$   | 2.51, 2.17          | >55            |
| [15]      | 3.38                      | 1.8, 3.6        | $0.153 \times 0.09$    | 0.4, 0.5            | >30            |
| [16]      | 2.55                      | 8, 9            | $1.325 \times 1.325$   | 2.86, 3.04          | >40            |
| [22]      | 2.2                       | 1.8, 2.35       | $0.178 \times 0.341$   | 1.34, 1.44          | >25            |
| [23]      | 2.65                      | 3.5, 4          | $0.944 \times 0.765$   | 1.95, 1.97          | >25            |
| This work | 3.55                      | 2.16, 2.91      | $0.217 \times 0.217$   | 1.25, 1.48          | >30            |

## 4. Conclusions

In this paper, a new type of TR-SRRs inspired bandpass filter unit is designed and then a highly compact diplexer based on the designed filters is synthesized and demonstrated. Such diplexer with size of  $0.217\lambda_d \times 0.217\lambda_d$  exhibits good characteristics, including the close channels, low insertion loss, wide out-of-band rejection, and high isolation, which can be flexibly integrated into miniaturized RF/microwave/millimeter wave circuits and systems.

## Conflict of Interests

The authors declare that there is no conflict of interests regarding the publication of this paper.

## Acknowledgments

This work was supported in part by the National Natural Science Foundation of China (Grant no. 61371047), Research Fund for the Doctoral Program of Higher Education of China (Grant no. 20110185110014), and the Fundamental Research

Funds for the Central Universities (Grant no. E022050205). Yongjun Huang also gratefully acknowledges the Scholarship Award for Excellent Doctoral Student granted by Ministry of Education of China (Grant no. A03003023901006).

## References

- [1] B. Strassner and K. Chang, "Wide-band low-loss high-isolation microstrip periodic-stub diplexer for multiple-frequency applications," *IEEE Transactions on Microwave Theory and Techniques*, vol. 49, no. 10, pp. 1818–1820, 2001.
- [2] Z. C. Hao, W. Hong, J. X. Chen, X. P. Chen, and K. Wu, "Planar diplexer for microwave integrated circuits," *IEE Proceedings—Microwaves, Antennas and Propagation*, vol. 152, no. 6, pp. 455–459, 2005.
- [3] Y.-S. Lin, P.-C. Wang, C.-W. You, and P.-Y. Chang, "New designs of bandpass diplexer and switchplexer based on parallel-coupled bandpass filters," *IEEE Transactions on Microwave Theory and Techniques*, vol. 58, no. 12, pp. 3417–3426, 2010.
- [4] M.-L. Chuang and M.-T. Wu, "Microstrip diplexer design using common T-shaped resonator," *IEEE Microwave and Wireless Components Letters*, vol. 21, no. 11, pp. 583–585, 2011.

- [5] Q. Xue, J. Shi, and J.-X. Chen, "Unbalanced-to-balanced and balanced-to-unbalanced diplexer with high selectivity and common-mode suppression," *IEEE Transactions on Microwave Theory and Techniques*, vol. 59, no. 11, pp. 2848–2855, 2011.
- [6] C. F. Chen, C. Y. Lin, B. H. Tseng, and S. F. Chang, "High-isolation and high-rejection microstrip diplexer with independently controllable transmission zeros," *IEEE Microwave and Wireless Components Letters*, vol. 24, no. 12, pp. 851–853, 2014.
- [7] F. Cheng, X. Q. Lin, Z. B. Zhu, L. Y. Wang, and Y. Fan, "High isolation diplexer using quarter-wavelength resonator filter," *Electronics Letters*, vol. 48, no. 6, pp. 330–331, 2012.
- [8] B. A. Belyaev, A. M. Serzhantov, and V. V. Tyurnev, "A microstrip diplexer based on dual-mode resonators," *Technical Physics Letters*, vol. 38, no. 8, pp. 743–746, 2012.
- [9] W. Che, X. Gao, and W. Feng, "Microstrip diplexer for GSM and WLAN bands using common shorted stubs," *Electronics Letters*, vol. 50, no. 20, pp. 1486–1488, 2014.
- [10] S. Srisathit, S. Patisang, R. Phromloungsri, S. Bunnjaweht, S. Kosulvit, and M. Chongcheawchamnan, "High isolation and compact size microstrip hairpin diplexer," *IEEE Microwave and Wireless Components Letters*, vol. 15, no. 2, pp. 101–103, 2005.
- [11] H. Liu, W. Xu, Z. Zhang, and X. Guan, "Compact diplexer using slotline stepped impedance resonator," *IEEE Microwave and Wireless Components Letters*, vol. 23, no. 2, pp. 75–77, 2013.
- [12] Q. Xue and J.-X. Chen, "Compact diplexer based on double-sided parallel-strip line," *Electronics Letters*, vol. 44, no. 2, pp. 123–124, 2008.
- [13] Z.-H. Bao, J.-X. Chen, E. H. Lim, and Q. Xue, "Compact microstrip diplexer with differential outputs," *Electronics Letters*, vol. 46, no. 11, pp. 766–768, 2010.
- [14] T. Yang, P.-L. Chi, and T. Itoh, "High isolation and compact diplexer using the hybrid resonators," *IEEE Microwave and Wireless Components Letters*, vol. 20, no. 10, pp. 551–553, 2010.
- [15] J.-Y. Zou, C.-H. Wu, and T.-G. Ma, "Miniaturized diplexer using synthesized microstrip lines with series LC tanks," *IEEE Microwave and Wireless Components Letters*, vol. 22, no. 7, pp. 354–356, 2012.
- [16] F. Cheng, X. Lin, K. Song, Y. Jiang, and Y. Fan, "Compact diplexer with high isolation using the dual-mode substrate integrated waveguide resonator," *IEEE Microwave and Wireless Components Letters*, vol. 23, no. 9, pp. 459–461, 2013.
- [17] R. Marqués, F. Martín, and M. Sorolla, *Metamaterials with Negative Parameters: Theory, Design and Microwave Applications*, John Wiley & Sons, Hoboken, NJ, USA, 2007.
- [18] J. Bonache, I. Gil, J. García-García, and F. Martín, "Complementary split ring resonators for microstrip diplexer design," *Electronics Letters*, vol. 41, no. 14, pp. 810–811, 2005.
- [19] Y. Dong and T. Itoh, "Substrate integrated waveguide loaded by complementary split-ring resonators for miniaturized diplexer design," *IEEE Microwave and Wireless Components Letters*, vol. 21, no. 1, pp. 10–12, 2011.
- [20] Y. Horii, C. Caloz, and T. Itoh, "Super-compact multilayered left-handed transmission line and diplexer application," *IEEE Transactions on Microwave Theory and Techniques*, vol. 53, no. 4, pp. 1527–1533, 2005.
- [21] T. Kodera and C. Caloz, "Integrated leaky-wave antenna-diplexer/diplexer using CRLH uniform ferrite-loaded open waveguide," *IEEE Transactions on Antennas and Propagation*, vol. 58, no. 8, pp. 2508–2514, 2010.
- [22] T. Yang, P.-L. Chi, and T. Itoh, "Compact quarter-wave resonator and its applications to miniaturized diplexer and triplexer," *IEEE Transactions on Microwave Theory and Techniques*, vol. 59, no. 2, pp. 260–269, 2011.
- [23] H. Zeng, G. Wang, D. Wei, and Y. Wang, "Planar diplexer using composite right-/left-handed transmission line under balanced condition," *Electronics Letters*, vol. 48, no. 2, pp. 104–106, 2012.
- [24] Y. Huang, G. Wen, and J. Li, "Systematical analysis for the mixed couplings of two adjacent modified split ring resonators and the application to compact microstrip bandpass filters," *AIP Advances*, vol. 4, no. 10, Article ID 107119, 2014.
- [25] B. Wu, X. Lai, T. Su, and C.-H. Liang, "Wideband cross coupled filter using split-ring resonator defected ground structure," *Journal of Electromagnetic Waves and Applications*, vol. 22, no. 11–12, pp. 1631–1638, 2008.
- [26] J. S. Hong and M. J. Lancaster, *Microstrip Filters for RF Microwave Application*, chapter 8, John Wiley & Sons, New York, NY, USA, 2001.